Modeling the Mechanics and Functionality of Soft Polymer Composites

Cerwyn Chiew

A dissertation

submitted in partial fulfillment of the
requirements for the degree of

Doctor of Philosophy

University of Washington

2023

Reading Committee:

Mohammad H. Malakooti, Chair

Lucas Meza

Junlan Wang

Program Authorized to Offer Degree:
Department of Mechanical Engineering

University of Washington

Abstract

Modeling the Mechanics and Functionality of Soft Polymer Composites

Cerwyn Chiew

Chair of the Supervisory Committee:
Professor Mohammad H. Malakooti
Department of Mechanical Engineering

Soft multifunctional polymer composites are a class of composite material that can exhibit low elastic modulus (<10MPa) while also have excellent thermal, electrical conduction, and energy storage properties. These functional properties are essential for the composite to be integrated into various devices such as soft thermal, dielectric actuators, tactile and strain sensors. Most existing soft polymers such as elastomers and hydrogels are highly deformable but are not necessarily ideal for device integration. Despite that, early pioneering studies had managed to use commercial elastomers such as Sylgard 184 and Ecoflex 00-30 to create pneumatic soft robots or flexible circuit boards for rigid electronics. However, these pristine polymers are electrically and thermally insulative which limits their potential in creating advanced devices. To overcome this, soft polymers such as elastomers are embedded with distinct types of conductive metallic, non-metallic solids, and more recently non-toxic liquid metals (LM) such as eutectic gallium-indium (EGaIn).

EGaIn polymer composite possesses attractive features for wearable applications because the combined fluidic and metallic nature of liquid metals enable the synthesized composite to retain high compliance while enhancing their final thermal, electrical conductivity, and permittivity. Despite that, high volume fraction (50%) of EGaIn inclusions is needed to achieve approximately ten times improvement to the conductive properties of the polymer composite. In addition, the native oxide shell formed around the EGaIn droplets highly influences the elasticity of the EGaIn polymer composite and their ability to form conductive pathways under mechanical loading. To understand the role of gallium oxide shell, two main modeling frameworks are introduced to correlate the relative size of this oxide shell with the bulk mechanical behaviors of EGaIn polymer

composite and to predict the rupture stress in the oxide shell when external mechanical loading is applied.

Alternately, solid conductive fillers can improve the functional properties such as the electrical, thermal conductivity, and permittivity of a soft composite by tenths to even hundredth times at low volume fraction. One of the promising nanomaterials capable of achieving such enhancement in a polymer composite is the recently found two dimensional (2D) metallic nanosheets known as MXenes. Titanium carbide (Ti_3C_2) is a common type of MXenes which can have an impressive lateral length of several microns with one nanometer thickness. In addition, Ti_3C_2 sheets are also an attractive nanomaterial because of their large intrinsic electrical conductivity and lower elastic modulus than other 2D nanomaterials, notably graphene. When these large 2D fillers are dispersed in polymers, these nanosheets can form percolation network at very low concentration (<1%) which can tremendously enhance the effective conductivity of the composite. However, the concentration of this 2D solid filler needs to be carefully optimized to ensure minimal stiffening effects of the overall soft matter composite while high enough for the composite to achieve large conductivity. To resolve this issue, the following dissertation presents a theoretical model that correlates the microstructure arrangement of MXene polymer composite with the resulting tradeoffs between their elastic modulus and their thermal or dielectric properties.

Viscoelasticity is a dominant mechanical behavior found in most soft matter composites, particularly those with hydrogel matrix. This property causes the composite to relax when constant strain is applied (stress relaxation) and to gradually increase in strain (Creep) when constant load is applied. This time-dependent mechanical behavior created a unique difficulty when conducting dynamic mechanical testing of layered-cell-in-gel composite as maintaining a constant mean stress/strain on the overall hydrogel composite is challenging. However, regulating this stress condition is vital to study the mechano-response of the embedded cells. Hence, to optimize the loading parameter applied on this hydrogel composite, the current dissertation presents an elegant predictive model based on micromechanics formulation which can help rapidly predict the stress-time behavior of the composite and to guide experiment executions.

Acknowledgements

I would like to express my sincere gratitude to the following individuals and organizations who have supported me throughout my thesis journey: First and foremost, I would like to thank my thesis advisor, Professor Mohammad H. Malakooti for his guidance, expertise, and support throughout the entire thesis process. I am grateful for the many hours of discussions, advice, and encouragement that he has provided, which have helped me to refine my research and develop my writing skills.

I would also like to thank the members of my thesis committee: Prof. Junlan Wang, Prof. Lucas Meza, and Prof. Navid Zobeiry for their time, expertise, and valuable feedback to the constructive improvement of my thesis.

I am also grateful to Wanwisa Kisalang, the UW mechanical engineering department graduate advisor, who has provided me with the resources, support, and encouragement necessary to complete my Ph.D.

I would like to acknowledge the support of my partner Tashi Sherpa, family, friends, and lab mates in the iMatter Lab, who have provided me with emotional support and encouragement throughout my academic journey. Their unwavering belief in me has been a constant source of motivation and inspiration.

Finally, with overwhelming gratitude, I want to pay tribute to the late Prof. Minoru Taya, who first introduced wondrous world of micromechanics to me and the elegance of Eshelby's method which as demonstrated in this work, it is a remarkably versatile technique that can solve a myriad of complex engineering problems such as in the modeling of soft matter composites.

Table of contents

Abstract i

Acknowledgements iii

Table of contents 1

Table of figures 6

List of tables 12

Chapter 1: Introduction 14

1.1 Soft matter composites 14

1.2 Soft multifunctional polymer composites 14

1.3 Liquid metal polymer composites 17

1.3.1 Gallium-based liquid metal nano- or micro- droplets 17

1.3.2 Synthesis of liquid metal polymer nanocomposites 19

1.4 Application of liquid metal polymer composites 23

1.5 MXene polymer composites 25

1.5.1 Synthesis of MXenes 25

1.5.2 Synthesis and applications of MXene polymer composites 27

1.6 Cell in agarose gel composite 27

1.7 Micromechanics modeling 28

1.8 Eshelby's equivalent inclusion method 31

1.9 Motivation and Overview 34

Chapter 2: Multiscale Micromechanics Modeling of Liquid Metal Polymer Composites 35

2.1 Introduction 35

2.2 Modeling Approach 38

2.2.1 Formulation of Double Inclusion Model 38

2.2.2 Effective Functional Properties 40

2.2.3 Finite Element Modeling 41
2.3 Results and Discussion 42
2.3.1 Mechanical Behavior of LMPCs 42
2.3.3 Functional Behavior of LMPCs 47
2.4 Conclusion 50
Chapter 3: Rupture Mechanics of Core-Shell Liquid Metal Droplets in Soft Matter Composites 51
3.1 Introduction 51
3.2 Modeling Approach 53
3.2.1 Geometric definition of Core-shell EGaIn particulate 54
3.2.2 Stress field inside and outside of EGaIn inclusion without oxide shell 55
3.2.3 Stress field inside and outside a core-shell EGaIn particulate 56
3.2.4 Stress interactions between neighboring core-shell LM droplets 59
3.3 Discussion 61
3.3.1 Validation with solutions of Benchmark problems 62
3.3.2 Stress in EGaIn core-shell inclusion with mild interaction 64
3.3.3 Size ratio of core-shell EGaIn droplets 67
3.3.4 Boundary conditions 68
3.3.5 Packing density 69
3.3.6 Prevent rupture of closely packed EGaIn droplets 70
3.4 Conclusion 71
Chapter 4: Novel Micromechanics Framework for Soft Multifunctional MXene Polymer Composites 72
4.1 Introduction 72
4.2 Modeling approach 74
4.2.1 Micromechanics model formulation 74

4.2.2 Effective properties of MXene clusters 76
4.2.3 Effective property of MXene polymer composites 78
4.2.4 Interchangeability of property tensors 79
4.2.5 Cauchy's cumulative probability function for modeling microstructure evolution 80
4.2.6 Resistance function (Functional Properties) 81
4.2.7 Finite element method 82
4.4 Results and discussion 83
4.4.1 Input properties for modeling MXPCs 83
4.4.2 Mechanical properties 84
4.4.3 Experimental comparison (Stiffness) 85
4.4.4 Finite element method validation (Stiffness) 86
4.4.5 Soft Interphase 87
4.4.6 Thermal properties 88
4.4.7 Finite element method comparison (Thermal conductivity) 89
4.4.8 Experimental comparison (Thermal Conductivity) 90
4.4.9 Thermal conductivity and elastic modulus correlation 91
4.4.10 Dielectric properties 93
4.4.11 Finite element method comparison (dielectric constants) 95
4.4.12 Experimental comparison (dielectric constants) 96
4.4.13 Dielectric constants and elastic modulus correlation 97
4.5 Summary and conclusion 98
Chapter 5: Viscoelastic Model for Cells Layered in Agarose Gel Composite 100
5.1 Introduction 100
5.2 Experimental details 104
5.3 Viscoelastic model 105

5.3.1 Homogenization of layered cell-in-agarose gel composite. 105
5.3.2 Boltzmann superposition theory 107
5.3.3 Modified Concentric Cylindrical Model (CCM) based on MSICD Experimental Setup 110
5.3.4 Corresponding Principle 113
5.4 Results and discussions 113
5.5 Summary and conclusion 115
Chapter 6: Summary and Future Work 117
6.1 Summary 117
6.2 Recommendations 118
6.2.1 Liquid metal polymer composite 118
6.2.2 MXene polymer composite 118
6.2.4 Viscoelastic behaviors in soft matter composites 119
Vita 120
Appendix 121
1. Supplementary Information for chapter 2 121
1.1 Eshelby's Tensor for Spherical Inclusion 121
1.2 Generalized Double Inclusion Model 121
1.3 Extending DI for Functional Properties 122
1.4 Formulation of Style's Model 122
1.5 Two-level Double Inclusion model with log-normal inclusion size distribution 123
1.6 Details of Finite Element Modeling 125
1.7 Interpolated Two-level DI model for Functional Properties. 127
2. Supplemental Information for chapter 3 128
2.1 Exterior Eshelby's Tensor 128

2.2 Internal Eshelby's Tensor 131
3. Supplemental Information for chapter 4 132
3.1 Eshelby's tensor (Mechanical Property) for finite cylinder and ellipsoidal inclusion .. 132
3.2 Flat/finite cylinder Eshelby's tensor (Functional Property) 134
3.3 Percolation volume fraction of MXPCs 135
4.6.3 Orientation averaging 135
3.4 Interchangeability of property in IMT model 137
3.5 Input material properties for IMT model and finite element method 138
3.6 Resistance Function 138
3.7 Boundary conditions in FEM 139
3.8 Multilayer MXene in hard or soft polymer matrix 140
4. Supplemental Information for chapter 5 142
4.1 Prony series parameters of agarose gel and cancer cells 142
4.2 Boltzmann Superposition Convolution Integral Solutions 145
4.3 Modifying Concentric Cylindrical Model (CCM) based on experimental setup. 148
Reference 152

Table of figures

Figure 1. Processing liquid metal nanoparticles (LMNPs) via high intensity sonication and shear mixing. Left: Image of bulk liquid metal being poured into a cup (Credit: Indium Corporation). Top right: Transmission electron microscopy (TEM) image of LM nanoparticles synthesized *via* sonication with thiol ligands. Reproduced with permission [57], copyright 2016, Wiley-VCH. Bottom right: 3D nano-CT image of LM particles produced by emulsion shearing in uncured polymer. Reproduced with permission [58], copyright 2019, Wiley-VCH. 18

Figure 2. (a) SEM (left) and 3D Nano-CT (right) image of LM composite with average diameter ~2 μm embedded in Sylgard 184. Reproduced with permission [58], copyright 2019, Wiley-VCH. (b) Microscopy images of cross-sections of LM composites with Sylgard 184 as the matrix to show the influence of mixing time on the final droplet sizes. The mixing rate was fixed at 1500 RPM (c) Average LM particle radius as a function of mixing time for fixed 1500 RPM. Reproduced with permission [80], copyright 2020, Wiley-VCH. 20

Figure 3. (a) Mean diameters of the Ga nanoparticles as a function of ultrasonication time at different ultrasonication powers at 20 °C. Reproduced with permission [59], copyright 2015, Wiley-VCH. (b) EGaIn droplets produced without thiol self-assembly and (c) EGaIn droplets produced with 1ATC9 and C12 thiol ligands. Reproduced with permission [53], copyright 2011, American Chemical Society. (d) Reversibly controlling the size of Ga NPs. The precursor Ga NPs were ultrasonicated in the presence of HCl and C12SH in 2-propanol at 50 °C (state 1→state 2) or 20 °C (state 1→state 3), and then again at 20 °C for 20 min (state 2 or 3→state 1) and (e) Mean diameters of the GaNPs in states 1–3. Reproduced with permission,[59] copyright 2015, Wiley-VCH. (f) The setup of dynamic temperature control for maintaining low sonication temperature when synthesizing LM nanodroplets with bPEG attachment. Reproduced with permission [84] copyright 2020, American Chemical Society. (g) EGaIn NP shape transformation and dealloying process with SEM image of shape transformed EGaIn NP. Reproduced with permission [85], copyright 2021, Wiley-VCH. 21

Figure 4. (a) Freezing and melting temperatures of bulk EGaIn and EGaIn particles encapsulated in different polymer matrices, (b) An electronic sleeve with a wearable thermoelectric generator powering a red LED light under large temperature gradient. Reproduced with permission [58], copyright 2019, Wiley-VCH. (c) Top: A schematic of the stretchable TEG with a thermally conductive EGaIn-PDMS composite as the material interface on the top and bottom. Bottom: A

stretchable thermoelectric wearable conforming to the forearm surface. Reproduced with permission [87], copyright 2020, American Chemical Society. (d) Time dependent infrared images of thermoelectric device with COOH-PDMS-CONH-PDMS-NH2 (unfilled PDMS) and surfaced modified liquid metal composite (SMEE) as thermal interfaces. Reproduced with permission [89], copyright 2021, Wiley-VCH. (e) Left: Schematic of dielectric generator (DEG) when stretched. The DEG consists of LM nanocomposite dielectric layer sandwiched by two EGaIn electrodes. Right: Using LM nanocomposite as dielectric layer improves the power output and efficiency than using pristine elastomer layer. Reproduced with permission [67], copyright 2019, Wiley-VCH. 25

Figure 5. (a) Scanning electron microscopy (SEM) image of the Ti_3AlC_2 (MAX phase) before etching. The resulting multilayered nanostructure of $Ti_3C_2T_x$ after etching with 30 wt. % Hydrofluoric acid. (c) Illustration showing single, several, and multilayer MXenes (i.e., $Ti_3C_2T_x$) randomly embedded in a soft polymer matrix. (d) SEM image of a single layered Ti_3C_2 on a porous alumina substrate. Retrieved images from Shuck et al.[98]. 26

Figure 6. The illustration of Eshelby's equivalent inclusion method. 31

Figure 7. (a) Schematic of liquid metal polymer composites (LMPCs), (b) Micrograph of dispersed EGaIn droplets in PDMS, (c) The core-shell structure of embedded liquid metal inclusions. 36

Figure 8. Micromechanics model: (a) Double inclusion (DI) model for LM fillers with the volume fraction of the core (f_Ω), shell (f_Γ), core-shell (f_R) and matrix (f_m) domains, (b) TDI: DI model with a two-level Mori-Tanaka (MT) homogenization technique, (c) GDI: generalized DI model with MT homogenization scheme. 38

Figure 9. Finite element model: (a) Cubic representative volume element (RVE) of the LMPCs, and (b) meshed RVE. 41

Figure 10. Effective elastic modulus (a) and shear modulus (b) of LMPCs predicted by two-level DI model for different volume fractions and shell thickness to diameter ratio (t/D) of LM inclusions. (c) Normalized effective elastic modulus of LMPCs for four different polymer matrices with nano or micro droplets (100nm, $t/D = 2\times10^{-2}$ and 10μm, $t/D = 2\times10^{-4}$). 43

Figure 11. The two-level double inclusion model is compared with Style's model [138,163] and experimental results [154] for effective elastic modulus of LMPCs with varying LM volume fractions and inclusion sizes. 44

Figure 12. FEA validation for the two-level DI (TLDI) model and comparison with GDI model. Estimated overall elastic modulus (a) and shear modulus (b) as a function of LM volume fraction and the ratio of oxide shell thickness to inclusion diameter. Insets: deformation of RVE under simple tension (a) and shear (b) and zoomed-in plot for GDI model. 46
Figure 13. Functional properties of LMPCs predicted using ITDI, TDI model and FEA and compared to experimental results: (a) effective dielectric constant (Experimental data [154]), (b) the effective thermal conductivity of the LM composites (Experimental data [152]). 48
Figure 14. (a) An illustration of a soft liquid metal polymer composite with layers of large and small LM droplets. (b) The individual large or small LM droplets can be modelled as a core-shell LM inclusion suspended in an infinite soft polymer matrix. Large spherical LM droplets will have small t/r2 while smaller spherical LM droplets will have large t/r2. 54
Figure 15. (a) The isolated core-shell liquid metal inclusion representing LMPC is decomposed into (b) single Ga oxide inhomogeneity and (c) single liquid metal inhomogeneity problems. Equivalent inclusion for (d) Ga oxide and (e) liquid metal single inhomogeneity problem to find the internal and external stresses of each case by EIM. (f) The equivalent inclusion for the LM inhomogeneity is applied with the eigenstrain stemming from the EIM of the Ga oxide inhomogeneity problem. 57
Figure 16. (a) Two generally distinct core-shell ellipsoidal liquid metal droplets embedded in a polymer matrix with a given arbitrary gap and direction in the composite. The two-interacting core-shell LM droplets are decomposed into an elastic problem involving just the (b) left hand side and the (c) right hand LM droplet in its respective polymer medium. (d) The superimposed stress/strain field of the two single inhomogeneity problems must be deducted with the case of an unfilled polymer medium under uniaxial stress loading to ensure equivalency to the original elastic problems involving two interacting LM droplets in their polymer composite. 60
Figure 17. (a) Two aligned interacting spherical cavities under triaxial loading following the benchmark problems from literature [193]. (b) The progression of the normal stress components along the x_2 axis predicted by the benchmark study matches exactly the results of our developed micromechanics model shown in (c). (d) Similarly, the normal stress components along x_3 axis that are obtained from the same benchmark study also illustrate good agreement with the predictions of our model in (e)..... 62

Figure 18. (a) A short fiber composite benchmark problem with the core has the same aspect ratios as the overall short fiber. (b) The predicted normal stresses ($\sigma 33/\sigma 0$) in the x3 direction by our micromechanics model when different aspect ratios (α) or interphase thickness (t) are considered. The original solution to the benchmark composite problem for (c) long aspect ratio fiber with thick interphase and (d) short aspect ratios fiber with thin coating. 64
Figure 19. (a) Uniaxially compressed polymer (Sylgard 184) composites with EGaIn inclusion that has no Ga oxide shell resulting in stress concentration distributions in the (b) x_3-, (c) x_2-, and (d) x_1- axis. The following stress heat maps represents the predicted stress distributions on the x_1x_2 plane which is at x_3=0. Other cases that are considered are the same composite but with (e) moderately large size ratio (t/r_2=0.1) and (i) extremely large size ratios (t/r_2 = 0.5). As a result, the final stress distribution for the normal stress concentrations at the x_3 (f and j), x_2 (g and k), and x_1 (h and l) directions are illustrated as heat map distributions. 66
Figure 20 (a) Uniaxial compression on Sylgard 184 composite with a pair of non-intersecting and spherical core-shell EGaIn droplets. The resultant normalized stress components when the ratio of the oxide shell thickness to the size of those droplets are small (b) and (c) large. Hydrostatic compression on a similar polymer composite that comprises of EGaIn droplets with thick oxide shell or small diameter. The resultant superimposed stress concentration when the center-to-center distance of the particles are (e) wide and (f) narrow. (g) When the polymer matrix is replaced with a softer elastomer medium, the stress concentration between the narrowly packed EGaIn droplets is reduced. The heap map stress concentration distribution for $\sigma 22/\sigma 0$ when the polymer matrix of the densely packed EGaIn droplets is used as (h) Sylgard 184 and (i) Ecoflex 00-30..... 68
Figure 21. (a) Micrograph of $Ti_3C_2T_x$ before exfoliation process, (b) schematic of MXene polymer composites with multilayered structured MXene fillers. 73
Figure 22. Illustration of the two-step homogenization approach of IMT model to evaluate the effective properties of MXPCs. (a) Each MXene cluster will be homogenized as equivalent medium embedded in a polymer matrix. (c) The equivalent medium substitutes the MC in the polymer matrix. (d) Final homogenization step to evaluate the overall properties of MXPCs with the (e) consideration of percolation microstructure based on Cauchy's cumulative probability function. 77
Figure 23. (a) The probability for the formation of interparticle contacts (overlapped interphase) of MC follows Cauchy's cumulative probability function (τ) as volume fraction (f_Ω) of MC

increases. (b) An illustration of MC dispersed in a polymer with the interparticle contacts forming a continuous percolation pathway. (c) The overlapped interphase phase of neighboring MC led to the local surge of functional property indicated by the drop in resistance function (T). 82
Figure 24. (a) RVE of MXPC with several layered MXenes. (b) The meshed body of the RVE with the layered MXenes configured as hexagonal packing. 82
Figure 25. (a) CCP interpolation function for MXene inclusions with different lateral diameter and layered structure. (b) IMT model predicts the effective elastic modulus of MXene-Sylgard 184 with fixed MXenes' size (a = 5 μm) but with distinct layered structures. (c) The effects of aspect ratio or diameter of monolayer MXene inclusions on the stiffness of MXene-Sylgard 184. (d) The measured elastic modulus of MXene-Sylgard 184 with L-MXene and MXene-NBR with S-MXene are compared with their respective predicted elastic modulus [205]. The elastic modulus of unfilled NBR is chosen as 2.24 MPa while for unfilled PDMS will be 0.4 MPa. (e) Longitudinal and (f) transverse elastic modulus evaluated from FEM are compared with the prediction results of IMT model..... 85
Figure 26. (a) Sylgard 184 composite with large (a=5μm) embedded single and multilayer MXenes exhibit suppressed stiffening behavior when PAAm is chosen as the interphase. (b) The use of smaller sized monolayer (n=1) MXene flakes with gel interphase results in the reduction of elastic modulus of MXene-Sylgard 184. 88
Figure 27. The IMT model predicted the longitudinal thermal conductivity of MXPCs with (a) different layers of embedded MC and (b) different lateral lengths of single sheet MXenes. (c) Experimental measurements [115,119] and (c) FEM results are compared with the predicted thermal conductivity of MXPCs. In this plot, the thermal conductivity of MXene-Sylgard 184 and MXene-PVDF are respectively normalized by the thermal conductivity of unfilled Sylgard 184 (κ_m=0.27) and unfilled PVDF (κ_m=0.19), respectively. The evaluated longitudinal thermal conductivity of MXPCs due to (e) changes in the MXenes' layered structures (fixed 5μm diameter) and (f) changes in the diameter of single sheet MXenes are compared with the predicted longitudinal elastic modulus of the composite due to the same respective variance in the layered structure and size of their MXene fillers..... 90
Figure 28. The predicted longitudinal dielectric constant of MXene-Sylgard 184 by IMT model due to (a) effects of layered structure of MXenes (fixed 5μm diameter) and (b) sizes of monolayer MXenes on the dielectric constants of the composite. All the dielectric constants presented in (a)

and (b) are all normalized with respect to the dielectric constants of the unfilled Sylgard 184 (εm = 2.7). (c) Finite element method results are compared with the predicted longitudinal (εL) and transverse (εT) dielectric constants of MXene-Sylgard 184. (d) The measured dielectric constants of PVDF-$Ti_3C_2T_x$ with assumed randomly oriented small (S-MXenes) and large MXenes (L-MXenes) are compared with modeling results [226]. (e) The predicted dielectric constants in Figure 28a is correlated with stiffness predictions in Figure 25b. (f) Similarly, the evaluated dielectric constants in Figure 28b is plotted with the stiffness predictions shown in Figure 25c. Both Figure 28e and Figure 28f are plotted for the predicted effective properties (dielectric constants and elastic modulus) up to 5% volume fraction (f_r) of MXenes. 94

Figure 29. (a) Illustration of the cell-in-agarose gel composite under compression by the dynamic plate movement (u(t)). (b) The layered cell-in-gel composite architecture. (c) Light microscopy image of MDA-MB-231 cancer cells at the bottom of cell-rich-layer with scale bar length of 200μm. Image retrieved from Takao et al.[228]. (d) Dynamic displacement loading dictating the compressive movement of the dynamic plate. (e) The measured force applied on the cell-in-gel composite during the dynamic displacement loading. 101

Figure 30. (a) The custom-built mechanical tester to apply dynamic loading on cell-in-gel composite. (b) Cross section view of the layered cell-in-gel composite architecture. 104

Figure 31. Standard linear solid model (SLS) made of Newtonian spring and dashpot. Two SLS in series representing layered agarose gel and cancer cells respectively (**Figure** 29B) in consistent to our experimental setup. Creep moduli are additive in this serial SLS configuration. 105

Figure 32. (A) The BCs defined mathematically from realistic experimental setup assuming homogenized gel cell medium. (B) A CCM model is used to visualize the realistic elastic problem. 110

Figure 34. (Left column) Experimentally measured displacement-time and force-time behavior of layered agarose gel and cells. (Right column) Viscoelastic model prediction of force-time response for displacement amplitude α=100μm. 114

Figure 34. (Left) Experimentally measured displacement-time and force-time behavior of layered agarose gel and cells. (Right) Viscoelastic model prediction of force-time response for small displacement amplitude (α=20μm). 114

List of tables

Table 1. Mechanical and functional properties of the phases in LM polymer composites 42

Table 2. Summary of the isotropic mechanical properties of the phases in a liquid metal polymer composite. 61

Some sections or verbatim in this dissertation are reproduced with permission from the following published journal articles listed below.

- Chiew C., Maria M., Malakooti M.H., (2021). Functional Liquid Metal Nanoparticles: synthesis and applications. Material Advances, 7799-7819, 2(24). [1]

- Chiew C., Malakooti M.H., (2021). A Double Inclusion Model for Liquid Metal Polymer Composites. Composite Sci. and Tech., 108752, 208. [2]

Chapter 1: Introduction

1.1 Soft matter composites

Soft matter composites are a class of materials that can be naturally found or synthetically made. These composites have unique properties that are enabled by the combination of two or more distinct phases, where at least one of these phases is considered as a soft material. Soft materials such as elastomers, colloids, hydrogels, and liquid crystals are materials that could deform easily when subjected to small external loads [3,4]. The following mechanical behaviors are the opposite of hard materials such as metals and ceramics which are significantly stiffer and brittle.

For a material to be categorized as soft, we refer to their measured elastic modulus which could be comparable to or lower than the stiffness of most human tissues (<10 MPa). For a more general definition, any multiphase material that showcases a certain degree of "squishiness" or highly deformable can be considered as soft matter composite. We could find many examples of soft and deformable matter in nature. One good example of naturally found soft matter composites is the cartilage which is a connective tissue found in the human body. Cartilage can be considered as a bio-composite made of predominantly water, flexible collagen fibers, and a protein matrix called proteoglycans which provide the composite with high toughness [5]. A combination of these two phases made the cartilage stiff yet tough and flexible enough to cushion the human joints from impact. This design of bio-composite is mimicked by many researchers to create synthetic hydrogel composite with high toughness. To mimic the role of flexible collagen fibers in the cartilage, researchers embed stiff cellulose [6] or metal fibers [4] in hydrogel matrix to strengthen and enhance the fracture energies of the overall soft composite. The resultant hydrogel composite does not only have high toughness and low stiffness but is also biocompatible which enables them to be potential biomaterials to replace damaged or wearied cartilages. Hence, soft matter composites can be engineered to be comparable to or even superior that the mechanical performance of naturally formed biomaterials which makes them an attractive field of research.

1.2 Soft multifunctional polymer composites

Soft matter composites are not only attractive for applications that require high mechanical compliance and toughness. When two or more distinct soft matter components are combined to form a composite, researchers can create soft composites with tunable multifunctionalities such as having high thermal, electrical conductivity, electrical permittivity, and magnetic properties. To

tune the mechanical and functional behaviors of the soft matter composite, the right blend of conductive solid or liquid nanoparticles in the soft matrix phase of the composite must be determined [3,7–9]. One example of such soft matter composite is polymer nanocomposites, where nanoparticles are dispersed in a polymer matrix. These nanoparticles can comprise of rigid or soft conductive materials such as metal alloys, metal oxides, ionic polymers, and carbon-based materials. For example, conductive solids such as carbon nanotubes, two-dimensional graphene, and MXenes have been successfully dispersed in soft elastomers such as polydimethylsiloxane (PDMS) to tremendously enhance the thermal conductivity or electrical conductivity of the elastomer composites [10,11]. Furthermore, the selection of the polymer matrix will also provide the soft composite to have additional intelligent behaviors such as self-healing [12–15], shape memory properties [16,17], and stimuli-responsiveness [18–20] which are all very important features to support their diverse applications in soft matter engineering. For instance, liquid crystal elastomers can be actuated by thermal stimulus and can demonstrate improved thermomechanical performances when conductive fillers are added in these polymers [21,22]. The presence of high concentrations of conductive fillers in a soft matter composite can also award novel smart features in the material. For example, when these conductive soft composites are stretched or deformed, this material can respond to those external stimuli by exhibiting change of resistance or piezoresistive effects as the extent of the filler's percolation networks decreases/increases when various modes of deformations are applied on this composite. Thus, apart being mechanically flexible, soft matter composites can be designed to behave as smart and intelligent materials which can possess all the unique capabilities of our skin such as self-healing property, pressure-, temperature- sensitivity and many other potential functionalities. Another unique soft matter composite is a gel-based composite which can exhibit viscoelastic behavior due to its embedded liquid phase and thus is also biocompatible. The following features are used to mimic the mechanical behaviors of actual human tissues and used for *in vitro* study of the mechanoresponsive behavior of cells. In this dissertation, all the following class of soft matter composites are referred to as soft multifunctional polymer composites.

An important factor that influences the final properties of a soft matter composite is the size, orientation, shape, concentration of their fillers (nano- or micro- particles), and the properties of both the matrix and the filler phases. Tuning the microstructures, the type of filler materials, and their polymer matrix is essential when creating soft matter composite with the targeted

combination of properties. For instance, the volume fraction of the solid particles added into a soft polymer matrix is often proportional to the effective elastic modulus and functional properties of the soft composite. When selecting the fillers' shape, the addition of two-dimensional (graphene and MXenes) [23,24] or one-dimensional particles (carbon nanotubes or fibers) [21,25–27] can significantly improve both the conductive properties and stiffness of the composite while also introducing large anisotropy in those composites if the orientations of these fillers are non-symmetric. Other than that, the size of fillers also plays a significant role in determining the final properties of soft matter composites. For example, if the aspect ratios (ratio of thickness or height to diameter) of the two- and one- dimensional particulates are large, we can create composites with large property enhancements at low filler concentrations. All in all, the following cases highlight the fact that depending on the intended final properties, composite designers must learn to navigate these wide range of microstructure parameters and then pick the appropriate processing techniques to achieve those optimized microstructure arrangements. Thus, the main motivation of this dissertation is to alleviate this conundrum by introducing several novel continuum modeling formulations that can accurately estimate the final properties of various emerging soft matter composites based on their designed microstructures.

The soft matter composites that are specifically investigated in this dissertation are the liquid metal polymer composites (LMPCs), MXene polymer composites (MXPCs), and the layered cell-in-gel composites. LMPCs and MXPCs are two recently emerged polymer composites that have potential applications in soft robotics, human computer interface, and wearable electronics. Liquid metal polymer composites are polymer composites which contain gallium-based room temperature liquid metal alloys that grant their composites with high compliance as well as high thermal and electrical conductivity [1,8]. MXene polymer composites on the other hand consist of highly conductive two-dimensional transition metal carbides/nitrides embedded in gels or PDMS [10]. This composite is unique as they can exhibit very impressively large thermal conductivity, dielectric, and electromagnet shielding properties at very dilute concentrations but suffer very large increase in their stiffness. Cell-in-gel composite is a biomimetic composite that is created to mimic the behavior of actual human tissues mechanically and physiologically. In this study, we are interested to understand and predict the stress time behaviors (i.e., viscoelasticity) of the soft biological composite where the developed model can also be translated to predict the viscoelastic behaviors of other class of soft matter composites.

Before establishing the key models used in this thesis study, I will provide a brief literature review of the current synthesis approaches and potential applications that are focused on LMPCs, MXPCs, and hydrogel-based composites. The review for the synthesis and applications of LMPCs was published previously in a review paper by Chiew et al.[1]

1.3 Liquid metal polymer composites

1.3.1 Gallium-based liquid metal nano- or micro- droplets

The fluidic and metallic properties of room temperature liquid metal alloys have attracted numerous studies to incorporate them as microfluidic-based stretchable conductors for soft and reconfigurable electronics [28,29] and cooling fluids for miniature electronics [30,31]. To serve these purposes, EGaIn (75% Gallium and 25% Indium by weight) and Galinstan (68.5% Gallium, 21.5 % Indium and 10% Tin by weight) are the two widely utilized Gallium (Ga) based room temperature LMs to date due to their low toxicity [28,32], low viscosity (2× of water) [33], high electrical conductivity [34], and high thermal conductivity [30,33]. With the recent adaptations of novel processing techniques, bulk LM alloys have also been facilely engineered as multifunctional nanocomposites[9,35] or functional nanoparticles [36] for diverse applications.

A unique feature of Ga-based LM alloys is their thin (1~3 nm) passivating Ga oxide interface which encapsulates the LM alloy droplets as a core-shell structure, even in trace amounts of oxygen [37,38] (Figure 1). This oxide interface exhibits viscoelastic behaviors [39], regulates the surface tension of Ga LM alloys and enables wettability with various surfaces [40,41]. With these features, bulk EGaIn had been directly used as soft cone-shaped microelectrode to accurately measure the electrical [42,43] and thermoelectric [44–46] properties of thin organic nanomaterials. Moreover, the reactive oxide skin on bulk Ga-based liquid metal alloys provided an advantage as catalyst for growing carbon nanotubes [47], thin films of inorganic thermoelectric materials [48], and novel 2D nanomaterials with high piezoelectric conversion [49,50]. When this bulk LM is downsized to nanodroplets, a large surface area of oxide layer is created, forming the primary stabilizing interface for synthesized LM micro or nanoparticles (NPs) in various mediums [51,52] Furthermore, the chemical reactivity of Ga oxide layer provides a customizable platform for targeted surface chemical functionalization or modification in order to tailor the nanoparticles' morphology and functional properties such as pH resistance, temperature changes, photothermal conversion, and electrical properties [36,53,54].

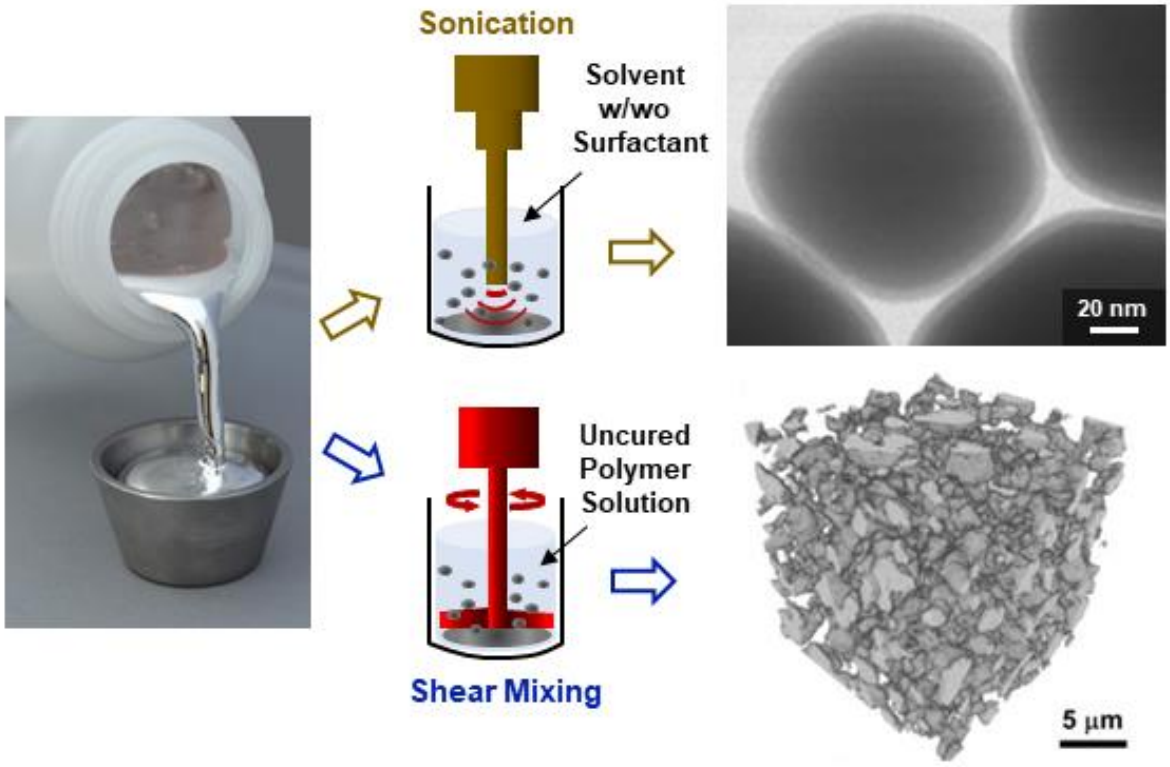

Figure 1. Processing liquid metal nanoparticles (LMNPs) via high intensity sonication and shear mixing. Left: Image of bulk liquid metal being poured into a cup (Credit: Indium Corporation). Top right: Transmission electron microscopy (TEM) image of LM nanoparticles synthesized *via* sonication with thiol ligands. Reproduced with permission [55], copyright 2016, Wiley-VCH. Bottom right: 3D nano-CT image of LM particles produced by emulsion shearing in uncured polymer. Reproduced with permission [56], copyright 2019, Wiley-VCH. The following grouped figure is reproduced with permission [1], copyright 2021.

The Ga oxide layer on the bulk liquid metal can be easily ruptured under applied surface stress. Once ruptured, it instantaneously reforms to stabilize the high surface tension (~0.5 $N \cdot m^{-1}$) of LM. Thus, when a continuous mechanical stress is applied, the oxide interface of the newly formed LM droplets will be repeatedly ruptured and reformed, allowing bulk LM to be rapidly downsized from the macro to micro and nanoscale. Some of the most common techniques to create micro/nanoscale LM particles include the sonication of bulk LM in a solvent via an ultrasonic probe [57,58] (Figure 1) or an ultrasonic bath [51,59]. *In situ* formation of LM microparticles in polymers or solvents has been done through mechanical shear forces between these two liquid phases. For this purpose, the bladeless planetary shear mixers[59–61] and overhead stirrers with impellers are chosen to provide more intense mixing [56,62,63]. To create a homogenous LM polymer nanocomposite, one or of these methods or their combinations are preferred [64,65]. The shear-based synthesis methods are attractive because of their much facile, scalable, and rapid processes to create LM particles with sizes ranging from hundreds of microns to hundreds of nanometers. Ultrasonication

methods, on the other hand, provide high mechanical energy *via* acoustic waves to rapidly downsize bulk LM to nanoscale and at the same time enable surface functionalization (i.e., surface *in situ* polymerizations, organic or inorganic material coatings) or chemical modifications on generated LM nanoparticles.

Reducing the size of LM droplets is desirable because it can suppress the freezing and melting points of its liquid core. For instance, the freezing point of EGaIn is suppressed from -5.9 to -84.1 °C while the melting point decreases from 17.8 to -25.6 °C [56]. Similarly, the following supercooling property is also found in Field's metal (i.e., eutectic bismuth-indium-tin alloy) based LM nanoparticles where its suppressed freezing temperature is closer to room temperature [63,66,67]. As a result, these supercooled LM nanoparticles can be used to create low temperature compliant thermal interfaces[56] and heat-free electronic soldering materials [63,67]. Also, in comparison to macroscale LM, nanoscale LM droplets have higher photothermal conversion efficiency for aiding intracellular drug delivery [54,68–70] and lower chemical reactivity with metals [71,72] while capable of increasing the thermal conductivity of traditional cooling fluids [73]. When LM nanoparticles are embedded in nanocomposites, their size and volume fractions are tailorable parameters that determine the final elastic and functional (i.e., dielectric, and thermal) properties of the composite [2,7,65]. For instance, liquid metal composites with embedded nanoscale LM particles have larger dielectric constants and stiffness, enabling soft dielectric and thermal actuators to generate higher actuation forces [64,65,74].

1.3.2 Synthesis of liquid metal polymer nanocomposites

Shear mixing in polymer precursor

Planetary shear mixing of two liquid phases in a dual axis centrifugal mixer is a common approach to synthesize liquid metal polymer composites. The final size of embedded liquid droplets depends on the viscosity of each liquid phase, their volume ratio, mixing speed, and duration of shear mixing. Initially, elastomer composites with LM inclusions with the average size varying from 20 to 140 μm were synthesized using mechanical shearing without an impeller [8,61,75,76]. In a recent effort, an overhead stirrer was used for *in situ* formation of EGaIn particles with an average size of 2 μm for a 50 % volume fraction EGaIn-PDMS composite [56]. In this process, the overhead stirrer or immersion mixer, commonly used for highly viscous fluids, applies intense mechanical shear forces to the polymer and LM to achieve the desired LM droplet size. Figure 5a

show the SEM image and 3D Nano-CT of the LM polymer composites that remain compliant and fully functional in extremely low temperatures (< −80 °C). In a more recent study, Ford et al. [77] conducted a systematic study on the role of processing parameters (i.e., RPM and time) in structural and functional properties of the LM composites that were synthesized using this method (Figure 2b). For example, at 200 RPM and 1500 RPM overhead mixing for 300 s, the obtained average radius of suspended LM droplets is 2.8 and 0.8 μm, respectively. On the other hand, if the mixing RPM is fixed at 1500 RPM, the average radius of LM droplets decreases to 5.8 μm and 0.8 μm after 10 s and 300 s total mixing time, respectively (Figure 2b-c). Despite the processing simplicity, the synthesized LM droplets have higher polydispersity compared to those synthesized via sonication.

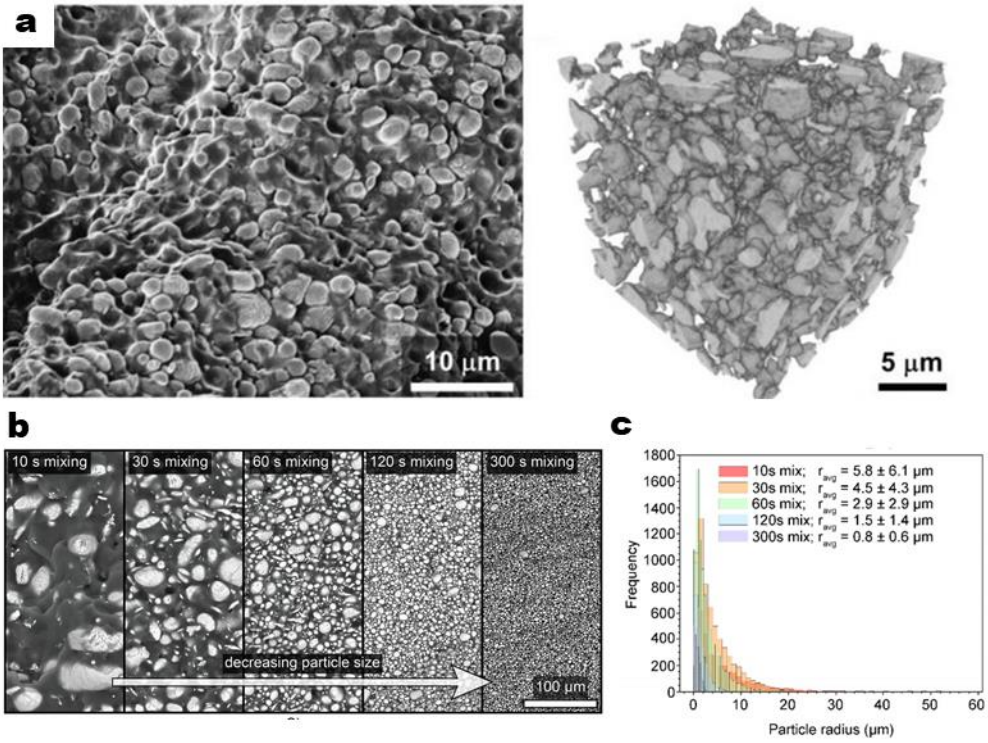

Figure 2. (a) SEM (left) and 3D Nano-CT (right) image of LM composite with average diameter ~2 μm embedded in Sylgard 184. Reproduced with permission [56], copyright 2019, Wiley-VCH. (b) Microscopy images of cross-sections of LM composites with Sylgard 184 as the matrix to show the influence of mixing time on the final droplet sizes. The mixing rate was fixed at 1500 RPM (c) Average LM particle radius as a function of mixing time for fixed 1500 RPM. Reproduced with permission [77], copyright 2020, Wiley-VCH. The following grouped figure is reproduced with permission [1], copyright 2021.

Sonication-based synthesis

To form a high concentration of nanoscale (i.e., <1 μm) LM droplets to be eventually encapsulated into a polymer composite, the passivating oxide shell of LM droplets must be ruptured at a faster rate than it is reforming. Mechanical shearing sometimes cannot apply a sufficient rate of applied

stress to produce a high yield of LM nanoparticles. This leads to the use of probe-based ultrasonication methods which can create continuous or pulsed acoustic cavitation to rapidly break down large liquid metal droplets into micro-/nanoscale particles. Intense shear mixing of bulk LM with an adsorbate (polyvinyl pyrrolidone or thiols) is only capable of slicing the LM alloys down to mostly micron scale whereas a sonication-assisted process can produce LM nanodroplets with narrower size distribution and as small as several tenths of orders of nanometers [58,78,79]. Also, using ultrasonication to produce LM nanodroplets is beneficial because it reduces the number of surfactants needed and consumes less energy than a shear-based synthesis process [80].

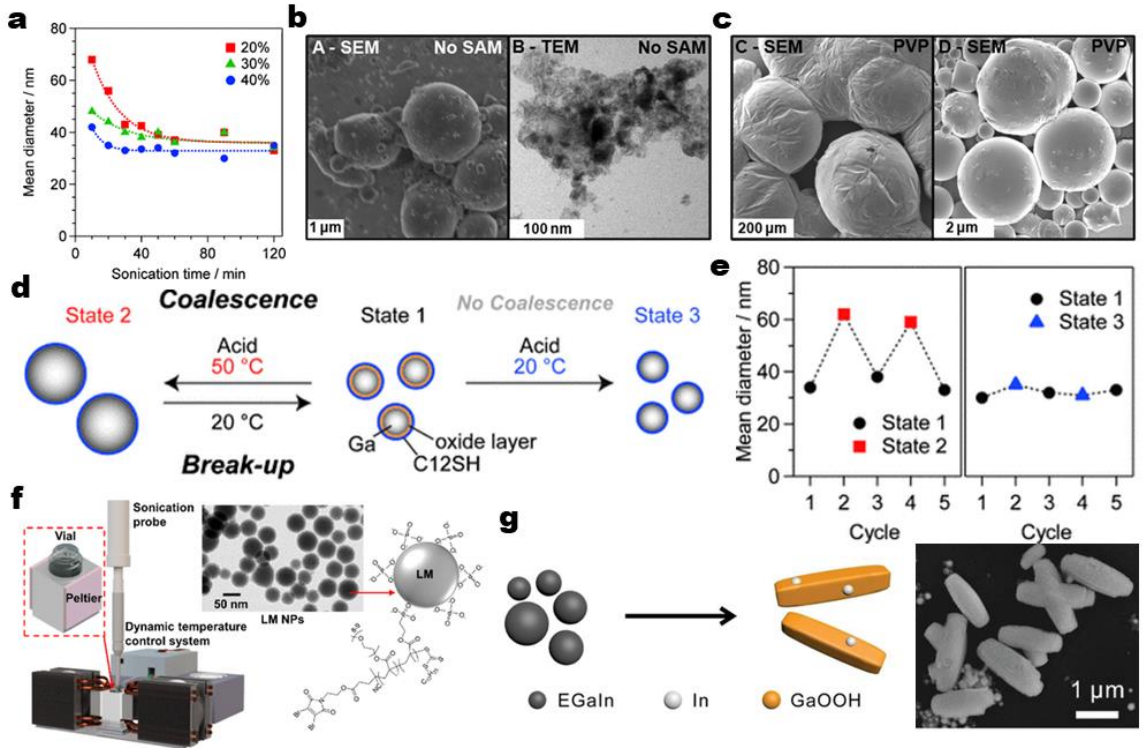

Figure 3. (a) Mean diameters of the Ga nanoparticles as a function of ultrasonication time at different ultrasonication powers at 20 °C. Reproduced with permission [57], copyright 2015, Wiley-VCH. (b) EGaIn droplets produced without thiol self-assembly and (c) EGaIn droplets produced with 1ATC9 and C12 thiol ligands. Reproduced with permission [51], copyright 2011, American Chemical Society. (d) Reversibly controlling the size of Ga NPs. The precursor Ga NPs were ultrasonicated in the presence of HCl and C12SH in 2-propanol at 50 °C (state 1→state 2) or 20 °C (state 1→state 3), and then again at 20 °C for 20 min (state 2 or 3→state 1) and (e) Mean diameters of the GaNPs in states 1–3. Reproduced with permission,[57] copyright 2015, Wiley-VCH. (f) The setup of dynamic temperature control for maintaining low sonication temperature when synthesizing LM nanodroplets with bPEG attachment. Reproduced with permission [81] copyright 2020, American Chemical Society. (g) EGaIn NP shape transformation and dealloying process with SEM image of shape transformed EGaIn NP. Reproduced with permission [82], copyright 2021, Wiley-VCH. The following grouped figure is reproduced with permission [1], copyright 2021.

Increasing the power and duration of the sonication will reduce the size of LM nanoparticles until the solution reaches an equilibrium. Yamaguchi et al.[57] illustrated this behavior for Ga particles

and the relationship between the delivered power and the size of particles (Figure 3a). However, sonication without surfactant in ethanol often results in LM nanodroplets with highly polydisperse size, undefined spherical shape (textured, oblong, and deformed spheres), and short-term dispersion stability as shown in Figure 3b [51,83]. The thin passivating oxide shell of LM nanodroplets can be weakened by various chemical stimuli (acidic, basic, and highly oxygenated surroundings) and often require additional interfacial reinforcement to prevent LM nanodroplets from recoalescing. During sonication, the high energy acoustic cavitation exposes the reactive LM alloy core, causing it to actively bind with self-assembling ligands (surfactants) while suppressing the formation of Ga oxide. As a result, the synthesized LM nanodroplets have a more rigid and chemically robust protective interface granted by the thiol layers. For example, well-formed and predominantly spherical LM particles are generated when bulk LM is sonicated in both 3-mercapto-N-nonylpropionamide (1ACT9) and 1-dodecanethiol (C12) ethanolic solution (Figure 3c). Comparing these two thiol ligands, LM nanoparticles generated with 1ACT9 surfactant result in a better yield of spherical nanoparticles.

With the oxide shell replaced by more resilient ligands, the formed nanoparticles will not recoalesce as easily and are more resistant to surrounding changes in pH or temperature. Nevertheless, regulating the acidity, temperature, and processing time can enable reversible size control of synthesized liquid metal nanoparticles [57]. For example, 35 nm liquid Ga particles can be synthesized by sonication at low temperatures (20 °C) and at high temperatures (50 °C) (state 1 to 2) in the presence of dodecanethiol (C12SH) surfactant (Figure 3d-e). Also, the size of these liquid Ga nanoparticles with C12SH surfactant is reversible. To demonstrate this, the Ga nanoparticles with a mean size of 35 nm are unchanged in the presence of acid when sonicated at low temperature (20 °C) because of the surface stabilization by C12SH thiol at the interface of the particles. However, when sonicating at a higher temperature, around 50 °C, the size of these same Ga nanoparticles doubles (~60 nm) despite having additional interfacial stabilization by C12SH as shown in Figure 3e. Since temperature and surfactants serve as critical processing parameters for the size and surface properties of synthesized LM nanodroplets, a dynamic temperature control (DTC) system for improving production of LM nanoparticles *via* probe sonication has been recently introduced [81]. Using DTC during sonication is beneficial because it enables a high concentration of LM nanoparticles to be produced by preventing the solvent from overheating and evaporating. For example, pulsed sonication of bulk LM in solvent for 15 minutes with DTC can

produce large concentrations of LM NPs with an average size of 50 nm (Figure 3f). The same LM nanoparticles can also be simultaneously grafted with stabilizing polyethylene glycol polymer brush (bPEG) at the interface for their long-term colloidal stability.

To produce nanoscale LM particles, longer sonication time is required but this often causes excessive production of heat in the solvent-LM mixture. Consequently, this longer processing duration can elevate the synthesis temperature and cause excessive oxidation, dealloying, and an undesirable shape or phase transformation of the generated LM nanoparticles as shown in Figure 3g [82]. Moreover, when sonicating LM in an aqueous solvent without surfactant, the observed phase and shape transformations of LM nanoparticles become more prevalent [52]. This happens due to the uncontrollable production of ellipsoidal shaped gallium oxide monohydroxide (GaOOH) which causes Ga to be separated from its constituent elements (i.e., indium and tin) of the eutectic metal alloy. One strategy to mediate the production of GaOOH and make the shape of generated LM nanoparticles controllable in water is utilizing water-soluble melanin nanoparticles (MNPs) as the additional protective layer. This is possible because MNP exhibits strong binding affinity with the Ga oxide layer while also being compatible and stable in water [68]. In addition, the incorporation of MNPs allows the synthesis of various EGaIn nanostructures, ranging from nanorice, nanosphere, and nanorod. With MNPs as the protective agent, the following shapes are now regulated by selecting the optimum amount of MNPs, sonication time, and temperature of aqueous solvent during the synthesis of LM nanoparticles.

1.4 Application of liquid metal polymer composites

Liquid metal composites with embedded micro or nanosized particles have been used as thermal interfaces and electrical interconnections for stretchable and wearable thermoelectric energy generators (TEG) [56,84,85] The use of nano-/microparticles enables the suppression of freezing and melting points of LM droplets from those of bulk LM. When this freezing point is lower than the glass transition temperature of the encapsulating polymer, the LM composite can remain soft and stretchable even at extremely low temperatures as the LM inclusions remain fluid. Moreover, this suppressed freezing point or supercooling property of LM micro/nanoparticles occurs independently of the type of encapsulating polymers (Figure 4a). Thus, this enables a broad range of LM polymer composites to remain compliant at extreme low temperatures, in the range of -85°C. To take advantage of this property, this LM composite is used as a compliant thermal

interface of a wearable TEG for harnessing body heat in cold conditions to electrically power an electronic sleeve (Figure 4b) in addition to powering a wearable pulse oximeter sensor [56]. One unique feature that set LM elastomer composite apart is it can remain electrically insulative even with high volume loading of LM droplets. At the same time, this composite can become electrically conductive when the embedded LM droplets coalesce by external loading which is a process known as “mechanical sintering”. > Thus, since LM composites can also form conductive traces by selective mechanical sintering, the composite can serve as both a thermal conductor and electrical interconnector [84]. With these combined functionalities, the LM composite can be used to fabricate soft and stretchable thermoelectric devices by replacing conventional stiff interconnectors such as copper and silver with stretchable activated traces of LM particles. In a more recent study, LM elastomer composites with enhanced thermal conductivity are used as thermal interface material to fabricate not only flexible but also stretchable thermoelectric generators as shown in Figure 4c.

Smaller liquid metal particles in elastomer composites prevent the leakage of LM at high volume fractions, which may cause undesirable LM contact on skin and the formation of short circuit within the device. However, reducing the particle size to the nanoscale level can stiffen the LM-PDMS composites with limited improvement of their thermal conductivity because of low LM volume fraction (<20%) in nanocomposite. Thus, to reap the benefits of LMNPs while maximizing thermal conductivity, high volume fractions of LMNPs should be embedded in the polymer matrix without a significant effect on the composite’s stiffness. A recent work overcomes this challenge by modifying the surface of LMNPs with carboxylic acid terminated PDMS to fabricate a stretchable LM nanocomposite with up to 44 % filler volume fraction and with reasonable stretchability (110 % strain break; 350 % for unfilled polymer) [86]. With this novel LM nanocomposite, a stretchable and thermally conductive thermal interface can be demonstrated to enhance the temperature gradient across a unit cell thermoelectric generator during active heating or cooling as shown in Figure 4d. Another use of LM nanodroplets is the production of stretchable high dielectric material for fabricating stretchable dielectric energy generators with high power conversion efficiency as shown in Figure 4e [65]. This is possible because nanoscale LM inclusions can increase the effective dielectric constant of LM composites with a moderate decrease in compliance.

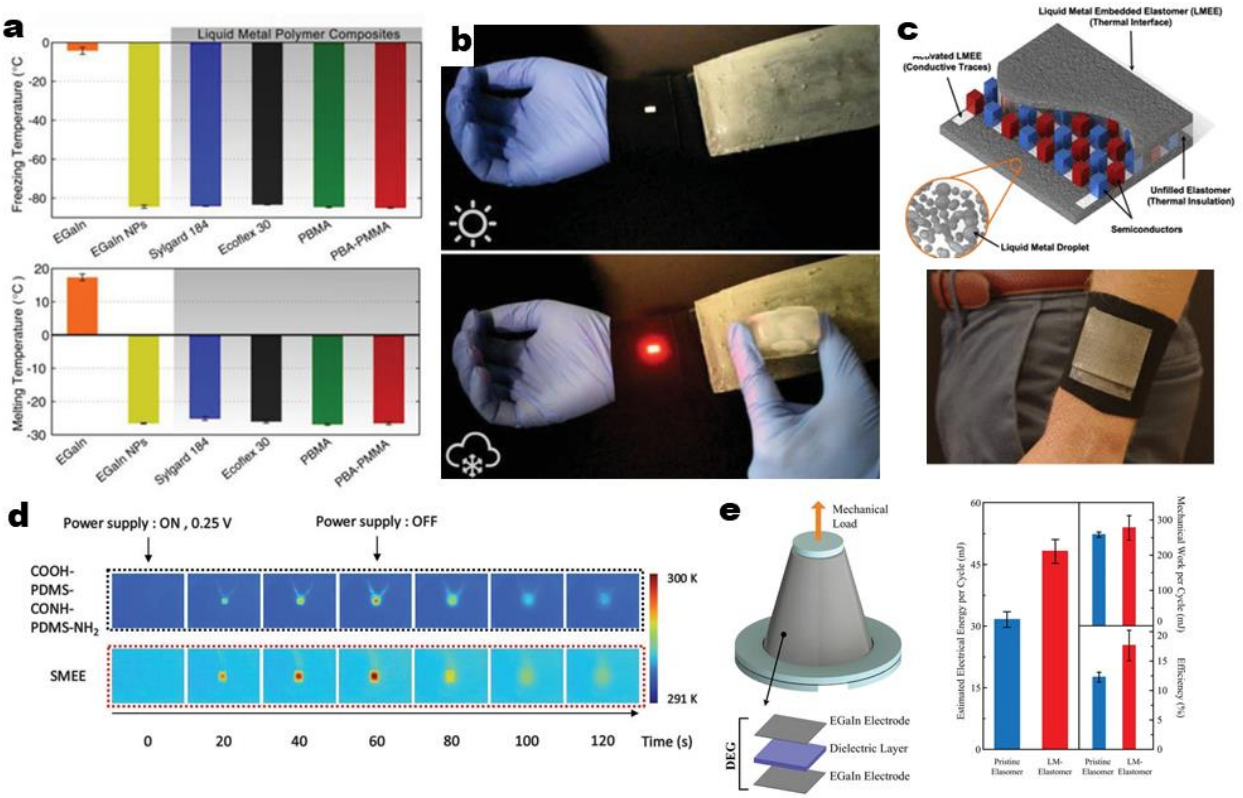

Figure 4. (a) Freezing and melting temperatures of bulk EGaIn and EGaIn particles encapsulated in different polymer matrices, (b) An electronic sleeve with a wearable thermoelectric generator powering a red LED light under large temperature gradient. Reproduced with permission [56], copyright 2019, Wiley-VCH. (c) Top: A schematic of the stretchable TEG with a thermally conductive EGaIn-PDMS composite as the material interface on the top and bottom. Bottom: A stretchable thermoelectric wearable conforming to the forearm surface. Reproduced with permission [84], copyright 2020, American Chemical Society. (d) Time dependent infrared images of thermoelectric device with COOH-PDMS-CONH-PDMS-NH2 (unfilled PDMS) and surfaced modified liquid metal composite (SMEE) as thermal interfaces. Reproduced with permission [86], copyright 2021, Wiley-VCH. (e) Left: Schematic of dielectric generator (DEG) when stretched. The DEG consists of LM nanocomposite dielectric layer sandwiched by two EGaIn electrodes. Right: Using LM nanocomposite as dielectric layer improves the power output and efficiency than using pristine elastomer layer. Reproduced with permission [65], copyright 2019, Wiley-VCH. The following grouped figure is reproduced with permission [1], copyright 2021.

1.5 MXene polymer composites

1.5.1 Synthesis of MXenes

MXene is the most recently discovered family of conductive two-dimensional (2D) nanomaterials derived from layered ternary MAX compound where 'M', 'A', and 'X' constitute the transition metals, group 13 or 14 elements, and carbon or nitrogen elements, respectively [87]. When 'A' atoms are chemically removed from the MAX precursor, MXene flakes are obtained with a general chemical formula of $M_{n+1}X_nT_x$ where T_x is the surface functional groups that can consist of oxygen, hydroxyl, chloride, or fluoride groups. Currently, titanium carbide ($Ti_3C_2T_x$) is the most used MXene derived from the removal of aluminum atoms from titanium aluminum carbide (Figure 5a) [10,88–90]. $Ti_3C_2T_x$ standouts than other nanomaterials because of its superior thermal (55.8W·m-

$^{1}\cdot K^{-1}$), electrical conductivity (i.e., $1 S\cdot cm^{-1}$ to $20{,}000 S\cdot cm^{-1}$), lateral sizes (100nm - 10µm), and highly ordered accordion nanostructures as shown in Figure 5a [91–95]. Despite that, MXene's impressive conductive properties and nanostructures are unstable [96]. For instance, when pristine $Ti_3C_2T_x$ reacts with oxygen, this MXene will decompose into titanium dioxide and carbon nanoparticles which cause the electrical conductivity of $Ti_3C_2T_x$ to degrade by 50% after only two weeks of exposure [97,98]. Surface treatment [98] and extreme cold storage [99] are several strategies that can maintain the property of MXenes for long-term storage. Nevertheless, one of the simpler methods to both preserve and harness the properties of MXenes for application purposes is by encapsulating MXenes in polymer matrices as MXene polymer composites as illustrated in Figure 5c [10,11].

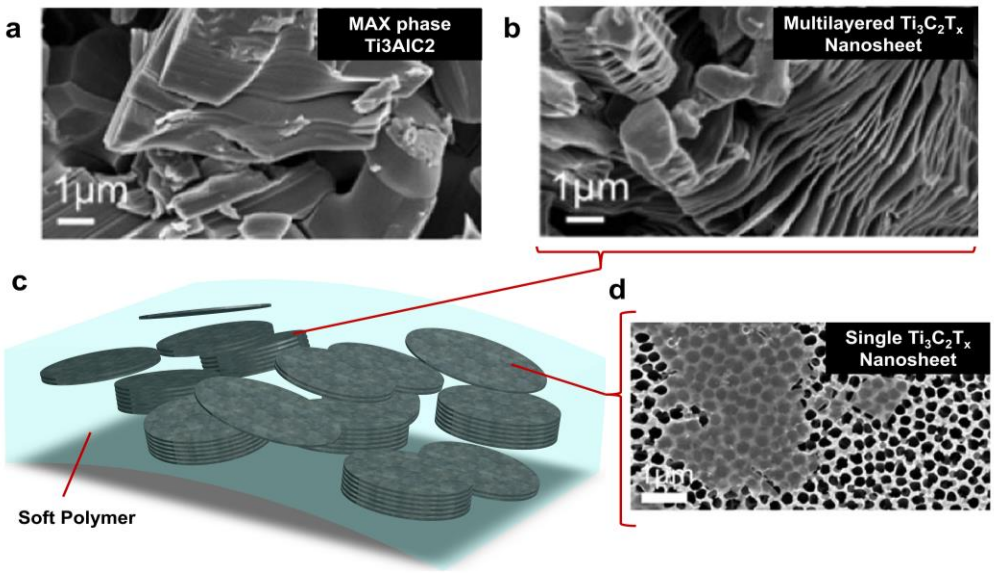

Figure 5. (a) Scanning electron microscopy (SEM) image of the Ti_3AlC_2 (MAX phase) before etching. The resulting multilayered nanostructure of $Ti_3C_2T_x$ after etching with 30 weight % Hydrofluoric acid. (c) Illustration showing single, several, and multilayer MXenes (i.e., $Ti_3C_2T_x$) randomly embedded in a soft polymer matrix. (d) SEM image of a single layered Ti_3C_2 on a porous alumina substrate. Reproduced with permission [100], copyright 2020.

Multilayer MXenes can be synthesized with higher yield (~100%) than single sheet MXenes because MXenes are originally derived as multilayer structure after the preliminary chemical etching process (Figure 5b). To obtain large single layer MXene nanosheets, a series of delamination and washing processes of multilayer MXenes are employed [101]. As a result, retrieving single layer MXenes (Figure 5d) is costly, not environmentally friendly, and not scalable for the sustainable production of MXene polymer composites. In contrast, multilayer MXene fillers are more favorable when it comes to making low cost, scalable, and green MXPCs. Although

single layer MXenes is preferable when it comes to creating MXPCs with the largest possible improvement in their thermal and electrical conductivity, these fillers can also cause their composite to have large stiffness enhancements even at dilute concentrations.

1.5.2 Synthesis and applications of MXene polymer composites

Initially, the packaging materials of most synthesized MXene polymer composites are predominantly water-soluble polymers such as polyvinyl alcohol [92,94], polydiallyldimethylammonium chloride [102], polyvinyl chloride [102], epoxy [103,104], and polyacrylamide [105–107]. These water-soluble polymer matrices are selected because the hydrophilic surface functional groups on MXene nanosheets allow MXenes to be solution processable and highly dispersible in these polymers. However, these polymers (i.e., hydrogels) either turn brittle when dehydrated [108–110] or some have elastic modulus (>1GPa) too stiff for certain wearable applications. As a result, polymer matrices with low Young's modulus such as elastomers and rubbers can be alternately used to create more compliant MXene polymer composites [24,111–115]. Since these polymers are often water-insoluble (i.e., hydrophobic), only low volume fraction of MXenes can be usually dispersed in these polymer matrices to prevent extensive particle agglomeration at higher filler concentration. Thus, MXenes concentrations in these polymers need to be limited. Nevertheless, MXenes that had been successfully embedded in these soft polymers (i.e., elastomers or rubbers) had resulted in the emergence of diverse flexible multifunctional composite that can exhibit excellent supercapacitance [92,116,117], electromagnetic shielding behaviors [91,118,119], triboelectricity [120–122], acoustic energy harvesting [123], thermal management [113], and ultrasensitive strain detection functionalities [89,116]. Despite these positive functional attributes, MXene is a solid filler with large surface areas. Thus, the Young's modulus of the following MXPCs will inevitably increase even when the volume fraction of MXenes in soft polymer matrix is kept low. This also means that the stretchability of MXPCs will also be significantly limited as well as the mechanical performance, and durability of MXPCs. Hence, a predictive tool that investigates this tradeoff between functionality and mechanical performance of this composite is desirable.

1.6 Cell in agarose gel composite

Agarose gel consists of open structures of polysaccharides which form by hydrogen bonds and filled by predominantly water [124,125]. The stiffness and viscoelastic behavior of the agarose gel

can be regulated by controlling the concentration of agarose powder during the gelation process which takes place when its aqueous solution is cooled. Historically, agarose gel had been used as diffusive medium for separating DNA fragments of varying sizes by electrophoresis due to its inherent porous biopolymer microstructure which can be done by varying gel concentrations [126]. The diffusive nature, biocompatibility and viscoelastic mechanical behavior of agarose gel had made it a popular phantom material for biomedical/biomechanics research to replicate the mechanical behavior of brain tissue [126], cartilage [127], and human skin [128]. For instances, agarose gel can emulate the poroelasticity of the brain tissue at low gel concentration (<0.6%) providing a realistic medium for testing brain infusion equipment and as a phantom material for human cartilage to enable the validation of the mechanical methods and modelling for determining dynamic stiffness of cartilage [127]. Urrea et al.[128] used agarose gel to investigate the extent of organ tissue damage at different needle insertion velocity. In recent years, agarose gel has been widely used for cell mechanics experiment to study the mechano- and physiological responses of cancer cells [129–132].

One way to study the mechano-response of cancerous or healthy cells is to embed or layer these cells in agarose gel [131,133,134]. The following agarose gel matrix serves as a medium separating the external environment with embedded cancer cells to supply nutrition, prevent contamination, and maintain isotonic condition for the life sustenance of the embedded or layered cancer cells. With this functionality, researchers can solely investigate the physiological response of those cells (growth, death rate, death modes) when confined or when mechanical stresses are applied externally through the gel. In this dissertation, I will consider the latter case when modeling the viscoelastic response of the layered cell in gel composite.

So far, we have introduced the background of the soft matter composite materials that will be investigated in this work. Next, to predict the mechanical and functional properties of soft matter composites, we will introduce the background of the modeling techniques mainly employed in the current study which is known as micromechanics modeling.

1.7 Micromechanics modeling

Micromechanics encompasses a branch of mechanics that relates the microstructure of materials with the effective mechanical properties of various types of heterogeneous materials. At its beginning stages, this method was simply an extension of continuum theory of elasticity to

estimate the stress and strain fields inside and outside a defect or inhomogeneities of a heterogeneous solid. Toshio Mura first demonstrated the versatility of this method in his seminal book published in 1987 "*Micromechanics of defects in solids*" which formalizes the micromechanics model alongside the prominent works contributed by other applied mechanicians at that time [135]. He had shown that micromechanics models can be used to model the common materials' mechanical behaviors such as plasticity, dislocations in metals, and to approximate the constitutive equations for composite materials. Alternatively, micromechanics models can also be a powerful tool used to understand the failure mechanisms of materials at the microscale such as fracture mechanics as well as fatigue failures.

The main motivation of micromechanics modeling in this work is to understand how the microstructure, composition, and properties of phases at the microscale influence the behavior of the soft matter composites at the bulk scale. To accomplish this, the micromechanics model needs to find the average field properties (i.e., stress and strains) of the constituent phases within the composite when the material is deformed (applied boundary conditions). The following quantities are useful to develop the constitutive laws such as stiffness ($\mathbf{C}$) tensor of the composite [136–139]. For example, consider a multiphase composite with *n* number of distinct phases. The mean stress vector ($\overline{\boldsymbol{\sigma}}$) of the overall composite is simply the sum of the product of mean stress field in each phase ($\overline{\boldsymbol{\sigma}_j}$) with the corresponding volume fraction of the phase (f_j) (Equation 1). Similarly, the mean strain field of the overall composite is also the sum of the product of mean strain field in each phase ($\overline{\boldsymbol{\varepsilon}_n}$) with the corresponding volume fraction of the phase (f_n). By taking the matrix product of mean stress vector with the transpose of the mean strain vector, we can obtain the stiffness tensor for the composite (Equation 3).

$$\overline{\boldsymbol{\sigma}} = \sum_{j}^{n} f_j \, \overline{\boldsymbol{\sigma}_j} \tag{1}$$

$$\overline{\boldsymbol{\varepsilon}} = \sum_{j}^{n} f_j \, \overline{\boldsymbol{\varepsilon}_j} \tag{2}$$

$$\mathbf{C} = \overline{\boldsymbol{\sigma}} : (\overline{\boldsymbol{\varepsilon}})^T \tag{3}$$

$$\overline{\boldsymbol{\varepsilon}_j} = \mathbf{A}_j : \overline{\boldsymbol{\varepsilon}} \tag{4}$$

Micromechanics models can be classified as numerical models or analytical models. For the analytical approach, a strain concentration tensor ($\mathbf{A}_j$) is introduced (Equation 4). This term is also generally known as polarization tensor which describes how much larger the magnitude of the average strain field in each distinct phase in comparison to the overall mean strain of the composite. Analytical micromechanics models will require to find $\mathbf{A}_j$ by utilizing mathematical tools (i.e., complex numbers, elliptical integrals, etc.) to provide compact closed-form solutions for the elastic boundary value problems which are often setup as a simplification of the real microstructure of the composite. To find $\mathbf{A}_j$, I will utilize Eshelby's equivalent inclusion method to find this important parameter which will be introduced in the next section. Another important consideration to obtain suitable $\mathbf{A}_j$ for the composite is to choose the best homogenization procedures (i.e., Mori-Tanaka, self-consistent, bounds, effective medium theories) for the composite material which depends on the distribution and extent of interparticle interactions in the composite.

The most common techniques used for numerical-based micromechanics model are the finite element methods [140,141] and more recently Fast Fourier transformation [142,143]. These methods are used to solve the elastic problem for boundary value problems (representative volume elements) with more complex microstructures. With this type of approach, we can determine $\bar{\boldsymbol{\sigma}}$ and $\bar{\boldsymbol{\varepsilon}}$ directly from the simulation results to extract the stiffness constitutive laws of the composite (Equation 4). For this dissertation, I have formulated an analytical micromechanics model to accurately predict the effective properties of LMPCs and MXPCs while utilizing finite element methods as a secondary way to validate my prediction results. Thus, micromechanics models are a powerful tool to design and optimize novel materials with specific properties. Micromechanics model can also be used to simulate and visualize the behaviors of materials under extreme conditions, such as high temperatures, pressures, and strains which are otherwise difficult to observe or measure experimentally. In my dissertation, the limitation of current existing micromechanics models will be addressed to be used for modeling, the mechanical and functional properties of various complex soft matter composites (LMPCs, MXPCs, and cell-in-gel composites).

1.8 Eshelby's equivalent inclusion method

To determine the effective properties of a multiphase material with micromechanics model, the mean stress or mean strain field ($\bar{\boldsymbol{\varepsilon}}$) perturbation at each distinct phase must be evaluated. To achieve this, a key concept in solid mechanics known as Eshelby's inclusion theory must be used. Eshelby's theory is a mathematical hypothesis in solid mechanics used to predict the internal stress ($\bar{\boldsymbol{\sigma}}_1$) and strain ($\bar{\boldsymbol{\varepsilon}}_1$) of an elastic inhomogeneous inclusion in an infinite medium [144]. John Douglas Eshelby [145] pioneered this concept in 1957 and has since found numerous practical analysis applications in material science, engineering [2,146,147], geomechanics [148], and biomechanics [149–151].

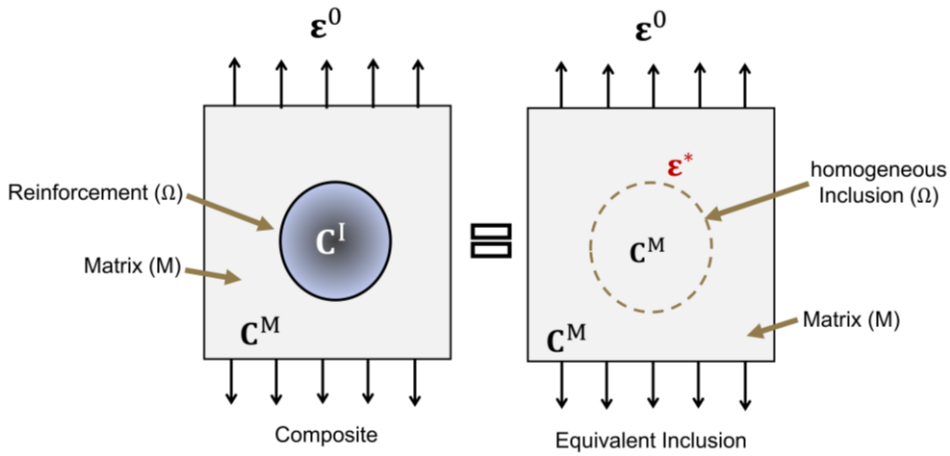

Figure 6. The illustration of Eshelby's equivalent inclusion method.

To best explain the fundamental concept of Eshelby's inclusion theory, let us consider a deformed composite material that has a single reinforcement or inclusion phase (Ω) of arbitrary shape and of dissimilar stiffness property ($\mathbf{C}^{\Omega}$) than its matrix ($\mathbf{C}^{\mathrm{M}}$) (Figure 6). Eshelby's equivalent inclusion theory (Equation 5) suggests that the reinforcement phase (Ω) of the following composite can be simulated by a homogenous inclusion (similar shape and size with Ω) which has a non-elastic strain transformation and suspended in a matrix phase of similar stiffness property (Figure 6). The following non-elastic transformation is known as "eigenstrain" and can physically exist as thermal expansion, phase transformation, or plastic strain in actual reinforcement phase of a composite. However, when it comes to finding the stress or strain concentration terms ($\mathbf{A}_i$), the following eigenstrain computation is exploited as a mathematical artifice which role is to match the internal stress or strain in the reinforcement phase of the composite with the actual stress or strain field

developed in the homogeneous equivalent inclusion. Hence, the nature of these described steps gives the method its popular name, that is the Eshelby's equivalent inclusion method (EIM).

To solve the equivalent inclusion problem, a transformation tensor known as Eshelby's tensor (**S**) is formulated which relates the eigenstrain ($\boldsymbol{\varepsilon}^*$) with the actual strain ($\boldsymbol{\varepsilon}$) in the equivalent inclusion or the reinforcement phase (Equation 6). This tensor is 4th order and is obtained by solving the strain field in the equivalent inclusion where the inclusion is given an eigenstrain ($\boldsymbol{\varepsilon}^*$). Due to the containment of the surrounding infinitely homogenous body, the effective strain ($\boldsymbol{\varepsilon}$ or ε_{ij}) in the homogenous inclusion can be determined using 2nd derivative of Green's function ($\mathbf{G}_{ij,kl}$) which is the solution to the static equilibrium equations for when the matrix materials are either isotropic or anisotropic. This tensor which is provided in its index notation S_{ijmn} can be calculated by solving the volume integral of the inclusion with the Green's function integrand (Equation 7). As a result, Eshelby's tensor generally depends only on the shape and elastic properties of the inclusion and those of its infinite matrix. One very interesting result of Eshelby's theory is that as long as the inclusion or reinforcement phase is an ellipsoid (or sphere), the strain or stress field in the inclusion remain uniform. Thus, this means we can simply assume that the mean strain ($\bar{\boldsymbol{\varepsilon}}$) of the reinforcement phase as simply $\boldsymbol{\varepsilon}$ if the shape of the fillers is close to ellipsoids.

EIM can also be used to find the stress or strain field outside an inclusion or reinforcing phase of a composite by using an exterior Eshelby's tensor. Here, the exterior Eshelby's tensor is simply obtained by changing the volume integral in Equation 7 in terms of the positions (**X**) outside the inclusion ($\mathbf{X} \notin \Omega$) which causes the strain outside the inclusion to be no longer uniform. Another important benefit of Eshelby's theory is that the same concept of equivalent inclusion can also be used to model the thermal and dielectric behaviors of composites as the mathematical form of the constitutive laws are quite similar [152,153]. For this case, the derived Eshelby's tensors are 2nd order as the field components of thermal and electric behaviors are only defined by the three orthogonal directions (x, y, and z) in Euclidean space.

$$\mathbf{C}^{\Omega}\colon(\boldsymbol{\varepsilon}^0+\boldsymbol{\varepsilon}^{\Omega})=\mathbf{C}^{\mathrm{M}}\colon(\boldsymbol{\varepsilon}^0+\boldsymbol{\varepsilon}^{\Omega}-\boldsymbol{\varepsilon}^*) \tag{5}$$

$$\boldsymbol{\varepsilon}=\mathbf{S}\colon\boldsymbol{\varepsilon}^* \tag{6}$$

$$\varepsilon_{ij}=\left[-C_{klmn}\int_{\Omega}\left(\frac{G_{ik,lj}+G_{jk,li}}{2}\right)dV(\mathbf{X})\right]\varepsilon^*_{mn}=S_{ijmn}\varepsilon^*_{mn} \tag{7}$$

To find the effective properties of soft matter composites, the Eshelby's tensor can be adapted to different mean-field homogenization theories, most prominently the Mori-Tanaka theory which will is the bread and butter of the current study [137,154]. In the homogenization theories, the Eshelby's tensor (**S**) will be used in multiple steps in the strain concentration tensors ($\mathbf{A}_j$) depending on the microstructure arrangement of the modelled soft matter composite. Hence, I will provide the necessary backgrounds and overview of the Mori-Tanaka theory and their novel formulation improvements at each subsequent chapter of this dissertation.

1.9 Motivation and Overview

Overall, the numerous selections of polymers, sizes, shapes, and interfacial modifications of solid or liquid fillers (cell included) make it challenging for researchers to optimize the standard processing procedures to create composite with the desired multifunctional properties. The current work presented in this dissertation aims to curb this challenge by equipping composite designers with an analytical micromechanics framework that can accurately predict the multiphysics behaviors of a multiphase soft matter composite at different length scale. To introduce the significance of this work, Chapter 1 provided the introduction as well as the literature review on the synthesis and applications of soft multifunctional polymer composites. Next, we will present the theoretical framework for modeling the effective properties of EGaIn (Chapter 2) and MXene (Chapter 4) polymer composites which are the two recently emerged classes of functional composite materials. Chapter 3 presents a micromechanics model that can approximate the rupture stress of the Ga oxide shell which determines whether the embedded EGaIn droplets can be sintered or not under different loading conditions and concentrations. Subsequently, Chapter 5 will introduce the viscoelastic model for modeling the viscoelastic response of hydrogel composites under complex sinusoidal displacement loading. The work presented in Chapter 5 provides a closed-form solution to rapidly predict the stress to time response of a hydrogel composite and allow optimization to the loading parameters before conducting the real experimentation. Lastly, Chapter 6 of this dissertation will summarize the main contributions of the current work and provide recommendations for future works. With the formalization of my dissertation, I am confident that the introduced micromechanics framework will find relevance among researchers from all backgrounds and to serve as a robust predictive tool to accelerate the development of various soft multifunctional polymer composites.

- Chapter 2: Multiscale Micromechanics Modeling of Liquid Metal Polymer Composites
- Chapter 3: Rupture Mechanics of Core-Shell Liquid Metal Droplets in Soft Matter Composite
- Chapter 4: Novel Micromechanics Framework for Soft Multifunctional MXene Polymer Composites:
- Chapter 5: Viscoelastic Model for Cells Layered in Agarose Gel Composite:
- Chapter 6: Summary and Future Work

Chapter 2: Multiscale Micromechanics Modeling of Liquid Metal Polymer Composites

Liquid metal elastomer composites have gained significant attention in advanced technologies including wearable electronics, soft robotics, and human-computer interactions. This is due to the combination of metallic conductivity and fluidic properties of liquid metal (LM) inclusions in addition to their facile fabrication process. With the emergence of gallium-based liquid metal nanocomposites and advances in synthesis and integration of LM nanoparticles in a variety of polymer matrices, there is a pressing need for a materials design tool to accelerate the development of these multifunctional composites. Here, we introduce a double inclusion (DI) model capable of predicting the properties of polymer composites with core-shell liquid metal droplets. The size-dependent elasticity of LM inclusions is modeled by considering the solid gallium oxide interphase between the liquid metal core and the solid polymer matrix. As the size of inclusions reduces from tens of microns to tens of nanometers, the role of the oxide interface (shell) becomes more dominant. The results of the DI model show excellent agreement with finite element analysis and experimental results for a wide range of droplet sizes and volume fractions. This model provides a design framework for the synthesis of LM composites with tailored multifunctional properties.

2.1 Introduction

Metallic alloys of gallium (Ga) that are liquid near or below room temperature, such as eutectic gallium indium (EGaIn) and eutectic gallium indium tin (known as Galinstan) have become popular functional materials in recent years [8,38,155,156]. These liquid metal (LM) alloys have low viscosity (~2 times that of water) [33], high thermal conductivity (20–30 $W \cdot m^{-1} \cdot K^{-1}$) [30,31], high electrical conductivity ($1–4 \times 10^6$ $S \cdot m^{-1}$) [33,157], and low toxicity [32]. This unique combination of metallic conductivity and fluidic properties of liquid metal has been utilized in a variety of soft and stretchable electronic devices.

Initially, bulk LMs were embedded as conductors in elastomer microchannels to create stretchable circuits with potential applications as soft artificial skin with tactile sensing [158,159]. More recently, liquid metal polymer composites (LMPCs) have been developed by dispersion of LM micro-/nanodroplets in soft polymer matrices, typically elastomers (Figure 7). These solid-liquid composites, also known as liquid metal embedded elastomers (LMEE), are a promising choice among different LM material architectures and other functional composites [35,59,60,76,84,160]. This is mainly due to the metallic properties of inclusions and their liquid phase at room

temperature. Unlike rigid carbon-based or metallic nanofillers, liquid inclusions do not introduce significant mechanical resistance in compliant polymer matrices or stress concentrations at the interface. This unique combination of properties has enabled the synthesis of soft polymer composites with increased thermal conductivity [160,161], electrical conductivity [59,76,162], electrical permittivity [60,64,163], and self-healing behavior [61,164]. These enhanced multifunctional properties of LMPC can benefit a variety of emerging wearable technologies [165].

In recent years, there has been an increasing interest to reduce the size of LM droplets and embedded LM inclusions presenting both advantages and challenges [9,36]. LM nanodroplets can show high stability and low reactivity when in direct contact with metals such as aluminum [166]. Moreover, the confinement of LM droplets to micro/nanometer length scale significantly lowers their freezing and melting points which increases the operating temperature range for both LM particles and their composites as they remain soft and stretchable at low temperatures [55,167,168]. This feature is desirable in applications such as wearable thermoelectric generators where the LM-elastomer composite functions as a compliant thermal interface to efficiently generate power from human body heat for biomonitoring at low temperatures [168]. Another application of LM nanoparticles is shown in dielectric actuators and energy harvesters. The dispersion of LM nanodroplets in elastomers produces soft and stretchable dielectric materials with higher breakdown strength, compared to embedded micron-sized LM droplets [163].

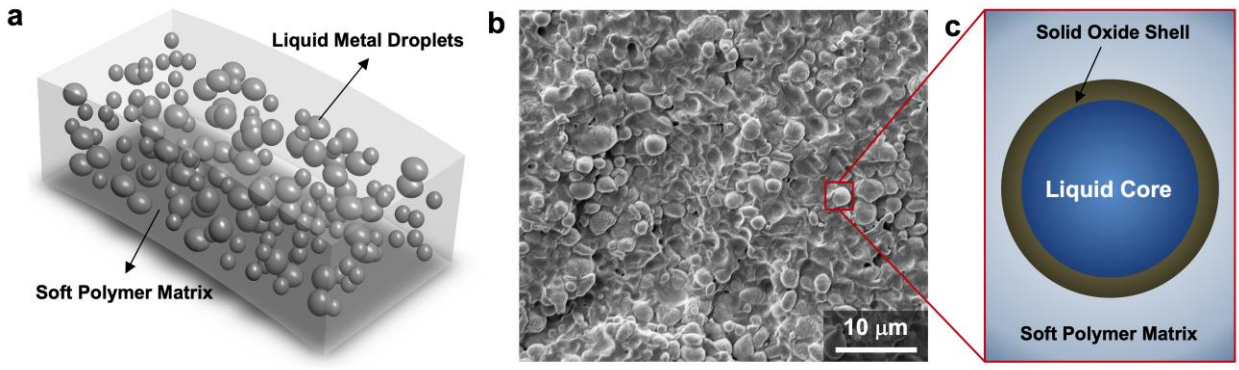

Figure 7. (a) Schematic of liquid metal polymer composites (LMPCs), (b) Micrograph of dispersed EGaIn droplets in PDMS, (c) The core-shell structure of embedded liquid metal inclusions.

An important structural feature of small-scale Ga-based LM droplets and inclusions is the encapsulation of the liquid metal phase with a solid gallium oxide (Ga_2O_3) layer. This passivating oxide layer forms rapidly in the presence of oxygen [169,170]. Although this oxide skin is

relatively thin (2-5 nm), it forms a core-shell structure that plays a crucial role in the performance and synthesis of nanoarchitectured LM systems (Figure 7c). For instance, it affects the structural stability of LM droplets which allows the synthesis of LM nanoparticles suitable for inkjet printing of stretchable conductors [79]. However, as the size of droplets reduces, rupturing the protective oxide skin becomes more challenging which can prevent the formation of coalesced electrically conductive pathways between neighboring ruptured LM nanoparticles [78,171]. This process is more difficult when those nanoparticles are suspended in a soft polymer matrix such as elastomers. However, this behavior of LM nanocomposites can be alternately viewed as an added advantage for preventing involuntary mechanical sintering (i.e., human touch, folding, and twisting) which can cause a short circuit within LM-based devices, particularly where the LMPCs are used as thermally conductive and electrically insulating materials [166,168]. These experimental studies show the importance of LM inclusion size and the stability of solid-liquid interfaces on the performance of LMPCs.

Analytical and numerical modeling tools are essential to accelerate the development of functional LM nanocomposites with tailored properties. Unlike the experimental studies on LMPCs, the modeling tools capable of predicting the effective properties of these composites are limited. A pioneering study by Style et al. [147,172] on the softening and stiffening effect of liquid inclusions has been widely adapted for validating the elastic behavior of LM composites. This model (termed Style's model here) is based on a modified Eshelby's inclusion theory, where the surface tension of small-scale incompressible liquid inclusions is considered. More recently, computational modeling studies have also been performed on LM composites to study the role of microstructures on the functional properties (i.e. thermal and electrical conductivity) of LMPCs [142,173,174].

In this study, we present a three-phase double inclusion (DI) model to predict the overall properties of liquid metal composites with a well-defined core-shell structure (Figure 7c). The size effect of embedded LM droplets on the elasticity of composite is also studied by altering the ratio of the oxide shell thickness (t) to the inclusion diameter (D), as this ratio (t/D) is negligible for larger LM droplets while it is considerable for LM nanoparticles. The micromechanics modeling results are validated with finite element analysis (FEA) and available experimental studies. Lastly, the core-shell structure of the LM fillers is considered to predict the thermal conductivity and dielectric properties of the liquid metal composites.

2.2 Modeling Approach

2.2.1 Formulation of Double Inclusion Model

As shown in Figure 8a, three-phase LMPCs which consist of core-shell structured LM fillers suspended in a soft polymer matrix are considered in the micromechanics modeling. Under the assumption of linear elastic deformations for both polymer matrix and oxide interface, the effective stiffness or compliance tensor of LMPCs can be determined by the Mori-Tanaka (MT) mean field homogenization approach. This approach is more explicit and computationally faster than other techniques (i.e., differential, and self-consistent) while being suitable for modeling composites with a well-distinguished matrix phase [139,154]. We utilize a two-level MT homogenization of DI model (TDI) to predict the behavior of LMPCs with nanoscale LM inclusions (Figure 8b). In this approach, the liquid core and solid shell (deepest level) are homogenized first then treated as one of the two phases with the polymer matrix for the overall homogenization of the composite (highest level) [138]. This is distinctive from the generalized DI model (GDI) that treats the core-shell inclusions as two separate phases in the matrix as shown in Figure 8c [136–138]. Although the GDI model with one level of MT homogenization is a common approach when dealing with a heterogeneous matter, the DI model with two levels of MT homogenization shows better performance for studying liquid inclusions with a solid interface and a compliant matrix.

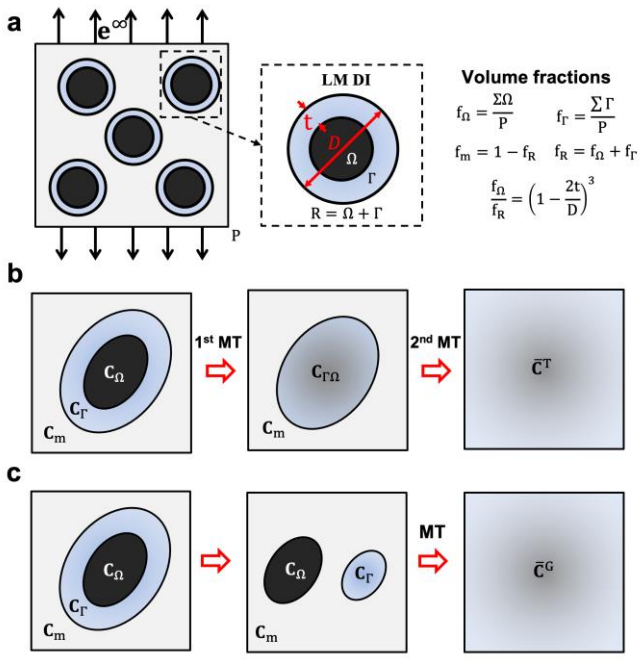

Figure 8. Micromechanics model: (a) Double inclusion (DI) model for LM fillers with the volume fraction of the core (f_Ω), shell (f_Γ), core-shell (f_R) and matrix (f_m) domains, (b) TDI: DI model with a two-level Mori-Tanaka (MT) homogenization technique, (c) GDI: generalized DI model with MT homogenization scheme.

The MT approach uses mean field theory that lumps the volume average stress ($\bar{\boldsymbol{\sigma}}_n$) and strain ($\bar{\mathbf{e}}_n$) vectors with respect to each n phases (n = Ω, Γ or m) into volume average stress ($\bar{\boldsymbol{\sigma}}$) and strain ($\bar{\mathbf{e}}$) vectors with respect to the overall composite volume (P) as shown in Figure 8a. These field vectors are linearly related by the effective stiffness tensor ($\bar{\mathbf{C}}$) of the LM polymer composite.

$$\bar{\boldsymbol{\sigma}} = f_m\,\bar{\boldsymbol{\sigma}}_m + f_\Gamma\bar{\boldsymbol{\sigma}}_\Gamma + f_\Omega\bar{\boldsymbol{\sigma}}_\Omega \quad (8)$$

$$\bar{\mathbf{e}} = f_m\,\bar{\mathbf{e}}_m + f_\Gamma\bar{\mathbf{e}}_\Gamma + f_\Omega\bar{\mathbf{e}}_\Omega \quad (9)$$

$$\bar{\boldsymbol{\sigma}} = \bar{\mathbf{C}}\colon\bar{\mathbf{e}} \quad (10)$$

In the first level of homogenization, the shell (Γ) and core (Ω) form a DI composite (Γ + Ω or simply ΓΩ) by using the MT approach and has a combined volume fraction of f_R. Thus, the effective stiffness of the inner DI composite ($\bar{\mathbf{C}}_{\Gamma\Omega}$) can be obtained as shown in Equation 11. The ":" operator represents matrix multiplications between any 4th order tensor:

$$\bar{\mathbf{C}}_{\Gamma\Omega} = \mathbf{C}_\Gamma + \frac{f_\Omega}{f_\Omega + f_\Gamma}\,(\mathbf{C}_\Omega - \mathbf{C}_\Gamma)\colon\mathbf{A}_{\Omega,\Gamma\Omega} \quad (11)$$

Where $\mathbf{C}_n$, and f_n are the stiffness tensor and the volume fraction of each phase (n = Γ or Ω), respectively. In this equation, $\mathbf{A}_{\Omega,\,\Gamma\Omega}$ is the strain concentration tensor that relates the volume average strain ($\bar{\mathbf{e}}_\Omega$) in the core with the volume average strain ($\bar{\mathbf{e}}_{\Gamma\Omega}$) within the core-shell domain or DI composite as indicated in Equation 12. This strain concentration tensor is dependent on the volume fractions, stiffnesses of the solid shell and liquid core of the composite, and inclusion's geometry (Equation 13-14). In the MT homogenization scheme, $\mathbf{A}_{\Omega,\Gamma\Omega}$ is also commonly recognized as the global strain concentration tensor, which is a function of the local strain concentration tensor ($\mathbf{B}_{\mathbf{C}_\Gamma,\mathbf{C}_\Omega}$). This dependency is essential to accurately predict the effective stiffness of the inner DI composite when it has large volume fraction of LM core surrounded by a dilute volume fraction of thin oxide shell [137,175]. In Equation 13-14, the **I** is a fourth order identity matrix and $\mathbf{S}_n$ is Eshelby's tensor. For LMPCs, Eshelby's tensor is only a function of the Poisson's ratio (ν_n) of the referenced n-matrix phase assuming LM double inclusions are coaxial spheres [135,176]. In the first step of the two-level DI model, this Poisson's ratio (ν_Γ) is equated to that of the solid shell since the solid shell behaves as the matrix in the deepest level for the liquid core. See the supplemental information to find the complete description of the spherical Eshelby's tensor.

$$\bar{\mathbf{e}}_\Omega = \mathbf{A}_{\Omega,\Gamma\Omega}\colon\bar{\mathbf{e}}_{\Gamma\Omega} \quad (12)$$

$$\mathbf{A}_{\Omega,\Gamma\Omega} = (f_\Omega + f_\Gamma)\mathbf{B}_{\mathbf{C}_\Gamma,\mathbf{C}_\Omega}\colon\left(f_\Gamma\mathbf{I} + f_\Omega\mathbf{B}_{\mathbf{C}_\Gamma,\mathbf{C}_\Omega}\right)^{-1} \quad (13)$$

$$\mathbf{B}_{\mathbf{C}_\Gamma,\mathbf{C}_\Omega} = \left(\mathbf{I} + \mathbf{S}_\Gamma\colon\left(\mathbf{C}_\Gamma^{-1}\colon\mathbf{C}_\Omega - \mathbf{I}\right)\right)^{-1} \quad (14)$$

In the second step, the overall stiffness of the three phase LMPC ($\bar{\mathbf{C}}^{\mathrm{T}}$) is computed by a MT homogenization but now taking the stiffness of the polymer matrix ($\mathbf{C}_{\mathrm{m}}$) and the effective elastic stiffness of the inner DI composite ($\bar{\mathbf{C}}_{\Gamma\Omega}$) which was calculated in the first level using Equation 11.

$$\bar{\mathbf{C}}^{\mathrm{T}} = \mathbf{C}_{\mathrm{m}} + (\mathrm{f}_{\Omega} + \mathrm{f}_{\Gamma})(\bar{\mathbf{C}}_{\Gamma\Omega} - \mathbf{C}_{\mathrm{m}}) : \mathbf{A}_{\Gamma\Omega,\mathrm{P}} \quad 15$$

This homogenization is conducted by introducing another strain concentration tensor ($\mathbf{A}_{\Gamma\Omega,\mathrm{P}}$). This tensor relates the volume average strain ($\bar{\mathbf{e}}$) in the overall composite volume (P) with the volume average strain ($\bar{\mathbf{e}}_{\Gamma\Omega}$) in the deepest DI composite (ΓΩ) as shown in Equation 16. Furthermore, in this second step of the TDI model, the Poisson's ratio of Eshelby's tensor in $\mathbf{B}_{\mathbf{C}_{\mathrm{m}},\bar{\mathbf{C}}_{\Gamma\Omega}}$ is equated to that of the polymer matrix (ν_{m}) because the polymer now behaves as the matrix for the inner two-phase composite. Similar to the first MT homogenization step, the dependency between $\mathbf{A}_{\Gamma\Omega,\mathrm{P}}$ and $\mathbf{B}_{\mathbf{C}_{\mathrm{m}},\bar{\mathbf{C}}_{\Gamma\Omega}}$ in this second step ensures the predicted stiffness of LMPC is accurate when the volume fraction of embedded DI composites is above dilute level of 5% [175].

$$\bar{\mathbf{e}}_{\Gamma\Omega} = \mathbf{A}_{\Gamma\Omega,\mathrm{P}} : \bar{\mathbf{e}} \quad 16$$

$$\mathbf{A}_{\Gamma\Omega,\mathrm{P}} = \mathbf{B}_{\mathbf{C}_{\mathrm{m}},\bar{\mathbf{C}}_{\Gamma\Omega}} : \left(\mathrm{f}_{\mathrm{m}}\mathbf{I} + (\mathrm{f}_{\Omega} + \mathrm{f}_{\Gamma})\mathbf{B}_{\mathbf{C}_{\mathrm{m}},\bar{\mathbf{C}}_{\Gamma\Omega}}\right)^{-1} \quad 17$$

$$\mathbf{B}_{\mathbf{C}_{\mathrm{m}},\bar{\mathbf{C}}_{\Gamma\Omega}} = \left(\mathbf{I} + \mathbf{S}_{\mathrm{m}} : \left(\mathbf{C}_{\mathrm{m}}^{-1} : \bar{\mathbf{C}}_{\Gamma\Omega} - \mathbf{I}\right)\right)^{-1} \quad 18$$

In contrast to the two-level homogenization approach, the well-known DI model treats the shell and the core as two separate single inclusion phases with the MT homogenization simultaneously applied over those three different phases (Figure 8c, Equation S5-S11).

2.2.2 Effective Functional Properties

The formulated elasticity DI models can also be extended to estimate the thermal and electrostatic behaviors of LM polymer composites. This is because their constitutive equations are of a similar mathematical form, so that Eshelby's inclusion solution (i.e., eigenstrain method) can be applied. Table S1 summarizes the volume average field and flux terms for mechanical, thermal, and electrostatic behaviors. For example, the constitutive law for the thermal behavior of materials is based on Fourier's law ($\bar{\mathbf{q}} = \bar{\mathbf{K}} : \bar{\boldsymbol{\theta}}$). This corresponds to Hooke's law ($\bar{\boldsymbol{\sigma}} = \bar{\mathbf{C}} : \bar{\mathbf{e}}$) of elasticity where the volume average of stress ($\bar{\boldsymbol{\sigma}}$), effective stiffness tensor ($\bar{\mathbf{C}}$) and volume average of strain field ($\bar{\mathbf{e}}$) are analogously interchangeable with the volume average of heat flux ($\bar{\mathbf{q}}$), effective thermal

conductivity tensor ($\bar{\mathbf{K}}$) and volume average of temperature gradient ($\bar{\boldsymbol{\theta}}$), respectively. Similarly, for the electrostatic behavior, the volume average of electric flux ($\bar{\mathbf{d}}$), electric field ($\bar{\mathbf{E}}$) and effective dielectric constants ($\bar{\boldsymbol{\varepsilon}}_r$) correspond to $\bar{\boldsymbol{\sigma}}$, $\bar{\mathbf{e}}$ and $\bar{\mathbf{C}}$, respectively. Therefore, the DI model (Equation 8-18) can be repurposed for studying thermal and electrostatic behaviors by interchanging their respective terms for flux, field and property tensors while utilizing an uncoupled Eshelby's tensor for assumed spherical LM core-shell fillers ($\mathbf{S} = \frac{1}{3}\mathbf{I}_{3\times3}$).

2.2.3 Finite Element Modeling

It is common to evaluate the accuracy of micromechanics models through FEA [146,177]. Here, the predictions made by the DI models for the effective mechanical, thermal, and dielectric properties of LM polymer composites are validated using FEA. To execute that, a centered spherical liquid core, layered with homogeneous solid shell embedded in a cubic polymer matrix is chosen as the representative volume element (RVE) of the LM polymer composite (Figure 9a). This RVE is assigned with appropriate boundary conditions (BCs) based on Table S3 to obtain the equivalent mechanical, thermal, and dielectric properties of LMPCs. Additional displacement constraints are applied on opposite faces to create periodic BCs and to ensure continuity between RVEs.

To predict the mechanical properties using FEA, the total strain energy of the RVE under simple tension and pure shear conditions is used to compute the components of the equivalent stiffness tensor and the shear modulus of the composite, respectively. The strain energy in the deformed RVE is acquired directly from ANSYS for each loading condition. With computed strain energy and known applied deformations, the components of effective stiffness tensor and subsequently the effective Young's and shear moduli are determined (Equation S19-S22). In a similar manner, the effective thermal conductivity and dielectric constant of LMPCs are determined by FEA (See the supplementary information of this chapter for further details).

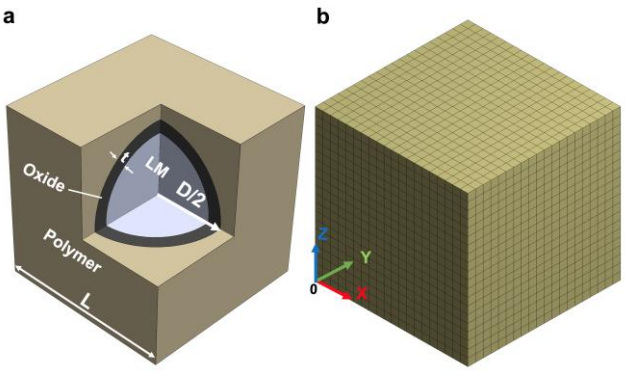

Figure 9. Finite element model: (a) Cubic representative volume element (RVE) of the LMPCs, and (b) meshed RVE.

2.3 Results and Discussion

2.3.1 Mechanical Behavior of LMPCs

To accurately investigate the mechanical behavior of a LM polymer composite using DI and FEA methods, the actual mechanical properties of the polymer matrix and oxide shell are considered, while the LM core is assumed to be incompressible and have zero elastic modulus (Table 1). The equivalent stiffness of LMPCs predicted by these models is isotropic because LM inclusions are spheres and input material constants for the phases are isotropic.

Table 1. Mechanical and functional properties of the phases in LM polymer composites

Phase	Elastic Modulus (MPa)	Poisson's ratio	Dielectric Constant	Thermal Conductivity (Wm^{-1} K^{-1})
Matrix (Sylgard 184)	1.5 [163]	0.49	3.3 [163]	0.17 [55]
Solid shell (Ga-oxide)	1060 [78]	0.31	18 [179]	11 [180]
Liquid core (EGaIn)	0.1 (fluidic)	0.49	∞ (conductor)	30 [33,38]

As shown in Figure 10a and b, the results of the DI model clearly demonstrate the size influence of core-shell LM droplets on the overall stiffness of LMPCs. For instance, as the ratio of shell thickness to inclusion diameter (t/D) of LM fillers increases, the two-level DI model predicts that both the equivalent elastic and shear moduli of LMPCs will increase regardless of LM volume fraction (f_R). In addition, as the volume fraction of LM inclusions increases, the Young's and shear moduli of LMPCs are predicted to increase (stiffen) or decrease (soften) depending on the size of inclusions. Most LM nanocomposites will be susceptible to stiffening behavior because the usual diameter of their inclusions is on the order of tens or hundreds of nanometers while the thickness of solid oxide shell among LM nanodroplets remains in a few nanometers [78]. This enables the resulting size ratios of inclusions to fall within the wide stiffening range ($6\times10^{-4}<t/D<0.5$) of the composite. In contrast, most micro-sized LM inclusions have diameters on the order of tens or hundreds of microns while their oxide shell thickness remains in the same range as those of LM

nanodroplets. Hence, their normalized shell thickness ratio is relatively small ($0<t/D<6\times10^{-4}$) and results in predicting the softening behavior of LMPCs.

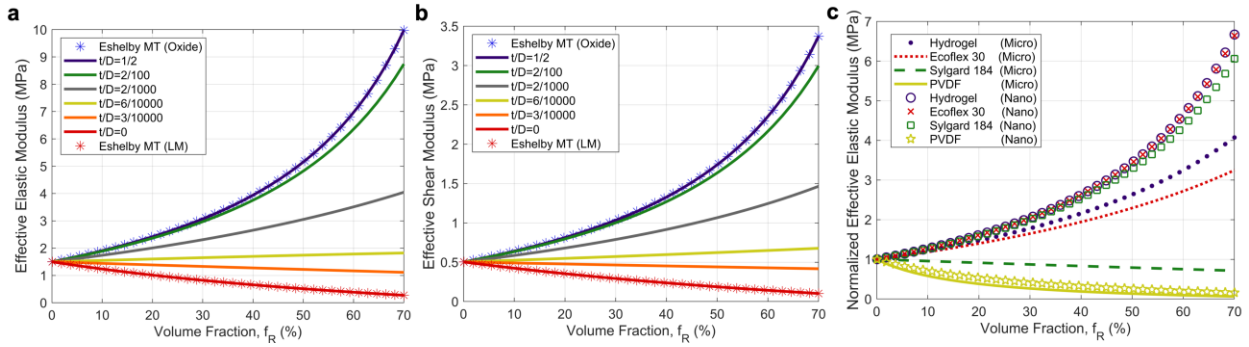

Figure 10. Effective elastic modulus (a) and shear modulus (b) of LMPCs predicted by two-level DI model for different volume fractions and shell thickness to diameter ratio (t/D) of LM inclusions. (c) Normalized effective elastic modulus of LMPCs for four different polymer matrices with nano or micro droplets (100nm, $t/D = 2\times10^{-2}$ and 10μm, $t/D = 2\times10^{-4}$).

It should be noted that the effective elastic and shear moduli of LMPCs become independent of inclusion size when the size ratio exceeds 0.02. Above this size ratio, the increased stiffness of LMPCs will be similar as the stiffening behavior of composites containing only solid Ga-oxide (t/D=0.5). This size-independent behavior occurs because of the dominant stiffness of the gallium oxide shell (1.06 GPa) in comparison to that of the polymer matrix (1.5 MPa).

The compliance of matrix material is another essential factor in the stiffening or softening effect of embedded liquid micro-/nano inclusions. In addition to silicone elastomers (Sylgard 184 and Ecoflex 00-30), other stiff and ultrasoft polymers such as polyvinylidene fluoride (PVDF) and hydrogels can be used in the synthesis of LMPCs [14,163]. These polymers have elastic moduli (E_m) spanning several orders of magnitude. Figure 10c shows the important role of polymer matrices in the effective Young's modulus of LMPCs when normalized by unfilled polymer's stiffness. Assuming unchanged stiffness of oxide layer (1.06 GPa), the TDI model clearly shows that when a relatively stiff matrix such as PVDF (E_m=2.6 GPa, ν_m=0.3) is used, both nanoscale (100 nm, $t/D=2\times10^{-2}$) and microscale (10 μm, $t/D=2\times10^{-4}$) droplets show softening effect. In contrast, when an ultrasoft soft hydrogel (E_m=90 kPa; ν_m=0.49) or Ecoflex 00-30 (E_m=125 kPa; ν_m=0.49) is chosen as the matrix, both the micro and nano droplets increase the stiffness. Hence, with the guidance of TDI model, the stiffness or compliance of LMPCs can be tailored by selecting the size and volume fractions of LM particles as well as the type of polymer matrix.

The TDI model is compared to Style's model which has been commonly used for LM composites. To apply Style's model, the diameter of inclusions is varied while a constant surface tension of 0.5 Nm^{-1} is assumed in Equation S12 to determine the equivalent inclusion stiffness (Ei). This stiffness value was used in Equation S13 to predict the composite's Young's modulus based on the size and volume fraction of LM fillers. The results of both models are compared to the experimental data for EGaIn-PDMS composites in Figure 11. For the composites with micron sized LM inclusions (D=10 µm), the equivalent elastic moduli predicted by both TDI and Style's models are in good agreement with each other and with the experimental results. However, the TDI model appears to be more accurate than Style's model as it closely predicts experimental results for LM nanocomposites with 1µm inclusion diameters. A constant solid oxide shell thickness of 2 nm in the TDI model is assumed to compare its stiffness predictions with those of Style's model and experimental results based on the diameter (D) of inclusions [78]. For instance, the prediction of TDI model for size ratio $t/D = 2\times10^{-3}$ is equivalent to Style's and experiment's result for 1µm inclusion diameter when the shell thickness is approximated to be 2 nm.

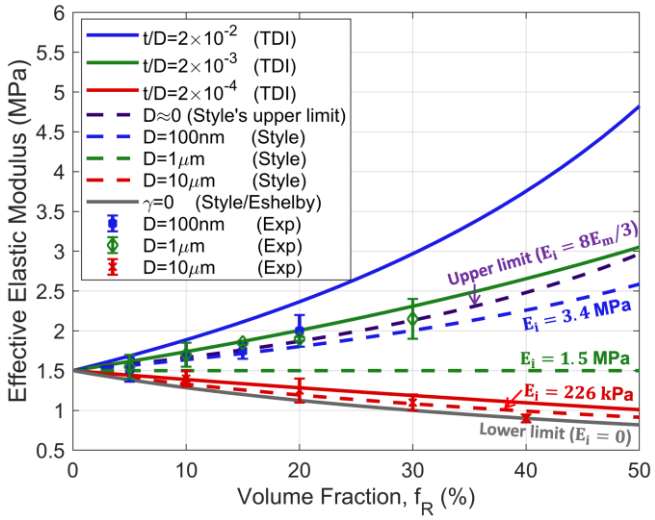

Figure 11. The two-level double inclusion model is compared with Style's model [147,172] and experimental results [163] for effective elastic modulus of LMPCs with varying LM volume fractions and inclusion sizes.

Overall, for liquid metal polymer nanocomposites, Style's model is inferred to be less accurate than TDI model when comparing both models against experimental results. An example of this is that the upper limit of Style's model appears to closely overlap the measured elastic modulus of LM composites with 1 µm and 100 nm inclusion diameters as shown in Figure 11. However, Style's upper limit is physically unattainable because it represents the maximum possible equivalent inclusion stiffness ($E_i=8E_m/3$) that occurs as the diameter of LM inclusions approaches

zero (D≈0). Therefore, this observed overlap of experimental value of D=100 nm with the following limiting curve is physically unrealistic. In addition, the results of TDI model are much closer to the experimental Young's modulus of LMPCs with 1μm inclusion diameter than Style's model.

It is also postulated that the surface tension on Ga-based LM droplets can decrease and vanish when the thickness of its oxide interface increases [40]. If this physical behavior is considered, Style's model would have predicted a much smaller effective elastic modulus (E_c) for LMPCs with core-shell structures. However, a constant surface tension (0.5 Nm^{-1}) was used in Style's model when compared to the experimental and TDI model in Figure 11. This assumption was made because negligible surface tension will lead to negligible equivalent inclusion elasticity in this model (Equation S12-S13) regardless of inclusion diameter. Hence, when considering the core-shell structure of LM droplets and its effect on interfacial surface tension, Style's model is not suitable for describing the overall mechanical behavior of liquid metal nanocomposites. This limitation was highlighted in a recent review article by Style et al. [7] where an alternative formulation was suggested to account for the oxide interphase layer. In contrast to the proposed equation, TDI model is a versatile mathematical tool that can be simply extended to study composites with different filler morphologies or anisotropic properties.

The two-level DI model accurately predicts the elastic modulus of LM composites with 1μm LM nanodroplets when compared to experimental results. However, it overpredicts the effective Young's modulus of LMPCs with 100 nm diameter. This overprediction arises because of the variations of elastic modulus, thickness of the Ga-oxide shell and polydispersity of LM fillers within fabricated LM nanocomposite specimens. The presence of residual macroscale LM droplets in the composite are believed to be the main factor contributing to errors in experimental results, particularly at larger volume fractions in the range of 20% [163]. In some cases, these larger LM droplets (smaller t/D) can diminish the stiffening effect introduced by the LM nanoparticles which coexist in the same polymer composite [177]. To study the role of polydispersity on the predicted elastic modulus of LM nanocomposites, a log-normal size distribution was considered for LM nanodroplets (Figure S1a). For a constant oxide thickness, the size of inclusions was varied from 100 nm ($t/D=2\times10^{-2}$) to 1μm ($t/D=2\times10^{-3}$). As indicated in Figure S1b, the results show that

although considering polydispersity in TDI model slightly improves the prediction, it is not the only reason for discrepancy between the modeling and experimental results.

The results of the two-level DI model are validated using FEA to further evaluate the accuracy of the proposed model for LM composites with core-shell structures. It is shown that the overall elastic (Figure 12a) and shear moduli (Figure 12b) predicted by the TDI model for different filler volume fractions and inclusion sizes (here t/D ratios) agree with FEA. Similar to the result of the TDI model, FEA verifies that there exists a consistent range of inclusion sizes (t/D) where the stiffening and softening behaviors of LMPCs are bound to occur, which is at $6\times10^{-4}<t/D<0.5$ and $0<t/D<6\times10^{-4}$, respectively. The inclusion's size ratio of 6×10^{-4} is predicted by both methods for the LM composite to exhibit no changes of compliance or stiffness at any volume fraction. This behavior arises because at this size, the enhanced compliance of LMPCs by the liquid core of LM inclusions is exactly offset by the structural rigidity provided by the solid oxide shell.

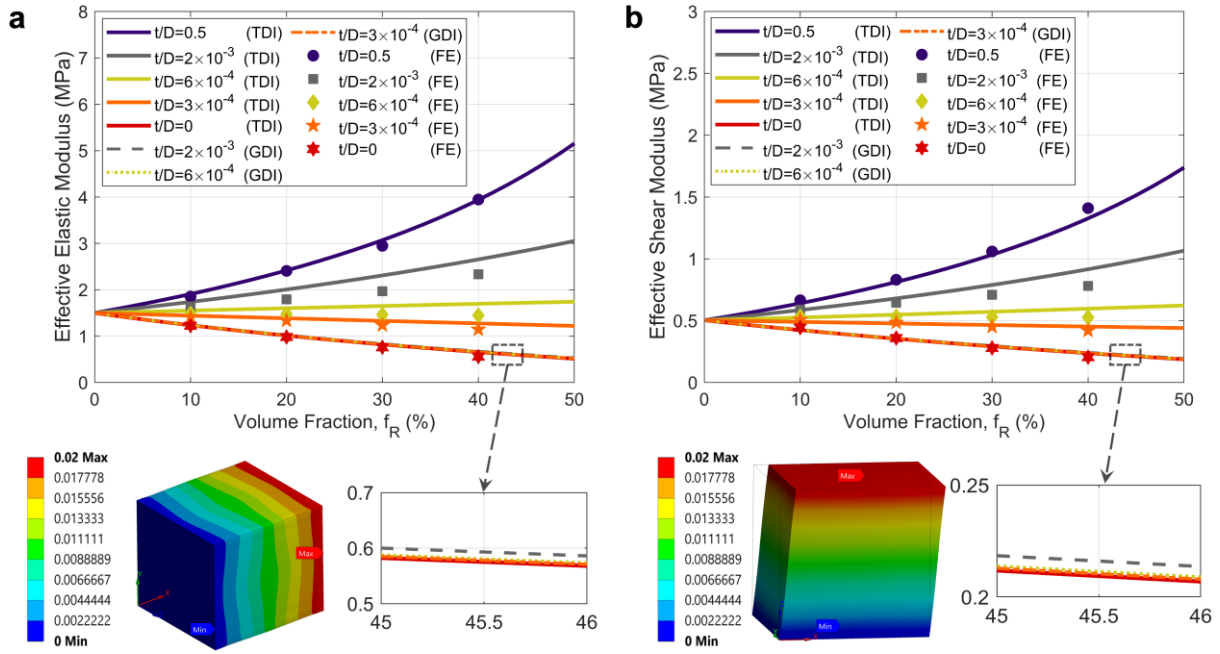

Figure 12. FEA validation for the two-level DI (TLDI) model and comparison with GDI model. Estimated overall elastic modulus (a) and shear modulus (b) as a function of LM volume fraction and the ratio of oxide shell thickness to inclusion diameter. Insets: deformation of RVE under simple tension (a) and shear (b) and zoomed-in plot for GDI model.

The generalized DI model predicts that the elastic and shear moduli of LM composites to be dependent on filler volume fraction but independent of inclusion size (Figure 12). For instance, the predictions of the GDI model for effective elastic and shear moduli of three distinct inclusion sizes ($t/D = 2\times10^{-3}$, 6×10^{-4} and 3×10^{-4}) are similar with each other and coincide with the results of

FEA for micron-sized inclusions (t/D=3×10^{-4}). This result occurs because the GDI model treats the LM core and gallium oxide interphase as two separate inclusions in a polymer matrix with Ga oxide phase having the smallest volume fraction because of its inherent thin-shell structure. In this configuration, this oxide phase will have a minimal role in the overall stiffness of LMPC. Despite that, GDI model is sufficient to predict the equivalent mechanical properties of LM composites with at least micron-sized inclusions.

At filler volume fractions higher than 20%, there is a slight discrepancy between two-level DI model and FEA results. This is because MT approach considers inter particle interaction that is not reflected in our chosen RVE. Although different RVEs can be selected in FEA and the polydispersity of the inclusions can be implanted in the DI model, further experimental results are required to evaluate the accuracy of each methodology. Overall, the FEA validation further confirms that the presented model can be used as a design framework to reliably predict the stiffness or compliance of LMPCs not only based on volume fraction but also considering the inclusion size and their core-shell structure. The two-level DI model can be applied to the emerging LM composites with tailored interfaces [53].

2.3.3 Functional Behavior of LMPCs

The double inclusion model can also be used to study the thermal and electrostatic behavior of LMPCs. Figure 13a shows the dielectric constants of LMPCs with different inclusion sizes and volume fractions based on the input material properties presented in Table S3. The predicted dielectric constants of LM composite by TDI model matches FEA results up to 40% volume fraction for distinct inclusion sizes (t/D=0.5, 5×10^{-3} and 0). However, those predictions made by TDI model are only in agreement with the measured dielectric constants up to 15% volume fraction of inclusions with diameters of 10 μm (t/D=2×10^{-4}), 1 μm (t/D=2×10^{-3}) and 100 nm (t/D=2×10^{-2}). To improve this model, a modified TDI model based on interpolation (ITDI) is introduced which can closely predict the measured dielectric constants of LMPCs up to a higher 30% volume fraction for both similar microscale and nanoscale LM inclusions. Here, the normalized size (t/D) and diameter (D) of LM inclusion are made comparable by assuming 2nm as the constant oxide shell thickness. The derivation details of this interpolated TDI model can be found in the supplementary information.

At most volume fractions, ITDI model predicts negligible change of dielectric constant of LMPC with respect to three distinct inclusion sizes (t/D=2×10^{-4}, 2×10^{-3} and 2×10^{-2}). However, when the volume fraction is above 15%, the experimental results show that LM composite with nanoparticles (D=100 nm) has higher dielectric constant than the composite with microparticles (D =1 μm and 10 μm). This result occurs in experiment because LM nanoscale inclusions are polydisperse with respect to their diameters which are normally distributed in the composites [163]. The following morphology enables LM nanoscale inclusions to act as fillers in between microscale LM inclusions to create multiple narrow inter-inclusion gaps. Each of these gaps has an insulating polymer phase separating the conductive fillers to concentrate inter-inclusion electric flux by behaving like a micro-capacitor. Thus, it is possible that this concentrated local electric flux increases the overall electrical permittivity of the LM nanocomposites.

At above 15% volume fraction, the interpolated TDI model is unable to predict the measured dielectric constant of LM composite because this model utilizes Eshelby's theory which is also often equivalent to effective medium theory. In both frameworks, a perfectly homogeneous filler dispersion in the polymer matrix is assumed. Based on this assumption, the DI model is generally unable to accurately consider a composite with more complex microstructures. As a result, the measured dielectric constant increases for LM nanoparticles while micromechanics such as TDI model and its interpolated version are unable to accurately predict this behavior.

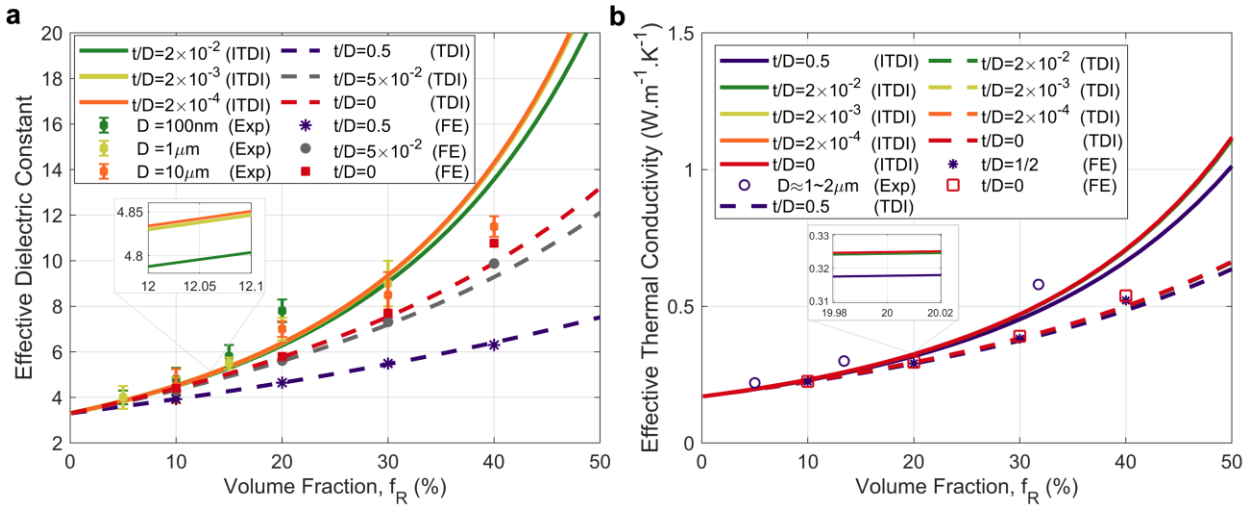

Figure 13. Functional properties of LMPCs predicted using ITDI, TDI model and FEA and compared to experimental results: (a) effective dielectric constant (Experimental data [163]), (b) the effective thermal conductivity of the LM composites (Experimental data [161]).

Figure 13b demonstrates the estimated thermal conductivity of LMPCs with different volume fractions and inclusion diameters. In this plot, the thermal conductivity of LM composite predicted by TDI model matches FEA results up to 40% volume fractions for the lower (t/D=0) and upper bound (t/D=0.5) inclusion sizes. The predictions for both sizes show negligible differences. However, those predictions made by TDI model are lower than the measured thermal conductivity of LM composite [161]. Therefore, a modified TDI model based on interpolation (ITDI) can be used to better predict the measured thermal conductivity of LM composite while also indicating that the effect of inclusion size on the thermal conductivity remains negligible. This occurs mainly because in comparison to other properties, the thermal conductivity differences between the oxide interphase and the LM core is much closer to each other. For instance, the thermal conductivity range of LM (i.e. EGaIn and Galinstan) and Ga-oxide are in the range of 20 to 30 $W \cdot m^{-1} \cdot K^{-1}$ and 10.9 to 27 $W \cdot m^{-1} \cdot K^{-1}$, respectively [33,38,180]. Despite selecting the thermal conductivities of each core and shell phase to have the largest contrasting value (Table S3), the DI model still predicts negligible size influence of core-shell LM inclusion on the overall thermal conductivity of LM composite. Since the size influence of inclusion is negligible and spherical geometry is assumed, the following results of DI model become consistent with other micromechanics model such as Bruggerman theory and Maxwell-Garnett model shown in a recent study [178].

This minimal size effect of core-shell structured LM fillers on the thermal properties of composites shows promising applications of LM nanocomposites as multifunctional units. While the advantages from reducing the diameter of LM fillers observed through experiment or modelling results had shown improved dielectric constant, dielectric breakdown strength, supressed freezing and melting temperatures, and limited corrosive effect, the thermal conductivity of LM composites will remain unchanged for the same filler volume fractions.

2.4 Conclusion

In this study, the effective structural and functional properties of liquid metal polymer composites were investigated using a two-level double inclusion model. This model examines the role of LM volume fraction and inclusion size by considering a core-shell structure for the embedded LM droplets. The results of the DI model for Young's modulus of LMPCs were also in better agreement with the experimental data when compared to a previous model based on surface tension of liquid inclusions and Eshelby's theory. Furthermore, finite element model validation had confirmed the accuracy of this modeling approach for elastomer composites with embedded core-shell liquid metal inclusions. Lastly, the DI model is extended to estimate the relative permittivity and thermal conductivity of the LM composites with different volume fractions and inclusion sizes. It can be concluded that the double inclusion model provides a versatile design framework for liquid metal composites with nano and microscale inclusions. Therefore, as new surface and interface modifications of LM droplets emerge, this model can accelerate the development of advanced liquid metal composites with low computational cost and complexity.

Chapter 3: Rupture Mechanics of Core-Shell Liquid Metal Droplets in Soft Matter Composites

One of the vital parameters when designing the microstructure of liquid metal polymer composite (LMPCs) is the size of the core-shell liquid metal droplets. Gallium-based liquid metal droplets such as eutectic gallium indium (EGaIn) have a defined core-shell structure which comprise of a conductive liquid metal core surrounded by a thin but rigid gallium (Ga) oxide shell. The rupture of this insulative oxide layer is needed to form continuous conductive traces between the suspended droplets. However, the same oxide shell also behaves as a rigid dielectric barrier. This interfacial barrier must be preserved when creating LMPCs with high thermal conductivity but electrically insulative [181]. Thus, in this chapter, a predictive model is developed to investigate the rupture mechanics of small or large embedded LM droplets that can have various packing density in their composite. This predictive model would pave the foundation to conduct further investigation of the toughening, fracture, and large deformation behaviors of LMPCs.

3.1 Introduction

Synthesized micro- and nano- sized liquid metal droplets such as EGaIn have a core-shell structure which can be observed in their micrographs [1,55,56]. These core-shell structures exist because of the presence of self-passivating thin oxide shell. As the size of EGaIn droplets is reduced to the nanoscale, the thickness of this rigid gallium oxide (Ga_2O_3) shell becomes relatively larger than the size of the LM droplet. When small core-shell LM droplets are embedded in a soft matrix phase such as an elastomer, it becomes challenging to sinter these LM droplets by external forces. This is because the applied forces are mechanically damped by the surrounding soft elastomer [77,160,182].

Enabling and preventing the mechanical sintering of EGaIn droplets in a polymer composite is one of the most important considerations when designing the microstructure of LMPCs. Successful mechanical sintering of the embedded EGaIn droplets enables the fabrication of stretchable electrical interconnections with strain-invariant resistance behavior [14,183–185]. For example, to create electrically conductive traces in LMPCs, the Ga oxide shell of the embedded EGaIn droplets must be ruptured by external loading. When the oxide shell is ruptured, the conductive EGaIn core is exuded and coalesces with its neighboring liquid metal droplets, but this is assuming that the insulating polymer barrier is also fractured during the process. On the other hand, the sintering of

the EGaIn droplets is undesirable if their composites must remain electrically insulative but also possess high thermal conductivity or electrical permittivity [84,85,181]. Hence, this raises a question of whether there is an optimum arrangement (volume fraction, packing factor, droplet size) or boundary conditions (uniaxial, hydrostatic pressure) that could maximize the localized stress concentration to rupture and coalesce the embedded EGaIn droplets into single continuous LM trace. Alternatively, it is also important to determine the optimum microstructures of the LM droplets that will prevent involuntary mechanical activation (short circuit) due to external deformation applied on the LMPCs.

The microstructure selections of LMPCs decides whether the suspended LM droplets are favorable for mechanical sintering. One of the simplest ways to achieve particle sintering is to embed predominantly large (microns) LM droplets where the thickness of the oxide shell is negligible in comparison to the size of the droplets [181,184]. However, selecting large LM droplets can lead to the leakage of the encapsulated LM droplets from its polymer packaging during the sintering procedure, which can lead to involuntary short circuit and lack of control in the resolution of the created conductive trace. Alternately, it is preferably to use LMPCs with smaller (several microns) EGaIn particles when the composite is intended to be used only as a thermal management [84,86,181] or dielectric components [60,65,186] of an electronic device. This is because smaller EGaIn droplets have structurally rigid core-shell structure which cannot be easily sintered and leak even when their composite is subjected to excessive mechanical loading. Despite that, it is possible to mechanically sinter the small LM droplets in their composite. This can be done by allowing these LM droplets to sediment in its precured polymer matrix for a prolonged period to create LM rich layer with high packing density of liquid metal droplets [184,187,188]. With this configuration, it becomes much easier to coalesce the liquid metal rich layer of the LMPCs by either applying shear (peeling) [184] or compressive forces [77,187,188]. Another recent study also demonstrated that it is possible to sinter microsized LM particulates in a printed 3D architecture LMPC by applying hydrostatic stresses which is transferred to the composite using another secondary matrix with viscoelastic characteristic [189]. These experimental observations highlight the importance of understanding the effects of microstructure arrangements and loading/boundary conditions when attempting to prevent or enable the sintering of LMPCs.

A full three-dimensional stress solution in a composite provides a fundamental mechanical parameter to predict the deformation and failure behaviors of liquid metal polymer composites at various length scales. Currently, the exact stress field in a liquid metal polymer composite can be simplified as a 2D elastic problem. In this formulation, the LM droplet is represented as a core-shell spherical inhomogeneities and the stress solutions has been derived using Airy's stress function approach to estimate the specific elastic energy stored in the EGaIn droplet [190] or to estimate the maximum shear stress of the thin oxide shell [183,185] when a composite is under a given mechanical loading. There are other stress function approaches which can help find the 3D stress solution for a general composite with an ellipsoidal inhomogeneity and an interphase. However, the formulation for such problem is laborious especially when different boundary conditions and additional interphases are considered [191,192]. Alternatively, in this current dissertation, we provided a compact modeling framework that can generally find the complete 3D stress field in a liquid metal polymer composite. This model can flexibly account for various morphologies of core-shell EGaIn droplets with additional interphases and interparticle interactions in a composite system.

3.2 Modeling Approach

The microstructure of LMPCs typically consists of polydisperse core-shell liquid metal (EGaIn) droplets suspended in a polymer matrix (Figure 14a). In both the large and small LM droplets, the core-shell structure comprises of a liquid core surrounded by uniform thickness of rigid Gallium (Ga) oxide shell (Figure 14b). These droplets can be modelled as either sphere or ellipsoids which are the common shapes of the synthesized EGaIn micro, or nano particles observed in different elastomers [8,60,160]. To explicitly formulate the full-field solutions of the stress and strain field inside and outside the core-shell liquid metal inclusion, we will use Eshelby's equivalent inclusion method (EIM) and the principle of superposition in elasticity [193,194]. Once the computed stress and strain components for a single core-shell EGaIn inclusion is found, we can reapply the same notion of superposition [148] to investigate the effects of interparticle interactions when the droplets are jammed at high packing density in their polymer matrix. Interparticle interactions are considered in this study as it can elevate the stress concentration at the Ga oxide shell and at the boundary of the Ga oxide and the polymer phase (i.e., oxide-polymer interface) which are the locations where the rupture of the core-shell particle take place.

3.2.1 Geometric definition of Core-shell EGaIn particulate

Considering a core-shell (Σ) ellipsoidal EGaIn inclusion embedded in an infinite polymer matrix ($D - \Sigma$) with the ellipsoid surface can be mathematically described by Equation 19. As illustrated in Figure 14b, this core-shell ellipsoid has a given height (r_3) to radius ($r_1 = r_2$) ratio of α and an oxide shell (Γ) of uniform thickness (t) which surrounds the liquid metal core (Ω). Since the LM core is also ellipsoidal, the surface geometry of the core can also be defined by Equation 20 and the aspect ratio (γ) of the core domain is larger than α because the oxide shell thickness tend to be much smaller than the outer radius (r_2) of the core-shell domain. However, both the aspect ratio of the core and overall core-shell structure becomes one when the considered core-shell inclusion is spherical.

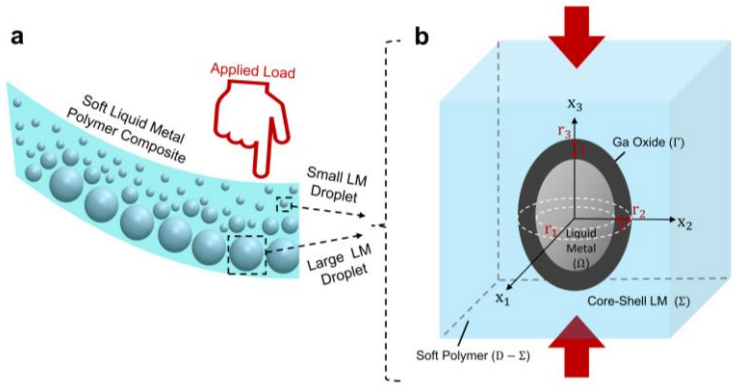

Figure 14. (a) An illustration of a soft liquid metal polymer composite with layers of large and small LM droplets. (b) The individual large or small LM droplets can be modelled as a core-shell LM inclusion suspended in an infinite soft polymer matrix. Large spherical LM droplets will have small $t/_{r2}$ while smaller spherical LM droplets will have large $t/_{r2}$.

To ascertain whether the position where the stress or strain components are evaluated is at the core, shell, or the polymer phase, several sets of mathematical criteria are introduced. For example, if the position vector $\mathbf{X} = (x_1, x_2, x_3)$ of a point of interest causes Equation 19 to be less or greater than one, the chosen location will be respectively inside ($\mathbf{X} \in \Sigma$) or outside [$\mathbf{X} \in (D - \Sigma)$] of the core-shell inclusion. Similarly, if the chosen position vector led Equation 20 to be smaller than one, the position of the point of interest will be within the core phase of the inclusion. Finally, if the chosen location of the point of interest is in the oxide shell, the evaluated value of Equation 19 will be less than one, but Equation 20 must be greater than one as indicated by Equation 21.

$$\frac{x_1^2}{r_1^2} + \frac{x_2^2}{r_2^2} + \frac{x_3^2}{r_3^2} = \begin{cases} a \le 1, \mathbf{X} \in \Sigma \\ a > 1, \mathbf{X} \in (D - \Sigma) \end{cases}, \qquad \alpha = \frac{r_1}{r_2} = \frac{r_1}{r_3} \tag{19}$$

$$\frac{x_1^2}{(r_1 - t)^2} + \frac{y_2^2}{(r_2 - t)^2} + \frac{z_2^2}{(r_3 - t)^2} = \begin{cases} b \le 1, \mathbf{X} \in \Omega \\ b > 1, \mathbf{X} \in (D - \Omega) \end{cases}, \qquad \gamma = \frac{r_1 - t}{r_2 - t} = \frac{r_1 - t}{r_3 - t} \tag{20}$$

$$a < 1 \ \& \ b > 1, \ \mathbf{X} \in \Gamma \tag{21}$$

3.2.2 Stress field inside and outside of EGaIn inclusion without oxide shell

To introduce the Eshelby's equivalent inclusion method [176], it will be simpler to begin with formulating the stress field inside and outside an incompressible ellipsoid inclusion (EGaIn) without the presence of an oxide shell (Figure 14b). This EGaIn inclusion which has isotropic stiffness tensor of $\mathbf{C}^{\Omega}$ is embedded in an infinite soft polymer matrix (M) with stiffness tensor of $\mathbf{C}^{\mathrm{M}}$. Here, the polymer matrix is under an applied stress ($\boldsymbol{\sigma}^{\mathrm{o}}$) and the ellipsoidal single inclusion (Ω) has aspect ratio of α and isotropic stiffness tensor of $\mathbf{C}^{\Omega}$. The effective stress ($\boldsymbol{\sigma}^{\Omega}$) in the inclusion can be summarized as Equation 22 which suggests that the internal stress is always spatially uniform regardless of the far field stress [135]. In this equation, the equivalent inclusion method (EIM) is used which allows us to evaluate the disturbance strain ($\boldsymbol{\varepsilon}^{\mathrm{d}}$) or strain concentration in the LM inclusion. This is possible because the stress field ($\boldsymbol{\sigma}^{\Omega}$) of an inhomogeneous inclusion (Ω) in a polymer matrix (M) can be made equivalent to the stress field of an inclusion in a homogeneous polymer medium as long as a proper eigenstrain ($\boldsymbol{\varepsilon}^{*}$) is computed. As a result, the disturbance strain field becomes proportional to the following eigenstrain and related by the 4$^{\text{th}}$ order internal Eshelby's tensor ($\mathbf{S}^{\mathrm{i}}$) as suggested in Equation 23. Furthermore, by substituting Equation 23 into Equation 22, the eigenstrain can be formulated as Equation 24 by explicitly expressing for $\boldsymbol{\varepsilon}^{*}$ in the EIM formulation. Further explanations for the concept of EIM used in this study are provided in the introduction of this thesis at section 1.8 Eshelby's equivalent inclusion method.

$$\boldsymbol{\sigma}^{\Omega} = \boldsymbol{\sigma}^{\mathrm{o}} + \mathbf{C}^{\Omega}\colon\boldsymbol{\varepsilon}^{\mathrm{d}} = \boldsymbol{\sigma}^{\mathrm{o}} + \mathbf{C}^{\mathrm{M}}\colon\left[\boldsymbol{\varepsilon}^{\mathrm{d}} - \boldsymbol{\varepsilon}^{*}\right], \qquad \mathbf{X} \in \Omega \tag{22}$$

$$\boldsymbol{\varepsilon}^{\mathrm{d}} = \mathbf{S}^{\mathrm{I}}\colon\boldsymbol{\varepsilon}^{*} \tag{23}$$

$$\boldsymbol{\varepsilon}^{*} = [\mathbf{C}^{\mathrm{M}}\colon\mathbf{S}^{\mathrm{I}}(\alpha) - \mathbf{C}^{\mathrm{M}} - \mathbf{C}^{\Omega}\colon\mathbf{S}^{\mathrm{I}}(\alpha)]^{-1}\colon[\mathbf{C}^{\Omega}\colon\{\mathbf{C}^{\mathrm{M}}\}^{-1} - \mathbf{I}]\colon\boldsymbol{\sigma}^{\mathrm{o}} \tag{24}$$

$$\boldsymbol{\sigma}^{\mathrm{M}}(\mathbf{X}) = \boldsymbol{\sigma}^{\mathrm{o}} + \mathbf{C}^{\mathrm{M}}\colon\mathbf{S}^{\mathrm{E}}(\mathbf{X},\alpha)\colon\boldsymbol{\varepsilon}^{*}, \qquad \mathbf{X} \in \mathrm{D} - \Omega \tag{25}$$

Finding the stress field outside the LM inclusion will help determine whether the created local stress concentration is sufficient to rupture the polymer phase which will allow neighboring LM droplets to coalesce when sintered. To achieve this, the stress ($\boldsymbol{\sigma}^{\mathrm{M}}$) in the polymer phase can be determined by summing the uniform far field stress with the stress concentration (2$^{\text{nd}}$ term) at a position ($\mathbf{X}$) outside the inclusion as described by Equation 25. As a result, the stress outside the liquid metal inclusion is no longer uniform. This is because near the inclusion, the stress fields are polarized due to the presence of inhomogeneity (i.e., LM particulates) while at far away from the

inhomogeneity the stress field must converge to the applied stress boundary conditions ($\boldsymbol{\sigma}^{M} \cong \boldsymbol{\sigma}^{o}$). To compute the stresses inside and outside the liquid metal inclusion, the external $[\mathbf{S}^{E}(\mathbf{X}, \alpha)]$ and internal Eshelby's tensor $[\mathbf{S}^{I}(\alpha)]$ is given by Equation S30 and Equation S38, respectively. Both these Eshelby's tensor are dependent on the aspect ratio (α) of the core-shell LM droplets but only the components of external Eshelby's tensor $[\mathbf{S}^{E}(\mathbf{X}, \alpha)]$ will vary at any point of interest outside the inclusion. The instructions to assemble these six-by-six tensors are given in the supplemental information.

3.2.3 Stress field inside and outside a core-shell EGaIn particulate

A mechanical parameter that determines whether the rigid oxide shell of an embedded liquid metal droplet will rupture or not fundamentally depends on the stress components inside and outside the core-shell droplets when their composite is under a mechanical load $[\boldsymbol{\sigma}^{o} = (\sigma_{11}^{o}, \sigma_{22}^{o}, \sigma_{33}^{o}, \sigma_{23}^{o}, \sigma_{13}^{o}, \sigma_{12}^{o})]$. The core-shell domain (Σ) of EGaIn droplet shown in Figure 15a illustrates that the liquid metal core (Ω), oxide shell (Γ), and the matrix phase (M) are expected to have distinct stress vectors of $\boldsymbol{\sigma}^{\Omega}$, $\boldsymbol{\sigma}^{\Gamma}(\mathbf{X})$, and $\boldsymbol{\sigma}^{M}(\mathbf{X})$ respectively. To determine these stress components, the core-shell domain (double inhomogeneity problem) must be decomposed into two separate single inhomogeneity problems or also known as two-phase composites [193]. For example, Figure 15b illustrates one of these composites as a single inhomogeneity body with a Ga oxide inclusion which is the same size as the original core-shell LM droplet (Σ) that is embedded in an identical polymer matrix (M). The other two-phase composite is illustrated in Figure 15c which consist of a liquid metal inhomogeneity suspended in a similar polymer matrix. Here, the ellipsoidal liquid metal phase has the same shape and size as the core domain (Ω) in the original double inhomogeneity problem (Figure 15a). Moreover, both these decomposed single inhomogeneity problems are applied with the same stress boundary conditions as those in the original core-shell liquid metal polymer composite.

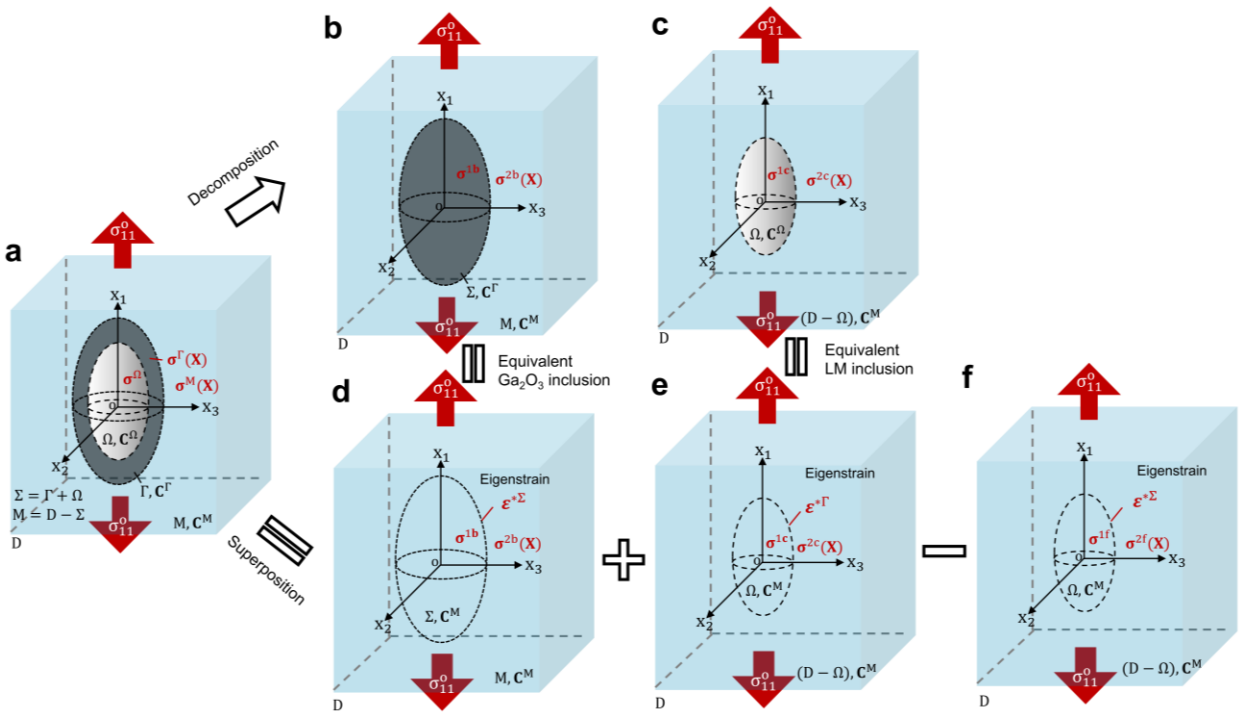

Figure 15. (a) The isolated core-shell liquid metal inclusion representing LMPC is decomposed into (b) single Ga oxide inhomogeneity and (c) single liquid metal inhomogeneity problems. Equivalent inclusion for (d) Ga oxide and (e) liquid metal single inhomogeneity problem to find the internal and external stresses of each case by EIM. (f) The equivalent inclusion for the LM inhomogeneity is applied with the eigenstrain stemming from the EIM of the Ga oxide inhomogeneity problem.

Finding the internal and external stress field of the inclusion for the two single inhomogeneity problems is straightforward with the help of Eshelby's equivalent inclusion method. By using EIM, the stress vector inside ($\boldsymbol{\sigma}^{1b}$) and outside [$\boldsymbol{\sigma}^{2b}(\mathbf{X})$] of the Ga oxide inhomogeneity can be evaluated using Equation 26 and Equation 27, respectively. To achieve this stress field solution, an eigenstrain ($\boldsymbol{\varepsilon}^{*\Sigma}$) for the equivalent inclusion of the Ga oxide inhomogeneity (Figure 15d) needs to be evaluated which can be done by simply replacing the stiffness tensor of the inhomogeneity body with the stiffness tensor ($\mathbf{C}^{\Gamma}$) of Ga oxide as shown in the previous formulation (Equation24). Similarly, with the help of EIM again, the stress field solution inside ($\boldsymbol{\sigma}^{1c}$) and outside [$\boldsymbol{\sigma}^{2c}(\mathbf{X})$] the liquid metal inhomogeneity (Figure 15c) can be expressed as Equation 29 and Equation 30, respectively. However, these equations are now modified by changing the stiffness tensor of the inhomogeneity body with the those of liquid metal phase. Finally, the internal ($\boldsymbol{\sigma}^{1c}$) and external stress [$\boldsymbol{\sigma}^{2c}(\mathbf{X})$] of the equivalent LM inclusion (Figure 15e) which are also equivalent to the internal and external stress field in the LM inhomogeneity problem (Figure 15c) can be determined when EIM finds the proper eigenstrain ($\boldsymbol{\varepsilon}^{*\Omega`}$) through EIM (Equation 31).

$$\boldsymbol{\sigma}^{1b} = \boldsymbol{\sigma}^{o} + \mathbf{C}^{\Gamma}\!:\mathbf{S}^{I}(\alpha)\!:\boldsymbol{\varepsilon}^{*\Sigma} \quad (26)$$

$$\boldsymbol{\sigma}^{2b}(\mathbf{X}) = \boldsymbol{\sigma}^{o} + \mathbf{C}^{m}\!:\mathbf{S}^{E}(\mathbf{X},\alpha)\!:\boldsymbol{\varepsilon}^{*\Sigma}, \qquad \mathbf{X} \in [D-\Sigma] \quad (27)$$

$$\boldsymbol{\varepsilon}^{*\Sigma} = [\mathbf{C}^{m}\!:\mathbf{S}^{I}(\alpha) - \mathbf{C}^{m} - \mathbf{C}^{\Gamma}\!:\mathbf{S}^{I}(\alpha)]^{-1}\!:[\mathbf{C}^{\Gamma}\!:\{\mathbf{C}^{m}\}^{-1} - \mathbf{I}]\!:\boldsymbol{\sigma}^{o} \quad (28)$$

$$\boldsymbol{\sigma}^{1c} = \boldsymbol{\sigma}^{o} + \mathbf{C}^{\Omega}\!:\mathbf{S}^{I}(\gamma)\!:\boldsymbol{\varepsilon}^{*\Gamma} \quad (29)$$

$$\boldsymbol{\sigma}^{2c}(\mathbf{X}) = \boldsymbol{\sigma}^{o} + \mathbf{C}^{m}\!:\mathbf{S}^{E}(\mathbf{X},\gamma)\!:\boldsymbol{\varepsilon}^{*\Gamma}, \qquad \mathbf{X} \in [D-\Omega] \quad (30)$$

$$\boldsymbol{\varepsilon}^{*\Gamma} = [\mathbf{C}^{m}\!:\mathbf{S}^{I}(\gamma) - \mathbf{C}^{m} - \mathbf{C}^{\Omega}\!:\mathbf{S}^{I}(\gamma)]^{-1}\!:[\mathbf{C}^{\Omega}\!:\{\mathbf{C}^{m}\}^{-1} - \mathbf{I}]\!:\boldsymbol{\sigma}^{o} \quad (31)$$

Now with internal and external stress components for each of the decomposed single inhomogeneity problems (biphasic composites) formulated, superposition can be employed to derive the effective stress fields in the core-shell liquid metal polymer composite (Figure 15a). For example, Figure 15f shows that the effective stress field in the liquid core $[\boldsymbol{\sigma}^{\Omega}(\gamma,\alpha)]$ becomes the vector sum (Equation 32) of the internal stress in the Ga oxide and the liquid metal inhomogeneity followed by the deduction with $\boldsymbol{\sigma}^{1f}$. This last term is the stress field in an equivalent LM inclusion (Ω) due to the eigenstrain ($\boldsymbol{\varepsilon}^{*\Sigma}$) used for the EIM evaluation of the Ga oxide inhomogeneity (Σ) elastic problem. The third term ($\boldsymbol{\sigma}^{1f}$) is introduced because the additional internal stress field ($\boldsymbol{\sigma}^{1b}$) contributed by the equivalent Ga oxide inclusion (Σ) at the space originally occupied by the liquid core (Ω) needs to be removed. Thus, this will enable the superimposed internal stress to match the internal stress of the liquid core domain in the actual three-phase composite.

$$\boldsymbol{\sigma}^{\Omega}(\gamma,\alpha) = \boldsymbol{\sigma}^{1b} + \boldsymbol{\sigma}^{1c} - \boldsymbol{\sigma}^{1f}, \qquad \mathbf{X} \in \Omega \quad (32)$$

$$\boldsymbol{\sigma}^{1f} = \boldsymbol{\sigma}^{o} + \mathbf{C}^{\Omega}\!:\mathbf{S}^{I}(\gamma)\!:\boldsymbol{\varepsilon}^{*\Sigma} \quad (33)$$

$$\boldsymbol{\sigma}^{\Gamma}(\mathbf{X},\gamma,\alpha) = \boldsymbol{\sigma}^{1b} + \boldsymbol{\sigma}^{2c}(\mathbf{X}) - \boldsymbol{\sigma}^{2f}(\mathbf{X}), \qquad \mathbf{X} \in \Gamma \quad (34)$$

$$\boldsymbol{\sigma}^{2f}(\mathbf{X}) = \boldsymbol{\sigma}^{o} + \mathbf{C}^{\Omega}\!:\mathbf{S}^{E}(\mathbf{X},\gamma)\!:\boldsymbol{\varepsilon}^{*\Sigma} \quad (35)$$

$$\boldsymbol{\sigma}^{M}(\mathbf{X},\gamma,\alpha) = \boldsymbol{\sigma}^{2b}(\mathbf{X}) + \boldsymbol{\sigma}^{2c}(\mathbf{X}) - \boldsymbol{\sigma}^{2f}(\mathbf{X}), \qquad \mathbf{X} \in M \quad (36)$$

Following the same superposition procedure, the effective stress $[\boldsymbol{\sigma}^{\Gamma}(\mathbf{X},\gamma,\alpha)]$ in the Ga oxide shell ($\mathbf{X} \in \Gamma$) of the embedded core-shell LM can be formulated as Equation 34. Here, $\boldsymbol{\sigma}^{\Gamma}(\mathbf{X},\gamma,\alpha)$ is found by employing EIM solution to find the internal and the external stress of the Ga oxide and LM inhomogeneity problem, respectively before subtracted with $[\boldsymbol{\sigma}^{2f}(\mathbf{X})]$. The final term of Equation 34 is the additional external stress stemming from the EIM solution for the Ga oxide inhomogeneity problem $[\boldsymbol{\sigma}^{2f}(\mathbf{X})]$. Lastly, the stress field outside the core-shell LM inclusion (M or $D-\Sigma$) can be found by adding the external stress solution for the Ga oxide and LM inhomogeneity problem followed by reduction with the external stress contributed by the

superimposed Ga oxide inhomogeneity problem (Equation 36). To simplify the formulation in the next section, the stress terms for $\boldsymbol{\sigma}^{\Omega}(\gamma, \alpha)$ and $\boldsymbol{\sigma}^{\mathrm{M}}(\mathbf{X}, \gamma, \alpha)$ are symbolized to be a function γ and α to indicate that these values are dependent on the aspect ratios of the referred core-shell LM inclusion.

3.2.4 Stress interactions between neighboring core-shell LM droplets

Size and packing density of the core-shell LM droplets in a composite can influence the local stress inside or outside the droplets. To theoretically demonstrate these effects, we can employ the principle of superposition to find the full stress solution of a composite with a pair of distinct (or identical) core-shell liquid metal particles. These core-shell particles are assumed to be always non-intersecting and are separated by a center-to-center distance of $\|\bar{\Delta}\|$ (Figure 16a). The core-shell LM inhomogeneity (labelled 0) near the global origin has aspect ratio of $\gamma = \gamma^0$ and $\alpha = \alpha^0$, while the neighboring core-shell LM inhomogeneity (labelled 1) has aspect ratio of $\gamma = \gamma^1$ and $\alpha = \alpha^1$.

With the consideration of interparticle interaction, the effective stress field $[\boldsymbol{\sigma}^{\Omega(0)}(\mathbf{X})]$ in the core ($\mathbf{X} \in \Gamma^0$) of the LM particle at origin can be evaluated by Equation 37. To find $\boldsymbol{\sigma}^{\Omega(0)}(\mathbf{X})$, the internal stress $[\boldsymbol{\sigma}^{\Omega}(\gamma^o, \alpha^0)]$ at the core phase ($\mathbf{X} \in \Omega^0$) of the same core-shell LM inhomogeneity (Figure 16b) that is in isolation (no interaction) is added with the external stress $[\boldsymbol{\sigma}^{\mathrm{M}}(\mathbf{X}, \gamma^0, \alpha^0)]$ induced by the 2nd isolated inhomogeneity problem at $\mathbf{X} \in \Omega^0$ (Figure 16c) before deducted by $\boldsymbol{\sigma}^0$ which ensure that the summed far field stress consistently matches the actual problem. Here, $\boldsymbol{\sigma}^{\Omega}(\gamma^o, \alpha^0)$ is formulated by replacing the aspect ratios used in Equation 32 with $\gamma = \gamma^0$ and $\alpha = \alpha^0$ while $\boldsymbol{\sigma}^{\mathrm{M}}(\mathbf{X}, \gamma^1, \alpha^1)$ is determined by having the aspect ratio in Equation 36 as $\gamma = \gamma^1$ and $\alpha = \alpha^1$. By following the same formulation concept, it is also possible to compute the stress field $[\boldsymbol{\sigma}^{\Omega(1)}(\mathbf{X})]$ in the LM core ($\mathbf{X} \in \Gamma^1$) of the neighboring LM droplet (Equation 38). Here, $\boldsymbol{\sigma}^{\Omega(1)}(\mathbf{X})$ is a term that represents the sum of the external stress $[\boldsymbol{\sigma}^{\mathrm{M}}(\mathbf{X}, \gamma^0, \alpha^0)]$ of the core-shell LM particle (labelled 0) at the origin together with the internal stress $[\boldsymbol{\sigma}^{\Omega}(\gamma^1, \alpha^1)]$ in the core phase of the neighboring LM inhomogeneity (labelled 1) and also followed by deduction with $\boldsymbol{\sigma}^0$.

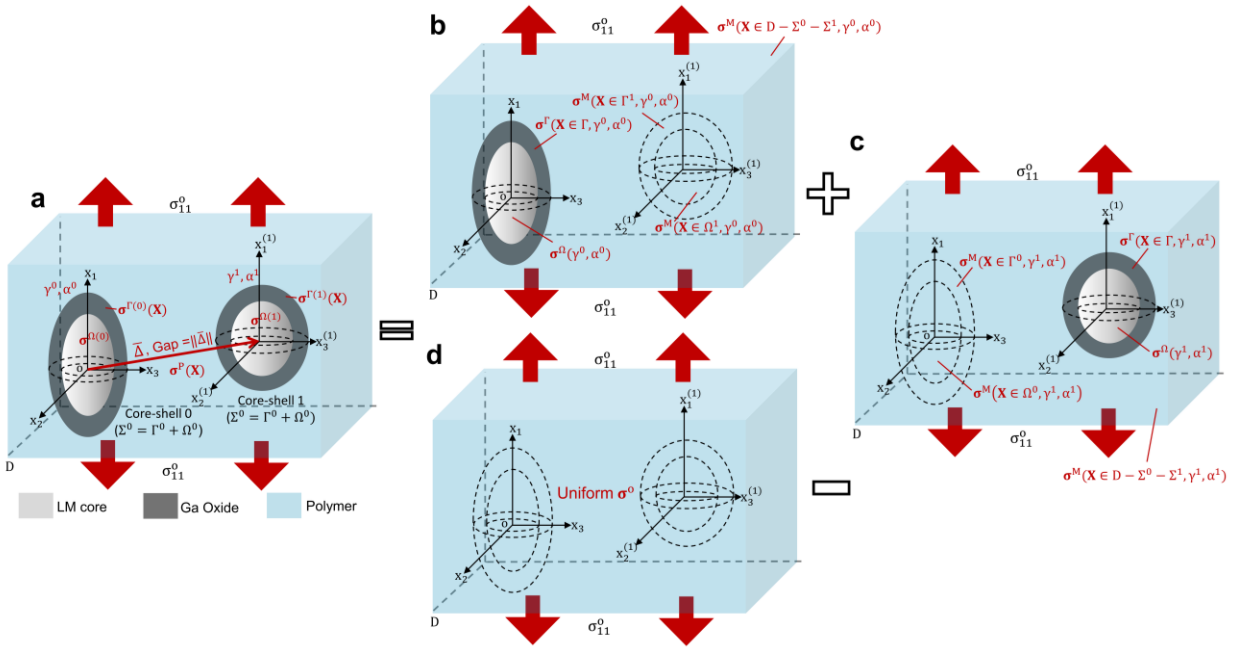

Figure 16. (a) Two generally distinct core-shell ellipsoidal liquid metal droplets embedded in a polymer matrix with a given arbitrary gap and direction in the composite. The two-interacting core-shell LM droplets are decomposed into an elastic problem involving just the (b) left hand side and the (c) right hand LM droplet in its respective polymer medium. (d) The superimposed stress/strain field of the two single inhomogeneity problems must be deducted with the case of an unfilled polymer medium under uniaxial stress loading to ensure equivalency to the original elastic problems involving two interacting LM droplets in their polymer composite.

The stress field of the Ga oxide phase at each of the neighboring core-shell LM inclusions can also be determined using superposition. For instance, the stress field $[\boldsymbol{\sigma}^{\Gamma(0)}]$ in the Ga oxide shell ($\mathbf{X} \in \Gamma^0$) of the interacting LM droplet at the origin can be evaluated by Equation 39. Here, $\boldsymbol{\sigma}^{\Gamma(0)}$ is found by taking the stress $[\boldsymbol{\sigma}^{\Gamma}(\mathbf{X}, \gamma^0, \alpha^0)]$ in the oxide interphase of the same LM droplet (at origin) added with the external stress field $[\boldsymbol{\sigma}^{\mathrm{M}}(\mathbf{X}, \gamma^1, \alpha^1)]$ induced at $\mathbf{X} \in \Gamma^0$ by the neighboring LM droplet before also subtracted with $\boldsymbol{\sigma}^0$. On the other hand, the stress in the Ga oxide shell $[\boldsymbol{\sigma}^{\Gamma(1)}(\mathbf{X})]$ of the other LM particle (away from origin) can be formulated by simply swapping the aspect ratios of the two interacting LM particulates in the internal and external stress terms (Equation 40). Moreover, the effective stress field $[\boldsymbol{\sigma}^{\mathrm{P}}(\mathbf{X})]$ at the polymer phase or outside the interacting LM droplets is not only affected by the aspect ratios of these droplets but also their separation distance. To predict $\boldsymbol{\sigma}^{\mathrm{P}}(\mathbf{X})$, we will have to superimpose the external stress field $[\boldsymbol{\sigma}^{\mathrm{M}}(\mathbf{X}, \gamma^0, \alpha^0)]$ induced by the LM droplet at origin with the external stress field $[\boldsymbol{\sigma}^{\mathrm{M}}(\mathbf{X}, \gamma^1, \alpha^1)]$ introduced by the second neighboring LM droplet and again followed by subtraction of the applied remote stress. With these micromechanics models fully introduced, it is possible to predict the stress components along any direction or region of interest in a LM polymer composite which has a pair of suspended core-shell

liquid metal droplets suspended at any arbitrary positions. Moreover, it is also possible to scale up the current framework to model the stress field of composites with more than a pair of interacting LM droplets by simply extending the superposition principle.

$$\boldsymbol{\sigma}^{\Omega(0)}(\mathbf{X}) = \boldsymbol{\sigma}^{\Omega}(\gamma^0, \alpha^0) + \boldsymbol{\sigma}^{\mathrm{M}}(\mathbf{X}, \gamma^1, \alpha^1) - \boldsymbol{\sigma}^0, \qquad \mathbf{X} \in \Omega^0 \tag{37}$$

$$\boldsymbol{\sigma}^{\Omega(1)}(\mathbf{X}) = \boldsymbol{\sigma}^{\Omega}(\gamma^1, \alpha^1) + \boldsymbol{\sigma}^{\mathrm{M}}(\mathbf{X}, \gamma^0, \alpha^0) - \boldsymbol{\sigma}^0, \qquad \mathbf{X} \in \Omega^1 \tag{38}$$

$$\boldsymbol{\sigma}^{\Gamma(0)}(\mathbf{X}) = \boldsymbol{\sigma}^{\Gamma}(\mathbf{X}, \gamma^0, \alpha^0) + \boldsymbol{\sigma}^{\mathrm{M}}(\mathbf{X}, \gamma^1, \alpha^1) - \boldsymbol{\sigma}^0, \qquad \mathbf{X} \in \Gamma^0 \tag{39}$$

$$\boldsymbol{\sigma}^{\Gamma(1)}(\mathbf{X}) = \boldsymbol{\sigma}^{\Gamma}(\mathbf{X}, \gamma^1, \alpha^1) + \boldsymbol{\sigma}^{\mathrm{M}}(\mathbf{X}, \gamma^0, \alpha^0) - \boldsymbol{\sigma}^0, \qquad \mathbf{X} \in \Gamma^1 \tag{40}$$

$$\boldsymbol{\sigma}^{\mathrm{P}}(\mathbf{X}) = \boldsymbol{\sigma}^{\mathrm{M}}(\mathbf{X}, \gamma^0, \alpha^0) + \boldsymbol{\sigma}^{\mathrm{M}}(\mathbf{X}, \gamma^1, \alpha^1) - \boldsymbol{\sigma}^0, \qquad \mathbf{X} \in (\mathrm{D} - \Sigma^0 - \Sigma^1) \tag{41}$$

3.3 Discussion

To find the full stress field solution of a liquid metal polymer composite such as EGaIn polymer composite, the isotropic stiffness properties of EGaIn, Gallium oxide, and the polymer phase need to be assigned in the model. For the Gallium oxide phase, the elastic modulus is chosen as E_s=1.06GPa and with Poisson's ratio of 0.2 which is close to the Poisson's ratio of most metallic materials [78]. These properties are summarized in Table 2 which shows the isotropic elastic modulus and Poisson's ratio of these phases used in our micromechanics model. It is also assumed that the EGaIn phase is less compressible than the polymer phase as the measured bulk modulus of elastomer (~4GPa) [195] tends to be smaller than EGaIn (~10GPa). Hence, the exact Poisson's ratio of EGaIn (0.499999) is chosen to be closer to 0.5 (i.e., perfectly incompressible) than the Poisson's ratio of elastomer (0.49). With these chosen finite Poisson's ratios, we ensure that the LM core will have hydrostatic compressive stress while preventing the bulk modulus of EGaIn from being infinite. On the other hand, the Young's modulus of elastomer is chosen as E_M=2MPa which is close to those of commercial elastomers such as Sylgard 184 [195].

Table 2. Summary of the isotropic mechanical properties of the phases in a liquid metal polymer composite.

Phase material	**Elastic modulus**	**Poisson's ratio**
Polymer (Sylgard 184)	E_M = 2MPa [195]	0.4999
Oxide Shell (Ga_2O_3)	E_S = 1060MPa [78]	0.2
Liquid core (EGaIn)	E_C =0.06Pa (Compression)	0.4999999

3.3.1 Validation with solutions of Benchmark problems

For our micromechanics model to be accurate when estimating the full stress field in an EGaIn polymer composite, the model must match existing benchmark solutions in literature that uses other modeling approaches. As shown in Figure 17a, one of these solutions provides the predicted stresses inside and outside two aligned [x_2 parallel to $x_2^{(1)}$] spherical cavities of mutual radius (r) suspended in a matrix phase that is under triaxial loading ($\boldsymbol{\sigma}^0 = [\sigma^0, \sigma^0, \sigma^0, 0,0,0]$) [196]. Also, both these spherical cavities in the benchmark problem are assumed to be separated by 4 times of their mutual radius.

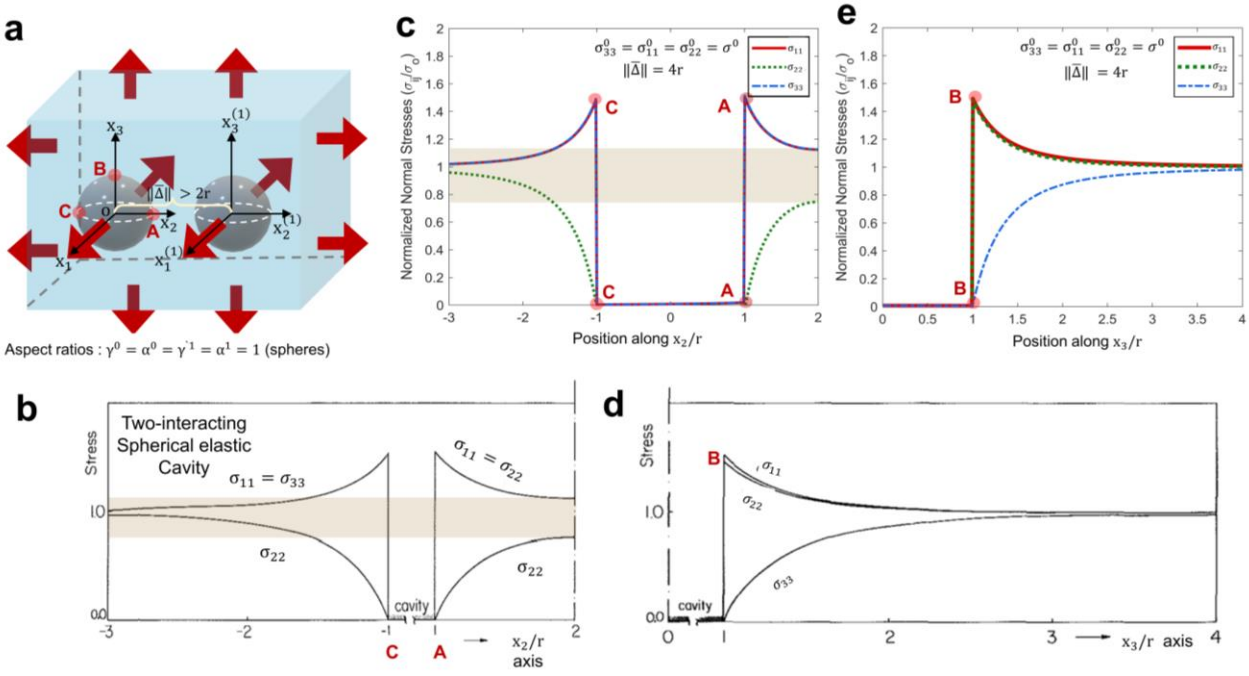

Figure 17. (a) Two aligned interacting spherical cavities under triaxial loading following the benchmark problems from literature [196]. (b) The progression of the normal stress components along the x_2 axis predicted by the benchmark study matches exactly the results of our developed micromechanics model shown in (c). (d) Similarly, the normal stress components along x_3 axis that are obtained from the same benchmark study also illustrate good agreement with the predictions of our model in (e).

Figure 17b illustrates one of the solutions from the benchmark study which shows the changes of the stress components from position $x_2/r = -3$ to $x_2/r = 2$ along the x_2 axis. The same stress solution at the exact positions is reproduced with our micromechanics model as shown in Figure 17c. According to both results, the magnitude of the stress components ($\sigma_{11}, \sigma_{22}, \text{and } \sigma_{33}$) at positions that are away (x_2< -1) from both spherical cavities is smaller than the magnitude of the stresses in between the neighboring spherical cavities (1r<x_2<4r). On the other hand, the benchmark study also produced the stress solutions along the x_3 axis of the left spherical cavity

(Figure 17d) which again can be successfully reproduced by our micromechanics model in Figure 17e. Based on these agreements, we had corroborated the accuracy of the current method to produce a stress solution for two interacting inhomogeneities in a matrix phase without having to use the much complex approach used in the selected benchmark studies.

One of the other objectives of our micromechanics model is to investigate the stress concentration within and outside a core-shell LM inclusion when their composite is under mechanical loading. However, we first need to ensure that the predicted stresses under the influence of interphase match the solution to a benchmark problem which shows the stress solution for a short fiber reinforced composite with interfacial coating. The solution to this benchmark problem uses a more laborious approach known as 3D stress functions [6] and we would like to demonstrate that our micromechanics model can produce similar results with a framework that is more intuitive, generalizable, and computationally less expensive. In this benchmark problem, the aspect ratios of the core (Ω) and the core-shell domain (Σ) are the same but the core-shell domain defined in our model has uniform shell thickness which suggests that aspect ratios of the core and shell cannot be equal. For only the purpose of this validation, this geometry discrepancy is rectified by having the aspect ratio of the short fiber to be the same as the overall fiber + coating domain (Figure 18a). Thus, the equation of ellipsoid describing the core fiber is redefined as Equation 42 where the aspect ratios is now α. Other than that, the Poisson's ratio of the short fiber, coating or interphase, and the matrix are all assumed to be 0.30 in the micromechanics model which are consistent with the setup for solving the benchmark problem.

$$\frac{x^2}{(R_1)^2}+\frac{y^2}{(R_2)^2}+\frac{z^2}{(R_3)^2}=1\ , \qquad \alpha=\frac{R_1}{R_2}=\frac{R_1}{R_3}, \qquad R_2=r_2-t \tag{42}$$

Both the micromechanics model (Figure 18b) and the solutions (Figure 18c and Figure 18d) from the chosen benchmark problem predict exactly similar stress behaviors of a single fiber composite under uniaxial loading. For example, both models predicted that the stress concentration (σ_{11}/σ^0) in the fiber and coating region are close to 9 and 2, respectively in a high aspect ratio ($\alpha = 20$) short fiber composite with thick coating ($t/R_3 = 1.1$). For this comparison, the elastic modulus of the fiber and the coating material are respectively 2 times and 5 times larger than those of their matrix phase. For the next validation case, the modeled composite has shorter fiber aspect ratio ($\alpha = 5$), thinner coating thickness ($t/R_3 = 1.05$), and less stiff fiber material while keeping other parameters unchanged. For this case, both models also estimated that the stress concentration (σ_{11}/σ^0) at the fiber and coating material decrease close to 3.5 times.

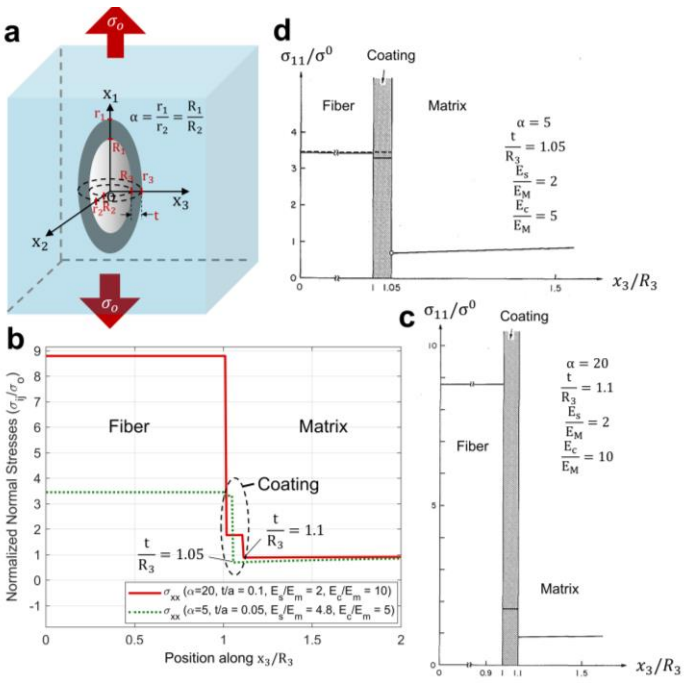

Figure 18. (a) A short fiber composite benchmark problem with the core has the same aspect ratios as the overall short fiber. (b) The predicted normal stresses (σ_{33}/σ^0) in the x3 direction by our micromechanics model when different aspect ratios (α) or interphase thickness (t) are considered. The original solution to the benchmark composite problem for (c) long aspect ratio fiber with thick interphase and (d) short aspect ratios fiber with thin coating.

3.3.2 Stress in EGaIn core-shell inclusion with mild interaction

By taking advantage of the closed-form feature of Eshelby's equivalent inclusion method, it is possible to rapidly predict the stress behaviors at any location within or outside of an EGaIn droplet in a composite. To demonstrate this feature, we will consider a composite under uniaxial compression ($\sigma_{33} = \sigma^0$) which contains a pair of spherical core-shell EGaIn droplet that is aligned and sparsely arranged (Figure 19). By using EIM, the resultant stress field variations inside and outside these EGaIn droplets at the x_1x_2 plane (i.e., $x_3 = 0$) of the composite are illustrated as stress color maps. With the visual aid of these color maps, it is possible to investigate how the Ga oxide shell thickness relative to the core-shell radius (t/r_2) will change the 3D stress (σ_{11}, σ_{22}, and σ_{33}) distributions inside and outside the core-shell LM droplets. The resultant stress distributions of this

study will provide a preliminary insight of whether the size of core-shell structure, packing density, and applied loading conditions can enable or prevent the rupturing or coalescing of EGaIn droplets in their composites.

When the embedded EGaIn droplets in a composite are very large (>10μm), the structural reinforcement provided by the rigid Ga oxide shell can be neglected since the shell thickness remains several nanometers regardless the size of EGaIn droplet. If a uniaxially compressed ($\sigma_{33} = \sigma^0$) composite contain the following large droplets (Figure 19a), our micromechanics model predicts that there will be 3 times increase in tensile stress concentration acting in the x_1 (Figure 19c) and x_2 (Figure 19d) directions near the LM-polymer interface at the x_1 and x_2 axis, respectively. Similarly, there will be also 3 times increase/decrease in compressive stress concentration ($\sigma_{33} \sim 3\sigma^0$) acting in the load direction at the proximity of the LM-polymer interface (Figure 19b). On the other hand, the EGaIn core in the identical composite remain under hydrostatic stresses ($\sigma_{11} = \sigma_{22} = \sigma_{33}$) which are at approximately 30% of the applied compressive stress ($-0.3\sigma^0$). Based on these stress distributions, the large local tensile stress (σ_{22}) in the polymer phase between the suspended EGaIn droplets entails that these droplets would easily expand in the x_1x_2 plane and eventually form Hertzian contacts or contact stresses between two curved body (i.e., EGaIn droplets). In theory, the contacts of these two LM particles would lead to their coalescence (aided by surface tension) and thus a fair indicator whether a single conductive phase can eventually form in the composite.

As the size of EGaIn droplet is reduced to several microns or hundreds of nanometers, the core-shell structure of the LM droplet becomes more dominant. At this size range, the relative size of the oxide shell to the radius ($t/r_1 = 0.1$) of the droplet cannot be neglected and should be included in the EIM computation. When a pair of this core-shell EGaIn droplet is suspended in a uniaxially compressed composite, the maximum stress concentration is dominant at the rigid oxide shell and is predicted to be at thousands orders in magnitudes ($\sim 1000\sigma^0$) while stress concentration right outside the core-shell droplet remain negligible. For example, the tensile normal stress concentration in the x_1 (Figure 19h) and x_2 (Figure 19g) directions in the rigid oxide shell appears to uniformly peak near $2\times10^3\sigma^0$ particularly near the LM core-oxide interface at the x_1 and x_2 axis, respectively. Moreover, the compressive stress (σ_{33}) in the Ga oxide phase of both EGaIn droplets appear to uniformly increase by also about a thousand times but the compressive stress outside

these droplets remain close to the magnitude of the applied compressive stress (Figure 19f). These results suggest that the thin oxide shell which separates two closely incompressible bodies (liquid metal and polymer) undergoes large mechanical stresses when the composite is under compression and could independently rupture with sufficient applied loading. However, since the stiffness of the oxide phase is very large, it is expected that there will still be limited deformation of the overall core-shell particle. In addition, there is limited increase in the stress concentration at the polymer phase separating the core-shell EGaIn droplets which makes it difficult to merge those two particles. Thus, it is possible that despite the stress in the Ga oxide is high, the stress at the polymer separating the droplets is insufficient to bridge the particles either by fracturing the polymer phase or by the shape change of the droplets, that is the shape transition from sphere to high aspect ratio ellipsoid.

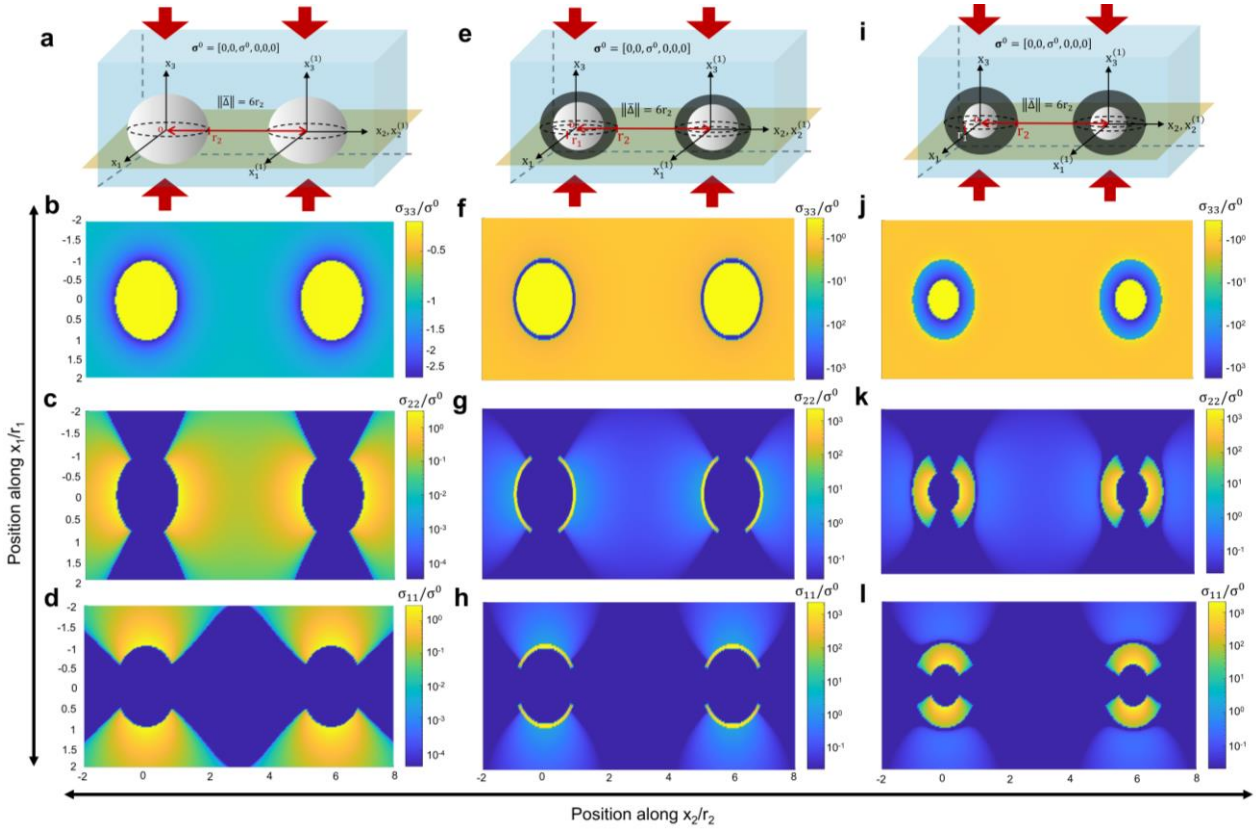

Figure 19. (a) Uniaxially compressed polymer (Sylgard 184) composites with EGaIn inclusion that has no Ga oxide shell resulting in stress concentration distributions in the (b) x_3-, (c) x_2-, and (d) x_1- axis. The following stress heat maps represents the predicted stress distributions on the x_1x_2 plane which is at x_3=0. Other cases that are considered are the same composite but with (e) moderately large size ratio (t/r_2=0.1) and (i) extremely large size ratios (t/r_2 = 0.5). As a result, the final stress distribution for the normal stress concentrations at the x_3 (f and j), x_2 (g and k), and x_1 (h and l) directions are illustrated as heat map distributions.

Based on Figure 19, if the size ratio of EGaIn droplets is further reduced ($t/r_1=t/r_2=0.5$) to an extremely small scale or due to extreme growth of the oxide shell (i.e., thick oxide skin), the average stress concentration in the oxide shell becomes lower ($\sim 10^2$) than the case when the oxide shell thickness was smaller ($t/r_1=0.1$). On the other hand, the stress concentrations for all components ($\sigma_{11}, \sigma_{22}, \text{and } \sigma_{33}$) outside the EGaIn droplets remain at the same order magnitude as the applied load. Therefore, these prediction results suggest that if the oxide shell becomes thick or the droplet size becomes much smaller, it will be both challenging to rupture the Ga oxide phase and coalesce the EGaIn particulates in the polymer matrix. Therefore, without additional surface treatment or surface functionalization to alter the structural rigidity of the Ga oxide shell in the EGaIn nanodroplets, it will be challenging to create conductive pathways in an elastomer composite by mechanical activation.

3.3.3 Size ratio of core-shell EGaIn droplets

Next, we will conduct a closer inspection for the stress distributions between the two core-shell EGaIn droplets when their composite is under compressive mechanical loading (Figure 20a). Figure 20b and Figure 20c illustrates the stress components along the parallel axis (x_2) that joins the centroids of both EGaIn droplets in the polymer phase when the radius of the droplets is large ($t/r_2=0.004$) and small ($t/r_2=0.1$), respectively. Based on these figures, aside the reduction in the large stress concentration in the Ga oxide shell, the stress concentration at the Ga oxide-polymer interface also reduces when smaller size or thicker oxide interphase of the embedded EGaIn droplets are present. For example, the tensile stress concentration in the x_1 (σ_{11}) direction decreases from 3 to 1.7 while the compressive normal stress concentration in the x_3 (σ_{33}) direction decreases from 2.8 to 1.7 in magnitude. Hence, the decreased stress concentration behaviors near the oxide-polymer interface suggests that if the rigid oxide shell can handle the internal stress induced by external load, the formation of internal defects or failure initiation in the polymer phase can be delayed. Thus, this prediction suggests that the strain at break of the composite could be increased.

The following behavior is also exhibited in the mechanical testing of liquid metal elastomer nanocomposite. For example, it is shown that the liquid metal elastomer composite will undergo reduced strain at break in comparison to pristine elastomer when the size of embedded LM droplets is large (i.e., $>10\mu m$) [65]. However, once the size of LM droplets is reduced (<1μm), the strain at break of the elastomer composite improves by about 70% for the same filler volume fraction.

This observation suggests that the size of the oxide shell relative to the size of EGaIn droplets serves as an important parameter in the toughening or strengthening behaviors of the overall soft composites.

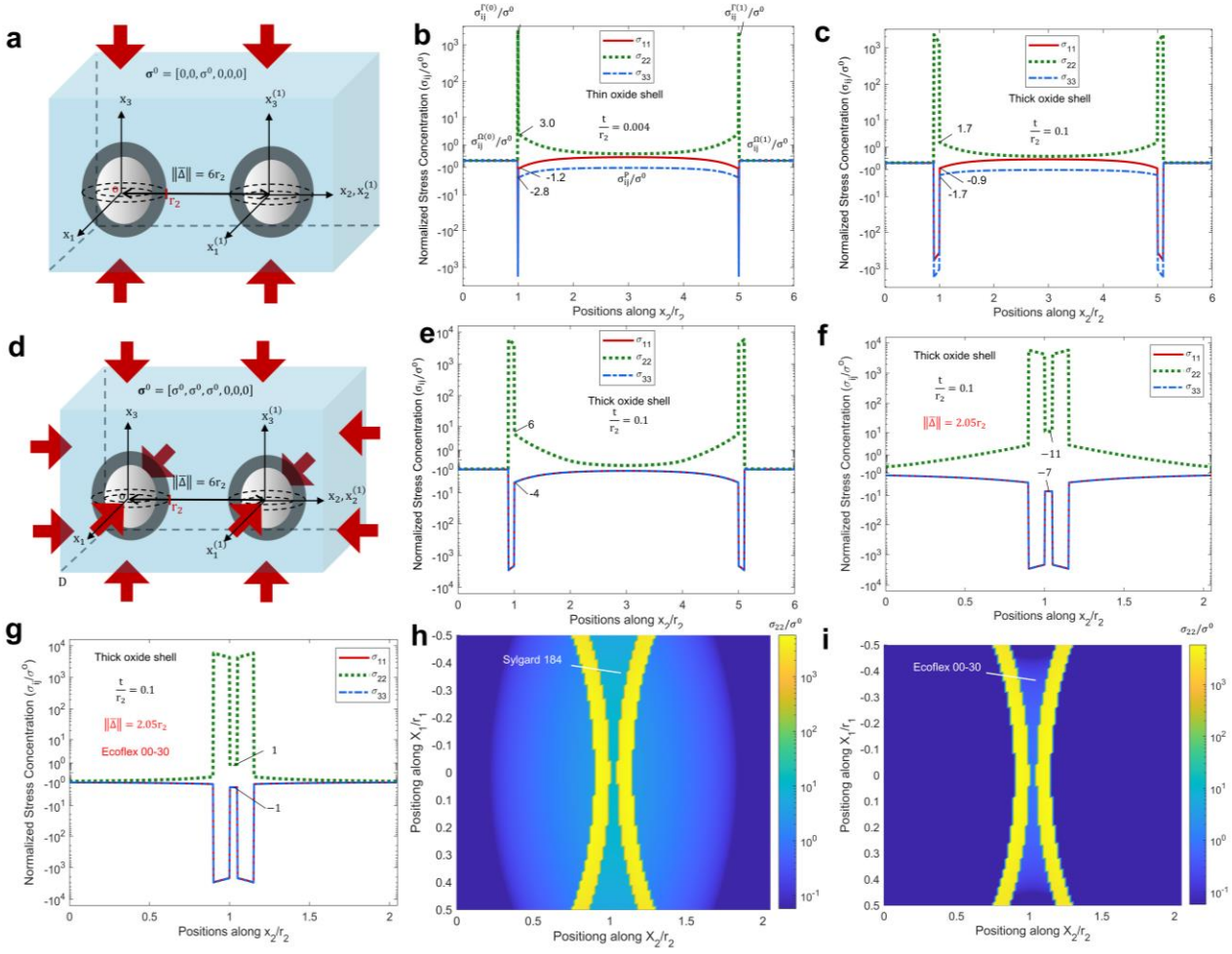

Figure 20 (a) Uniaxial compression on Sylgard 184 composite with a pair of non-intersecting and spherical core-shell EGaIn droplets. The resultant normalized stress components when the ratio of the oxide shell thickness to the size of those droplets are small (b) and (c) large. Hydrostatic compression on a similar polymer composite that comprises of EGaIn droplets with thick oxide shell or small diameter. The resultant superimposed stress concentration when the center-to-center distance of the particles are (e) wide and (f) narrow. (g) When the polymer matrix is replaced with a softer elastomer medium, the stress concentration between the narrowly packed EGaIn droplets is reduced. The heap map stress concentration distribution for σ_{22}/σ^0 when the polymer matrix of the densely packed EGaIn droplets is used as (h) Sylgard 184 and (i) Ecoflex 00-30.

3.3.4 Boundary conditions

So far, we learned that the stress concentration in the rigid oxide shell of EGaIn droplets are predicted to be hundreds order of magnitudes under compressive stress, but the large stiffness of the oxide shell means these droplets are not very deformable as the thickness of the rigid shell becomes significantly larger in relative to the size of the particle. With the help of our

micromechanics model, we now demonstrated that by a combination of hydrostatic compression of the composite alongside high packing density of the embedded LM droplets, it is possible to maximize the chance for a pair of EGaIn particulate to coalesce. This is because the following arrangement allows the EGaIn particulates to maximize the local stress in the phases separating the droplets which can increase the chance of rupturing the oxide shell barrier and the polymer phase that are hindering those droplets to coalesce.

According to Figure 20e, hydrostatic compression on the liquid metal polymer composite can amplify the stress concentration in the rigid oxide shell by several orders of magnitude in comparison to when the composite is applied with uniaxial compression. For example, the stress concentration (σ_{22}/σ^0) in the x_2 direction at the oxide shell of nanoscale LM droplet (t/r_2=0.1) increases from 2×10^3 to 7×10^3 when the boundary conditions of the composite are switched from uniaxial compression to hydrostatic compression, respectively. Similarly, the other stress components (σ_{22} and σ_{33}) that are in compression also increases by several times to about 2×10^3. Also, in comparison to applying uniaxial compression, hydrostatic compression of the composite will also increase the stress concentration at the oxide shell-polymer interface. For instance, σ_{22}/σ^0 at the boundary (x_2/r_2=1) separating the Ga oxide and the polymer phase rise by 6 times when hydrostatic compressive loading is applied on the composite. In contrast, when the composite is applied with uniaxial compressive loading, the same stress concentration component at the same compared location increases to only 1.7 times.

3.3.5 Packing density

Another method that can further increase the local stress near the interface of both EGaIn core-shell droplets is by placing both droplets in proximity. Highly packing density LM droplets are found in various LM composites that have jammed or sedimented liquid metal droplets in their polymer matrix. The purpose of this configuration is to reduce the activation force needed to sinter these particles. Here, micromechanics model is used to investigate the effects of packing density of a pair of EGaIn core-shell droplets on the stress distributions in their composite. This result will help us to deduce whether the sintering of embedded LM particles can be possible or hindered.

When the center-to-center distance between both liquid metal droplets is reduced to $\|\bar{\Delta}\| = 2.05$, the large local stress concentration at the interface of each droplet will be further superimposed (Figure 20f). In this case, the stress concentration in the x_1 direction at the small gap between the droplets nearly doubled to 11 times while the compressive stress concentration in the x_3 direction also almost doubled to 7 times. Similarly, the stress in the oxide shell of each droplet is also expected to increase but the amplification is not as much as at the polymer phase that is sandwiched between the droplets. Hence, the following simulation results indicate that the loaded LMPCs with densely packed LM particles will experience larger stress in their oxide shell and polymer phase therefore correlate to higher likelihood for particle sintering.

3.3.6 Prevent rupture of closely packed EGaIn droplets

For other engineering purposes, it is desirable to preserve the core-shell structure of the LM droplets to limit the dielectric loss, dielectric breakdown strength, or involuntary activation (electrically conductive) of the composite. One way to preserve the structural integrity of the highly packed LM droplets is to utilize ultrasoft polymer matrix to absorb any extreme or repetitive external forces when the composite is subjected to various modes of deformations (twisting, compression, tension, etc.). To prove this, our micromechanics model demonstrates that the stress at the polymer phase separating a closely packed LM inclusions can be drastically reduced when a stiffer (2MPa) elastomer matrix (Sylgard 184) is replaced by a more compliant (0.3MPa) elastomer known as Ecoflex 00-30 (Figure 20g). Now, consider a liquid metal polymer composite that is under hydrostatic compression embedded with a pair of identical core-shell spherical LM droplets of large size ratio $t/r_2 = 0.1$ and narrow center-to-center separation of $2.05r_2$.

When the Sylgard 184 matrix is replaced by Ecoflex 00-30 as the polymer phase, the σ_{11}/σ^0 in the polymer phase located between those particles decreases from 11 to 1 while the magnitude of σ_{22}/σ^0 at the same location decreases from 7 to 1. Both these stress concentrations are referring to the values along the x_2 axis as shown in Figure 20d. Although the overall stress concentrations is damped in the polymer phase, the magnitude of stress concentrations in the oxide shells appears to be unchanged ($\sim 10^3$) when the stiffer elastomer matrix (Figure 20h) is replaced with the much softer elastomer (Figure 20i). Therefore, based on these modeling results, the use of ultrasoft polymer matrix can tremendously reduce the local stress concentration between the closely packed LM droplets which suggests that the chance for the densely packed LM inclusion to be coalesced

is significantly lowered. However, the large stress concentration at the Ga oxide shell is unchanged which means that this phase could eventually rupture. However, if the structural integrity of the insulative polymer phase barrier remains unaffected, the coalescing of the neighboring droplets remains hindered.

3.4 Conclusion

A closed form micromechanics model that is formulated using Eshelby's equivalent inclusion method and superposition principle is used to find the full 3D stress solutions for a pair of interacting core-shell EGaIn droplets in a polymer composite. With these stress solutions, we can investigate the role of the microstructure, nanostructure of EGaIn particulates, packing density, and the applied loading conditions on deciding whether these embedded liquid metal droplets are susceptible to sintering or not. Based on the produced prediction results, the rupture of the oxide shell barrier in liquid metal nanodroplets can be encouraged if hydrostatic compressive forces are applied on the composite and the packing density of the LM droplets is high. If the sintering of the droplets needs to be prevented whilst maintaining their high packing density arrangement to form thermal percolation pathways, the size ratio of the particles will either need to be reduced or more compliant polymer matrix needs to be selected.

The full stress solution obtained from our micromechanics model can be taken advantage of as a predictive tool to predict the failure mechanism of the composite at various length scales. In the future, we shall consider different potential failure criteria appropriate for predicting the failure of the multiphase composite. Moreover, the formulated micromechanics model can also be used to determine the stress intensity factor or energy release rate in the presence of microdefects in the composite to predict the fracture initiation of the polymer composite. Other than that, it is also possible to expand the same developed framework to predict the effective stress distributions when there is more than a pair of LM droplets as well as the presence of multiple interphases, in addition to the native oxide shell. With that being said, the current micromechanics framework paves an exciting starting point to help understand and regulate the sintering behaviors of liquid metal nanoparticles in their nanocomposites. Moreover, another attractive benefit of the current framework is it can also consider various ellipsoidal shapes of the inclusions with multiple interphases as well as predicting large deformation behaviors of liquid metal polymer composites.

Chapter 4: Novel Micromechanics Framework for Soft Multifunctional MXene Polymer Composites

MXenes are two-dimensional (2D) metallic nanomaterials with high electrical, thermal conductivity, and aspect ratios. Recently, efforts have been made to disperse MXenes in compliant polymer matrices to develop flexible and stretchable composites with embedded functionalities. Experimental results indicate that MXene polymer composites (MXPCs) can function as flexible electrical, thermal conductors, or dielectric components with potential applications in soft matter engineered systems. However, the 2D structure of MXene inclusions and their relatively large elastic modulus can significantly increase the stiffness of the polymer matrix and limit the mechanical flexibility of these functional materials. Here, we present a micromechanics model that can predict the structural and functional properties of MXene composites and to evaluate their applicability as functional soft matters. In particular, we are interested in investigating the effect of MXene's size, layered structure, and percolation arrangements on the effective properties of their composites. The predicted elastic modulus, thermal conductivity, and dielectric constant of MXene elastomer composites are found to be in good agreement with results obtained through finite element analysis. With the current framework, we can theoretically identify the microstructures of MXenes that are necessary to create MXPCs with the desired synergy in mechanical and functional properties.

4.1 Introduction

Two dimensional carbides and nitrides, called MXenes, are a rising family of functional nanomaterials that can show excellent electrical, thermal, and optical properties in different systems [87,197,198]. MXenes are atomically thin 2D materials composed of early-transition metals (M element, e.g., Ti, Zr, or Mo), and carbon or nitrogen (X element). When 'A' atoms are chemically removed from the MAX phase precursor, MXene flakes are obtained with a general chemical formula of $M_{n+1}X_nT_x$ where T_x is the surface functional groups that can consist of oxygen, hydroxyl, chloride, or fluoride groups. Titanium carbide ($Ti_3C_2T_x$) is one of the commonly studied MXenes (Figure 21a). These $Ti_3C_2T_x$ nanoflakes can have high thermal conductivity (55.8 $W \cdot m^{-1} \cdot K^{-1}$) [94] and electrical conductivity (i.e., <20,000 $S \cdot cm^{-1}$) [91–93] with a wide range of lateral sizes (100 nm – 10 μm) [91,92,95] as a single or highly ordered multilayer nanostructures.

MXene polymer composites are currently gaining attentions because of their potential application as multifunctional and intelligent materials [10,11]. In these composites, exfoliated MXene nanosheets are dispersed in a polymer matrix. For instance, epoxy resins and water-soluble polymers such as polyvinyl alcohol have been used as the matrix material to produce high-strength functional nanocomposites [94,103,104]. More recently, MXenes are considered as a nanoscale building blocks for creating soft multifunctional composites [88]. In these composites, MXenes are embedded in compliant polymers such as elastomers (e.g., polydimethylsiloxane – PDMS) and gels. Even at low volume fractions of MXene nanosheets, the following soft multifunctional composites exhibit promising electromagnetic shielding behavior [24,118,199], triboelectricity [113,120–122], thermal management [113,199], and high strain sensitivity [200,201] which makes MXPCs desirable for applications in wearable electronics, soft robotics, and human-computer interactions.

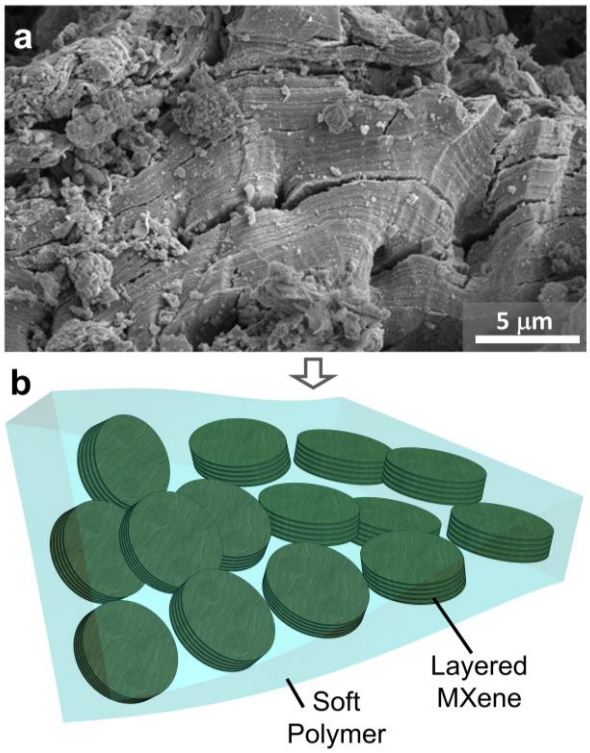

Figure 21. (a) Micrograph of $Ti_3C_2T_x$ before exfoliation process, (b) schematic of MXene polymer composites with multilayered structured MXene fillers.

The nanostructure, volume fraction, and orientation of embedded MXenes are several primary microstructure parameters that dictate the effective properties of MXene polymer composites. Unlike zero-dimensional functional nanomaterials (i.e., solid nanoparticles), the alignment and orientation of dispersed MXenes contribute to the anisotropic mechanical and conductive behaviors of their nanocomposites [202]. In addition, synthesized MXenes can have several to multiple layered structures with various lateral sizes [87,95,203]. Large MXenes with several layered structures are often selected to create high dielectric [204,205] and thermally conductive [117,206] MXene polymer composites at low concentration, while the mechanical stiffening in MXene-based soft composites is found proportional to the lateral size of embedded $Ti_3C_2T_x$ [206,207]. As illustrated in Figure 21b, utilizing multilayered MXenes allows the sustainable production of MXPCs because layered MXenes can be synthesized close up to 100% yield without

the several exfoliation and washing steps that are required for producing monolayer MXenes [95,100]. Therefore, material design tools must be developed to predict the effective properties of MXene polymer composites.

Most current studies investigate the mechanical behaviors of MXene polymer nanocomposites using computational techniques. For instance, finite element method (FEM) is used to study the effects of MXenes' multilayer structure on the fracture toughness, strength, and stiffness of MXene epoxy composites [208]. In other studies, FEM simulations are used to investigate the effective Young's modulus [209] and damage mechanics [210] of multiphase epoxy composites with other 2D fillers such as graphene. The same FEM technique can also be used to computationally demonstrate how agglomerated MXene platelets with non-uniform aspect ratios and random orientations can suppress the stiffening effects in their polymer composites [210]. Most of these modeling efforts focus on approximating the mechanical behaviors of MXene nanocomposite with stiff polymer matrices (elastic modulus of ~1 GPa) while also emphasizing the structural reinforcement of the composite enabled by MXenes. On the contrary, the stiffening effect of MXPCs should be minimized for soft-matter engineering applications while the enhancement of thermal conductivity and dielectric constants (i.e., functional properties) are improved. To achieve this goal, the size, shape, structure, and volume fraction of embedded MXenes must be optimized. Thus, we develop a micromechanics model that can consider the influence of these microstructures on the bulk properties of soft multifunctional MXene polymer nanocomposites. Furthermore, this model can consider the percolation behavior and the layered structure of MXenes. The results of this study will help outline the tradeoff between the stiffness and functional behaviors of MXene polymer composites based on the size and structural arrangement of MXenes. To the best of our knowledge, this is the first micromechanics model that is formulated to predict the effective behaviors of soft multifunctional MXene polymer composites.

4.2 Modeling approach

4.2.1 Micromechanics model formulation

Mori-Tanaka (MT) theory is the common micromechanics model used to estimate the effective mechanical and functional properties of composites with 2D inclusions [137,154]. However, when these 2D inclusions have high aspect ratios such as MXene and are embedded in polymer matrix with low elastic modulus, the accuracy of this model declines even at mild filler volume fractions

[211]. Moreover, Mori-Tanaka theory generally assumes that each of the inclusions in consideration are well separated and always surrounded by the matrix material. However, this configuration contradicts the fact that most MXenes in their composites have tightly layered arrangements. To address this modeling incompatibility, we had modified the existing Interpolated Mori-Tanaka (IMT) model [212,213] to consider MXene's highly ordered nanostructure and percolation behaviors by incorporating Cauchy's interpolating function [214–216]. This modified IMT model is used to evaluate the effective properties of MXPCs based on the properties of polymer matrix and the homogenized properties of clustered or multilayered MXenes which have been determined first by MT theory. This two-level homogenization approach is necessary for our IMT model to consider the multilayer structure, lateral lengths, interphase, orientations, and interactions between suspended MXenes at different length scales in the composite. In this section, the IMT model will be formulated to determine the general properties of MXPCs before eventually being redefined to predict the effective mechanical and functional behaviors of the composite.

MXene polymer composites can be treated as a three-phase composite which constitutes the isotropic polymer matrix, interphase, and MXenes (Figure 22a-b). To include the influence of MXenes' multilayer structure or cluster on the final properties of MXPCs, an equivalent medium (Ω) is used to represent the locally averaged properties of MXene clusters (MC) which will be evaluated by MT theory at the first level of homogenization. The overall property of the MC depends on the properties of interphase ($\mathbf{L}_i$), monolayer MXene ($\mathbf{L}_\Gamma$), thickness (t), diameter (a), distance between single layer MXenes (d), and number of stacked layers (n) as shown in Figure 22b. In addition, the shape of this equivalent medium is assumed to be aligned and centered to the flat cylindrical shape of layered MXenes (Figure 22b-c).

The ratio of volume fraction of MXenes (f_Γ) to those of equivalent medium ($f_\Omega = f_\Gamma + f_i$) is defined by expression R which does not depend on the number of layers (n) of MXenes in the cluster (Equation 43). Instead, R converges to one when the interlaminar distance (d) approaches zero as the thickness to diameter ratio of MXene is very small. If the gap between monolayer MXenes is equal to the thickness of single layer MXene, R will converge to 0.5 because the width (W) of MC remains unchanged (Figure 22b). In the case of MXPCs without MXene clusters (n =1), R will be one (t=0) unless a distinct interphase with finite thickness exists which alternately will have $R = a^2/(a+t)^2$. In general, the relationship between the volume fraction of polymer matrix (f_m),

interphase (f_i), and MXenes (f_Γ) in the composite is determined by Equation 44 where their total summation must be one.

$$R = \frac{f_\Gamma}{f_\Gamma + f_i} = \frac{t\,n\,a^2}{W^2 H} = \frac{t\,n\,a^2}{(a+t)^2(nt+nd)} \quad (43)$$

$$f_i = \left(\frac{1}{R} - 1\right) f_\Gamma;\ \ f_m = 1 - \frac{f_\Gamma}{R};\ f_\Omega = \frac{f_\Gamma}{R} \quad (44)$$

4.2.2 Effective properties of MXene clusters

Mori-Tanaka model is first used to determine the effective property of the MXene clusters which is the equivalent medium ($\mathbf{L}_\Omega$) as shown in Equation 45. In this method, a global field concentration tensor ($\mathbf{A}_{\Gamma,\Omega}$) is computed to relate the average field in the MXene phase ($\bar{\mathbf{\Phi}}_\Gamma$) with the average field in the equivalent medium ($\bar{\mathbf{\Phi}}_\Omega$) (Equation 46-47). For elastic properties, this field concentration tensor will become the strain concentration tensor. Thus, when a strain field is applied on the composite, $\mathbf{A}_{\Gamma,\Omega}$ quantifies the load transfer efficiency between the interphase and MXene nanosheets within the equivalent medium. According to Equation 48, $\mathbf{A}_{\Gamma,\Omega}$ is dependent on the local field concentration tensor ($\mathbf{B}_{\mathbf{L}_i,\mathbf{L}_\Gamma}$) which is a quantity that considers the field concentration values when single layer MXenes are clustered or layered within their interphase of the equivalent medium or MC. In Equations 46 and 48, the term **I** represents the general identity matrix while ':' is the multiplication operator either for 2nd (functional properties) or 4th (elastic properties) order tensors.

$$\mathbf{L}_\Omega = \mathbf{L}_i + R(\mathbf{L}_\Gamma - \mathbf{L}_i) : \mathbf{A}_{\Gamma,\Omega} \quad (45)$$

$$\mathbf{A}_{\Gamma,\Omega} = f_\Omega\, \mathbf{B}_{\mathbf{L}_i,\mathbf{L}_\Gamma} : \left(f_i \mathbf{I} + f_\Gamma \mathbf{B}_{\mathbf{L}_i,\mathbf{L}_\Gamma}\right)^{-1} \quad (46)$$

$$\bar{\mathbf{\Phi}}_\Gamma = \mathbf{A}_{\Gamma,\Omega} : \bar{\mathbf{\Phi}}_\Omega \quad (47)$$

$$\mathbf{B}_{\mathbf{L}_i,\mathbf{L}_\Gamma} = \left(\mathbf{I} + \mathbf{S}_\Gamma : (\mathbf{L}_i^{-1} : \mathbf{L}_\Gamma - \mathbf{I})\right)^{-1} \quad (48)$$

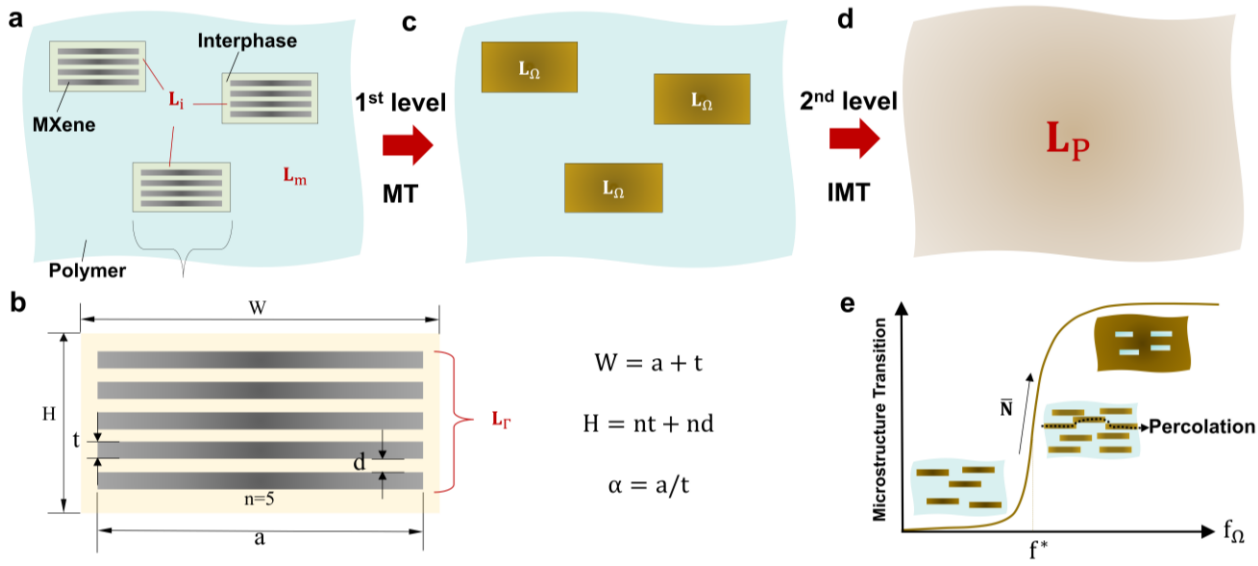

Figure 22. Illustration of the two-step homogenization approach of IMT model to evaluate the effective properties of MXPCs. (a) Each MXene cluster will be homogenized as equivalent medium embedded in a polymer matrix. (c) The equivalent medium substitutes the MC in the polymer matrix. (d) Final homogenization step to evaluate the overall properties of MXPCs with the (e) consideration of percolation microstructure based on Cauchy's cumulative probability function.

The improved properties of the equivalent medium ($\mathbf{L}_\Omega$) rely on the morphology of the encircled monolayer MXenes which behaves as field polarizers or reinforcement bodies of the MC (Figure 22b). Hence, IMT model must consider the aspect ratio ($\alpha = a/t$) of single layer MXene in the first homogenization step. This can be achieved by employing Eshelby's tensors ($\mathbf{S}_\Gamma$) to analytically determine the average strain, electric potential field, or thermal gradient in MXenes [2,135,138,176,217]. These Eshelby's tensors can be defined as Equation S39 and S51 when evaluating the mechanical and functional properties of the equivalent medium, respectively. For instance, the mechanical Eshelby's tensor ($\mathbf{S}_\Gamma$) in $\mathbf{B}_{\mathbf{L}_i,\mathbf{L}_\Gamma}$ will depend on the Poisson's ratio of the interphase (ν_i) and the aspect ratio (α) of monolayer MXenes. On the other hand, to determine the functional properties of the equivalent medium, the same Eshelby's tensors ($\mathbf{S}_\Gamma$) will be replaced by a 2nd order (Equation S51) Eshelby's tensor which is only dependent on the aspect ratio of MXene (α). It is also important to emphasize that the current study utilizes flat cylinder [218,219] instead of standard flat ellipsoid Eshelby's tensor [135] to model the field polarization behaviors of 2D MXene inclusions. This is because the modified micromechanics model in this study is found to significantly overestimate the properties of soft MXPCs when the embedded MXenes are simplified as flat ellipsoids or penny shape.

4.2.3 Effective property of MXene polymer composites

Once the effective properties of MXene clusters or the equivalent medium ($\mathbf{L}_\Omega$) is determined, IMT method is applied in the second homogenization step. In this step, the homogenized MXene clusters are now the field polarizers or reinforcement bodies in a polymer matrix phase (Figure 22c-d). Therefore, IMT model is used here to determine the effective anisotropic property ($\mathbf{L}_P$) of MXPCs with aligned MXene clusters (Equation 49). However, in most synthesized composites, the embedded MXene clusters are either misoriented or randomly oriented, resulting in the presence of anisotropy among MXPCs. Hence, it could be necessary to estimate the effective property of MXPCs ($\mathbf{L}_P^r$) with randomly oriented MC (Equation 50). This can be done by conducting numerical orientation averaging (<·>) on the second term of Equation 50 [220]. The definition of this orientation averaging operation for 4th order (mechanical property) and 2nd order (functional properties) tensors are expressed by Equation S54 and S58, respectively.

$$\mathbf{L}_P = \mathbf{L}_m + f_\Omega(\mathbf{L}_\Omega - \mathbf{L}_m): \mathbf{A}_{\Omega,P} \quad 49$$

$$\mathbf{L}_P^r = \mathbf{L}_m + f_\Omega < (\mathbf{L}_\Omega - \mathbf{L}_m): \mathbf{A}_{\Omega,P} > \quad 50$$

$$\bar{\mathbf{\Phi}}_\Omega = \mathbf{A}_{\Omega,P}: \bar{\mathbf{\Phi}}_P \quad 51$$

$$\beta = w/H \quad 52$$

$$\mathbf{A}_{\Omega,P} = \bar{\mathbf{N}}: (f_m\mathbf{I} + f_\Omega\bar{\mathbf{N}})^{-1} \quad 53$$

$$\bar{\mathbf{N}} = \Big((1-\tau)\big(\mathbf{B}_{\mathbf{L}_m,\mathbf{L}_\Omega}\big)^{-1} + \tau\mathbf{B}_{\mathbf{L}_\Omega,\mathbf{L}_m}\Big)^{-1} \quad 54$$

$$\mathbf{B}_{\mathbf{L}_m,\mathbf{L}_\Omega} = \big(\mathbf{I} + \mathbf{S}_\Omega: (\mathbf{L}_m^{-1}: \mathbf{L}_\Omega - \mathbf{I})\big)^{-1} \quad 55$$

$$\mathbf{B}_{\mathbf{L}_\Omega,\mathbf{L}_m} = \Big(\mathbf{I} + \mathbf{S}_m: (\mathbf{L}_\Omega^{-1}: \mathbf{L}_m - \mathbf{I})\Big)^{-1} \quad 56$$

At the final homogenization of MXPCs, the role of the field concentration tensor ($\mathbf{A}_{\Omega,P}$) of IMT model is to relate the average field in the overall composite body ($\bar{\mathbf{\Phi}}_P$) with the average field in the equivalent medium ($\bar{\mathbf{\Phi}}_\Omega$) (Equation 51). Since MC can have large aspect ratios (Equation 52), these fillers are very likely to interact and form a percolating network when the volume fraction of the clusters is high. To consider this effect, $\mathbf{A}_{\Omega,P}$ is made dependent on the interpolated field concentration tensor ($\bar{\mathbf{N}}$) (Equation 53). As the volume fraction (f_Ω) of MC increases, $\bar{\mathbf{N}}$ will interpolate between the local field concentration tensor evaluated when the distance between

neighboring layered MXenes is large ($\mathbf{B}_{\mathbf{L}_m,\mathbf{L}_\Omega}$) and when embedded MC are so densely interconnected that the polymer phase appears disconnected ($\mathbf{B}_{\mathbf{L}_\Omega,\mathbf{L}_m}$) (Figure 22e). The interpolation progression between these two tensors is dictated by Cauchy's cumulative probability function (τ) which realistically simulate the percolation evolution of layered MXenes (Ω) as their volume fraction (f_Ω) approaches and exceed a percolation threshold (f^*) from a scale of zero to one [214–216,221].

In the second homogenization step, the flat cylinder Eshelby's tensors are dependent on the aspect ratio (β) of the equivalent medium which is now treated as the reinforcement body for the polymer matrix. When modeling the functional property of MXPCs, both $\mathbf{S}_\Omega$and $\mathbf{S}_m$ are 2nd order tensors (Equation S51) which solely depends on β. On the other hand, when evaluating the stiffness of MXPCs, $\mathbf{S}_\Omega$ is a 4th order Eshelby's tensor (Equation S39) that relies on the Poisson's ratio (ν_m) of polymer matrix and β. Similarly, $\mathbf{S}_m$ will be a 4th order Eshelby's tensor which depends on the Poisson's ratio of MXene (ν_Γ) in addition to β. This is done because the composite's microstructure represented by $\mathbf{B}_{\mathbf{L}_\Omega,\mathbf{L}_m}$ suggests that the polymer phase is disconnected and appears as 2D shaped inclusions surrounded by MC when MXenes' volume fraction ($f_\Omega \cong 1$) is high (Figure 22e). Also, it is important to clarify that in eigenstrain theory for elasticity, $\mathbf{S}_m$ (Mechanical Eshelby's tensor) would be dependent on the anisotropic property of the equivalent medium which is non-trivial to solve [135]. Instead, $\mathbf{S}_m$ is assumed to be dependent on MXene's Poisson's ratio as an upper approximation for $\mathbf{B}_{\mathbf{L}_\Omega,\mathbf{L}_m}$.

4.2.4 Interchangeability of property tensors

In the formulation of interpolated Mori-Tanaka model, the property tensors of each λ^{th} phase in MXPCs are represented as $\mathbf{L}_\lambda$. This general term is interchangeable when evaluating the mechanical or functional properties of MXene polymer composites [152]. Table S5 summarizes the appropriate replacement of $\mathbf{L}_\lambda$ in Equation 45 to 56 when the effective stiffness ($\mathbf{C}_P$), relative permittivity ($\boldsymbol{\varepsilon}_p$), and thermal conductivity ($\boldsymbol{\kappa}_P$) of MXPCs are evaluated. Also, the introduced general average field vector ($\bar{\boldsymbol{\Phi}}_\lambda$) can be considered as the strain, electric potential field, and temperature gradient of λ^{th} phase when the mechanical, dielectric, and thermal properties of MXPCs are respectively evaluated.

4.2.5 Cauchy's cumulative probability function for modeling microstructure evolution

Single or layered MXenes are initially sparsely distributed in MXene polymer composites when the volume fraction is below a percolation limit (f^*). As the volume fraction (f_Ω) of MXene clusters increases, the probability of MXenes forming multiple interparticle contacts increases (Figure 23a). Eventually, when the volume fraction exceeds a percolation limit, MXPCs will be saturated with layered MXenes that the polymer phase becomes disconnected. This microstructure transition can be simulated by Cauchy's cumulative probability (CCP) function (Equation 57) before incorporated into IMT model (Equation 54).

$$\tau = 1 - \frac{\tan^{-1}\left((1-f^*)\gamma^{-1}\right)+\tan^{-1}\left(f^*\gamma^{-1}\right)}{\tan^{-1}\left((f_\Omega-f^*)\gamma^{-1}\right)+\tan^{-1}\left(f^*\gamma^{-1}\right)} \quad 57$$

$$f^* = \frac{18\left(S_\Omega^{11}\right)^2-9S_\Omega^{11}}{18\left(S_\Omega^{11}\right)^2-3S_\Omega^{11}-4} \text{ and } \gamma^{-1} = n \quad 58$$

Based on Equation 57, CCP function increases rapidly at the percolation limit (f^*) which depends on the first component (S_Ω^{11}) of the Eshelby's tensor ($\mathbf{S}_\Omega$) [214,215]. The concise expression for S_Ω^{11} is given in Equation S52. Since S_Ω^{11} is only dependent on the aspect ratio of multilayer MXene (β), f^* will be strictly dependent on the morphologies of MC (Figure S3). The estimated f^* assumes that MXenes are randomly dispersed in a composite and is used to approximate the percolation limit of MXene clusters in their composites MXPCs. Based on Figure S3, f^* is expected to decrease when the aspect ratio of MC (ζ^{-1}=β) in the composite is large which occurs when the number of layer (n) increases or the size (a) of MXenes decreases.

The rapid increase of Cauchy's cumulative probability function (τ) reflects the formation of percolation microstructures within MXPCs. For instance, CCP function suggests that MXPCs with large MXenes ($\alpha = 500$) will form percolation microstructure at lower volume fraction than MXPCs with small ($\alpha = 50$) MXene fillers (Figure 23a). When the size of MXene is unchanged, a greater number of stacked layers (n) of embedded MXenes will cause the formation of percolation pathways to delay (f^* shift higher) but the formation rate (γ^{-1}) to increase (Equation 58). This trend is realistic because for the same volume fraction and diameter, multilayer MXenes cannot form wider interconnected networks than few layer MXenes within the polymer composite. To create wider percolation networks, additional volume fraction of MC is needed to saturate the polymer matrix.

4.2.6 Resistance function (Functional Properties)

MXenes' percolation microstructure leads to the commonly observed sudden thermal conductivity and dielectric constant enhancement of MXPCs at a concentration threshold. This is because when percolation networks are formed, numerous neighboring MC will be in close contact with their respective interphase partially intersects each other (Figure 23b). As a result, these overlapped interphases ($\mathbf{L}_i$) undergo large localized thermal conductivity or dielectric constant enhancement which respectively contributes to the sharp thermal or dielectric property improvement of MXPCs. Hence, a resistance function (T) is introduced to associate the function's resistance drop to the sudden enhancement in the local thermal conductivity ($\boldsymbol{\kappa}_i$) and dielectric constant ($\boldsymbol{\varepsilon}_i$) within the percolated MXene clusters (Equation 59 and 60). In thermal property modeling, the sharp drop of resistance function within the interphase signifies the reduction in interfacial (Kapitza resistance) or contact thermal resistance among percolated MC [216,222]. Alternately, in dielectric property modeling, the rapid drop of resistance function mimics the spontaneous formation of nanocapacitors or the onset of Maxwell-Wagner-Sillars (MWS) effects among percolated MC. Therefore, Figure 23c suggests that MXPCs with large ($\alpha = 500$) monolayer MXenes will have a sharp decrease in resistance function or large functional property enhancement at 2.5 % volume fraction. In contrast, MXPCs with small ($\alpha = 50$) monolayer MXenes will have acute drop in resistance function or sudden functional property improvement at 10% volume fraction.

$$\mathbf{L}_i = \mathbf{L}_m \mathrm{T}^{-1} \quad \text{when} \quad \mathbf{L}_\lambda = \boldsymbol{\kappa}_\lambda \text{ or } \boldsymbol{\varepsilon}_\lambda \tag{59}$$

$$\mathrm{T} = \frac{\tan^{-1}\left(\left(1-\mathrm{f}'/\mathrm{R}\right)\gamma_o^{-1}\right)+\tan^{-1}\left(\mathrm{f}'\gamma_o^{-1}/\mathrm{R}\right)}{\tan^{-1}\left(\left(\mathrm{f}_\Omega-\mathrm{f}'/\mathrm{R}\right)\gamma_o^{-1}\right)+\tan^{-1}\left(\mathrm{f}'\gamma_o^{-1}/\mathrm{R}\right)} \tag{60}$$

In this study, a scaling parameter (γ_o) of 0.02 is used which is the approximated statistical value previously used for modeling the percolation evolution in graphene polymer composites [216]. For simplicity, the percolation threshold (f^*) used to model CCP function and the critical volume fraction (f') for resistance function are assumed equal when modeling MXPCs with different sizes or layers of MXenes. It is also important to notice that at low volume fraction, Equation 60 suggests that the thermal or dielectric property of interphase converges to those of polymer matrix ($\mathbf{L}_i = \mathbf{L}_m$) because of negligible interparticle interactions.

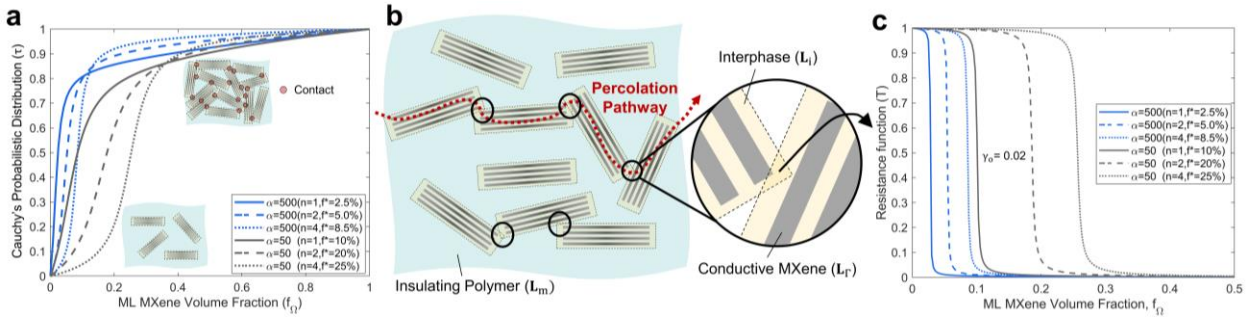

Figure 23. (a) The probability for the formation of interparticle contacts (overlapped interphase) of MC follows Cauchy's cumulative probability function (τ) as volume fraction (f_Ω) of MC increases. (b) An illustration of MC dispersed in a polymer with the interparticle contacts forming a continuous percolation pathway. (c) The overlapped interphase phase of neighboring MC led to the local surge of functional property indicated by the drop in resistance function (T).

4.2.7 Finite element method

Finite element method is an effective way to validate the results of micromechanics model and to identify potential limitations of the model when predicting the effective properties of composites [2,146,223]. To achieve this, the representative volume element (RVE) chosen for finite element evaluation needs to be sufficiently large to realistically reflect the microstructures of MXene polymer composite while is small enough to reduce computational resources [224]. Hence, we chose the breadth (b) and height (h) of RVE to be at least two times larger than the diameter (a) and thickness (t) of MXenes, respectively (Figure 24a). In this cubic RVE, there are hexagonal arrangements of flat cylinders representing MC dispersed in polymer matrix. In addition, the embedded MXenes can have several (n = 1 to 3) clustered flat cylinders uniformly separated by the thickness (d = t) of single layer MXene. For RVE with larger volume fraction of MXenes, the height of RVE is increased but the breadth is unchanged because the aspect ratio of MXenes is fixed. Each flat cylinders will have a diameter of 500 and thickness of one unit length in order to represent single layer MXene with aspect ratio of 500. We evaluated twenty four RVE of MXPCs with volume fraction of MC ranging between 1 % to 10 % and clustered layers of one to three. In all these RVE, both the bodies of the polymer and thin

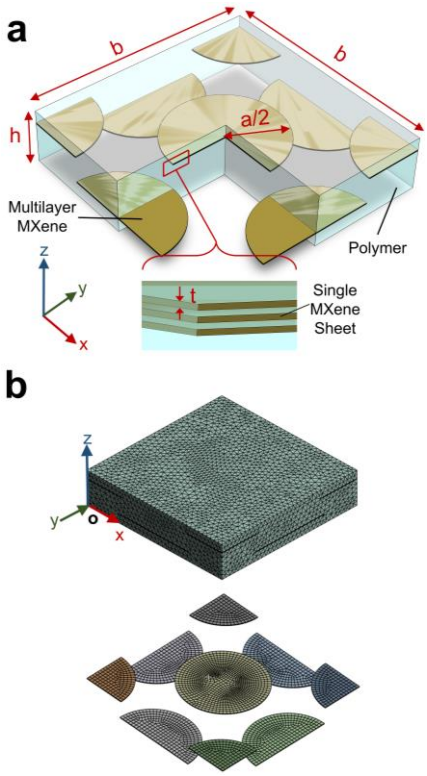

Figure 24. (a) RVE of MXPC with several layered MXenes. (b) The meshed body of the RVE with the layered MXenes configured as hexagonal packing.

cylindrical MXenes are meshed with three node elements in ANSYS where the maximum allowable mesh size is set 500 times smaller than the breadth of RVE.

To prevent wall effects, the meshed RVEs are constructed to satisfy the material periodicity so the volume element behaves as they originate from the bulk nanocomposite [224]. To do this, the thin plate inclusions (stacked or single layer) at the corners or boundaries of RVE are allowed to penetrate the borders but must reappear at the opposite edge (Figure 24b). This guarantees that the opposites sides to have similar property and the evaluated final properties of the RVE to be transversely isotropic. Finally, homogeneous boundary conditions are used to evaluate the anisotropic elastic modulus, thermal conductivity, and static dielectric constants of the RVE. The detailed assembly of these boundary conditions are in the supplemental information: 3.7 Boundary conditions in FEM.

4.4 Results and discussion

4.4.1 Input properties for modeling MXPCs

To accurately predict the effective properties of MXene polymer composites, a realistic range of input material properties for monolayer MXene and polymer matrix is needed. These input material properties are summarized in Table S6 which includes the measured elastic modulus of single layer $Ti_3C_2T_x$ by atomic force microscopy test [225] and the measured elastic modulus of the polymer matrix (Sylgard 184) obtained from conducted tensile tests [226]. The measured elastic modulus of single layer MXene can vary between 9 GPa and 70 GPa [225]. In this modeling, the elastic modulus of MXene sheet is assumed to be 9 GPa (isotropic) as the effective stiffness of MXPCs with soft polymer matrix is found negligibly unchanged when MXenes' elastic modulus ranges from the lowest (9 GPa) to the highest (70 GPa) stiffness (Figure S5a). Moreover, the Poisson's ratio (ν_λ) of Sylgard 184 and MXene is approximated as $\nu_m = 0.49$ and $\nu_\Gamma = 0.2$, respectively. Table S6 also includes the selected dielectric constants and thermal conductivity of the polymer matrix (Sylgard 184) and MXenes ($Ti_3C_2T_x$) which are used to predict the effective functional properties of MXPCs. Lastly, we assume that the thickness (t) and the separation distance (d) of MXenes is 1 nm. This approximation is appropriate because according to most X-ray diffraction measurements, the separation distance of multilayer MXenes can range between 0.5 nm to about 1 nm.

4.4.2 Mechanical properties

As the number of layers of large (a = 5 μm) $Ti_3C_2T_x$ inclusions increases from one to ten layers, the large elastic modulus enhancement of MXene in Sylgard 184 composite (MXene-Sylgard 184) shifts to higher volume fraction (f_Γ). This behavior is predicted because the mechanical reinforcement behavior of the composite depends on the filler distribution (Figure 25a) and involves MXenes' microstructure transitions when their volume fraction increases. When the number of layers of embedded MXenes are small (n < 4), this interpolation function surges at low volume fraction (f_Ω < 2.4 %). As a result, the elastic modulus of MXene-Sylgard 184 with single and two-layer MXenes (a = 5 μm) increases by 800 % (~12 MPa) and 400 % (~6 MPa), respectively at 1 % volume fraction (Figure 25b). In contrast, when the embedded MXenes have ten layers, the increase in the elastic modulus of the composite is initially slow (< 200 %) but escalates near 1.5 % volume fraction. According to Figure 25a, this volume fraction (f_Γ ~ 1.5 %) is consistent to the volume fraction ($f_\Omega = f_\Gamma/R \cong 3\ \%$) where the corresponding interpolation function of ten layer MXene clusters begins to increase. At above 3 % volume fraction (f_Γ), the predicted stiffness of MXene-Sylgard 184 with two or more layers of MXene inclusions becomes approximately equivalent to each other. These results indicate that the large stiffening effects of MXPCs at low volume fraction can be minimized when multilayer instead of single layer $Ti_3C_2T_x$ inclusions are selected.

MXene-Sylgard 184 with nanosized single layer $Ti_3C_2T_x$ sheets will have lower stiffness enhancements than MXene-Sylgard 184 with microsized single layer MXene sheets (Figure 25c). For example, at 4 % volume fraction, the effective elastic modulus of MXene-Sylgard 184 with large (a = 5 μm) and small (a = 100 nm) single layer MXenes are predicted to improve by 53 times (~80 MPa) and 3 times (~4.5 MPa), respectively. In addition, the stiffness increment of MXPCs with small monolayer $Ti_3C_2T_x$ remains mild even at 10% volume fraction (f_Γ). This is because as the volume fraction of smaller size MXenes increases, the microstructure transition (τ) of these fillers from sparse (low f_Ω) to dense (high f_Ω) distribution occurs much gradually. As a result, the stress or strain field around the smaller MXene fillers is only close enough to interact with their neighboring fillers when the filler volume fraction is sufficiently high.

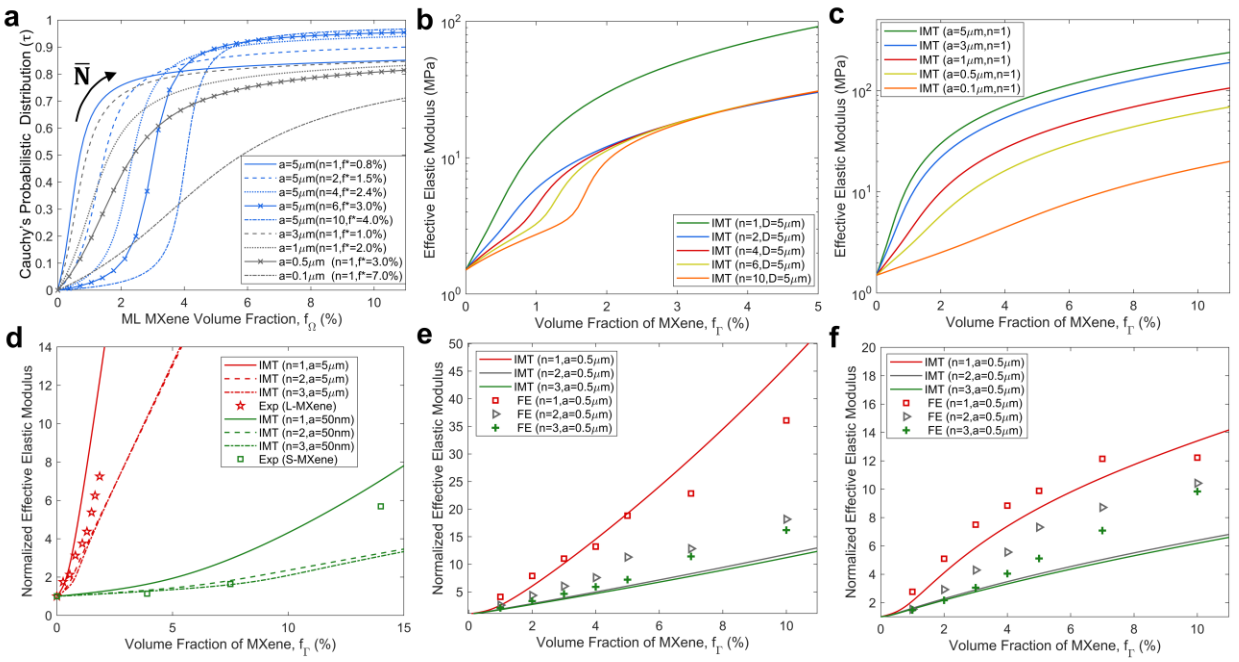

Figure 25. (a) CCP interpolation function for MXene inclusions with different lateral diameter and layered structure. (b) IMT model predicts the effective elastic modulus of MXene-Sylgard 184 with fixed MXenes' size (a = 5 μm) but with distinct layered structures. (c) The effects of aspect ratio or diameter of monolayer MXene inclusions on the stiffness of MXene-Sylgard 184. (d) The measured elastic modulus of MXene-Sylgard 184 with L-MXene and MXene-NBR with S-MXene are compared with their respective predicted elastic modulus [206,207]. The elastic modulus of unfilled NBR is chosen as 2.24 MPa while for unfilled PDMS will be 0.4 MPa. (e) Longitudinal and (f) transverse elastic modulus evaluated from FEM are compared with the prediction results of IMT model.

4.4.3 Experimental comparison (Stiffness)

The results of Interpolated Mori-Tanaka model are compared with the measured Young's modulus of MXene elastomer composites. Since most fabricated MXene nanocomposites have randomly oriented rather than aligned MXenes, we will approximate the orientations of MXenes inclusions to be random in this experimental validation. With this assumption, the interpolated Mori-Tanaka model is able to accurately predict the measured Young's modulus of MXene in PDMS composite (MXene-PDMS) which has large 5 μm size MXenes (termed L-MXene) as shown in Figure 25d. For example, when single, double, or triple layers of L-MXenes are randomly distributed in the following PDMS composite, the predicted effective elastic modulus matches the measured stiffness of MXene-PDMS up to 3% volume fractions. This range of layers is chosen because the embedded MXenes in the following cited study have measured thickness of several nanometers. Thus, the non-uniformity in this reported thickness measurement indicates that the embedded MXenes have predominantly a few layered structures as the thickness of individual MXenes can be approximated as 1nm. Also, upon closer comparison, the measured elastic modulus of MXene-PDMS composite appears to be between the predicted elastic moduli of the composite with single

and double layered MXene clusters (Figure 25d). This is because in the test specimens, there could be a mixture of single and several layer MXene fillers with variable lateral sizes, which may explain the slight gap exists between the experimental and theoretical results.

Interpolated Mori-Tanaka model can also accurately estimate the measured elastic modulus of MXene in Nitrile-Butadiene-rubber composite (MXene-NBR) which contain small size MXenes (termed S-MXene) [206]. Initially, the measured elastic modulus of MXene-NBR shows negligible increase up to 8% volume fractions. This minimal stiffening behavior is consistent to the predictions of IMT model when the following composite is assumed to have two to three layers of MXene clusters (Figure 25d). Eventually, at about 14% volume fraction, the measured elastic modulus of MXene-NBR has increased by six times but according to IMT model, this is only achievable when only single layer MXenes are assumed randomly dispersed in the composite. However, it is extremely challenging to fabricate composites with only monolayer MXenes because nanosized MXenes would often agglomerate aggressively at such high concentration and would instead decrease the mechanical reinforcement of their composite. Thus, it is possible that other unaccounted factors such as the irregular lateral size distribution, orientation, and shapes of MXenes to cause the observed discrepancies between the predicted and measured results.

4.4.4 Finite element method validation (Stiffness)

To validate our proposed micromechanics model, the anisotropic (longitudinal and transverse) elastic modulus of MXene-Sylgard 184 that are predicted by IMT model and finite element method will be compared with each other. To produce these predictions using IMT model, it is assumed that the diameter of individual MXenes is fixed at 500 nm (α=500) which is consistent with the size of MXenes in the created RVEs (Figure 24a). Since the following MC have high aspect ratio, well-aligned, and well separated in the RVEs, the percolation threshold (f^*) of IMT model is approximated to be close to zero (i.e., f*~0.01) while the formation rate (γ^{-1}) of CCP function is set to one. This small percolation threshold is chosen because the predicted percolation threshold for randomly oriented MXenes is already at 0.02 when the considered aspect ratio (ζ^{-1}) is 500 (Figure S3). Hence, we can use the same modeling parameters when validating the thermal and dielectric properties of MXene polymer composites that are evaluated by FEM.

When comparing the longitudinal elastic modulus, both IMT model and FEM results appear to yield similar prediction behaviors. The elastic modulus predicted by IMT model and FEM for

composites with single layer MXenes show the best agreement up to 5% volume fraction. On the other hand, the agreement between the theoretical and experimental results for composites with two and three layers of MXenes are up to a low volume fraction before beginning to deviate at higher filler concentration (Figure 25e). Similarly, the transverse elastic modulus of MXPCs predicted by both IMT model and FEM also have comparable trend. However, in this comparison, the predicted transverse elastic modulus by the micromechanics model can only remain in close agreement with the results of FEM up to several percent volume fraction (Figure 25f) and at higher filler concentration, IMT model will begin to underpredict the transverse elastic modulus evaluated by FEM particularly for the case of MXene-Sylgard 184 with single and two-layer $Ti_3C_2T_x$ inclusions. This discrepancy occurs because at high volume fraction, the interface of layered MXenes becomes close to the boundaries of RVE. As a result, this will cause large wall effects which will reduce the accuracy of the FEM results. Despite this, most of the anisotropic elastic modulus of MXPCs that are predicted by both FEM and IMT model are close to each other up to 3% volume fraction, which is realistically the concentration limit for MXenes this large size to remain uniformly dispersed in their composites.

4.4.5 Soft Interphase

The introduction of distinct interphase surrounding the embedded multilayer MXenes can change the stress transfer between the applied load to the fillers in their composite. To investigate these effects, the proposed two-step homogenization model will treat the suspended MXenes in a MXene polymer composite to be encapsulated by an interphase that is softer than the polymer matrix. With this formulation, we can now investigate the effect of weak or soft interphase on the overall composite's stiffness. For example, if a hydrogel such as a polyacrylamide (PAAm) is chosen as the interphase, which is assumed to be about five times more compliant (300KPa) than Sylgard 184, the overall stiffness of MXene-Sylgard 184 will decrease by several orders of magnitude.

According to our micromechanics model, the large stiffening behavior of MXPCs can be suppressed with the help of soft interphase which can be done in composites with either microscale multilayer (Figure 26a) or nanoscale single layer MXenes (Figure 26b). For instance, when 5 μm size single layer MXenes are embedded in Sylgard 184 at 1% volume fraction, the stiffness of MXPCs is predicted to increase by only 1.9 times when a soft interphase is presence or otherwise can increase up to 8 times when the soft interphase is not considered (i.e., perfect bonding). If the

soft interphase does not exist, the stiffness of the interphase and the polymer matrix will be equivalent in the model (Figure 26a).

The reduction in the elastic modulus enhancement of MXene-Sylgard 184 with incorporation of soft PAAm interphase is also more profound in MXPCs with single layer MXenes than for composite with layered MXenes. For example, the final elastic modulus of MXene-Sylgard 184 with one- and two- layer MXenes with the same lateral size (5 µm) is approximately equivalent to each other when PAAm is introduced as the interphase. Moreover, it is also theoretically determined that the soft interphase is efficient in mitigating the structural reinforcement caused by single-layer MXenes particularly when the size of the fillers is large (Figure 26b). For example, when hydrogel interphase is introduced, the normalized elastic modulus of MXene-Sylgard 184 with 5µm and 100nm monolayer MXenes reduces from 50 (without soft interphase) to 5 and 10 (without soft interphase) to 2, respectively at 4% concentration. Hence, the following modeling results indicate that the surface treatment of multilayer MXenes with a soft interphase could be an effective processing technique to create highly stretchable and flexible MXPCs.

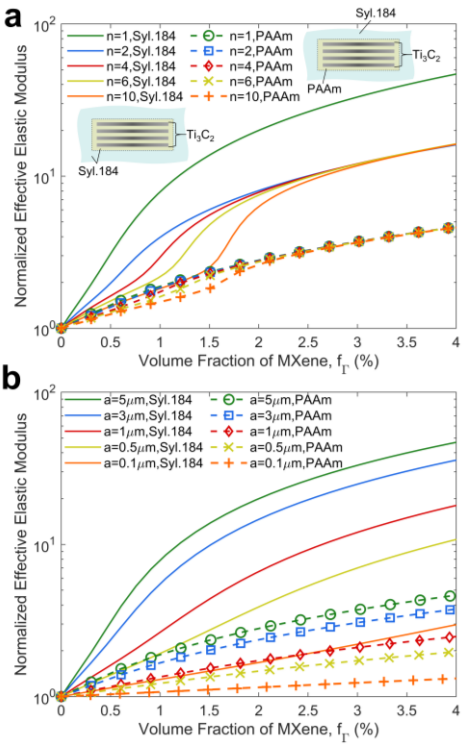

Figure 26. (a) Sylgard 184 composite with large (a=5µm) embedded single and multilayer MXenes exhibit suppressed stiffening behavior when PAAm is chosen as the interphase. (b) The use of smaller sized monolayer (n=1) MXene flakes with gel interphase results in the reduction of elastic modulus of MXene-Sylgard 184.

4.4.6 Thermal properties

By using the Interpolated Mori-Tanaka model, we can theoretically investigate the effects of MXenes' micro or nano structures on the final properties of their composites. The model predicts that as the number of layers of large (5 µm) $Ti_3C_2T_x$ increases from one to ten, the largest thermal conductivity improvement of MXPCs shifts from low to high volume fractions (Figure 27a). For example, MXene-Sylgard 184 can achieve thermal conductivity improvement of 7 times (~2 $W \cdot m^{-1} \cdot K^{-1}$) when either 2.0 % volume fraction of monolayer MXenes or 2.5 % volume fraction of ten-

layered MC are used. This is because monolayer $Ti_3C_2T_x$ has the largest surface area to volume and can form very wide thermal networks at low volume fraction. In contrast, multilayer $Ti_3C_2T_x$ (n > 1) are locally clustered in their composite and are unable to form a comparably wide conductive networks at the same low concentration despite having the same size. On the other hand, when the filler volume fraction is very low (< 0.5 %) and have no chance to percolate, the predicted thermal conductivity of MXene-Sylgard 184 becomes approximately the same regardless of the number of layers in the embedded MXene clusters.

At low filler volume fraction, nanoscale MXenes are less efficient than microscale MXenes when it comes to improving the thermal property of MXPCs. For instance, the thermal conductivity of MXene-Sylgard 184 will improve by 7 times (2 $W \cdot m^{-1} \cdot K^{-1}$) and 1.5 times (0.4 $W \cdot m^{-1} \cdot K^{-1}$) when 2 % volume fraction of monolayer $Ti_3C_2T_x$ that are 5 μm and 100 nm in size are respectively used (Figure 27b). This is because as the size of monolayer MXenes reduces, the volume fraction where there will be sufficient MXene fillers to form thermal conductive pathways and undergo reduced interfacial thermal resistance will increase. IMT model can model these behaviors because the following critical volume fraction (i.e., percolation limit) that dictates the microstructure transition (inflection point of CCP function) and reduced interfacial thermal resistance (resistance drop) are inversely proportional to the aspect ratio (β) of the embedded MXene clusters.

4.4.7 Finite element method comparison (Thermal conductivity)

To validate our proposed micromechanics model, Figure 27c compares the predicted longitudinal and transverse thermal conductivity of MXene-Sylgard 184 with the results of finite element method. Here, the thermal conductivity of the interphase used in IMT model is equated to those of polymer matrix ($\boldsymbol{\kappa_i = \kappa_m}$) because the multilayer $Ti_3C_2T_x$ in the created RVEs are always separated. Based on Figure 27c, the longitudinal (κ_L) and transverse (κ_T) thermal conductivity of MXene-Sylgard 184 predicted by IMT model agrees reasonably well with the results of FEM, particularly at low volume fraction. Furthermore, both models suggest that the estimated thermal conductivity of MXene-Sylgard 184 with two- and three- layered MC are approximately similar while the composite with single layer MXenes (same lateral size) exhibits the best thermal property enhancement.

MXPCs with aligned MXene clusters can have large thermal conductivity at the in-plane direction but have very small out-of-plane thermal conductivity. For instance, the transverse thermal

conductivity of MXene-Sylgard 184 shows negligible enhancement even when the filler volume fraction is high. This is because the heat flow in this direction is impeded by multiple alternating layers of thermally insulating interphase and by the insulative polymer matrix phase that is separating the aligned MXene clusters. Nevertheless, it is important to note that this ideal filler separation may not exist in realistic MXPCs. For example, an experimental study demonstrated that the transverse thermal conductivity of MXene epoxy composite with aligned MXenes can still improve by several times. This occurs because the presence of smaller MXene flakes created an additional heat transfer bridges within the interphase or at the spacing between the aligned MXene clusters in the composite [227]. Although the following arrangement cannot be fully considered in this study, IMT model is capable of generally explaining the influence of MXenes' orientation and multilayer structure on the effective thermal property of MXene polymer composites.

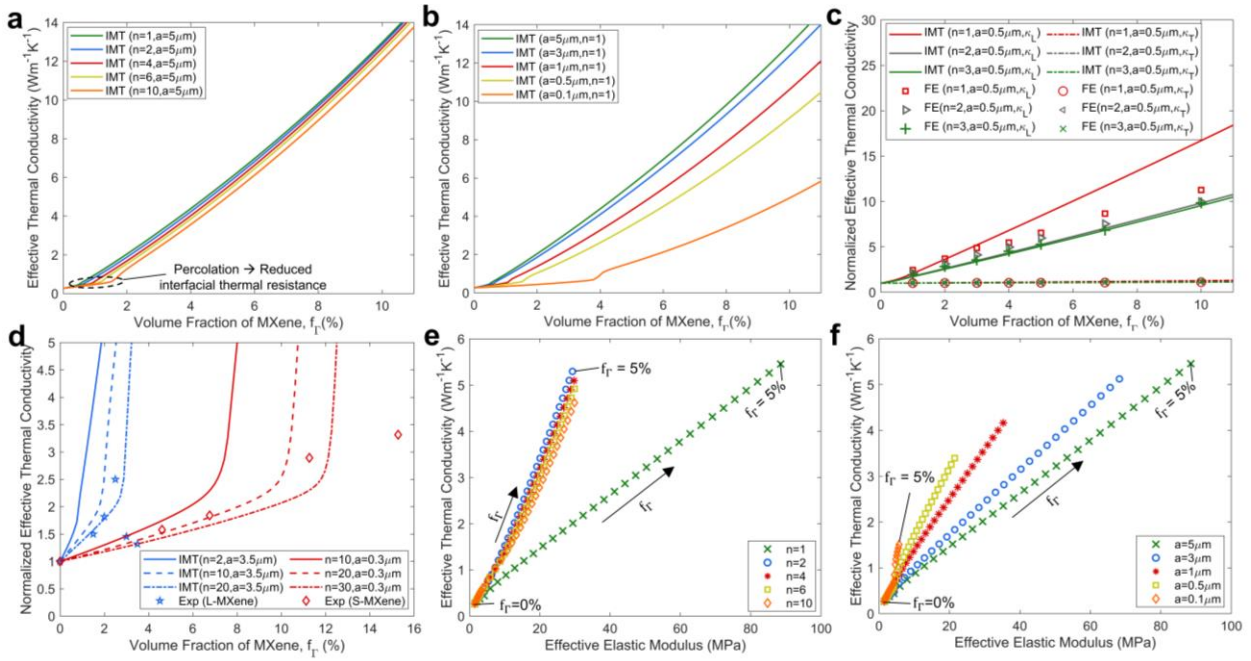

Figure 27. The IMT model predicted the longitudinal thermal conductivity of MXPCs with (a) different layers of embedded MC and (b) different lateral lengths of single sheet MXenes. (c) Experimental measurements [113,117] and (c) FEM results are compared with the predicted thermal conductivity of MXPCs. In this plot, the thermal conductivity of MXene-Sylgard 184 and MXene-PVDF are respectively normalized by the thermal conductivity of unfilled Sylgard 184 (κ_m=0.27) and unfilled PVDF (κ_m=0.19), respectively. The evaluated longitudinal thermal conductivity of MXPCs due to (e) changes in the MXenes' layered structures (fixed 5µm diameter) and (f) changes in the diameter of single sheet MXenes are compared with the predicted longitudinal elastic modulus of the composite due to the same respective variance in the layered structure and size of their MXene fillers.

4.4.8 Experimental comparison (Thermal Conductivity)

For further validation, the results are compared to the measured thermal conductivity of MXene polymer composites that have large (3.5 µm) and small (300 µm) MXene fillers [113]. In this

comparison, the measured thermal conductivity of MXene-Sylgard 184 with 3.5 µm size MXenes (L-MXene) is closely approximated by our micromechanics model when ten to twenty sheets of MXene clusters are assumed to be randomly suspended in this composite (Figure 27d). On the other hand, the IMT model is also used to accurately predict the thermal conductivity of MXenes embedded in Polyvinylidene Fluoride composite (MXene-PVDF) [117]. In this case, the suspended MXenes in the following composite have size of approximately 300 nm (S-MXene) but their size distribution and range of layers are not reported. Nevertheless, for this composite, we determined that the measured thermal conductivity of MXene-PVDF best matches the predictions of IMT model when the composites have MC that comprise of twenty to thirty layers. Despite this assumption, the chosen number of layers in the simulation are realistic because most synthesized MXene clusters consist of at least several layers of $Ti_3C_2T_x$ and only a small handful of single layers $Ti_3C_2T_x$ which can be realistically produced. Thus, it is reasonable to assume in our model that the average number of layers among the embedded MXene clusters in the fabricated composites could be in the tenths of orders.

Above the percolation volume fractions, the IMT model predicts that the thermal property of MXPCs would continue to significantly increase. However, the experimental results show that the thermal conductivity improvement of MXene-PVDF with L-MXenes will slow down. Similarly, when the appeared percolation limit (f_Γ) of 2.2% is surpassed, the measured thermal conductivity of MXene-Sylgard 184 with S-MXenes appears to decrease, but the theoretical model predicts that the composite's thermal property will continue to escalate. These prediction mismatches occur because in the micromechanics model, MXene clusters (large or small) are always assumed to be uniformly dispersed in their composite but in the actual composite, the MC would progressively agglomerate as their volume fraction increases. As a result, this phenomenon will reduce the available contact surface area for suspended MXenes to maintain or widen the formed thermal pathways, thus impeding the high conduction heat transfer within the thermally insulating polymer matrix.

4.4.9 Thermal conductivity and elastic modulus correlation

To answer the question whether MXene is suitable for soft multifunctional composite, it is important to investigate the tradeoffs between the stiffness and thermal conductivity of their composites based on the selected size and structure of MXenes. To visually evaluate these

tradeoffs, two material property chart (i.e., Ashby's plots) are created from the results of IMT model to correlate the predicted effective thermal conductivity with the predicted effective elastic modulus (without soft interphase) of MXene-Sylgard 184 (Figure 27e and f). In the first correlation, the influence of the number of layers and sizes of MXene clusters on these paired properties of the composite is investigated. From this correlation, it is determined that it is possible to preserve the thermal conductivity enhancement while reducing the stiffening effects of MXPCs by favoring layered (n>1) instead of single layer MXene fillers. For example, as the volume fraction of 5 μm size single layer MXene increases to 5 %, the estimated longitudinal elastic modulus and longitudinal thermal conductivity of MXene-Sylgard 184 converge to 88 MPa and 5.5 $W \cdot m^{-1} \cdot K^{-1}$, respectively (Figure 27e). In contrasts, as the volume fraction of 5 μm diameter MXene with two clustered sheets increases to 5 %, the longitudinal elastic modulus and longitudinal thermal conductivity of MXene-Sylgard 184 are predicted to be 30 MPa and 5.3 $W \cdot m^{-1} \cdot K^{-1}$, respectively. This theoretical finding is promising because we had shown earlier that with the introduction of soft interphase (PAAm) around the embedded MC, it is possible to further minimize the stiffening effects of MXPCS without compromising the thermal conductivity gain as long as the thermal property (~0.3 $W \cdot m^{-1} \cdot K^{-1}$) of the substituted soft interphase is close to those of the polymer matrix. The following minimization of the stiffening effects by selection of layered MC in a composite uniquely works when the difference in the elastic modulus between the fillers and their polymer matrix is large. As a counter example, IMT model shows that layered and monolayer MXenes will induce similar mechanical reinforcement behavior when these fillers are embedded in a stiff polymer (epoxy) matrix despite both fillers having identical lateral size (Figure S5b).

The second material property chart correlates the predicted effective thermal conductivity with the predicted effective elastic modulus of MXene-Sylgard 184 when the size of dispersed MXenes (monolayer) is varied (Figure 27f). The following comparison reveals that at 5% volume fraction, MXene-Sylgard 184 with nanosized (100 nm) monolayer MXenes will have both the lowest longitudinal thermal conductivity (~1.5 $W \cdot m^{-1} \cdot K^{-1}$) and smallest longitudinal elastic modulus (~5.7 MPa) enhancement. In contrast, MXene-Sylgard 184 with large 5 μm size MXene fillers will have both the highest thermal conductivity and largest Young's modulus at the same filler concentration. Hence, without the presence of MXene clusters, it appears to be challenging to suppress the large stiffness reinforcement while maintaining the thermal property improvements

of MXPCs. In theory, by increasing the volume fraction (>5%) of those small single layer $Ti_3C_2T_x$ sheet, we could potentially increase or extrapolate the thermal conductivity to stiffness ratio of MXPCs. However, in practice these nanosized fillers will begin to locally bind due to strong Van der Walls interactions, which will instead cause the composites' effective thermal conductivity improvement to deteriorate as the formation of thermal conduction networks within the polymer matrix are now limited.

4.4.10 Dielectric properties

Figure 28a displays the predicted values for longitudinal dielectric constants of MXene-Sylgard 184 when one to ten sheets of aligned $Ti_3C_2T_x$ with 5μm size are used. As the number of layers of MXene fillers increases, the large dielectric constant enhancement of MXene-Sylgard 184 shifts from low to high volume fraction. For example, the large jump in the dielectric constants of MXPCs with ten- and one- layer $Ti_3C_2T_x$ occurs at 1.5% and 0.4% volume fraction, respectively. In this result, the MXPCs with one to several layer MXenes have dominant increase in dielectric constants at low volume fraction. This is because both the microstructure transition (Figure 25a) and the onset of Maxwell-Wagner-Sillars effects (Figure S4) among these MXene clusters are active at low percolation volume fraction ($f_\Gamma = R \cdot f_\Omega$<2%). Hence, these combined factors suggest that MXenes with large size and a few layered structures can efficiently create composites with high electrical permittivity at low concentration. In contrast, when the filler volume fraction is large (>4%), the dielectric constants of MXene-Sylgard 184 with ten-layer MXenes becomes higher than the dielectric constants of the composites that have a few layer MXenes. This is because once percolation is attained, the introduction of additional multilayer MXenes will saturate the composite at a faster rate and shorten the average interparticle distance. In practice this continuously improved dielectric behavior of MXPCs is only possible assuming that there is no electron tunneling by ohmic conduction at the interphase, which happens when many neighboring MC are in direct contact with each other [228].

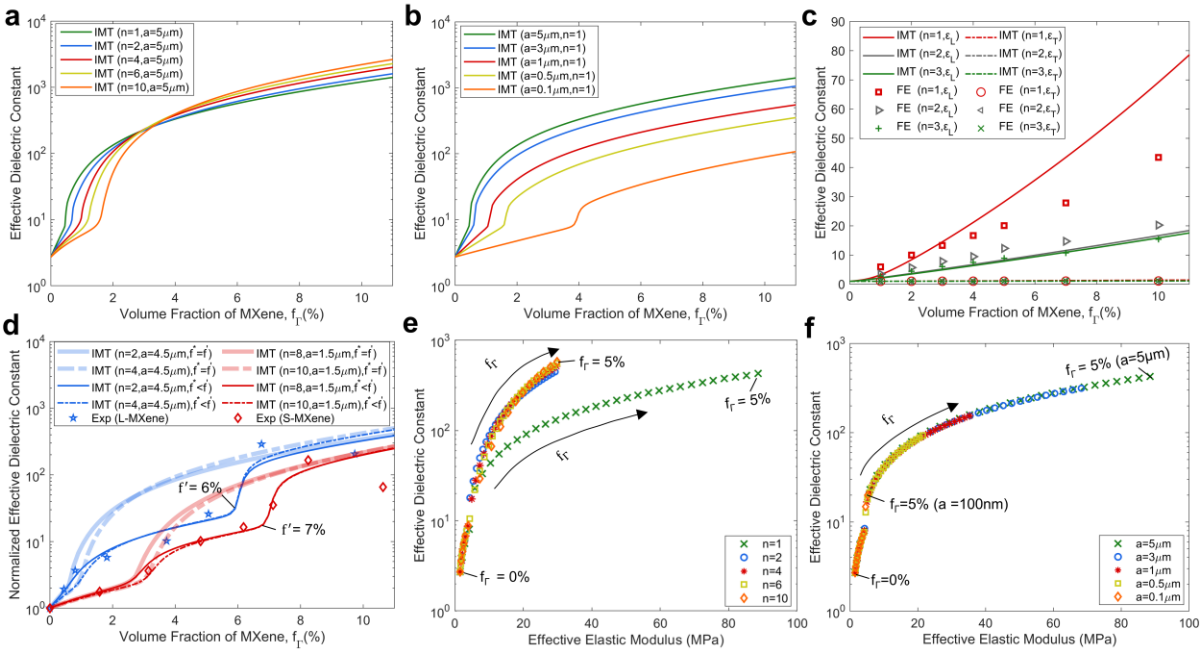

Figure 28. The predicted longitudinal dielectric constant of MXene-Sylgard 184 by IMT model due to (a) effects of layered structure of MXenes (fixed 5μm diameter) and (b) sizes of monolayer MXenes on the dielectric constants of the composite. All the dielectric constants presented in (a) and (b) are all normalized with respect to the dielectric constants of the unfilled Sylgard 184 ($\varepsilon_m = 2.7$). (c) Finite element method results are compared with the predicted longitudinal (ε_L) and transverse (ε_T) dielectric constants of MXene-Sylgard 184. (d) The measured dielectric constants of PVDF-$Ti_3C_2T_x$ with assumed randomly oriented small (S-MXenes) and large MXenes (L-MXenes) are compared with modeling results [229]. (e) The predicted dielectric constants in Figure 28a is correlated with stiffness predictions in Figure 25b. (f) Similarly, the evaluated dielectric constants in Figure 28b is plotted with the stiffness predictions shown in Figure 25c. Both Figure 28e and Figure 28f are plotted for the predicted effective properties (dielectric constants and elastic modulus) up to 5% volume fraction (f_Γ) of MXenes.

The dielectric constants of MXPCs can also be improved with the help of nanosized MXenes. However, a high-volume fraction of these nanoscale fillers is required to maximize the dielectric constants of the composite. For example, to create MXene-Sylgard 184 with a longitudinal dielectric constant of 10, we can either utilize 4% volume fraction of 100nm size single layer MXene or 0.5% volume fraction of 5μm size monolayer $Ti_3C_2T_x$ (Figure 28b). Thus, smaller MXene fillers are less efficient in enhancing the dielectric constants of their composites. This is because a high filler volume fraction is needed for their average neighboring distance to be short enough (near percolation) to induce large electric field polarization or large nanocapacitance effects. The following behavior is expected in our micromechanics model because the percolation microstructure transition (Figure 25a) and the MWS effects for MXPCs with small monolayer MXenes can only theoretically take place at high volume fraction, that is when the suspended MC are probabilistically the closest with each other (Figure S4).

4.4.11 Finite element method comparison (dielectric constants)

The finite element method can also be used to estimate the anisotropic dielectric constants of MXPCs. Here, we will predict the dielectric constants of MXene-Sylgard 184, which comprises of unidirectional MXenes that are 500nm in diameter (Figure 28c). In this FEM modeling, the relative permittivity of the interphase will be treated as equivalent to those of the polymer matrix (Sylgard 184). This is because MWS effects are absent and the created circular plates (MXene cluster) are well separated in the RVE.

As the MXenes' volume fraction in MXene-Sylgard 184 increases, both the interpolated Mori-Tanaka model and finite element method solutions appear to predict a similar improvement trend for the longitudinal dielectric constants (ε_L) of the composite. For instance, each model suggests that MXPCs with single layer $Ti_3C_2T_x$ will have the largest overall improvement in the longitudinal dielectric constants while the composite with two- and three- layer MXene fillers will have lower and almost equivalent ε_L at the same filler concentration. Based on these prediction comparisons, the electrical permittivity predictions are closest to the results of FEM up to only 3% volume fraction for the case of MXPCs with single layer MXenes. In contrast, there is much better agreement between both models when estimating the longitudinal dielectric constants of MXene-Sylgard 184 with two or three layers of MXene fillers. Therefore, the proposed IMT model can be a reliable predictive tool to evaluate the dielectric constants of MXPCs with low volume fraction or composites with layered and large size MXenes.

In comparison to longitudinal dielectric constants, the Interpolated Mori-Tanaka model predicts that the transverse dielectric constants (ε_T) of MXPCs are much smaller and show negligible improvements even at high filler volume fraction. This is because the electrically insulating gaps (i.e., interphase or polymer) which exist between aligned multilayer MXenes tend to be smaller in the longitudinal direction than in the transverse direction, especially at high concentration. Moreover, in this transverse orientation, the nano/micro capacitors formed by the aligned MXene clusters can be imagined to be in serial connection [228]. Hence, according to the theory of electric circuits, the effective capacitance or relative permittivity will be least improved in this configuration. As a result, there will be lower interfacial electric field polarization at the interphase and smaller effective dielectric constant enhancement in the orientation perpendicular to the

suspended MXenes than in the direction parallel to MXenes [205]. Thus, the orientation of multilayer $Ti_3C_2T_x$ can have a dominant effect on the final dielectric properties of MXPCs.

4.4.12 Experimental comparison (dielectric constants)

For the Interpolated Mori-Tanaka model to be a reliable predictive tool for experimentalists, the model needs to be reasonably capable of predicting the measured dielectric constants of MXene polymer composites. To demonstrate this, the IMT model is used to approximate the measured dielectric constant of MXenes in poly(vinylidene fluoride-trifluoro-ethylene-chlorofluoroethylene) composite or shorthanded as MXene-P[VDF-TrFE-CFE] (Figure 28d). Here, the accuracy of our micromechanics model will be evaluated by comparing our model predictions with the measured dielectric constants of MXene-P[VDF-TrFE-CFE] that have large (L-MXenes) and small (S-MXenes) MXene fillers [204,229]. In these composites, the L-MXenes have average lateral sizes of 4.5 μm while the S-MXenes have mean length of 1.5μm. Both fillers are assumed to be randomly oriented in their respective composites with a thickness of one nanometer.

According to Figure 28d, the interpolated Mori-Tanaka model can closely predict the measured dielectric constants of MXene-P[VDF-TrFE-CFE] with L-MXenes. This agreement is only achievable if the embedded $Ti_3C_2T_x$ clusters are assumed to have two to four layers. Similarly, the established micromechanics model is also capable of estimating the measured dielectric constants of MXene-P[VDF-TrFE-CFE] with S-MXenes when the randomly suspended $Ti_3C_2T_x$ are assumed to have eight to ten layers. This range of chosen layers in the model are reasonable and consistent to the actual filler microstructures of most MXPCs. However, to achieve the best agreements, the critical volume fraction (f') of the resistance function needs to be empirically selected from the experiments which is at 6% and 7% (largest DC jump) for the composite with L- and S- MXenes, respectively.

If the critical and percolation volume fraction are equal ($f^* = f'$) which is assumed in the original formulation, the IMT model will overestimate the dielectric constants of these composites even at moderate concentration (>1%). This is because the peak microstructure transition (inflection point of CCP function) and MWS effects take place simultaneously. However, the following behavior is not portrayed in the actual composite as the largest dielectric constants enhancement takes place at a higher filler concentration than the theoretical percolation limit (f^*<4%). This can potentially

happen if the morphologies (multilayer structure, polydispersity, etc.) of suspended MXenes at high volume fraction is drastically different than those at low volume fraction. For example, if large MXene clusters agglomerate at high volume fraction, the real critical volume fraction or percolation limit will be much higher than the theoretical estimate. This is because in our micromechanics model, all the suspended MXenes are treated to have uniform structures and distributions regardless of their concentration in the composite. Furthermore, it is also possible that the particle agglomeration at high filler concentration lowers the chance for more nano/micro capacitors to form in the composite. This means that unless additional filler volume fraction is introduced, the actual MWS effects can only occur at a greater volume fraction which could explain the secondary surge observed in the measured dielectric constant of MXene-P[VDF-TrFE-CFE].

As volume fraction continues to increase, both the MXPCs with large and small MXenes begin to portray decreasing measured dielectric constants. However, the micromechanics model predicts that the dielectric constants will continue to improve. This disagreement occurs because in the IMT model, it is assumed that once MWS effects take place, it will remain active even when the filler concentration continues to increase. However, in the real composite, the stored charges among the highly percolated MC will eventually experience electron or charge leakages (electrical conductors) when electric field is applied. As a result, this phenomenon will negate the effective charge storage property and the final dielectric property of the composite.

4.4.13 Dielectric constants and elastic modulus correlation

Next, by correlating the predicted dielectric constants with the predicted elastic modulus of MXPCs, we can examine the tradeoffs between these properties when changes are made to the layered structure and size of embedded MXenes. Figure 28e illustrates this by correlating the predicted longitudinal dielectric constants with the predicted longitudinal elastic modulus of MXene-Sylgard 184. In this correlation, one to ten sheets of 5 μm size $Ti_3C_2T_x$ inclusions are considered in the composite. Alternately, Figure 28f correlates the predicted longitudinal dielectric constants with the predicted longitudinal Young's modulus of MXene-Sylgard 184 when the size of single layer MXenes ranges between 100 nm to 5 μm.

Based on Figure 28e, MXene-Sylgard 184 with multilayer $Ti_3C_2T_x$ can achieve dielectric constants in the order of hundreds while attaining minimal elastic modulus (<30 MPa) enhancement at low

volume fraction (<5%). For example, the MXPCs with ten-layer $Ti_3C_2T_x$ and with size of 5 μm will have dielectric constants of 580 and elastic modulus of 30 MPa at 5% volume fraction. In contrast, MXene-Sylgard 184 with single layer $Ti_3C_2T_x$ and diameter of 5 μm will have dielectric constants of 430 and stiffness of 90MPa at 5% volume fraction. Hence, these modeling results suggest that large size MXene fillers with multilayer structure can create MXene polymer composites with sufficiently high dielectric constants and minimal mechanical stiffening. On the other hand, large MXene fillers with single to a few layered structures are much more ideal for creating stiff and high strength composite materials, where having high dielectric constants is not a priority in the applications.

Alternately, it is also possible to use small single or a few layer MXenes to create compliant MXene polymer composites. However, according to our theoretical model, it will be challenging to create MXene-Sylgard 184 with both high dielectric constant and low stiffness with these fillers. This is because when the size of single layer MXenes is reduced to 100nm, MXene-Sylgard 184 is predicted to have both low elastic modulus (20MPa) and low dielectric constants (20) at 5% volume fraction (Figure 28f). In contrasts, MXene-Sylgard 184 with large (a=5μm) single layer MXenes will have both high dielectric constants (~400) and large Young's modulus (90MPa) at 5% volume fraction. Therefore, based on these correlations, MXene fillers with large single or a few layered structures may not be suitable to create MXPCs that require both high dielectric constants and high mechanical compliance.

4.5 Summary and conclusion

A modified micromechanics framework termed as interpolated Mori-Tanaka model is introduced in this study to predict the effective mechanical, thermal, and dielectric properties of MXene polymer composites. The IMT model first locally evaluates the property of the multilayer MXenes at nanoscale length before computing the overall bulk property of MXPCs. This scheme allows the model to effectively account the effects of multilayer structure, size, orientation, interphase, and the percolation microstructure on the effective properties of the composite. Moreover, the prediction results of IMT model are reasonably accurate for low to moderate filler concentrations when compared with the results of finite element method and various measured properties of soft multifunctional MXene polymer composites.

Our micromechanics model suggests that we can efficiently create a highly compliant MXPCs (MXene-Sylgard 184) with maximum functional properties (thermal conductivity and dielectric constants) by having large and aligned multilayer MXene fillers surrounded by soft or weakened interphase. The following suppressed stiffening effects of MXPCs is proportional to the number of layers in the embedded MXenes. In contrast, MXPCs with large single layer MXenes are predicted to cause both large enhancement in the mechanical and functional properties as their volume fraction increases. Therefore, these predictions prove that large size multilayer MXene fillers should be highly favorable when it comes to creating soft multifunctional MXene polymer composites. These results can help us tune the nanostructures and microstructures of MXenes that are essential parameters to create composites with the optimum mechanical and functional properties suited for their diverse soft matter engineering applications.

Chapter 5: Viscoelastic Model for Cells Layered in Agarose Gel Composite

Cells in agarose gel are a common bio-composite that is used to study the mechanobiology of embedded cells. Recently, we had adopted the following composite material to execute *in vitro* dynamic or quasi-static mechanical testing of breast cancer cell lines such as MDA-MB-231 and BT-474. To ensure consistent stress conditions such as the mean stress and amplitude stress, it is important to control the displacement, or the strain loading applied on the composite. However, it can be challenging to maintain the desired stress/force conditions over a long duration by appropriate displacement loading due to the stress relaxation behaviors of both the cells and hydrogel matrix. To overcome this challenge, the current work had introduced a closed form viscoelastic model which homogenizes and predicts the dynamic stress (DS) behaviors of layered cell in agarose gel composite. With this model, we can accurately predict the measured force temporal data of the following hydrogel composite for a loading duration up to 200s with applied dynamic compressive strains that range between from 1% to 5%. The experimental study for this work has been published in Biology Open with me listed as the co-author [131].

5.1 Introduction

Time dependent mechanical behavior or viscoelastic property in solids is commonplace among soft polymers, particularly those with high water contents such as hydrogels. Even if the fillers in these soft polymers are stiff or non-viscoelastic, the resultant soft composite will still exhibit time-dependent mechanical behavior. This temporal stress behavior creates a unique challenge when adapting soft composites in soft robotics applications because of the delay between the inputs and responses caused by the relaxation or creep behaviors of the utilized soft composite material. There are several soft functional composites that utilizes highly viscoelastic polymer matrix such as silver embedded in polyacrylamide-alginate [13] and liquid metal embedded in liquid crystal elastomer [74,230]. The gel-based composite can be used soft actuators by varying the water content in the medium by varying dehydration and drying process whereas the liquid crystal elastomer-based composites is thermally responsive which can be applied as a soft thermal actuator.

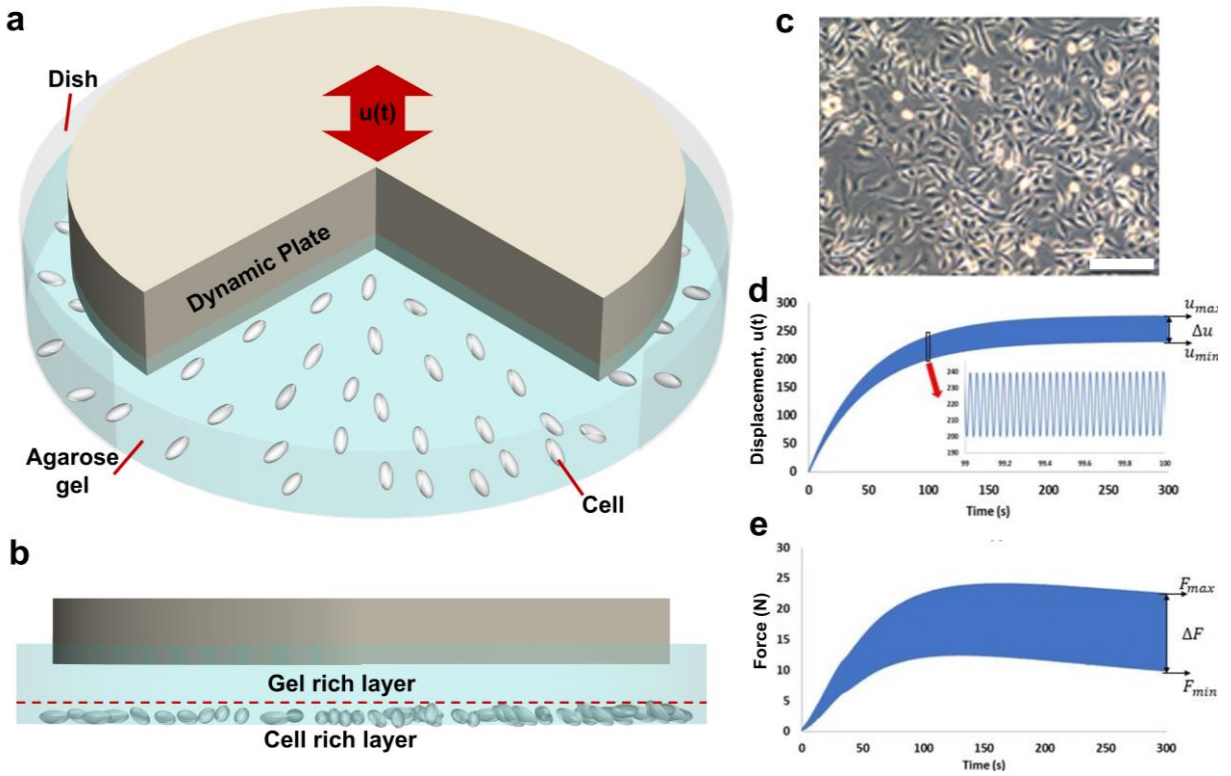

Figure 29. (a) Illustration of the cell-in-agarose gel composite under compression by the dynamic plate movement (u(t)). (b) The layered cell-in-gel composite architecture. (c) Light microscopy image of MDA-MB-231 cancer cells at the bottom of cell-rich-layer with scale bar length of 200μm. Image retrieved from Takao et al.[131]. (d) Dynamic displacement loading dictating the compressive movement of the dynamic plate. (e) The measured force applied on the cell-in-gel composite during the dynamic displacement loading.

Controlling the actuation force and predicting the deformation behavior of these viscoelastic composites are challenging because of the inherent stress relaxation and creep behavior of this composite, respectively. For a thermally responsive polymer composite, it is possible to vary the temperature changes to increase the blocking force or to change their shape. However, due to the relaxation behavior of the polymer, the generated force will decrease with time, or the final actuation displacement will take time to reach steady state, respectively. Therefore, to predict the stress and deformation behavior of these active soft actuators, we need a robust physical model than can approximate the stress or strain response when the viscoelastic composite is under quasi static or dynamic loading conditions. With this model, future users can sequentially adjust the applied inputs (displacement or other stimuli) to maintain the applied force on the medium or vice versa which pave the way to the creation of a simple and closed loop system.

To understand the effects of viscoelastic behaviors in soft composites, we developed a model that can predict the stress temporal behaviors of a cell-in-agarose gel composite under dynamic

loading. To avoid confusion to the reader, we first like to clarify that the introduction and methodology of this theoretical framework will be elucidated based on the purpose of studying the mechanical stress induced cell death (MSICD). This perspective motivated the initial development of the viscoelastic model which can also be translated into modeling the viscoelastic behaviors of other soft multifunctional polymer composites.

Water-soluble soft matter such as agarose gel is commonly used in biomedical applications. Agarose gel had been mainly used as nano filtration medium for separating DNA fragments of varying sizes by electrophoresis [126] The water diffusivity, biocompatibility and viscoelastic behaviors of agarose gel had made it a preferred phantom material to replicate the mechanical property of brain tissue [126], cartilage [127], and human skin [128]. When cells are encapsulated in this gel, the viscoelastic behaviors and physiological response of cells under different dynamic mechanical stimulation can be investigated [129–132]

For *in vitro* MSICD experiments, agarose gel separates the external environment from the cancer cells to supply nutrients, prevent bacterial contamination, and maintain isotonic condition for sustaining the cultured cancer cells (Figure 29a and Figure 29b) [130]. Hence, by removing other non-mechanical variables that also contribute to cell death, we can record reliable results of cell death counts strictly induced by mechanical stimulation. Since agarose gel has high water contents (up to 90 %), the embedded cells are not only provided with life-supporting nourishments, but also a highly viscoelastic interface that prevents cells from receiving direct forces induced by the rigid surface of the load (Figure 29b). Alternately, the gel matrix uniformly distributes the external load to the embedded cells, so each cell receives equal mechanical stresses. When preparing gel samples for *in vitro* mechanical stress experiments, the common microstructural arrangement for the cell-in-gel composite is either randomly dispersed cells [129,130] or a composite consisting of rich cell and rich gel layers such as those shown in Figure 29b [231–234]. In this study, the viscoelastic model is developed based on the layered cell-in-gel composite configuration which is much easier to be mathematically homogenized.

In mechanical testing, there is an option to either use a displacement control which is commonly used in uniaxial testing or to use force-based control which is commonly used for fatigue testing. Comparing both methods, it is much simpler to precisely apply the dynamic or static compressive displacement on the cell-in-gel composite without needing any force feedback during the test

(Figure 29c) [231–233,235]. For instance, the amplitude, frequency, rise time, and mean compressive displacement can be maintained by a piezo controller during experiment while the resultant forces as a function of time are measured simultaneously which is used to correlate with the observed cell deaths' frequency in the gel. Although the applied dynamic displacement remains unchanged, the resultant dynamic force tends to relax with unpredictable rate as the loading time progresses (Figure 29d). For example, if the variable displacement peaks too soon (low rise time), the resultant compressive force on the gel composite will decrease too rapidly before converging to zero (no mechanical stimulus). The following observed trends occur because of the strain rate sensitivity and viscoelastic nature of the cell-in-gel composite as studied in several modeling works [151,236]. As a result, the non-uniform stress conditions created difficulty in ensuring the repeatability of the results in MSICD related tests. One way to address this challenge is to tediously rely on trial-and-error selection for the best combinations of the input variable displacements that will produce the desired temporal stress outcomes of the cell-in-gel composite. Clearly, this solution is not practical and cost-effective because culturing each cell-in-gel composite can take up to a week if done successfully. Therefore, to streamline the experimental process, it is advantageous to have a predictive model that can accurately tune the expected dynamic forces prior to running the MSICD test to ensure the success of the experiment.

Although the cell-in-agarose gel composite system is completely not related to the field of soft multifunctional polymer composites introduced earlier, the proposed viscoelastic model can be easily substituted with other categories of soft composites by simply replacing the viscoelastic constitutive properties. Furthermore, the proposed viscoelastic model is in a closed form and can be used to rapidly predict the dynamic stress relaxation, creep behaviors, and storage or loss modulus of the material simply with the help of the measured stress relaxation modulus. Another advantage of this model is it can consider complex sinusoidal displacement loading with exponentially increasing amplitude and mean values. In contrast, most viscoelastic finite element methods of soft matters are limited to much simpler loading conditions such as quasi static (step strain), linear (ramp strain), and purely sinusoidal input loading as these boundary conditions minimizes the computational cost needed to complete the simulation. Thus, the prowess of the proposed viscoelastic model allows us to rapidly estimate the temporal stress behaviors of viscoelastic composites which can help designers to tune the actuation performance of soft robotics systems that rely on actuators that made of viscoelastic materials.

5.2 Experimental details

To study the effects of dynamic mechanical stress on cancer cells a custom-built mechanical tester consisting of a piezo actuator attached to a dynamic platen and load cell (PiezoMove, Physik Instrument, USA) is designed (Figure 30a) [131]. The piezo actuator movement shown in Figure 30a is governed by Equation 61 implemented via LabVIEW Data Acquisition (DAQ) program (National Instruments, USA).

$$u(t) = \frac{\alpha}{2}\{\sin(2\pi ft) + 1\}\left\{1 - e^{-\frac{t}{\tau_1}}\right\} + \beta\left\{1 - e^{-\frac{t}{\tau_2}}\right\} \quad 61$$

In this governing displacement function, t is time, α is displacement amplitude, f is displacement frequency (Hz), β is minimum mean compressive displacement, τ_1 is the time constant for displacement amplitude and τ_2 is the time constant for mean compressive displacement. The following parameters are varied to investigate the effects of frequency, force amplitude (ΔF) and mean force on final cell death counts. When a chosen set of displacement parameters are added to dictate the displacement loading, a viscoelastic force-time response of the layered cell-in-gel composite is acquired by the load cell (Figure 29e). For example, we can control the force amplitude (ΔF) by optimizing the displacement amplitude (Δu) of the plate to ensure that the averaged measured forces decays slowly. As introduced earlier, the viscoelastic nature of cell-in-gel composite has made the maintenance of force amplitude (ΔF) and mean force during the mechanical testing to be challenging. Hence, having a reliable viscoelastic model to predict force-time behaviors under a given complex displacement function will be very useful for designing a repeatable experiment.

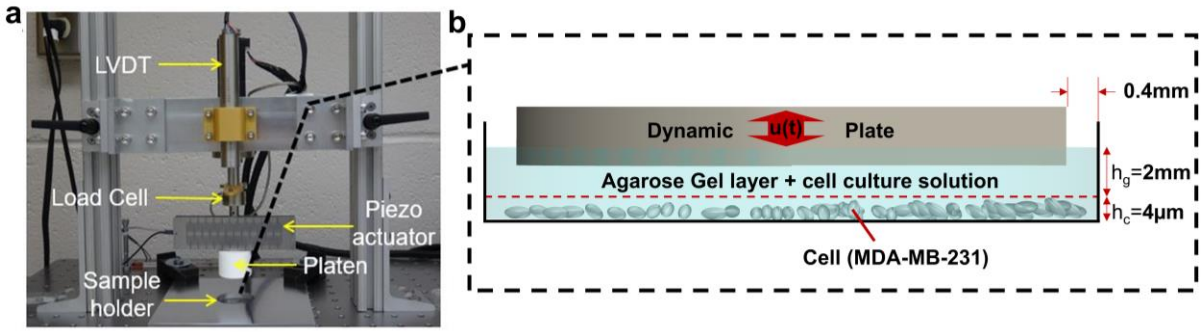

Figure 30. (a) The custom-built mechanical tester to apply dynamic loading on cell-in-gel composite. (b) Cross section view of the layered cell-in-gel composite architecture.

Our initial work investigated two breast cancer cell lines, BT-474 (less metastatic) and MDA-MB-231 (highly metastatic triple negative breast cancer cells) which are layered with 3 weight %

agarose gel (i.e., 97 wt. % water). In the current framework, MDA-MB-231 will be selected as the embedded cells in agarose gel and the preparation details (culturing and curing of gel) of this layered cell-in-agarose gel composite can be found in the previous work [131]

5.3 Viscoelastic model

5.3.1 Homogenization of layered cell-in-agarose gel composite.

To compute the stress-time response, we first need to homogenize the relaxation modulus of the layered agarose gel and cells composite as two distinct standard linear solid model (SLS) configured in series (Figure 31a). Each SLS representative of agarose gel and cancer cells is governed by a Prony series expressed in Equation 62 and Equation 63, respectively [131,237–239] The Prony series for 3 wt.% agarose gel fits the stress relaxation measurement of the gel under step displacement loading [240] For the MDA-MB-231 cancer cells, their SLS model are taken based on the stress relaxation measurements obtained by atomic force microscopy [238,239,241] or shear assay technique[242]. The SLS stress relaxation modulus of the cancer cells retrieved from literature is rearranged as simplified Prony series [$G_c(t)$].

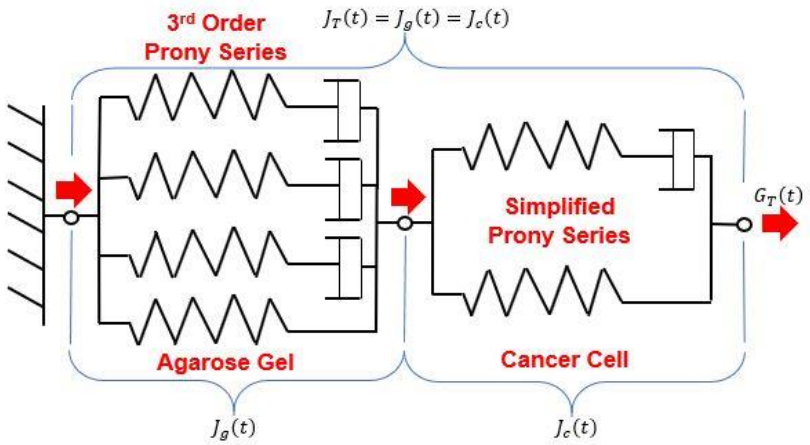

Figure 31. Standard linear solid model (SLS) made of Newtonian spring and dashpot. Two SLS in series representing layered agarose gel and cancer cells respectively (Figure 29B) in consistent to our experimental setup. Creep moduli are additive in this serial SLS configuration.

$$G_g(t) = G_o - \sum_{i=1}^{3} G_i(1 - e^{-\alpha_i t}) \ , \alpha_i = \frac{1}{\tau_i} \qquad 62$$

$$G_c(t) = G_O^c - G_1^c\left(1 - e^{-\beta t}\right) \qquad 63$$

When two SLS models are configured in series, the overall displacement change will be the sum of displacement change in each SLS model while the forces in both spring-damper models are always equivalent. Hence, to homogenize these layered cell-in-gel composite, the creep moduli of agarose gel and cancer cells are added as shown in Equation 64.

$$J_T(t)h_T = J_g(t)h_g + J_c(t)h_c \quad (64)$$

$$s^2 G_i(s)J_i(s) = 1 \quad (65)$$

$$G_g(s) = \frac{G_o}{s} - \sum G_i\left(\frac{1}{s} - \frac{1}{s+\alpha_i}\right) \quad (66)$$

$$G_c(s) = \frac{G_o^c}{s} - G_1^c\left(\frac{1}{s} - \frac{s}{s+\beta}\right) \quad (67)$$

$$J_T(s)h_T = J_g(s)h_g + J_c(s)h_c \quad (68)$$

In Equation 64, h_g is the initial thickness of gel, h_c is the thickness of cancer cell (4μm for MDA-MB-23) [242], h_T is total initial thickness of layered gel and cell, J_g is agarose gel creep modulus, J_c is cancer cell creep modulus, and J_T is effective creep modulus of composite. In linear viscoelasticity, a simple constitutive relation between general creep modulus $J_i(t)$ and relaxation modulus $G_i(t)$ exists in the Laplace domain, where subscript i can be the gel (g) or cells (c) [240,243]. To conveniently utilize viscoelastic constitutive relationship in Equation 65, we obtained Laplace transform of Equation 62, 63, and 64 as Equation 66, 67, and 68 respectively to transform all of them into the frequency domain. Finally, to determine the effective relaxation modulus of layered cell-in-gel composite, Equation 65 and 67 are substituted into Equation 68 to be rearranged into Equation 69. In this expression, the two newly introduced shorthand terms are defined as $V_g=h_g/h_T$ and $V_c=h_c/h_T$.

$$G_T(s) = \frac{1}{s^2 J_T(s)} \quad (69)$$

$$= \frac{\left\{G_o - \sum G_i\left(\frac{\alpha_i}{s+\alpha_i}\right)\right\}\{sG_o^c + \beta(G_o^c - G_1^c)\}}{V_g s\{sG_o^c + \beta(G_o^c - G_1^c)\} + V_C s(s+\beta)\left\{G_o - \sum G_i\left(\frac{\alpha_i}{s+\alpha_i}\right)\right\}}$$

$$G_T(t) = G_{T_o} - \sum_{i=1}^{n} G_{T_i}(1 - e^{-\alpha_{T_i} t}) \quad (70)$$

To formalize $G_T(s)$, the Prony series coefficients for agarose gel and cancer cells can be found in Table S7. By applying inverse Laplace transform on $G_T(s)$, the time domain effective relaxation modulus $G_T(t)$ can be retrieved. To complete this transformation, the MATLAB residual function is used to obtain the explicit partial fractions of Equation 69 which can be found in Equation S73. The following partial fractions can then be conveniently inversed and arranged into the Prony series representing the effective stress relaxation modulus of layered cell-in-gel composite. The following detailed derivations for Equation 70 and its resulting coefficients (see Table S8) are included in the supplemental information.

Dynamic displacement loading on the gel composite is governed by the complex displacement function shown in Equation 61. By using linear viscoelasticity and corresponding principle, we can predict the resultant force-time response using Boltzmann superposition theory while also considering the boundary conditions imposed by the petri dish wall on the cell-in-gel composite [244].

5.3.2 Boltzmann superposition theory

Viscoelastic material stress or strain responses are dictated by its deformation histories. For example, it is found that as the rise time of the mean and amplitude displacement increases, the average force applied on the gel composite decreases more rapidly. In a mathematical standpoint, the current stress at time (t) is the sum of multiplication between the relaxation modulus of the gel composite and previous strain histories (τ) where $t \leq \tau$. This computation is essentially the Boltzmann superposition theory where the relationship between time-dependent stress and strain involves solving the convolution integral shown in Equation 71. In this expression, $\varepsilon(t)$ is the applied time-dependent strain on the gel composite which is the ratio of compressive displacement change with its initial thickness (i.e., $\varepsilon(t) = \frac{u(t)-h_T}{h_T}$) where the initial thickness is just the addition h_c and h_g as shown in Figure 30b.

$$\sigma(t) = \int_{0^+}^{t} G_T(t-\tau)\frac{d\varepsilon(t)}{d\tau}\,d\tau \quad (71)$$

$$\sigma(s) = sG_T(s)\varepsilon(s) \quad (72)$$

To avoid solving lengthy convolution integral and obtain a closed-form solution, Equation 71 can be converted into Equation 72 by Laplace transform. This method is preferred because the

algebraic form of the stress and strain expressions in terms of laplace variable (s) is easier to handle if the inverse laplace transform can be done analytically. Hence, the Laplace transform of Equation 70 and Equation 61 are substituted into Equation 72 before expressed as Equation 73. In Equation 73, several terms are redefined as follow: $\omega = 2\pi f, G_i = G_{T_i}, \frac{1}{T_i} = \alpha_{T_i}$.

$$\sigma(s) = \frac{\alpha}{2h}\left\{\frac{G_o\omega}{s^2+\omega^2} - \sum_{i=1}^{3} G_i\left(\frac{\omega}{s^2+\omega^2} - \frac{s\omega}{\left(s+\frac{1}{T_i}\right)(s^2+\omega^2)}\right) - \frac{G_o\omega}{\left(s+\frac{1}{\tau_1}\right)^2+\omega^2}\right.$$
$$+ \sum_{i=1}^{3} G_i\left(\frac{\omega}{\left(s+\frac{1}{\tau_1}\right)^2+\omega^2} - \frac{s\omega}{\left(s+\frac{1}{T_i}\right)\left(\left(s+\frac{1}{\tau_1}\right)^2+\omega^2\right)}\right) + \frac{G_o}{s}$$
$$\left. - \sum_{i=1}^{3} G_i\left(\frac{1}{s} - \frac{1}{s+\frac{1}{T_i}}\right) - \frac{G_o}{s+\frac{1}{\tau_1}} + \sum_{i=1}^{3} G_i\left(\frac{1}{s+\frac{1}{\tau_1}} - \frac{s}{\left(s+\frac{1}{T_i}\right)\left(s+\frac{1}{\tau_1}\right)}\right)\right\}$$
$$+ \frac{\beta}{h}\left\{\frac{G_o}{s} - \sum_{i=1}^{3} G_i\left(\frac{1}{s} - \frac{1}{s+T_i}\right) - \frac{G_o}{s+\frac{1}{\tau_2}}\right.$$
$$\left. + \sum_{i=1}^{3} G_i\left(\frac{1}{s+\frac{1}{\tau_2}} - \frac{s}{\left(s+\frac{1}{T_i}\right)\left(s+\frac{1}{\tau_2}\right)}\right)\right\} \quad (73)$$

We can derive closed form of stress-time equation by conducting inverse Laplace transform of Equation 73, but the partial fraction of each term needs to be done first for mathematical convenience. The derivation details for Equation 72, 73, and 74 are given in the supplemental section.

$$\sigma(t) = \frac{\alpha}{2h}\Bigg\{G_o \sin(\omega t) - \sum_{i=1}^{3} G_i\left(\sin(\omega t) - a e^{-\frac{t}{T_i}} - b\cos(\omega t) - \omega b T_i \sin(\omega t)\right) - G_o e^{-\frac{t}{\tau_1}} \sin(\omega t) + \sum_{i=1}^{3} G_i\left(e^{-\frac{t}{\tau_1}} \sin(\omega t) - d e^{-\frac{t}{T_i}} + d e^{-\frac{t}{T_i}} \cos(\omega t) - \frac{d}{\tau_1 \omega} e^{-\frac{t}{\tau_1}} \sin(\omega t) - \frac{f}{\omega} e^{-\frac{t}{\tau_1}} \sin(\omega t)\right) + G_o - \sum_{i=1}^{3} G_i\left(1 - e^{-\frac{t}{T_i}}\right) - G_o e^{-\frac{t}{\tau_1}} + \sum_{i=1}^{3} G_i\left(e^{-\frac{t}{\tau_1}} - g e^{-\frac{t}{T_i}} - h e^{-\frac{t}{\tau_1}}\right)\Bigg\} + \frac{\beta}{h}\Bigg\{G_o - \sum_{i=1}^{3} G_i\left(1 - e^{-\frac{t}{T_i}}\right) - G_o e^{-\frac{t}{\tau_2}} + \sum_{i=1}^{3} G_i\left(e^{-\frac{t}{\tau_2}} - g' e^{-\frac{t}{T_i}} - h' e^{-\frac{t}{\tau_2}}\right)\Bigg\} \quad (74)$$

The coefficients of the terms in Equation 74 (a, b, c, d, e, f, g, h, f', g' and h') are the result of partial fraction simplifications. See their respective expressions attached in the supplemental information. Up to this point, we had successfully obtained the closed form solution of σ(t) but upon computing this equation, there was a significant underprediction of force amplitude (ΔF) shown in Figure S7. This underprediction exists because we believe the gel composite is under hydrostatic compression because of the circular boundary conditions imposed by the inner wall of petri dish.

5.3.3 Modified Concentric Cylindrical Model (CCM) based on MSICD Experimental Setup

Upon closer inspection of the experimental setup (Figure 30b), the layered cell-in gel composite sits in the petri dish with negligible gap (<0.1mm) between the inner surface of dish and cylindrical surface of the composite medium. It is suspected that the underprediction of ΔF illustrated in Figure S7 occurs because of the absence of these appropriate boundary conditions in our viscoelastic model. Simultaneously, another boundary condition arises from the plane stress surface at the gap (0.4mm) between platen and inner diameter of dish. During platen compression, the agarose gel at this gap will expand upward due to Poisson's effects. Currently, the following boundary conditions are not considered in the derived stress-time response (Equation 74). Thus, we will include these boundary conditions in the proposed viscoelastic model and show that the effective stiffness of the cell-in-gel composite increases by an order of magnitude because of the highly incompressible nature of agarose gel (97wt. % water) [125,242,245]. To achieve this, we first obtain the exact elastic solution with the help of concentric cylindrical model (CCM) as illustrated in Figure 32 [246]. Here, CCM is used as a boundary value elastic problem that can help predict the effective stiffness of our cell-in-gel composite by idealizing two internal and external annular cylindrical regions with distinctive elastic supports (Figure 32). For our modelling objective, we modified CCM (Figure 32A) to match our experimental setup (Figure 30a) by having those two cylinders (internal and external) having similar material (cell-in-agarose gel composite). The internal cylinder (r<b) and external cylinder (b<r<a) are areas where compression loading ε(t) is applied and has free surface traction at Z=h, respectively. Also, the radial displacement of cylindrical cell-in-gel composite is bounded at r=a while the traction and displacement continuity are enforced at r=b (Figure 32A). By solving these boundary conditions alongside the static equilibrium conditions (Equation 75), strain-

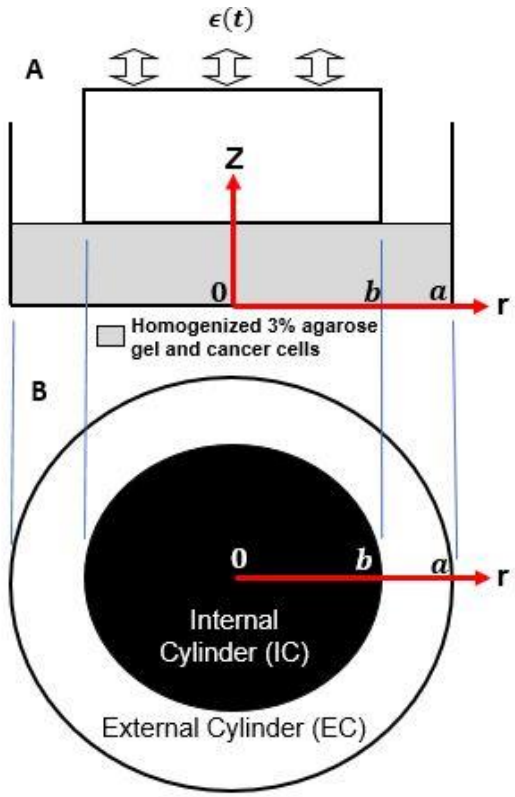

Figure 32. (A) The BCs defined mathematically from realistic experimental setup assuming homogenized gel cell medium. (B) A CCM model is used to visualize the realistic elastic problem.

displacement relationship (Equation 76) and presumed isotropic linear elastic constitutive law (Equation 77), we can establish the effective stiffness of the cell-in-gel composite.

$$\sigma_{ji,j} = 0 \quad (75)$$

$$e_{ij} = \frac{1}{2}\left(u_{j,i} + u_{i,j}\right) \quad (76)$$

$$\sigma_{ij} = \frac{E}{1+v}\left(e_{ij} + \frac{v}{1-2v} e_{kk}\delta_{ij}\right) \quad (77)$$

To establish the concentric cylindrical method, the static equilibrium equation (Equation 75) is expressed in cylindrical coordinates. This equation is simplified by assuming axisymmetric condition about the Z-axis with frictionless boundary conditions at Z=0 and r=a to simplify Equation 15 into Equation 18.

$$\sigma_{rr,r} + \frac{\sigma_{rr} - \sigma_{\theta\theta}}{r} = 0 \quad (78)$$

$$e_{rr} = u_{r,r}\ , e_{\theta\theta} = \frac{u_r}{r}, e_{zz} = u_{z,z} \quad (79)$$

The following terms σ_{rr}, $\sigma_{\theta\theta}$, e_{rr}, $e_{\theta\theta}$, e_{zz}, and u_r in Equation 78 are the radial stress, angular stress, radial strain, angular strain, out of plane strain and radial displacement, respectively. Similarly, strain-displacement relationship in Equation 76 can be simplified into Equation 79 because of the frictionless boundary condition. Note that frictionless and axisymmetric assumption had nulled all components of shear stresses ($\sigma_{r\theta}$, σ_{rz} and $\sigma_{z\theta}$) and partial differential terms of Z and θ. Hence, this simplifies Equation 75 into an easily solvable differential equation (Equation 78). For instance, Equation 78 can be solved using Cauchy-Euler solution (i.e., Equation 80 and Equation 81. Equation 80 and 81 are the radial displacement expression within the internal and external cylinder respectively. The internal region will have its constant $C_2^I = 0$ because radial displacement of gel cell medium must be 0 at $r = 0$. C_i^j is a generic representation of constants with i^{th} subscript (i=1, 2) and j^{th} superscript (j= I, E).

$$u_r^I = C_1^I r + C_2^I r^{-1} \quad (80)$$

$$u_r^E = C_1^E r + C_2^E r^{-1} \quad (81)$$

$$u_r^I(r = b) = u_r^E(r = b)\ , \qquad \sigma_{rr}^I(r = b) = \sigma_{rr}^E(r = b) \quad (82)$$

$$\sigma_{zz}^{E} = 0 = \frac{E}{(v+1)(2v-1)}\left\{(v-1)\epsilon_{z}^{E} - v\frac{\partial u_{r}^{E}}{\partial r} - \frac{v}{r}u_{r}^{E}\right\} \quad 83$$

$$u_{r}^{E}(r=a) = 0 \quad 84$$

So far, there are three unsolved coefficients (C_1^E, C_2^E, and C_1^I) that will require three other linearly independent equations to solve. These equations arise from radial displacement and radial stress continuity at r=b (Equation 80), zero surface tractions at Z=h of external cylinder (Equation 84) and from bounded radial displacement at r=a (Equation 84). Equation 82 can be obtained from substituting Equation 79 into Equation 77 with zero stress in the Z direction ($\sigma_{zz} = 0$) at Z=h_T in the external cylinder. From Equation 80 to 84, the solution for C_1^I (Equation 85) and C_1^E (Equation 86) where ν is Poisson's ratio and E is the assumed equivalent elastic modulus of the gel composite. After determining C_1^I for u_r^I, the expression for out of plane stress in the internal region, (Equation 87) can be determined by using strain-displacement relationship (Equation 79) and constitutive elastic relation (Equation 77). Now, the derived σ_{zz}^I becomes spatially independent because of the assumed axisymmetric and frictionless boundary conditions. In our experiment, the resultant force is measured by a load cell. Hence, the theoretical force measurement can be derived by taking the surface integral of σ_{zz}^I in z-direction (Equation 88) to obtain the theoretical force (P_{zz}) when the gel composite is under applied step strain (ϵ).

$$C_1^I = \frac{\left(1-\left(\frac{a}{b}\right)^2\right)}{\frac{2v}{v-1} - \frac{(2v^2-4v+2)}{v(v-1)}\frac{a^2}{b^2}} \quad 85$$

$$C_1^E = \frac{1}{\frac{2v}{v-1} - \frac{(2v^2-4v+2)}{v(v-1)}\frac{a^2}{b^2}} \quad 86$$

$$\sigma_{zz}^I = \frac{E}{(v+1)(2v-1)}\{(v-1) - 2vC_1^I\}\epsilon \quad 87$$

$$P_{zz}^I = \int_0^b \sigma_{zz}^I 2\pi r dr \quad 88$$

$$K = \frac{\pi b}{(v+1)(2v-1)}\left\{(v-1)b - \frac{2v\left(1-\left(\frac{a}{b}\right)^2\right)b}{\frac{2v}{v-1} - \frac{(2v^2-4v+2)}{v(v-1)}\frac{a^2}{b^2}}\right\}, \quad P_{zz}^I = KE\epsilon \quad 89$$

The incompressible nature of gel and cell composites with Poisson's ratio v=0.5 will cause the effective stiffness of gel cells medium to converge to infinity when $a \approx b$. From Equation 89, the smaller the gap between platen and inner dish cylindrical surface, the larger the effective stiffness (K). Therefore, larger ΔF can be predicted when smaller strain (ϵ) is applied. In the next section, we will use corresponding principle to convert elastic solution to viscoelastic solution.

5.3.4 Corresponding Principle

A given solved elastic solution can be converted into viscoelastic solution using corresponding principle [240,243]. Once we determined our elastic exact solution (Equation 89), we can apply Laplace transform by having strain (ϵ) as a function of time (t) (Equation 90), apply corresponding principle (Equation 91) and lastly apply inverse Laplace transform (Equation 92). In these equations, $(.)_e$ and $(.)_v$ terms denote elastic solution and viscoelastic solution respectively of given variable defined in the bracket.

$$(P_{zz}^{I})_e = KE\epsilon(s) \quad (90)$$

$$(P_{zz}^{I})_v = KsE\epsilon(s) \quad (91)$$

$$\left(P_{zz}^{I}(t)\right)_v = KE * d\epsilon \quad (92)$$

Inverse Laplace transform of Equation 91 is equivalent to solving Boltzmann Convolution Integral in the time domain which the solution is already provided by Equation 74. Hence, we can express the theoretical force-time equation from Equation 92.

5.4 Results and discussions

In the previous section, we had derived a viscoelastic model (Equation 92) to predict the experimentally measured force-time behavior (Figure 32 and Figure 33). We will compare force amplitude, max force (F_{max}) and min force (F_{min}) at steady state at various displacement amplitude (α) (Equation 61) for fixed values of β, τ_1, τ_2 and f (β=230 μm, τ_1=τ_2=50 s and f=30 Hz).

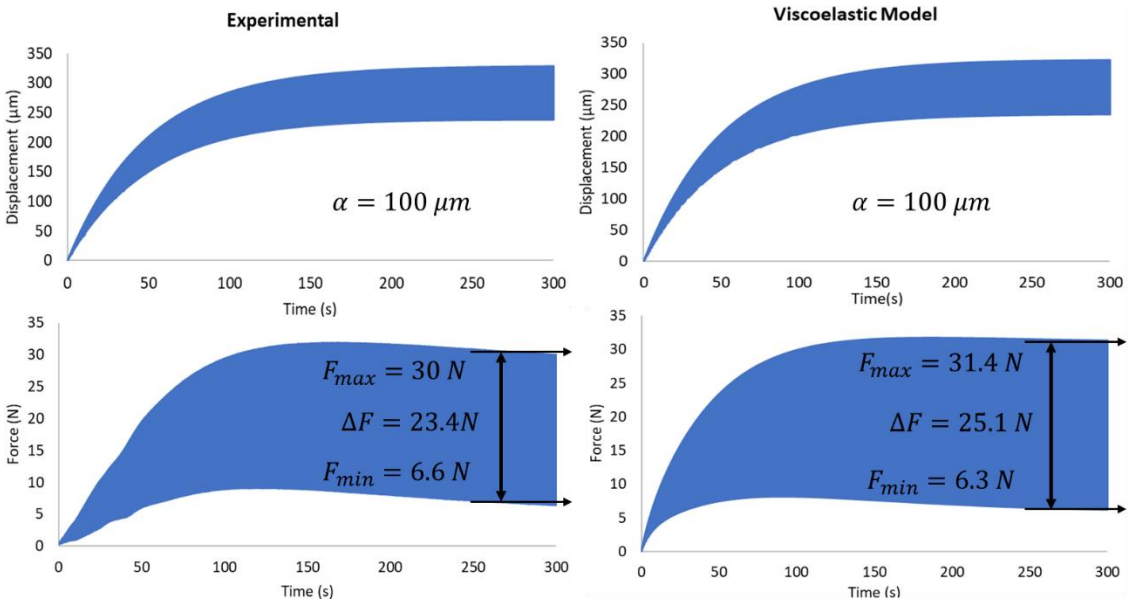

Figure 33. (Left column) Experimentally measured displacement-time and force-time behavior of layered agarose gel and cells. (Right column) Viscoelastic model prediction of force-time response for displacement amplitude α=100μm.

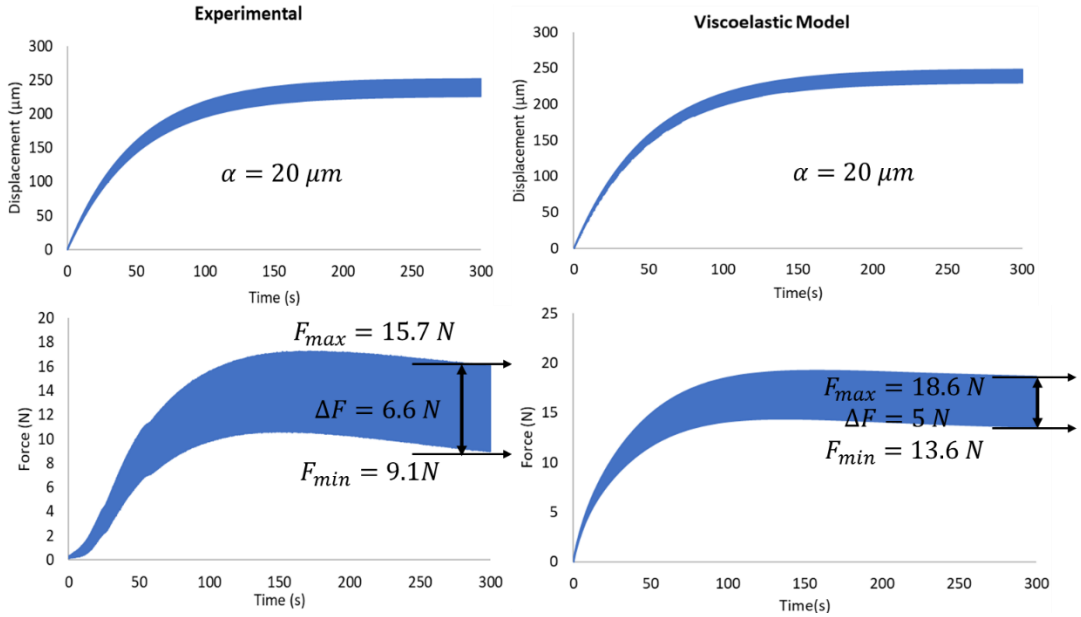

Figure 34. (Left) Experimentally measured displacement-time and force-time behavior of layered agarose gel and cells. (Right) Viscoelastic model prediction of force-time response for small displacement amplitude (α=20μm).

By using different values of α ranging from 20 μm (Figure 34) to 100 μm (Figure 33) while setting β fixed at 230 μm as well as the time constants (50 s) and frequency (50 Hz), we approximated the resultant force amplitudes (ΔF) at steady state (210 s < t < 300 s) at the corresponding set displacement amplitudes. The comparison of the predicted forces by the viscoelastic model and the corresponding force measurements for different displacement amplitude (α) is summarized in Table 3.

Table 3. Comparison table between viscoelastic model prediction of ΔF, F_{min} and F_{max} with respective MSICD experimental results.

α (μm)	Experiment ΔF (N)	Model ΔF (N)	Experiment F_{min} (N)	Model F_{min} (N)	Experiment F_{max} (N)	Model F_{max} (N)
20	6.6	5.0	9.1	13.6	15.7	18.6
50	12.3	12.5	7.6	10.9	19.9	23.4
80	22.1	20.1	7.7	8.1	30.1	28.2
100	23.4	25.1	6.6	6.3	30.0	31.4

From Table 3 our viscoelastic model consistently predicts the force amplitude (ΔF) of the experiment at small and large alpha (α) at steady state. Moreover, it can also be visually observed that at the transient stages (t<50s) of the dynamic loading, the measured dynamic forces [Figure 33 (left) and Figure 34 (left)] matches really close to the force-time behavior predicted by the viscoelastic model regardless of the input displacement amplitudes. However, when the amplitude displacement is small (20 μm), it appears that the measured force tends to decay much rapidly than those predicted by the model. For example, both the measured and predicted force amplitude when the cell-in-gel composite is dynamically loaded with small displacement amplitude (Figure 34) have approximately similar force amplitude of 6.6 N and 5.0 N, respectively. On the other hand, at steady state both the predicted maximum (18.6 N) and minimum forces (13.6 N) applied on the same composite are much larger than the respective measured maximum and minimum forces. It is possible that as loading time increases the measured peak forces appear to be consistently lower than the predicted ones because agarose gel loses its water content (i.e., water exudation) or redistribute itself during compressional loading which results in the formation of hollow cavities within the hydrogel matrix [132,245,247]. Thus, the formation of cavities or porous structures can cause reduction in stiffness over time which is unable to be considered by our model. As a result, this could potentially explain why the measured minimum (F_{min}) and the maximum (F_{max}) forces tend to be much lower than the predicted forces of the viscoelastic model for the same displacement loading conditions. Despite that, based on the comparison made in Figure 33 and Figure 34, this current viscoelastic model is a sufficiently accurate model to predict the force time behavior of the layered cell-in-agarose gel composite within moderate duration with reliable range of force amplitude.

5.5 Summary and conclusion

Our viscoelastic model homogenizes and predicts the dynamic stress behavior of layered cell-in-agarose gel composite when applied by variable compressive displacement loading. The proposed

viscoelastic model is capable of accurately predicting the measured force-time data from MSICD experiment for treatment time under 200 s before the stiffness of the gel decreases due to the formation of porous structures by water exudation. In the future, similar models can be expanded for modelling any viscoelastic layers under periodic displacement functions such as pulsatile loading since such functions are simply Fourier series consisting of sines and cosines. In addition, this will also allow the development of force control algorithm to determine the appropriate pre-programmed displacement loading progression to apply uniform dynamic stress on a viscoelastic material.

Chapter 6: Summary and Future Work

6.1 Summary

Soft multifunctional composite materials are a unique class of soft matter composites that can be designed to have high conductivity while remaining mechanically compliant. This combined high conductivity and low stiffness features had been taken advantage in their applications as compliant thermal interface for flexible energy harvesting device, stretchable thermal actuators for soft robotics, and robust electrical conductors for flexible electronics. Some of the recently emerging soft matter composite studied in this dissertation are the liquid metal polymer composites and the MXene polymer composites. LMPCs have the benefit of being able to achieve high thermal conductivity while remaining electrically insulative and soft. However, it can also be electrically conductive if the embedded liquid metal inclusions are mechanically sintered. In contrast, MXPCs have the advantage of having very large thermal and dielectric properties at dilute filler volume fraction. However, this composites' stretchability can deteriorate due to the enhanced stress concentration at the filler-polymer interface. In this dissertation, I introduced several novel micromechanics frameworks that help accurately predict the bulk properties of these composites based on the microstructure and nanostructure of these composite. Thus, here are the notable contributions achieved by the developed models presented in this dissertation:

1. A micromechanics model known as the two-step Mori-Tanaka model can successfully account the effects of the size of core-shell liquid metal inclusions on the elastic property of liquid metal polymer composites. The same modeling framework can be used to predict the thermal conductivity and dielectric properties of LMPCs. It is determined that the size of embedded liquid metal particles has negligible influence of these properties.
2. An analytical model based on Eshelby's equivalent inclusion method predicts that the stress around the embedded liquid metal droplets and the oxide shell is highest when the packing density is high, and their composite is under hydrostatic compression. These conditions could be favorable for sintering small size core-shell liquid metal inclusions or LMPCs with ultrasoft polymer matrices which confirms most reported experimental observations.
3. Interpolated Mori-Tanaka model demonstrates that multilayer structures of MXene fillers are a critical factor when producing MXPCs with maximum functional properties and

compliance. This new insight will be useful for MXenes' composite designers in changing their synthesis approach to create more compliant and functional MXPCs.

4. A compact viscoelastic model capable of rapidly predicting the force-time response of hydrogel composites which is advantageous over numerical simulations.

6.2 Recommendations

6.2.1 Liquid metal polymer composite

The current TDI and EIM model assume that all the phases in the liquid metal polymer composites are linear elastic, and the shape of the fillers does not significantly change. Thus, in the large deformation regime, the following model no longer reflects the actual mechanical behavior of the composite. To improve the current models, here are several suggestions:

1. Extend the two-step MT theory and EIM to predict the large strain behavior as well as the hyperelastic stress developed in the bulk LMPCs and in the embedded LM droplets.
2. Validate the estimated internal stress in the LM droplets with those predicted by high-fidelity finite element models.
3. Execute mechanical testing of LMPCs with different loading conditions and packing density of the embedded EGaIn droplets to corroborate whether the sintering likelihood of these droplets correlate to the predictions of EIM.

6.2.2 MXene polymer composite

An interpolated Mori-Tanaka model is used to predict the overall properties of MXene polymer composites which accounts for the multilayered structure of MXenes and the formation of conductive networks when their volume fraction approaches the percolation limit. Here are several suggestions for future studies:

1. Conduct comprehensive experimental studies that will systematically characterize the microstructures parameters (i.e., size, dispersion, number of layers, type of interphases, and filler volume fractions) of MXPCs to be correlated with their measured effective properties.
2. Use the following experimental studies to evaluate the overall accuracy of the developed interpolated MT model and determine whether multilayer MXenes are indeed suitable to create MXPCs with the best synergy in their mechanical and conductive properties.

6.2.4 Viscoelastic behaviors in soft matter composites

Another dominant mechanical behavior that exists in many soft matter composites is the viscoelastic behavior. The analytical modeling of this time-dependent mechanical behavior is complex as the addition of time variable needs to be considered in the formulation. As demonstrated in Chapter 5, even for a simple boundary value problem, the derivation to evaluate the overall force-time response of a homogenized cell in agarose gel composite is laborious. Nevertheless, there are potential options to augment the current micromechanics model to simulate the viscoelastic behavior of such gel-based composite by utilizing numerical-based micromechanics model such as extended Mori-Tanaka theory to predict the effective creep behavior of a soft multiphase composite [149,151,243]. One mathematical convenience of the micromechanics model is when it is converted to the frequency domain by Fourier transform, the effective complex modulus of the soft matter composite can be explicitly evaluated as the convolution integral is converted to simple multiplication operation in the frequency variable. Now. through the complex modulus, the storage, loss modulus, and $\tan\delta$ of the soft composite can also be estimated which are otherwise difficult to be measured, unless specialized testing apparatus (i.e., dynamic mechanical analysis) are used.

Vita

Education

Doctor of Philosophy, Mechanical Engineering (June 2023)

University of Washington,

Seattle, Washington

M.S. Mechanical Engineering (June 2022)

University of Washington,

Seattle, Washington

B.S. Mechanical Engineering (June 2018)

University of Washington,

Seattle, Washington

Publications

- **Chiew C.** and Malakooti M.H., (2021). A Double Inclusion Model for Liquid Metal Polymer Composites. Comp. Sci. Tech., Vol. 208, 108752.
- **Chiew C.** and Malakooti M.H., (2022). Micromechanics Modeling of Multifunctional EGaIn-Polymer Composites. Nondestructive Characterization and Monitoring of Advanced Materials. (Conf. Paper).
- Takao S., **Chiew C**., Taya M., (2019). Mechanical Stress-induced Cell Death in breast cancer cells. Biology Open, Vol. 8.
- Zadan M., **Chiew C.,** Majidi C., Malakooti. M.H., (2021). Liquid metal architectures for soft and wearable energy harvesting devices, Multifunctional Materials, Vol. 4, 1, 012001.
- **Chiew C.,** Morris M., Malakooti M.H., (2021). Functional liquid metal nanoparticles: synthesis and applications. Material Advances. Vol. 2, 7799-7819.

Appendix

1. Supplementary Information for chapter 2

1.1 Eshelby's Tensor for Spherical Inclusion

Spherical Eshelby's tensor is a 4th order tensor as shown in Equation S1 where the non-zero tensor components are expressed from Equation S2 to Equation S4. Variable n refers to the phase treated as the matrix in the first and second level of MT homogenization step [135].

$$\mathbf{S}(\nu_{\mathrm{n}}) = \begin{Bmatrix} \mathrm{S}_{1111} & \mathrm{S}_{1122} & \mathrm{S}_{1133} & & & \\ \mathrm{S}_{2211} & \mathrm{S}_{2222} & \mathrm{S}_{2233} & & 0 & \\ \mathrm{S}_{3311} & \mathrm{S}_{3322} & \mathrm{S}_{3333} & & & \\ & & & 2\mathrm{S}_{2323} & & \\ & \mathrm{Sym} & & & 2\mathrm{S}_{3131} & \\ & & & & & 2\mathrm{S}_{1212} \end{Bmatrix} \quad \text{S1}$$

$$\mathrm{S}_{1111} = \mathrm{S}_{2222} = \mathrm{S}_{3333} = \frac{7 - 5\nu_{\mathrm{n}}}{15(1 - \nu_{\mathrm{n}})} \quad \text{S2}$$

$$\mathrm{S}_{1122} = \mathrm{S}_{2233} = \mathrm{S}_{3311} = \mathrm{S}_{1133} = \mathrm{S}_{2211} = \mathrm{S}_{3322} = \frac{5\nu_{\mathrm{n}} - 1}{15(1 - \nu_{\mathrm{n}})} \quad \text{S3}$$

$$\mathrm{S}_{1212} = \mathrm{S}_{2323} = \mathrm{S}_{3131} = \frac{4 - 5\nu_{\mathrm{n}}}{15(1 - \nu_{\mathrm{n}})} \quad \text{S4}$$

1.2 Generalized Double Inclusion Model

The equivalent stiffness tensor ($\bar{\mathbf{C}}^{\mathrm{G}}$) of a composite computed by one-level of MT homogenization is determined in Equation S5.

$$\bar{\mathbf{C}}^{\mathrm{G}} = \mathbf{C}_{\mathrm{m}} + \mathrm{f}_{\Omega}(\mathbf{C}_{\Omega} - \mathbf{C}_{\mathrm{m}}) : \mathbf{A}_{\Omega} + \mathrm{f}_{\Gamma}(\mathbf{C}_{\Gamma} - \mathbf{C}_{\mathrm{m}}) : \mathbf{A}_{\Gamma} \quad \text{S5}$$

In this common approach, two global strain concentration tensors ($\mathbf{A}_{\Omega}$ and $\mathbf{A}_{\Gamma}$) are introduced concurrently. $\mathbf{A}_{\Omega}$ and $\mathbf{A}_{\Gamma}$ relate the volume average strain ($\bar{\mathbf{e}}_{\Omega}$) in the core phase and volume average strain ($\bar{\mathbf{e}}_{\Gamma}$) in the interphase respectively with the volume average strain ($\bar{\mathbf{e}}$) in the total composite volume (P). This GDI model can be made equivalent with the original Eshelby's single inclusion model when f_{Ω} or f_{Γ} in Equation S5-S11 is zeroed where each simplification corresponds to modelling biphasic LMPCs with solid oxide or pure liquid inclusion respectively [176].

$$\mathbf{A}_{\Omega} = \mathbf{B}_{\mathbf{C}_{\mathrm{m}},\mathbf{c}_{\Omega}} : \left(\mathrm{f}_{\mathrm{m}}\mathbf{I} + \mathrm{f}_{\Omega}\mathbf{B}_{\mathbf{C}_{\mathrm{m}},\mathbf{c}_{\Omega}} + \mathrm{f}_{\Gamma}\mathbf{B}_{\mathbf{C}_{\mathrm{m}},\mathbf{c}_{\Gamma}}\right)^{-1} \quad \text{S6}$$

$$\bar{\mathbf{e}}_{\Omega} = \mathbf{A}_{\Omega} : \bar{\mathbf{e}} \quad \text{S7}$$

$$\mathbf{B}_{\mathbf{C}_m,\mathbf{c}_\Omega} = \left(\mathbf{I} + \mathbf{S}_m : \left(\mathbf{C}_m^{-1} : \mathbf{C}_\Omega - \mathbf{I}\right)\right)^{-1} \quad \text{S8}$$

$$\mathbf{A}_\Gamma = \mathbf{B}_{\mathbf{C}_m,\mathbf{c}_\Gamma} : \left(f_m\mathbf{I} + f_\Gamma \mathbf{B}_{\mathbf{C}_m,\mathbf{c}_\Gamma} + f_\Omega \mathbf{B}_{\mathbf{C}_m,\mathbf{c}_\Omega}\right)^{-1} \quad \text{S9}$$

$$\bar{\mathbf{e}}_\Gamma = \mathbf{A}_\Gamma : \bar{\mathbf{e}} \quad \text{S10}$$

$$\mathbf{B}_{\mathbf{C}_m,\mathbf{c}_\Gamma} = \left(\mathbf{I} + \mathbf{S}_m : \left(\mathbf{C}_m^{-1} : \mathbf{C}_\Gamma - \mathbf{I}\right)\right)^{-1} \quad \text{S11}$$

The effective stiffness of liquid metal polymer composites is predicted using DI model which consists of both two-level and one-level/generalized MT homogenization schemes. The effectiveness and accuracy of each model are identified based on the size (t/D ratio) and volume fractions (f_R) of the core-shell structured LM inclusions.

1.3 Extending DI for Functional Properties

Table S1. Extending elastic DI model to functional properties in liquid metal polymer composites [152].

Behavior	Constitutive law	Avg Flux vector	Avg Field vector
Mechanical	$\bar{\boldsymbol{\sigma}} = \bar{\mathbf{C}} : \bar{\mathbf{e}}$	$\bar{\boldsymbol{\sigma}}$	$\bar{\mathbf{e}}$
Thermal	$\bar{\mathbf{q}} = \bar{\mathbf{K}} : \bar{\boldsymbol{\theta}}$	$\bar{\mathbf{q}}$	$\bar{\boldsymbol{\theta}}$
Electrostatic	$\bar{\mathbf{d}} = \bar{\boldsymbol{\varepsilon}} : \bar{\mathbf{E}}$	$\bar{\mathbf{d}}$	$\bar{\mathbf{E}}$

1.4 Formulation of Style's Model

According to Style's model, when the radius of LM fillers is smaller than its capillary length (L), the interfacial surface tension will be dominant to cause overall stiffening of LMPC as a function of volume fraction. L here is defined as the ratio of surface tension (γ) to elastic modulus of polymer matrix (E_m). In this model, the effect of the Ga-oxide shell (specific to LM inclusions) is not considered although the presence of this oxide interface can diminish the surface tension of LM fillers from a maximum value of 0.5~0.6 Nm^{-1} to approximately zero [40,248]. Moreover, gallium oxide has a relatively large Young's modulus (0.4~1.4 GPa) in comparison to the modulus of common elastomer matrices (<10 MPa) used to encapsulate LM droplets [40,78,249]. As a result, while the predicted properties by Style's model agree with experimental behavior of LMPCs containing microscale inclusions, it is not suitable to physically describe the elasticity of LM nanocomposites.

In the formulation of Style's model, the increase in elastic modulus (Ec) of the LM polymer composite is based on a higher inclusion-matrix interfacial surface tension when the liquid inclusion diameter (D) gets smaller or when the elastic modulus of polymer matrix (Em) is relatively low as shown in Equation S12-S13 [147,172,250]. This surface tension effect can be represented by using Eshelby's equivalent inclusion analogy where the equivalent elastic modulus of inclusions (E_i) depends on the surface tension (γ), diameter of liquid inclusions (D) and the elastic modulus of its polymer matrix (E_m). As the diameter of the LM inclusion decreases, this equivalent inclusion elasticity will increase which leads to an overall larger elastic modulus of the composite as a function of filler volume fraction (f_R). In the context of Style's model, f_R described here refers to the volume fraction of a pure liquid inclusion with diameter equivalent to the core-shell inclusion in DI model.

$$\frac{E_c}{E_m} = \frac{1 + \frac{2}{3}\frac{E_i}{E_m}}{\left(\frac{2}{3} - \frac{5f_R}{3}\right)\frac{E_i}{E_m} + \left(1 + \frac{5}{3}f_R\right)} \quad \text{S12}$$

$$\frac{E_i}{E_m} = \frac{48\frac{\gamma}{E_m D}}{10 + 18\frac{\gamma}{E_m D}} \quad \text{S13}$$

For Style's model, predicting the stiffening behavior of the composite by liquid inclusions (without a core-shell structure) is done by considering EGaIn's surface tension of 0.5 $N \cdot m^{-1}$ and using similar elastomer's elastic modulus selected in DI model as input material constants [34,40].

1.5 Two-level Double Inclusion model with log-normal inclusion size distribution

The predicted effective elastic modulus of LM composite based on log-normal size distribution of LM inclusions can be found using Equation S14. In this equation, X_i refers to the volume fraction of each i^{th} inclusion size (t/D) following a log-normal distribution with its total summation equivalent to unity (Figure S1a). $\bar{C}^i_{\Gamma\Omega}$ and $A^i_{\Gamma\Omega,P}$ are the effective stiffness of the inner DI composite (Equation 11) and strain concentration tensor (Equation 12-13) for various inclusion sizes (i^{th}), respectively. Based on Table S2, 7 (N=7) discrete inclusion sizes (t/D) are chosen between 2×10^{-3} to 2×10^{-2} to represent the assumed log-normal distribution.

$$\bar{\mathbf{C}} = \mathbf{C}_m + f_R \sum_{i=1}^{N} X_i \left(\bar{\mathbf{C}}^i_{\Gamma\Omega} - \mathbf{C}_m\right) : \mathbf{A}^i_{\Gamma\Omega,P} \quad \text{S14}$$

$$\bar{\mathbf{C}}^{i}_{\Gamma\Omega} = \mathbf{C}_{\Gamma} + \left(1 - 2\frac{t}{D}\right)^{3} (\mathbf{C}_{\Omega} - \mathbf{C}_{\Gamma}) : \mathbf{B}_{\mathbf{C}_{\Gamma},\mathbf{C}_{\Omega}} : \mathbf{A}^{i}_{\Omega,\Gamma\Omega} \quad \text{S15}$$

$$\mathbf{A}^{i}_{\Omega,\Gamma\Omega} = f_R \mathbf{B}_{\mathbf{C}_{\Gamma},\mathbf{C}_{\Omega}} : \left(f_R \left(1 - 2\frac{t}{D}\right)^{3} \mathbf{I} + f_R \left\{ 1 - \left(1 - 2\frac{t}{D}\right)^{3} \right\} \mathbf{B}_{\mathbf{C}_{\Gamma},\mathbf{C}_{\Omega}} \right)^{-1} \quad \text{S16}$$

$$\mathbf{A}^{i}_{\Gamma\Omega,P} = \mathbf{B}_{\mathbf{C}_m,\bar{\mathbf{C}}^{i}_{\Gamma\Omega}} : \left(f_m \mathbf{I} + f_R \sum_{i=1}^{N} X_i \mathbf{B}_{\mathbf{C}_m,\bar{\mathbf{C}}^{i}_{\Gamma\Omega}} \right)^{-1} \quad \text{S17}$$

$$\mathbf{B}_{\mathbf{C}_m,\bar{\mathbf{C}}^{i}_{\Gamma\Omega}} = \left(\mathbf{I} + \mathbf{S}_m : \left(\mathbf{C}_m^{-1} : \bar{\mathbf{C}}^{i}_{\Gamma\Omega} - \mathbf{I} \right) \right)^{-1} \quad \text{S18}$$

$\bar{\mathbf{C}}^{i}_{\Gamma\Omega}$ and $\mathbf{A}^{i}_{\Omega,\Gamma\Omega}$ can be derived from Equation 11 and 13 respectively by noting that $\frac{f_\Omega}{f_R}$ is equivalent to $\left(1 - 2\frac{t}{D}\right)^{3}$ for core-shell sphere (Figure 8a). Similarly, $\mathbf{A}^{i}_{\Gamma\Omega,P}$ and $\mathbf{B}_{\mathbf{C}_m,\bar{\mathbf{C}}^{i}_{\Gamma\Omega}}$ are obtained by respectively modifying Equation 17 and 18 to consider each ith inclusion size (t/D) of the log-normal distribution.

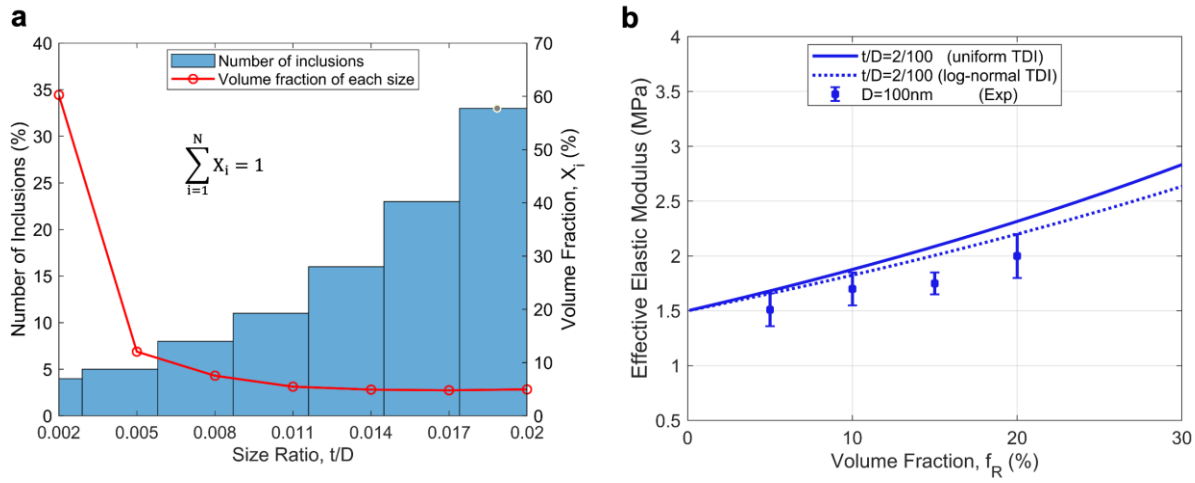

Figure S1. (a) Size distribution of liquid metal droplets with diameters varying from 100nm (t/D=0.02) to 1 mm (t/D=0.002), (b) TDI model predicting the effective elastic modulus for both monodisperse and polydisperse LM inclusions, compared to experimental data [251].

Table S2. A log-normal size distribution (Figure S1a) of inclusions for LM nanocomposite.

i^{th} inclusion size	1	2	3	4	5	6	7
Size Ratio, t/D	2×10^{-3}	5.0×10^{-3}	8.0×10^{-3}	1.1×10^{-2}	1.4×10^{-2}	1.7×10^{-2}	2.0×10^{-2}
Number of Inclusions, N_i (%)	4	5	8	11	16	23	33
Volume Fraction, X_i (%)	60.3	12.1	7.5	5.4	4.9	4.8	5

1.6 Details of Finite Element Modeling

To predict the mechanical properties using FEA, the total strain energy (U) of the RVE under simple tension (e_{11}) and pure shear (e_{31}) conditions is used to compute the components of the equivalent stiffness tensor ($\bar{C}_{1111}$) and the shear modulus ($\bar{\mu}$) of the composite, respectively. The strain energy in the RVE is acquired directly from ANSYS by applying loading BCs for simple tension and pure shear conditions. Additional displacement constraints are applied on opposite faces to create periodic BCs and to ensure the continuity between RVEs (Table S3). With known strain energy and applied deformations, the components of effective stiffness tensor are computed. Furthermore, the relationships between elastic constants can be used to determine the effective Young's modulus ($\bar{E}$) where $\bar{\nu}$ is the Poisson's ratio of the composite as shown in S19-S22.

$$U = \frac{L^3}{2}\bar{C}_{ijkl}e_{ij}e_{kl} \quad \text{S19}$$

$$\bar{C}_{1111} = \frac{2U}{L^3 e_{11}^2} \quad \text{S20}$$

$$\bar{\mu} = \frac{2U}{L^3 e_{31}^2} = \frac{\bar{E}}{2(1+\bar{\nu})} \quad \text{S21}$$

$$\bar{C}_{1111} = 2\bar{\mu} + \frac{\bar{E}}{(1+\bar{\nu})(1-2\bar{\nu})} \quad \text{S22}$$

Instead of applying known deformations, known thermal gradient (ΔT_{11}) and potential difference (ΔV_{11}) are applied between selected faces of the RVE to determine $\bar{\mathbf{K}}$ and $\bar{\boldsymbol{\varepsilon}}$, respectively. Simultaneously, other faces of the cubic RVE are assigned with zero heat (q) and zero electric (d)

flux as indicated in Table S3. Once the total rate of heat flow ($\mathbb{Q}$) through X direction is computed, the effective thermal conductivity can be estimated from Fourier's law in Equation S23. Similarly, once the total rate of electric field flow ($\mathbb{D}$) through x direction is computed, the effective dielectric constant can be determined using dielectric constitutive law in Equation S24. In Equation S23-S24, A, which equates to L^2, is the surface area of each cubic RVE face.

$$\bar{\mathbf{K}} = \frac{\mathbb{Q}}{A\Delta T_{11}}\,\mathbf{I_{3\times3}} \qquad \text{S23}$$

$$\bar{\boldsymbol{\varepsilon}} = \frac{L\mathbb{D}}{A\Delta V_{11}}\,\mathbf{I_{3\times3}} \qquad \text{S24}$$

Table S3. The boundary conditions for computing the equivalent mechanical, thermal, and dielectric properties of LMPCs using FE model. u, v and w are displacement components in x, y and z directions, respectively defined in Fig. 3b. T and q are the respective scalar temperature and heat flux density at the boundaries.

Boundaries	Tensile conditions	Pure shear conditions	Thermal conditions	Electrostatic conditions
X faces	$u(L,y,z) = e_{11}L$ $u(0,y,z) = 0$ $v(0,y,z) = 0$ $w(0,y,z) = 0$	$u(L,y,z) = u(0,y,z)$ $v(L,y,z) = v(0,y,z)$ $w(L,y,z) = w(0,y,z)$	$T(0,y,z)$ $-T(L,y,z)$ $= \Delta T_{11}$	$V(0,y,z)$ $-V(L,y,z)$ $= \Delta V_{11}$
Y faces	$v(x,L,z) = v(x,0,z)$ $w(x,L,z) = w(x,0,z)$	$v(x,L,z) = v(x,0,z)$ $w(x,L,z) = w(x,0,z)$	$q(x,L,z) = 0$ $q(x,0,z) = 0$	$d(x,L,z) = 0$ $d(x,0,z) = 0$
Z faces	$v(x,y,L) = v(x,y,0)$ $w(x,y,L) = w(x,y,0)$	$u(x,y,L) = e_{31}L$ $u(x,y,0) = 0$ $v(x,y,0) = 0$ $w(x,y,0) = 0$	$q(x,y,0) = 0$ $q(x,y,L) = 0$	$d(x,y,0) = 0$ $d(x,y,L) = 0$

1.7 Interpolated Two-level DI model for Functional Properties.

Two-level DI model underpredicts the measured thermal properties of LMPCs when the volume fraction of inclusions exceeds 20%. To rectify this, an interpolated two-level double inclusion (ITDI) model expressed as $\bar{\mathbf{K}}^{\mathrm{IT}}$ is proposed. In this model, the local thermal gradient concentration tensor at the highest level of MT homogenization is modified into a linearly interpolated concentration tensor ($\mathbf{B}^{\mathrm{IT}}_{\mathbf{K}_m,\bar{\mathbf{K}}_{\Gamma\Omega}}$) [213,217]. This modification allows DI model to show better agreement with the measured thermal conductivity of LMPCs at higher volume fractions [178].

$$\bar{\mathbf{K}}^{\mathrm{IT}} = \mathbf{K}_m + (f_\Omega + f_\Gamma)(\bar{\mathbf{K}}_{\Gamma\Omega} - \mathbf{K}_m) : \mathbf{B}^{\mathrm{IT}}_{\mathbf{K}_m,\bar{\mathbf{K}}_{\Gamma\Omega}} : \left(f_m\mathbf{I} + (f_\Omega + f_\Gamma)\mathbf{B}^{\mathrm{IT}}_{\mathbf{K}_m,\bar{\mathbf{K}}_{\Gamma\Omega}}\right)^{-1} \quad \text{S25}$$

$$\mathbf{B}^{\mathrm{IT}}_{\mathbf{K}_m,\bar{\mathbf{K}}_{\Gamma\Omega}} = \left\{ (1 - f_R)\left(\mathbf{B}_{\mathbf{K}_m,\bar{\mathbf{K}}_{\Gamma\Omega}}\right)^{-1} + f_R\mathbf{B}_{\bar{\mathbf{K}}_{\Gamma\Omega},\mathbf{K}_m} \right\}^{-1} \quad \text{S26}$$

$$\mathbf{B}_{\bar{\mathbf{K}}_{\Gamma\Omega},\mathbf{K}_m} = \left(\mathbf{I} + \mathbf{S} : (\bar{\mathbf{K}}^{-1}_{\Gamma\Omega} : \mathbf{K}_m - \mathbf{I})\right)^{-1} \quad \text{S27}$$

$$\mathbf{B}_{\mathbf{K}_m,\bar{\mathbf{K}}_{\Gamma\Omega}} = \left(\mathbf{I} + \mathbf{S} : (\mathbf{K}^{-1}_m : \bar{\mathbf{K}}_{\Gamma\Omega} - \mathbf{I})\right)^{-1} \quad \text{S28}$$

In Equation S26, $\mathbf{B}^{\mathrm{IT}}_{\mathbf{K}_m,\bar{\mathbf{K}}_{\Gamma\Omega}}$ is a local concentration tensor that linearly interpolates with respect to volume fraction (f_R) between $\mathbf{B}_{\mathbf{K}_m,\bar{\mathbf{K}}_{\Gamma\Omega}}$ and $\mathbf{B}_{\bar{\mathbf{K}}_{\Gamma\Omega},\mathbf{K}_m}$. The thermal property of the core-shell domain ($\bar{\mathbf{K}}_{\Gamma\Omega}$) within $\mathbf{B}^{\mathrm{IT}}_{\mathbf{K}_m,\bar{\mathbf{K}}_{\Gamma\Omega}}$ needs to be determined beforehand at the deepest level of MT homogenization to ensure ITDI model still accounts for the size effect of core-shell LM inclusions. The $\mathbf{B}_{\mathbf{K}_m,\bar{\mathbf{K}}_{\Gamma\Omega}}$ and $\mathbf{B}_{\bar{\mathbf{K}}_{\Gamma\Omega},\mathbf{K}_m}$ are thermal gradient concentration tensors when LM fillers are sparsely (low f_R) and densely (high f_R) distributed, respectively, in the composite. When LM fillers are sparsely distributed, the core-shell LM are inclusions and the polymer is the matrix. In contrast, when LM fillers are densely distributed, the polymer appears as a filler confined in LM rich regions. Thus, the polymer phase becomes the inclusions that are surrounded by homogenized core-shell LM matrix. In a similar approach, this interpolation can be utilized to predict the effective dielectric properties of LMPCs.

2. Supplemental Information for chapter 3

2.1 Exterior Eshelby's Tensor

A key computational ingredient to evaluate the stress field outside an ellipsoid inclusion is to explicitly derive the external Eshelby's tensor $[\mathbf{S}^{e}(\mathbf{X})]$ which is a well-known difficulty in Eshelby's inclusion problem [145]. Despite that, several recent studies had demonstrated a mathematically simpler way to evaluate the three-dimensional stress or strain components outside an ellipsoid inclusion [148,194,252]. This is achieved by defining the following external Eshelby's tensor in terms of the components of a unit normal vector $[\bar{\mathbf{n}}(\mathbf{X})]$ at an imaginary ellipsoid. The following imaginary ellipsoid has the same aspect ratio as the actual inclusion of the composite, but the surface is external to the inclusion and its surface host the location $(\mathbf{X})$ where the exact stress $[\sigma^{m}(\mathbf{X})]$ or strain $[\varepsilon^{m}(\mathbf{X})]$ fields are to be evaluated. With the help of the external Eshelby's tensor $[\mathbf{S}^{e}(\mathbf{X})]$, these exact stress and strain components can be exactly determined at any positions outside the ellipsoid inclusion. Here, we will compactly present the components (S29) for the six-by-six external Eshelby's tensor (S30) in terms of index notation [194]. The term δ_{ij} in the following equation is known as Kronecker's delta which becomes one when indices $i = j$ and become zero when $i \neq j$. Also, the variable ν in the first term of S29 is the isotropic Poisson's ratio of the polymer matrix.

$$\begin{aligned} S^{E}_{ijkl}(\alpha) = {} & \delta_{ij}\delta_{kl}\left[\frac{\nu}{1-\nu}J_i + A^{(1)}_{ik}\right] + \left[\frac{J_i + J_j}{2} + A^{(1)}_{ij}\right]\left[\delta_{ik}\delta_{jl} + \delta_{il}\delta_{jk}\right] \\ & + A^{(2)}_{i}\left[\delta_{ij}n_k n_l + \delta_{il}n_j n_k\right] + A^{(2)}_{j}\left[\delta_{jk}n_i n_l + \delta_{jl}n_i n_k\right] + A^{(2)}_{k}[\delta_{kl}n_i n_j \\ & + \delta_{ik}n_j n_l] + \frac{1}{2}\left[A^{(3)}_{ijkl} + A^{(3)}_{jikl}\right] + A^{(4)}_{ijkl}n_i n_j n_k n_l \end{aligned} \quad \text{S29}$$

$$\mathbf{S}^{E}(\alpha) == \begin{Bmatrix} S^{E}_{1111}(\alpha) & S^{E}_{1122}(\alpha) & S^{E}_{1133}(\alpha) & & & \\ S^{E}_{2211}(\alpha) & S^{E}_{2222}(\alpha) & S^{E}_{2233}(\alpha) & & \mathbf{0} & \\ S^{E}_{3311}(\alpha) & S^{E}_{3322}(\alpha) & S^{E}_{3333}(\alpha) & & & \\ & & & S^{E}_{2323}(\alpha) & 0 & 0 \\ & \mathbf{0} & & 0 & S^{E}_{1313}(\alpha) & 0 \\ & & & 0 & 0 & S^{E}_{1212}(\alpha) \end{Bmatrix}, \alpha = \frac{r_1}{r_2} = \frac{r_1}{r_3} \quad \text{S30}$$

$$> 1$$

$$n_i = \frac{x_i}{(r_i^2 + \lambda)\sqrt{\frac{x_1^2}{(r_1^2+\lambda)^2} + \frac{x_2^2}{(r_2^2+\lambda)^2} + \frac{x_3^2}{(r_3^2+\lambda)^2}}} \quad \text{S31}$$

$$\lambda = \frac{1}{2}[x_1^2 + x_2^2 + x_3^2 - r_1^2 - r_3^2] + \sqrt{\frac{1}{4}[x_1^2 + x_2^2 + x_3^2 + r_1^2 - r_3^2]^2 + (r_3^2 - r_1^2)x_1^2} \quad \text{S32}$$

$$\frac{x_1^2}{r_1^2 + \lambda} + \frac{x_2^2}{r_2^2 + \lambda} + \frac{x_3^2}{r_3^2 + \lambda} = 1, \quad \text{for } \mathbf{X} \in \text{outside } \Omega \quad \text{S33}$$

Based on Equation S29 the components of $\mathbf{S}^E(\mathbf{X})$ are dependent on the normal unit vector components $\bar{\mathbf{n}}(\mathbf{X}) = [n_1, n_2, n_3]$ at the surface of position X of the imaginary ellipsoid which is defined in Equation S31. Another important parameter that describes the overall geometry of the imaginary ellipsoid is λ, which is a geometric value that dictates the general equation describing the surface of the imaginary ellipsoid (Equation S32). With this variable, the position of interest can be ascertained whether to be located inside or outside of the actual inclusion by determining if the computed λ will be smaller or greater than zero, respectively. Hence, to utilize $\mathbf{S}^E(\mathbf{X})$ in the model, the evaluated λ at a given position (X) of interest must be greater than zero.

For this study, we only consider the case of oblate spheroid ($r_1 > r_2 = r_3$) and spherical inclusion ($r_1 = 1.001r_2 = 1.001r_3$). In both cases, the axis minor radius (r_2 , r_3) of the ellipsoid inclusion must always be equal and r_1 cannot ever be equal to r_2 because the utilized solution for $\mathbf{S}^E(\mathbf{X})$ in this study is specifically for prolate-type ellipsoid. The purpose of the remaining undefined variables is for the brevity of the presented Eshelby's tensor and thus, the rest of their definitions are provided from Equation S34 to Equation S36. For the complete derivation details of the Eshelby's tensor, please refer to the cited original studies [148,194].

$$J_1 = \frac{r_3^2 r_1}{\sqrt{(r_1^2 - r_3^2)^3}}\left[\ln(\bar{p} + \bar{q}) - \frac{\bar{q}}{\bar{p}}\right]$$

$$J_2 = J_3 = \frac{r_3^2 r_1}{2\sqrt{(r_1^2 - r_3^2)^3}}[\ln(\bar{p} - \bar{q}) + \bar{p}\,\bar{q}]$$

$$J_{12} = J_{13} = J_{21} = J_{31} = \frac{r_1 r_3^2}{2(r_1^2 - r_3^2)^{\frac{5}{2}}}\left[\ln(\bar{p} - \bar{q}) - 2\ln(\bar{p} + \bar{q}) + \bar{p}\,\bar{q} + 2\frac{\bar{q}}{\bar{p}}\right]$$

$$J_{11} = \frac{r_1 r_3^2}{3(r_1^2 - r_3^2)^{\frac{5}{2}}}\left[\frac{(r_1^2 - r_3^2)^{\frac{5}{2}}}{(r_1^2 + \lambda)^{\frac{3}{2}}(r_3^2 + \lambda)} - \ln(\bar{p} - \bar{q}) + 2\ln(\bar{p} + \bar{q}) - \bar{p}\,\bar{q} - 2\frac{\bar{q}}{\bar{p}}\right] \quad \text{S34}$$

$$J_{22} = J_{23} = J_{33}$$

$$= \frac{r_1 r_3^2}{8(r_1^2 - r_3^2)^{\frac{5}{2}}}\left[\frac{2(r_1^2 - r_3^2)^{\frac{5}{2}}}{(r_3^2 + \lambda)^2\sqrt{r_1^2 + \lambda}} - \ln(\bar{p} - \bar{q}) + 2\ln(\bar{p} + \bar{q}) - \bar{p}\,\bar{q} - 2\frac{\bar{q}}{\bar{p}}\right]$$

$$\bar{p} = \sqrt{(r_1^2 + \lambda)/(r_3^2 + \lambda)}$$

$$\bar{q} = \sqrt{(r_1^2 - r_3^2)/(r_3^2 + \lambda)} \qquad \text{S35}$$

$$A_{ik}^{(1)} = \frac{r_k^2 J_{ik} - J_i}{2 - 2\nu} = A_{ki}^{(1)}$$

$$A_i^{(2)} = \frac{\Lambda}{2 - 2\nu}(1 - \rho_i^2), \qquad \rho_i = \sqrt{\frac{r_i^2}{r_i^2 + \lambda}}\ , \Lambda = \rho_1\rho_2\rho_3$$

$$A_{ijkl}^{(3)} = -\Lambda\left(\delta_{ik}n_l n_j + \delta_{il}n_k n_j + \frac{\nu}{1 - \nu}\delta_{kl}n_i n_j\right)$$

$$A_{ijkl}^{(4)} = \frac{\Lambda}{2 - 2\nu}\left[2\left(\frac{r_i^2}{r_i^2 + \lambda} + \frac{r_j^2}{r_j^2 + \lambda} + \frac{r_k^2}{r_k^2 + \lambda} + \frac{r_l^2}{r_l^2 + \lambda}\right) + Q\right]$$

$$Q = \rho_m\rho_m - 4\rho_m^2 n_m n_m - 5 = \rho_1^2 + \rho_2^2 + \rho_3^2 - 4\rho_1^2 n_1 n_1 - 4\rho_2^2 n_2 n_2 - 4\rho_3^2 n_3 n_3 - 5 \qquad \text{S36}$$

2.2 Internal Eshelby's Tensor

Unlike the external Eshelby's tensor defined beforehand, the components of the six-by-six internal Eshelby's tensor are not dependent on position X. It is possible to recover the components of the internal Eshelby's tensor (Equation S37) to determine the stress or strains in the inclusion by simply taking $\lambda = 0$ and all the components of the normal vector ($\overline{\mathbf{n}}$) to be zero. Hence, the remaining simplified terms which are J_i and $A_{ik}^{(1)}$ will be the same as those defined in Equation S35 and S36, respectively but with λ equated to zero. With the help of computer programming in MATLAB, we had created a function to generate either the internal or the external Eshelby's tensor at any arbitrary input position vector (X) that are inside or outside the inclusion, respectively.

$$S_{ijkl}^{I}(\alpha) = \delta_{ij}\delta_{kl}\left[\frac{\nu}{1-\nu}J_i + A_{ik}^{(1)}\right] + \left[\frac{J_i + J_j}{2} + A_{ij}^{(1)}\right]\left(\delta_{ik}\delta_{jl} + \delta_{il}\delta_{jk}\right) \quad \text{S37}$$

$$\mathbf{S}^{I}(\alpha) == \begin{Bmatrix} S_{1111}^{I}(\alpha) & S_{1122}^{I}(\alpha) & S_{1133}^{I}(\alpha) & & & \\ S_{2211}^{I}(\alpha) & S_{2222}^{I}(\alpha) & S_{2233}^{I}(\alpha) & & \mathbf{0} & \\ S_{3311}^{I}(\alpha) & S_{3322}^{I}(\alpha) & S_{3333}^{I}(\alpha) & & & \\ & & & S_{2323}^{I}(\alpha) & 0 & 0 \\ & \mathbf{0} & & 0 & S_{1313}^{I}(\alpha) & 0 \\ & & & 0 & 0 & S_{1212}^{I}(\alpha) \end{Bmatrix} \quad \text{S38}$$

3. Supplemental Information for chapter 4

3.1 Eshelby's tensor (Mechanical Property) for finite cylinder and ellipsoidal inclusion

Franciosi et al.[218,219] derived the Eshelby's tensor for a flat cylinder inclusion by using both volume averaging and radon transform formulation of the elastostatic green's function. This tensor is used to either model stress/strain concentration behavior of monolayer or multilayer MXenes in this study which are embedded in a reference matrix λ which could be either the interphase ($\lambda = \mathrm{i}$) or the polymer matrix ($\lambda = \mathrm{m}$) of MXPCs.

$$\mathbf{S_\lambda} = \begin{Bmatrix} \frac{3A}{8}\Psi + \psi & \frac{A}{8}\Psi & \frac{A}{2}\beta + \frac{1}{2}\psi & & & \\ \frac{A}{8}\Psi & \frac{3A}{8}\Psi + \phi & \frac{A}{2}\beta + \frac{1}{2}\psi & & \mathbf{0} & \\ \frac{A}{2}\beta + \frac{1}{2}\psi & \frac{A}{2}\beta + \frac{1}{2}\psi & A\Phi + 2\phi & & & \\ & & & A\psi\phi + (0.5\psi + \phi) & & \\ & \mathbf{0} & & & A\psi\phi + (0.5\psi + \phi) & \\ & & & & & \frac{A}{4}\Psi \end{Bmatrix} : \mathbf{C} \quad \text{S39}$$

$$\mathbf{C} = \frac{1}{(1-2\nu_\lambda)} \begin{Bmatrix} (1-\nu_\lambda) & \nu_\lambda & \nu_\lambda & & & \\ \nu_\lambda & (1-\nu_\lambda) & \nu_\lambda & & \mathbf{0} & \\ \nu_\lambda & \nu_\lambda & (1-\nu_\lambda) & & & \\ & & & 0.5(1-2\nu_\lambda) & & \\ & \mathbf{0} & & & 0.5(1-2\nu_\lambda) & \\ & & & & & 0.5(1-2\nu_\lambda) \end{Bmatrix} \quad \text{S40}$$

$$A = (1-\nu_\lambda)^{-1} \quad \text{S41}$$

Based on Equation S39and S40, the 4th order Eshelby's tensor is dependent on the Poisson's ratio (ν_λ) of the reference matrix medium (λ) of the flat cylinder inclusion. This Poisson's ratio could be redefined as the Poisson's ratio of MXene (ν_Γ), interphase (ν_i), or the polymer phase (ν_m) in IMT model. From radon transformation and volume integral computation, the shape functions (i.e., Ψ, ψ, Φ, β and ϕ) of the finite cylinder Eshelby's tensor are derived and summarized in Equation. S42 to S46. Furthermore, the following shape functions are also dependent on the thickness to diameter ratio (ζ) of the finite cylinder inclusion. In the first homogenization step of the micromechanics IMT model, this ζ is assigned to the reciprocal aspect ratio ($\zeta = \alpha^{-1}$) of monolayer MXene. Alternately, in the second homogenization step of IMT model, ζ becomes the reciprocal aspect ratio of the equivalent medium ($\zeta = \beta^{-1}$). To verify the validity of these shape functions, we ensured that the plotted shape functions in relation to ζ (Figure S2) is identical to those shown in

the original work [218]. Based on Figure S2, the majority of MXene sheets embedded in MXPCs have size ratio (ζ) that are below 1/500. Hence, when ζ is small, the Eshelby's tensor will represent MXenes as flat cylinder inclusions in the composite.

$$\Psi = \frac{8}{3\pi^2}\left\{\frac{3}{2} + \frac{3\pi}{4}\zeta - \frac{3+3\zeta^2}{2\zeta}\tan^{-1}\zeta\right\} + \frac{2a_5}{\pi^2}\sqrt{\zeta}\{a_1(\mathrm{I}-\mathrm{III}) + \alpha\zeta_2(\mathrm{IV}-\mathrm{II}) + a_3\zeta^2\mathrm{III} - a_4\zeta^3\mathrm{IV}\} \quad \text{S42}$$

$$\psi = \frac{8}{3\pi^2}\left\{1 + \frac{3\pi}{2}\zeta - \frac{3\zeta^2+1}{\zeta}\tan^{-1}\zeta + \zeta^2\ln\left(\frac{\zeta^2}{1+\zeta^2}\right)\right\} + 2a_5\pi^{-2}\left(\mathrm{I}\zeta^{0.5}(a_1 - a_3\zeta^2) - \mathrm{II}\zeta^{\frac{3}{2}}(a_2 - a_4\zeta^2) + 2\zeta^2\left(a_3 - \frac{a_4}{3}\right)\right) \quad \text{S43}$$

$$\Phi = \frac{8}{3\pi^2}\left\{\frac{5}{2} - \frac{9\pi}{4}\zeta + \frac{1+9\zeta^2}{2\zeta}\tan^{-1}\zeta - 2\zeta^2\ln\left(\frac{\zeta^2}{1+\zeta^2}\right)\right\} + 1 - \frac{8}{\pi^2} - \frac{2a_5}{\pi^2}\sqrt{\zeta}\left\{a_1\mathrm{I} - a_2\zeta\mathrm{II} + a_3(2\zeta^{1.5} - \zeta^2\mathrm{I}) + a_4\left(\mathrm{II}\zeta^2 - \frac{2}{3}\zeta^{1.5}\right)\right\} \quad \text{S44}$$

$$\phi = \frac{8}{3\pi^2}\left\{2 - \frac{3\pi}{2}\zeta + \frac{3\zeta^2+1}{\zeta}\tan^{-1}\zeta - \zeta^2\ln\left(\frac{\zeta^2}{1+\zeta^2}\right)\right\} + 1 - \frac{8}{\pi^2} - 2a_5\pi^{-2}\left(\mathrm{I}\zeta^{0.5}(a_1 - a_3\zeta^2) - \mathrm{II}\zeta^{\frac{3}{2}}(a_2 - a_4\zeta^2) + 2\zeta^2\left(a_3 - \frac{a_4}{3}\right)\right) \quad \text{S45}$$

$$\beta = \frac{8}{3\pi^2}\left\{-\frac{1}{2} + \frac{3\pi}{4}\zeta + \frac{1-3\zeta^2}{2\zeta}\tan^{-1}\zeta + \zeta^2\ln\left(\frac{\zeta^2}{1+\zeta^2}\right)\right\} + a_5\pi^{-2}\left(\mathrm{III}\zeta^{0.5}(a_1 - a_3\zeta^2) - \mathrm{IV}\zeta^{1.5}(a_2 - a_4\zeta^2) + 2\zeta^2\left(a_3 - \frac{a_4}{3}\right) - \zeta^{2.5}(\mathrm{I}a_3 - \mathrm{II}\zeta a_4)\right) \quad \text{S46}$$

In Equation S42 to S46, the coefficient values of a_1, a_2, a_3, a_4, and a_5 are provided in Table S4. Moreover, the shorthand terms (i.e., I, II, III, and IV) introduced in these equations are also dependent on ζ. These shorthanded terms are all listed from Equation S47 to S50.

$$\mathrm{I} = \frac{\sqrt{2}}{2}\left[\pi + \frac{1}{2}\ln\left(\frac{\zeta + \sqrt{2\zeta} + 1}{\zeta - \sqrt{2\zeta} + 1}\right) - \tan^{-1}\left(1 + \sqrt{2\zeta}\right) - \tan^{-1}\left(\sqrt{2\zeta} - 1\right)\right] \quad \text{S47}$$

$$\mathrm{II} = \frac{\sqrt{2}}{2}\left(\pi - \frac{1}{2}\ln\left(\frac{\zeta + \sqrt{2\zeta} + 1}{\zeta - \sqrt{2\zeta} + 1}\right) - \tan^{-1}\left(\sqrt{2\zeta} + 1\right) - \tan^{-1}\left(\sqrt{2\zeta} - 1\right)\right) \quad \text{S48}$$

$$\mathrm{III} = \frac{\sqrt{2}}{8}\left\{\pi + \frac{1}{2}\ln\left(\frac{\zeta + \sqrt{2\zeta} + 1}{\zeta - \sqrt{2\zeta} + 1}\right) - \tan^{-1}\left(\sqrt{2\zeta} + 1\right) - \tan^{-1}\left(\sqrt{2\zeta} - 1\right) + \frac{2\sqrt{2}\zeta\sqrt{\zeta}}{(\zeta^2 + 1)}\right\} \quad \text{S49}$$

$$IV = \frac{3\sqrt{2}}{8}\left(\pi - \frac{4\sqrt{\zeta}}{3\sqrt{2}(\zeta^2+1)} - \frac{1}{2}\ln\left(\frac{\zeta+\sqrt{2\zeta}+1}{\zeta-\sqrt{2\zeta}+1}\right) + \tan^{-1}(1-\sqrt{2\zeta}) - \tan^{-1}(\sqrt{2\zeta}+1)\right) \quad \text{S50}$$

Table S4: Coefficient values of a_1 to a_5 define the shape function of finite cylinder Eshelby's tensor.

a_1	a_2	a_3	a_4	a_5
$1+\sqrt{2}/6$	$2+\sqrt{2}/2$	$1+\sqrt{2}/2$	$\sqrt{2}/6$	0.729

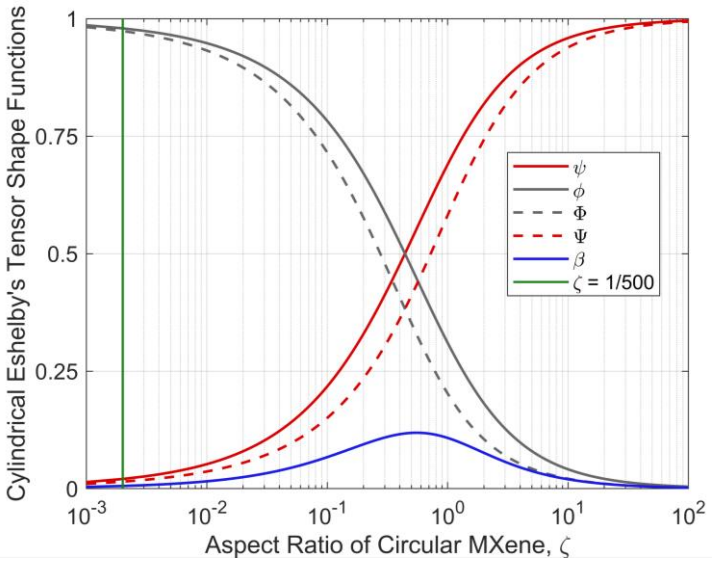

Figure S2. The weight fraction that results from the radon transforms volume integral of circular cylinder for finding the components of Eshelby's tensor. In our study, we will mostly use the weight functions left to the green line which is the majority aspect ratios of our MXene clusters.

3.2 Flat/finite cylinder Eshelby's tensor (Functional Property)

To model the thermal and dielectric behaviors of MXene polymer composites, the field polarization by MXene inclusions can be evaluated with the help of 2nd order Eshelby's tensor for finite cylinder inclusion [218,219]. This 2nd order Eshelby's tensor in Equation S51 is used in IMT model to predict the functional properties of MXPCs based on the aspect ratios of embedded single or multilayer MXenes. In the first Mori-Tanaka homogenization step, the following 2nd order Eshelby's tensor is dependent on the aspect ratio of monolayer MXene ($\zeta = \alpha^{-1}$) of the MXene cluster. For the final homogenization step using the interpolated Mori-Tanaka, the same Eshelby's tensor will be used but with the aspect ratio replace with the aspect ratio of the considered MXene cluster ($\zeta = \beta^{-1}$).

$$\mathbf{S}_{\lambda} = \begin{Bmatrix} \frac{1}{2}\psi & 0 & \frac{1}{4}\psi \\ 0 & \frac{1}{2}\psi & \frac{1}{4}\psi \\ \frac{1}{4}\psi & \frac{1}{4}\psi & \phi \end{Bmatrix} \quad \text{S51}$$

$$S_{\Omega}^{11} = \frac{1}{2}\psi \quad \text{for } \zeta = \beta^{-1} \quad \text{S52}$$

3.3 Percolation volume fraction of MXPCs

The first row and column element (i.e., S_{Ω}^{11}) of Equation S52 and can be used to evaluate the percolation volume fraction (f^*) of MXPCs with randomly oriented single or multilayer MXenes of a prescribed aspect ratio (ζ^{-1}) by using Equation 58. The following relationship between f^* and ζ^{-1} is illustrated in Figure S3. As the diameter to height ratio of multilayer MXene ($\zeta^{-1} = \beta$) increases from 1 to 10^3, the predicted percolation threshold decreases from 0.33 to approximately close to zero.

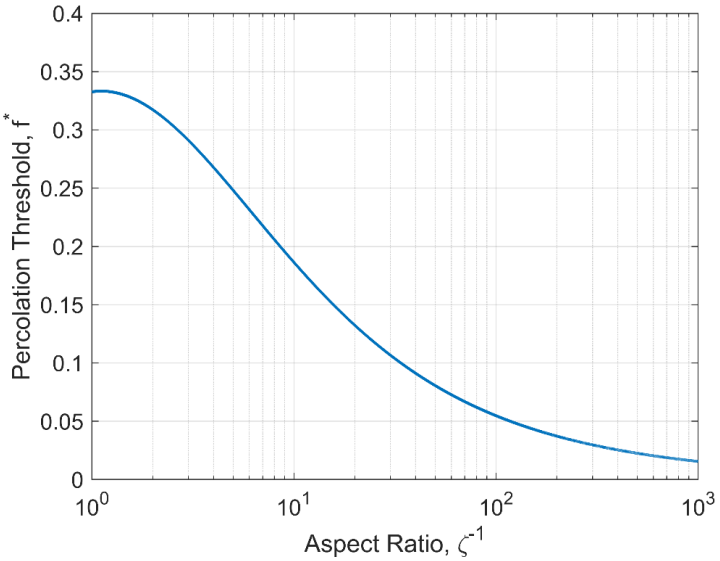

Figure S3. The predicted percolation threshold volume fraction (f^*) as a function of the aspect ratio of multilayer MXenes ($\zeta^{-1} = \beta$).

4.6.3 Orientation averaging

When multilayer MXene sheets with high aspect ratios are randomly dispersed in the composite, the effective mechanical and functional properties of the composite will be approximately isotropic. For example, the elastic modulus of the composite in each orthogonal direction (i.e., x, y, and z in Cartesian space) are approximately equivalent to each other. This is because the orientation of the dispersed MXene inclusions (i.e., flat cylinders) are assumed to be uniformly

distributed with respect to each Euler coordinate angles ($\phi, \gamma,$ and ψ). To consider random orientation of MXene inclusions in IMT model, the orientation averaging operator (Equation S54) is used [220]. Equation S54 is the orientation averaging operator for a given 4^{th} order depolarization tensor (**M**) which enables IMT model to compute the effective isotropic mechanical property of MXPCs. The components of this six-by-six matrix (**M**) and the orientation averaged matrix <**M**> are represented as index notation in Equation S55 and S56, respectively. Equation S57 lists the components for the transformation tensor which allows IMT model to account the mechanical reinforcement contributed by individual MXenes embedded at different orientations in the composite.

The property tensor for thermal and dielectric properties of MXPCs are 2^{nd} order tensors. As a result, the orientation averaging operator for IMT model should be compatible for accommodating the orientation averaging of 2^{nd} order tensor (Equation S58). The components of now 3 by 3 depolarization matrix (**M**) and the resultant orientation averaged matrix (<**M**>) are listed in Equation S55. Both Equation S56 and S58 are solved using standard rectangular numerical integration established in MATLAB.

$$< \mathrm{A} >_{\mathrm{klmn}} = \frac{1}{2\pi^2}\int_{-\pi}^{\pi}\int_{0}^{\pi}\int_{0}^{\frac{\pi}{2}} \Theta_{\mathrm{kp}}\Theta_{\mathrm{lq}}\Theta_{\mathrm{mr}}\Theta_{\mathrm{ns}}\mathrm{M}_{\mathrm{pqrs}}\sin(\gamma)\,\mathrm{d}\phi\mathrm{d}\gamma\mathrm{d}\psi \quad \text{S53}$$

$$\mathbf{M} = \begin{Bmatrix} \mathrm{M}_{1111} & \mathrm{M}_{1122} & \mathrm{M}_{1133} & & & \\ \mathrm{M}_{2211} & \mathrm{M}_{2222} & \mathrm{M}_{2233} & & \mathbf{0} & \\ \mathrm{M}_{3311} & \mathrm{M}_{3322} & \mathrm{M}_{3333} & & & \\ & & & \mathrm{M}_{2323} & & \\ & \mathbf{0} & & & \mathrm{M}_{1313} & \\ & & & & & \mathrm{M}_{1212} \end{Bmatrix} \quad \text{S54}$$

$$< \mathbf{M} > = \begin{Bmatrix} < \mathrm{M} >_{1111} & < \mathrm{M} >_{1122} & < \mathrm{M} >_{1133} & & & \\ < \mathrm{M} >_{2211} & < \mathrm{M} >_{2222} & < \mathrm{M} >_{2233} & & \mathbf{0} & \\ < \mathrm{M} >_{3311} & < \mathrm{M} >_{3322} & < \mathrm{M} >_{3333} & & & \\ & & & < \mathrm{M} >_{2323} & & \\ & \mathbf{0} & & & < \mathrm{M} >_{1313} & \\ & & & & & < \mathrm{M} >_{1212} \end{Bmatrix} \quad \text{S55}$$

$$\begin{aligned} \Theta_{11} &= \cos(\phi)\cos(\psi) - \sin(\phi)\cos(\gamma)\ \sin(\psi) \\ \Theta_{22} &= -\sin(\phi)\sin(\psi) + \cos(\phi)\cos(\gamma)\cos(\psi) \\ \Theta_{33} &= \cos(\gamma) \\ \Theta_{21} &= -\cos(\phi)\sin(\psi) - \sin(\phi)\cos(\gamma)\cos(\psi) \\ \Theta_{23} &= \sin(\gamma)\cos(\psi) \\ \Theta_{31} &= \sin(\phi)\sin(\gamma) \\ \Theta_{32} &= -\cos(\phi)\sin(\gamma) \\ \Theta_{12} &= \sin(\phi)\cos(\psi) + \cos(\phi)\cos(\gamma)\sin(\psi) \end{aligned} \quad \text{S56}$$

$$< \mathrm{A} >_{\mathrm{ij}} = \frac{1}{2\pi^2}\int_{-\pi}^{\pi}\int_{0}^{\pi}\int_{0}^{\frac{\pi}{2}} \Theta_{\mathrm{ik}}\Theta_{\mathrm{jl}}\mathrm{A}_{\mathrm{kl}}\sin(\gamma)\,\mathrm{d}\phi\mathrm{d}\gamma\mathrm{d}\psi \quad \text{S57}$$

$$\mathbf{M} = \begin{Bmatrix} \mathrm{M}_{11} & \mathrm{M}_{12} & \mathrm{M}_{13} \\ \mathrm{M}_{21} & \mathrm{M}_{22} & \mathrm{M}_{23} \\ \mathrm{M}_{31} & \mathrm{M}_{32} & \mathrm{M}_{33} \end{Bmatrix} \quad \text{and} \quad < \mathbf{A} > = \begin{Bmatrix} < \mathrm{M} >_{11} & < \mathrm{M} >_{12} & < \mathrm{M} >_{13} \\ < \mathrm{M} >_{21} & < \mathrm{M} >_{22} & < \mathrm{M} >_{23} \\ < \mathrm{M} >_{31} & < \mathrm{M} >_{32} & < \mathrm{M} >_{33} \end{Bmatrix} \quad \text{S58}$$

3.4 Interchangeability of property in IMT model

Table S5 shows that the generalized property tensor ($\mathbf{L}_\lambda$) of polymer matrix (λ=m), intercalant (λ=i), and MXene (λ=Γ) in the interpolated Mori-Tanaka model formulation can be interchanged into stiffness, thermal conductivity, and dielectric tensors.

Table S5. Conversion of general property tensor into mechanical and functional property matrix. $\mathbf{I}^{3\times3}$ is a three-by-three (2nd order) identity matrix or otherwise (I) will be a six-by-six identity matrix.

Phase	Mechanical Stiffness $\mathbf{L}_\lambda = \mathbf{C}_\lambda$	Thermal Conductivity $\mathbf{L}_\lambda = K_\lambda \mathbf{I}^{3\times3}$	Relative Permittivity $\mathbf{L}_\lambda = \varepsilon_\lambda \mathbf{I}^{3\times3}$
Polymer (λ=m)	$\mathbf{C}_m$	$K_m \mathbf{I}^{3\times3}$	$\varepsilon_m \mathbf{I}^{3\times3}$
Intercalant (λ=i)	$\mathbf{C}_i$	$K_i \mathbf{I}^{3\times3}$	$\varepsilon_i \mathbf{I}^{3\times3}$
MXene (λ=Γ)	$\mathbf{C}_\Gamma$	$K_\Gamma \mathbf{I}^{3\times3}$	$\varepsilon_\Gamma \mathbf{I}^{3\times3}$

3.5 Input material properties for IMT model and finite element method

Table S6. Input mechanical and functional properties of constituents in various MXene composites retrieved from literatures.

Phase	Elastic Modulus (MPa)	Poisson's ratio	Thermal conductivity ($W \cdot m^{-1} \cdot K^{-1}$)	Dielectric Constant (DC)
$Ti_3C_2T_x$ MXene (filler)	9,000 to 70,000 [225]	0.49	55.8[94]	1×10^7
PDMS (Sylgard 184)	1.5 [226]	0.49	0.27	2.7

3.6 Resistance Function

Figure S4 shows the resistance function behaviors when the number of layers, lateral size, and volume fraction of MXenes in MXPCs are changed. This plot is created based on Equation 60 where it is assumed that f' is equal to f^* at a given considered aspect ratio ($\zeta^{-1} = \beta$) of multilayer MXene. The following resistance function behaviors represent the change in interphase property when the volume fraction of MXene fillers increases and is sufficient to form percolation microstructure. As a result, this resistance function will influence the predicted thermal conductivity and dielectric properties of MXene polymer composites when different sizes and layers of MXene fillers are considered.

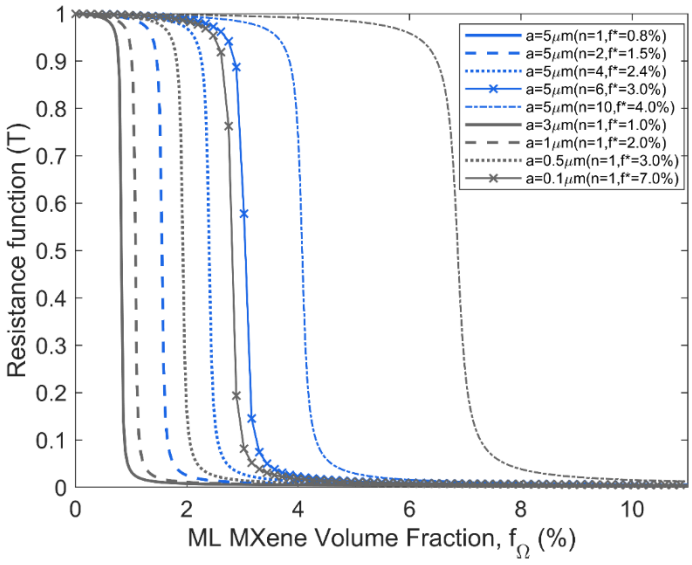

Figure S4. The resistance function as a function of volume fraction due to changes in size (a) and layers (n) of multilayer MXenes. In all this illustrated resistance functions, the resistance decomposition rate (γ_o) is chosen as 0.02.

3.7 Boundary conditions in FEM

3.7.1 Mechanical property evaluation

To evalute the longitudinal Young's modulus of RVE, a uniform normal strain (e_x) is applied on one surface normal to the x-direction (x=b) with the opposite surface (x=0) set to zero normal displacement (Figure 24). Simultaneously, the surface boundaries of RVE at y=0 and z=0 will have zero normal displacement while the remainder faces are allowed to freely deform due to Poisson's effect. The obtained reaction force on the fixed surface at x=0 is normalized with the surface area of xz plane (h·b) to evaluate the applied longitudinal stress (σ_x). By taking the ratio of σ_x and e_x, the longitudinal elastic modulus can be evaluated. To find the transverse (i.e., z-direction) Young's modulus of RVE, a uniform normal strain (e_z) is alternately applied on the surface normal to z-direction (z=h) while the opposite surface (z=0) is constrained to zero normal displacement. Now, the surface boundaries at x=0 and y=0 of RVE will have zero normal displacement while other boundaries are left unconstrained. The retrieved reaction force at the constrained surface (z=0) normal to applied strain is divided by the surface area of xy plane (b^2) to evaluate the applied transverse stress (σ_z). By taking the ratio of σ_z and e_z, the transverse elastic modulus of the RVE is computed.

3.7.2 Thermal and dielectric property evaluation

The longitudinal thermal conductivity (κ_P^x) of RVE can be evaluated by applying temperature difference (ΔT) between the surface boundaries at x=0 and x=b while other surface boundaries are assumed perfectly insulated (Figure 24b). Then, the total reaction heat flux in x-direction is obtained and normalized with the surface area of xz plane ($h \cdot b$) to recover the heat flux density (q_x) in x-direction. κ_P^x of the representative volume element can be evaluated using the anisotropic Fourier's law in Equation S59. Similarly, the transverse thermal conductivity (κ_P^z) is evaluated by applying temperature gradient (ΔT) between the surface boundaries at z=0 and z=L while other surface boundaries to have zero heat flux. Once again, the total reaction heat flux propagating in the z-direction is retrieved and divided by surface area of xy plane (b^2) to derive the heat flux density (q_z). By following Equation S60, the transverse thermal conductivity (κ_P^z) of the RVE is retrieved.

$$\kappa_P^x = q_x\left(\frac{b}{\Delta T}\right) \quad \text{S59}$$

$$\kappa_P^z = q_z\left(\frac{h}{\Delta T}\right) \quad \text{S60}$$

Determining the longitudinal (ε_P^x) and transverse (ε_P^z) dielectric property is identical to the steps taken for finding the anisotropic thermal conductivity of RVE. The main difference lies in replacing the notion of temperature difference, heat flux, and heat flux density as applied potential field (ΔV), electric flux, and electric flux density. This conversion is possible because the linear constitutive laws of transport properties have similar mathematical form. Hence, the formulae in Equation S59 and S60 can be converted to Equation S61 and S62, respectively. In Equation S61, the electric flux density (D_x) in x-direction needs to be obtained from FEM to evaluate ε_P^x. Similarly, in Equation S62, the electric flux density (D_z) in z-direction is retrived from FEM to find ε_P^z.

$$\varepsilon_P^x = D_x\left(\frac{b}{\Delta V}\right) \quad \text{S61}$$

$$\varepsilon_P^z = D_z\left(\frac{h}{\Delta V}\right) \quad \text{S62}$$

3.8 Multilayer MXene in hard or soft polymer matrix

Several atomic force microscopy experiments had shown that the measured elastic modulus of $Ti_3C_2T_x$ can range between 9 GPa to 70 GPa while density functional theory simulation had shown

that the elastic modulus of $Ti_3C_2T_x$ ranges several hundreds of GPa [225]. Hence, it is important to investigate if the following range of measured elastic modulus (9 Gpa – 70 GPa) of MXenes can influence the effective stiffness of MXPCs.

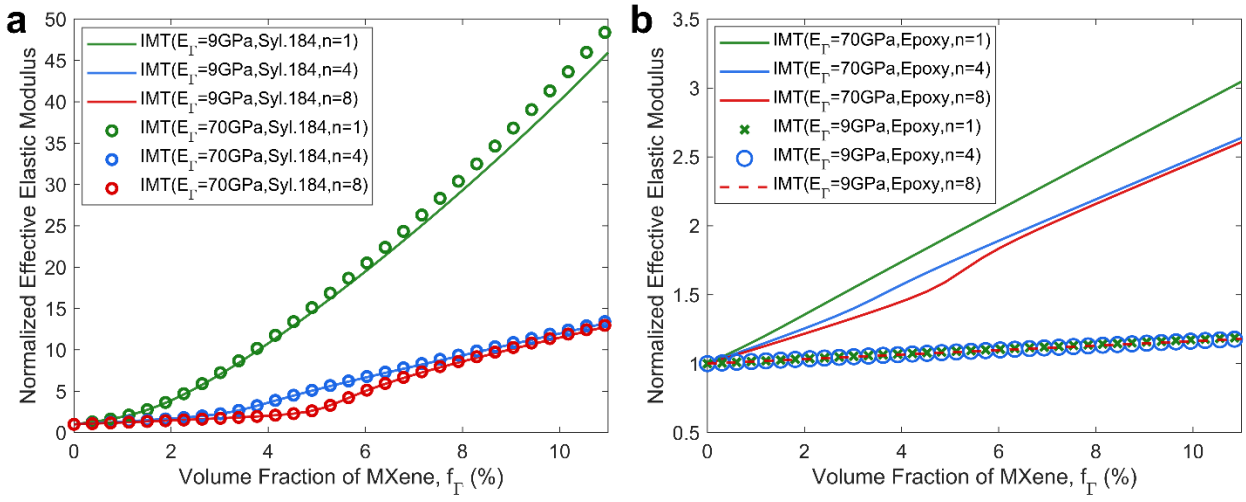

Figure S5. The effects of variation in elastic modulus and multilayer structure of MXene fillers on the predicted elastic modulus of (a) MXene-Sylgard 184 and (b) MXene-Epoxy composite. Both results assume the size ratio of embedded MXenes are fixed at $\alpha = 500$. Both the predicted elastic modulus of MXPCs in (a) and (b) are respectively normalized by the elastic modulus of unfilled Sylgard 184 and Epoxy polymer.

In Figure S5a, the predicted stiffness of MXene-Sylgard 184 when MXenes' elastic modulus is low (9 GPa) or high (70 GPa) are approximately similar. In addition, this mechanical behavior seems to occur regardless of the number of layers that are considered in the embedded MXenes despite all these fillers having the same lateral size (a=500). On the contrary, IMT model demonstrates that when the considered elastic modulus of MXene is high (70GPa), the predicted stiffness of MXene in Epoxy composite will be larger than the predicted stiffness of the same Epoxy composite that has low elastic modulus (9 GPa) MXenes (Figure S5b). Hence, this result shows that the predicted elastic modulus of MXene-Epoxy composite is less affected (negligible stiffness suppression effects) by the number of layers present in the embedded MXenes. Based on these comparisons, it can also be concurred that when the polymer matrix of MXPCs is stiff (E_m~3.5 GPa) such as epoxy, the stiffness of MXene fillers can more dominantly influence the final elastic modulus of MXPCs rather than the multilayer structure of MXenes. On the other hand, when the elastic modulus (E_m~1.5 MPa) of the polymer matrix (Sylgard 184) is low, the effective stiffness of MXPCs becomes more affected by the multilayer structure rather than the stiffness of the MXene fillers.

4. Supplemental Information for chapter 5

4.1 Prony series parameters of agarose gel and cancer cells

Table S7 tabulates the Prony series stress relaxation parameters of agarose gel obtained by non-linear fitting of stress relaxation test data. MDA-MB-231 cancer cells stress relaxation modulus is taken from Efremov et al., and rearranged into simplified Prony series expression (Equation 63).

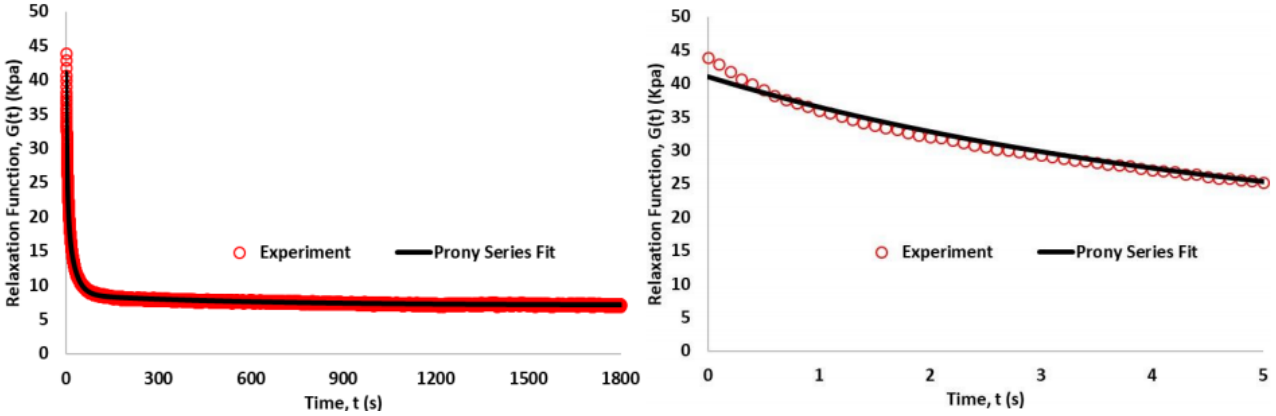

Figure S6. Prony series non-linear fitting on the truncated stress relaxation-time data of 3% agarose gel under 10% static displacement compression.

Table S7. The Prony series coefficients and time constants fitted with different applied quasi-static compressive displacement.

Static Disp. (um)	Strain, ϵ_o (%)	$\mathbf{G_o}$ **(KPa)**	$\mathbf{G_1}$ **(KPa)**	$\mathbf{G_2}$ **(KPa)**	$\mathbf{G_3}$ **(KPa)**	$\boldsymbol{\tau_1}$ **(s)**	$\boldsymbol{\tau_2}$ **(s)**	$\boldsymbol{\tau_3}$ **(s)**
50	2.5	29.5	2.53	15.81	4.6	84.04	8.2	0.53
200	10	41.03	1.55	13.43	18.97	545.09	23.96	4.24
300	15	143.65	24.02	40.39	44.22	580.51	115.1	11.89

Table S8: Prony series parameters obtained from relaxation test of 3 wt.% agarose gel at 25% strain and alongside its simplified Prony series of MDA-MB-231 taken from Efremov et al. [239].

Parameters	G_o (KPa)	G_1 (KPa)	G_2 (KPa)	G_3 (KPa)	τ_1 (s)	τ_2 (s)	τ_3 (s)
3% Agarose Gel	29.5	2.53	15.81	4.6	84.04	8.2	0.53
Parameters	G_o^c (KPa)	$G_1{}^c$(KPa)	N/A	N/A	β (s^{-1})	N/A	N/A
MDA -MB-231[159]	2	1	N/A	N/A	0.2	N/A	N/A

Shorthanded variables are introduced ($J, K, L, M, N, \hat{N}, P_i$ and M) to simplify Equation 69 into Equation S63. These shorthanded variables are expressed as the following. The numerator and denominator of Equation 69 are multiplied by J before simplified as Equation S71 and Equation S72, respectively.

$$G_T(s) = \frac{G_o^c(S+N)(G_oJ - P_1K - P_2L - P_3M)}{s\{Jm(S+\hat{N}) - V_c(s+\beta)(P_1K + P_2L + P_3M)\}} \quad \text{S63}$$

$$J = (s+\alpha_1)(s+\alpha_2)(s+\alpha_3) \quad \text{S64}$$

$$K = (s+\alpha_2)(s+\alpha_3) \quad \text{S65}$$

$$L = (s+\alpha_1)(s+\alpha_3) \quad \text{S66}$$

$$M = (s+\alpha_1)(s+\alpha_2) \quad \text{S67}$$

$$N = \beta - \frac{G_1^c}{G_o^c}\beta, \hat{N} = \beta - \frac{\beta V_g G_1^c}{V_g G_o^c + V - c\, G_o} \quad \text{S68}$$

$$P_i = G_i\alpha_i, i = 1,2,3 \quad \text{S69}$$

$$m = V_g G_o^c + V_c G_o \quad \text{S70}$$

$$(sG_oG_o^c + G_oG_o^c\beta - G_oG_1^c\beta)J - G_1\alpha_1(sG_o^c + \beta G_o^c - \beta G_1^c)K - G_2\alpha_2(sG_o^c + \beta G_o^c - \beta G_1^c)L - G_3\alpha_3(sG_o^c + \beta G_o^c - \beta G_1^c)M \quad \text{S71}$$

$$s\{J\left(V_g\, G_o^c + V_c\, G_o\right)\{s+\beta-\left(\beta V_g\, G_1^c\right)/\left(V_g\, G_o^c + V_c\, G_o\right)\} - V_c\,(s+\beta)\{G_1\,\alpha_1\,K + G_2\,\alpha_2\,L + G_3\,\alpha_3\,M\} \quad \text{S72}$$

With the parameters of Table S8 and volume fraction (V_c) of cells in agarose gel of 0.2%, we can input these values into Equation S71 and Equation S72 before obtaining the closed form partial fraction expressions shown in Equation S73with the help of residual functions in MATLAB. Inverse Laplace transformation of Equation S73 will produce Equation S74 which can be rearranged in the form of Prony series Equation S75 using the relationship enabled by Equation S76 and S77. To equate Equation S74 to the mathematical form of the Prony series (Equation S73), the relationship provided by Equation S76 and S77 is again referred. Eventually, the coefficients of the Prony series representing the effective stress relaxation modulus of layered cell-in-agarose gel composite are found in Table S9.

$$G_T(s) = \frac{6487.86}{s} + \frac{13426.51}{s+0.1275} + \frac{2467.27}{s+0.0118} + \frac{1956}{s+0.0951} + \frac{4370.83}{s+1.875} \quad \text{S73}$$

$$G_T(t) = G_o' + \sum_{i=1}^{n} G_i' e^{-\alpha' t} \quad \text{S74}$$

$$G_T(t) = G_{T_o} - \sum_{i=1}^{n} G_{T_i}(1 - e^{-\alpha_{T_i} t}) \quad \text{S75}$$

$$G_{T_o} = G_o' + \sum_{i=1}^{n} G_i' \quad \text{S76}$$

$$\alpha_{T_i} = \alpha', \qquad G_{T_i} = G_i' \quad \text{S77}$$

Table S9: Parameters of equivalent Prony series Equation S13 for effective stress relaxation modulus of layered agarose gel and cancer cell composite medium.

Parameters	$\mathbf{G_{T_o}}$ **(KPa)**	$\mathbf{G_{T_1}}$ **(KPa)**	$\mathbf{G_{T_2}}$**(KPa)**	$\mathbf{G_{T_3}}$ **(KPa)**	$\mathbf{G_{T_4}}$ **(KPa)**	$\boldsymbol{\tau_1}$ **(s)**	$\boldsymbol{\tau_2}$ **(s)**	$\boldsymbol{\tau_3}$ **(s)**	$\boldsymbol{\tau_4}$**(s)**
Layered 3% Agarose Gel +MDA-MB-231 Cells	28.71	13.43	4.371	2.467	1.956	7.843	0.533	84.75	10.52

4.2 Boltzmann Superposition Convolution Integral Solutions

The relationship of Stress-Strain in laplace domain because of laplace transform is as Equation S78 [253].

$$\sigma(s) = sG(s)\varepsilon(s) \tag{S78}$$

Where G(s) is the frequency domain of G(t), that is the Prony series shown in Equation S79 obtained by experimental measurements.

$$G(t) = G_o - \sum_{i=1}^{3} G_i\left(1 - e^{-\frac{t}{T_i}}\right) \tag{S79}$$

Taking the Laplace Transform of Equation S79, the complex modulus, $G^*(s) = s \cdot G(s)$ is determined and expressed as Equation S80.

$$G^*(s) = G_o - \sum_{i=1}^{3} G_i\left(1 - \frac{s}{s + \frac{1}{T_i}}\right) \tag{S80}$$

Next, take the laplace transform of variable strain function from Equation 61 and divide it by the total thickness (h_T) of the layered cell-in-gel composite to express the frequency domain of strain function (Equation S81).

$$\varepsilon(s) = \frac{\alpha}{2h}\left\{\frac{\omega}{s^2 + \omega^2} - \frac{\omega}{\left(s + \frac{1}{\tau_1}\right)^2 + \omega^2} + \frac{1}{s} - \frac{1}{s + \frac{1}{\tau_1}}\right\} + \frac{\beta}{h}\left\{1 - e^{-\frac{t}{\tau_2}}\right\} \tag{S81}$$

With these expressions, Equation S80 and Equation S81 into Equation S78 as Equation S75 in main text. There are four terms that need to be separated by partial fraction in Equation 73 to enable convenient Inverse laplace transformation. Hence, the following shorthand variables are introduced to simplify this partial fraction identification.

$$I_1 = \frac{s\omega}{\left(s + \frac{1}{T_i}\right)(s^2 + \omega^2)} \quad \text{S82}$$

$$I_2 = \frac{s\omega}{\left(s + \frac{1}{T_i}\right)\left(\left(s + \frac{1}{\tau_1}\right)^2 + \omega^2\right)} \quad \text{S83}$$

$$I_3 = \frac{s}{\left(s + \frac{1}{T_i}\right)\left(s + \frac{1}{\tau_1}\right)} \quad \text{S84}$$

$$I_4 = \frac{s}{\left(s + \frac{1}{T_i}\right)\left(s + \frac{1}{\tau_2}\right)} \quad \text{S85}$$

The partial fraction expressions for Equation S82 is Equation S86 with its constants a, b and c defined in Equation S87.

$$I_1 = \frac{a}{s + \frac{1}{T_i}} + \frac{bs + c}{s^2 + \omega^2} \quad \text{S86}$$

$$a = -\frac{\omega T_i}{\omega^2 T_i^2 + 1}, a = -b, c = \frac{\omega^3 T_i^2}{1 + \omega^2 T_i^2} \quad \text{S87}$$

$$I_2 = \frac{d}{s + \frac{1}{T_i}} + \frac{es + f}{\left(s + \frac{1}{\tau_1}\right)^2 + \omega^2} \quad \text{S88}$$

Equation S88 requires further algebraic manipulation for convenient Inverse Laplace transform as Equation S89. By partial fraction the coefficients d, e and f can be derived as Equation S90. Hence, the inverse Laplace Transform of Equation S88 becomes Equation S91. (Note to prevent confusion with exponent symbol $\boldsymbol{e}$ we substituted constant e in Equation S90 with -d). Now, only I_3 and I_4 terms remained to achieve the complete inverse laplace transform. Since these terms have similar algebraic form, we only need to conduct partial fraction for both I_3 and I_4 once which are solved using the solutions of Equation S93 and Equation S95, respectively.

$$e\left\{\frac{s + \frac{f}{e}}{\left(s + \frac{1}{\tau_1}\right)^2 + \omega^2}\right\} \quad \text{S89}$$

$$= e\left\{\frac{s + \frac{1}{\tau_1}}{\left(s + \frac{1}{\tau_1}\right)^2 + \omega^2} - \frac{1}{\tau_1 \omega}\frac{\omega}{\left(s + \frac{1}{\tau_1}\right)^2 + \omega^2} + \frac{f}{e\omega}\frac{\omega}{\left(s + \frac{1}{\tau_1}\right)^2 + \omega^2}\right\}$$

$$\frac{\frac{\omega}{\tau_1^2}+\omega^3}{\frac{1}{\tau_1^2}+\omega^2+\frac{\mu}{T_i}}, \qquad e=\frac{\frac{\omega}{T_i}}{\frac{1}{\tau_1^2}+\omega^2+\frac{\mu}{T_i}}, \qquad e=-d, \qquad \mu=\frac{1}{T_i}-\frac{2}{\tau_1}, \qquad \frac{f}{e}=T_i\left(\frac{1}{\tau_1^2}+\omega^2\right) \tag{S90}$$

$$I_2=-de^{-\frac{t}{\tau_1}}\cos(\omega t)+\frac{d}{\tau_1\omega}e^{-\frac{t}{\tau_1}}\sin(\omega t)+\frac{f}{\omega}e^{-\frac{t}{\tau_1}}\sin(\omega t) \tag{S91}$$

$$I_3=\frac{g}{s+\frac{1}{T_i}}+\frac{h}{s+\frac{1}{\tau_1}} \tag{S92}$$

$$g=\frac{\tau_1}{\tau_1-T_i}, h=\frac{T_i}{T_i-\tau_1} \tag{S93}$$

$$I_4=\frac{g'}{s+\frac{1}{T_i}}+\frac{h'}{s+\frac{1}{\tau_2}} \tag{S94}$$

$$g'=\frac{\tau_2}{\tau_2-T_i}, h'=\frac{T_i}{T_i-\tau_2} \tag{S95}$$

Finally, with this complete inverse laplace transform of the partial fractions, the full inverse the overall predicted time dependent stress σ(t) shown as Equation 74 in the main text is obtained.

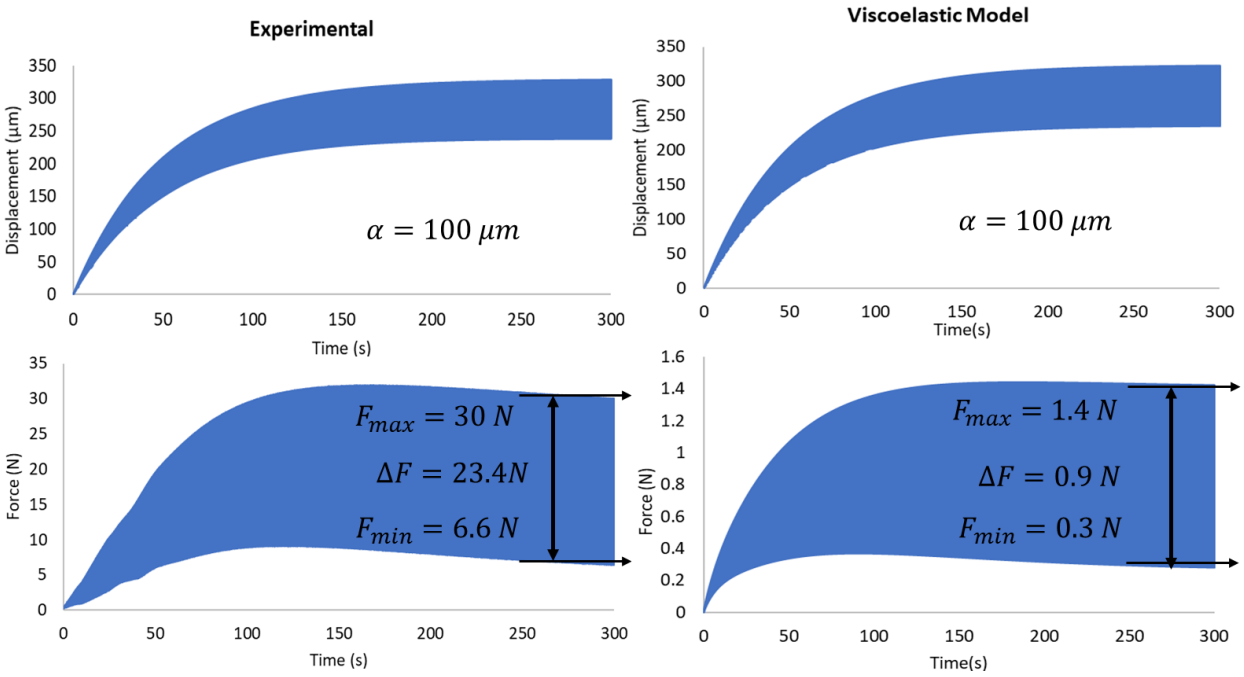

Figure S7. (Left) Experimentally measured displacement-time and force-time behavior of layered agarose gel and cells. (Right) Viscoelastic model prediction of force-time response under displacement amplitude α=100μm without BC consideration resulting in 20 time smaller ΔF prediction than experimental measurement.

4.3 Modifying Concentric Cylindrical Model (CCM) based on experimental setup.

- **Isotropic Hooke's Law in cylindrical coordinates**

$$\sigma_{rr} = \frac{E}{(1+v)(2v-1)}\{(v-1)e_{rr} - v(e_{\theta\theta} + e_{zz})\} \quad \text{S96}$$

$$\sigma_{\theta\theta} = \frac{E}{(1+v)(2v-1)}\{(v-1)e_{\theta\theta} - v(e_{rr} + e_{zz})\} \quad \text{S97}$$

$$\sigma_{zz} = \frac{E}{(v+1)(2v-1)}\{(v-1)e_{zz} - v(e_{rr} + e_{\theta\theta})\} \quad \text{S98}$$

- **Cauchy-Euler solution derivation**

We first take partial derivative of Equation S96 with respect to radius (r) to get Equation S100. Next, the subtraction of Equation S96 and Equation S97 shown in Equation S99 before substituted into Equation S80 to get Equation S102 after simplification.

$$\sigma_{rr} - \sigma_{\theta\theta} = \frac{E}{(v+1)(2v-1)}[(2v-1)e_{rr} + (1-2v)e_{\theta\theta}] \quad = \frac{E}{v+1}\{e_{rr} - e_{\theta\theta}\} \quad \text{S99}$$

$$\sigma_{rr,r} = \frac{E}{(v+1)(2v-1)}\left\{(v-1)\frac{\partial^2 u_r}{\partial r^2} - v\left(-\frac{u_r}{r^2} + \frac{1}{r}\frac{\partial u_r}{\partial r}\right)\right\} \quad \text{S100}$$

$$\frac{v-1}{2v-1}\frac{\partial^2 u_r}{\partial r}-\frac{v}{r(2v-1)}\frac{\partial u_r}{\partial r}+\frac{v}{2v-1}\frac{u_r}{r^2}+\frac{1}{r}\frac{\partial u_r}{\partial r}-\frac{u_r}{r^2}=0 \quad \text{S101}$$

$$\frac{\partial^2 u_r}{\partial r^2}+\frac{1}{r}\frac{\partial u_r}{\partial r}-\frac{u_r}{r^2}=0 \quad \text{S102}$$

$$u_r = r^m \quad \text{S103}$$

The 2nd order ordinary differential equation (ODE) of Equation S102 by using Cauchy-Euler Solution Equation S104 where m is the eigenvalue Equation S106 of the ODE and solving Equation S102 with Equation S104 provide the fundamental solution of Equation S107 that give rise to Equation 80 showing the displacement expression for the internal and external cylinder region.

$$m(m-1)r^{m-2}+\frac{1}{r}mr^{m-1}-\frac{r^m}{r^2}=0 \quad \text{S104}$$

$$m_{1,2}=1,-1 \quad \text{S105}$$

$$u_r = C_1 r+\frac{C_2}{r} \quad \text{S106}$$

- **Apply boundary conditions on modified CCM**

To complete the displacement solution, the following boundary condition (BC) of $u_r^I(r=0)=0$ needs to be enforced. Hence, C_2^I is set to zero to prevent strain singularity at r=0. Another BC is displacement continuity at the boundary between internal and external region (r=b) where the displacement change need to be continuous [i.e., $u_r^I(r=b)=u_r^P(r=b)$]to finally retrieve the following relationship in Equation S107.

$$C_1^I = C_1^p(1-a^2b^{-2}) \quad \text{S107}$$

To explicitly find C_1^I and C_1^P, additional BC need to be considered which is the stress continuity at r=b using Equation S109 with ϵ is the input strain applied by the platen in the z direction.

$$\sigma_{rr}^I(r=b)=\sigma_{rr}^P(r=b) \quad \text{S108}$$

$$\sigma_{rr}^I=\frac{E}{(v+1)(2v-1)}\left\{(v-1)\frac{\partial u_r^I}{\partial r}|_{r=b}-\frac{v}{r}u_r^I|_b-v\epsilon\right\} \quad \text{S109}$$

$$\sigma_{rr}^P=\frac{E}{(v+1)(2v-1)}\left\{(v-1)\frac{\partial u_r^P}{\partial r}-\frac{v}{r}u_r^P-v\epsilon_z^P\right\} \quad \text{S110}$$

After that, we need to find the strain expansion (i.e., ϵ_z^P) between the platen and dish (external circular region) shown in Equation S66 knowing that there is zero out of plane stress (σ_{zz}^E) at Z = h_T. This is done by substituting Equation S98 (stiffness relation) into Equation S111 and equating the stress in z direction as zero because of plane stress condition (Equation S112).

$$\sigma_{zz}^P = 0 = \frac{E}{(v+1)(2v-1)}\left\{(v-1)\epsilon_z^P - v\frac{\partial u_r^P}{\partial r} - \frac{v}{r}u_r^P\right\} \quad \text{S111}$$

$$\epsilon_z^P = 2\frac{vC_1^P}{v-1} \quad \text{S112}$$

Next, Equation 80 from the main text is substituted into strain-displacement relation (Equation 79) to be substituted into Equation S110and Equation S111. As a result, this allows us to compute the radial stresses for the inner (Equation S114) and outer (Equation S115) cylinder region of the compressed cell-in-gel composite.

$$\sigma_{rr}^I = \frac{E}{(v+1)(2v-1)}\{(v-1)C_1^I - C_1^I v - v\epsilon\} \quad \text{S113}$$

$$\sigma_{rr}^P = \frac{EC_1^P}{(v+1)(2v-1)}\{(1+v) - (-a^2 + va^2)r^{-2}\} \quad \text{S114}$$

The following radial stresses need to satisfy stress continuity at (r=b) described by Equation S109 to find C_1^P coefficient.

$$C_1^P\left\{(-1+k+kv) - \frac{a^2}{b^2}\left(-\frac{1}{v}\right) - k(-1+v)\frac{a^2}{b^2}\right\} = v\epsilon \quad \text{S115}$$

Equation S116 allows us to find $C_1{}^P$ where in this expression, k=(2v-1)/(v-1). Next, we simplify Equation S116 to get Equation 84 before obtaining Equation 83 from the expression of Equation S108. Similarly, the expressions of radial stress σ_{rr} (i.e., Equation S118 and S119), out of plane stress σ_{zz} (Equation S116 and Equation S117), and angular stress $\sigma_{\theta\theta}$ (Equation S120 and S121) in the internal (I) and external (P) cylinder region are eventually obtained to formalize the overall concentric cylinder model.

$$\sigma_{zz}^I = \frac{E}{(v+1)(2v-1)}\{(v-1) - 2vC_1^I\}\epsilon \quad \text{S116}$$

$$\sigma_{zz}^p = 0 \quad \text{S117}$$

$$\sigma_{rr}^{I} = \frac{E}{(v+1)(2v-1)}\{-C_1^I - v\}\epsilon \quad \text{S118}$$

$$\sigma_{rr}^{p} = -\frac{EC_1^p}{v^2-1}\left\{(1+v) - (-a^2 + va^2)\frac{r^{-1}}{r}\right\}\epsilon \quad \text{S119}$$

$$\sigma_{\theta\theta}^{I} = \frac{E}{(v+1)(2v-1)}\{-C_1^I - v\}\epsilon \quad \text{S120}$$

$$\sigma_{\theta\theta}^{p} = \frac{E}{(v+1)(2v-1)}\left\{\frac{v-1}{r}\left(C_1^p r - C_1^p a^2 r^{-1}\right)\epsilon - v\left(C_1^p + C_1^p a^2\frac{r^{-1}}{r}\right)\epsilon - v\epsilon_z^p\right\} \quad \text{S121}$$

Reference

[1] C. Chiew, M.J. Morris, M.H. Malakooti, Functional liquid metal nanoparticles: synthesis and applications, Mater. Adv. 2 (2021) 7799–7819. https://doi.org/10.1039/D1MA00789K.

[2] C. Chiew, M.H. Malakooti, A double inclusion model for liquid metal polymer composites, Compos Sci Technol. 208 (2021) 108752. https://doi.org/10.1016/j.compscitech.2021.108752.

[3] C. Majidi, Soft-Matter Engineering for Soft Robotics, Adv Mater Technol. 4 (2019) 1800477. https://doi.org/10.1002/admt.201800477.

[4] W.R.K. Illeperuma, J.-Y. Sun, Z. Suo, J.J. Vlassak, Fiber-reinforced tough hydrogels, Extreme Mech Lett. 1 (2014) 90–96. https://doi.org/10.1016/j.eml.2014.11.001.

[5] J.M. Mansour, Biomechanics of cartilage, in: Kinesiology: The Mechanics and Pathomechanics of Human Movement, 2003: pp. 66–79.

[6] F. Yang, J. Zhao, W.J. Koshut, J. Watt, J.C. Riboh, K. Gall, B.J. Wiley, A Synthetic Hydrogel Composite with the Mechanical Behavior and Durability of Cartilage, Adv Funct Mater. 30 (2020) 2003451. https://doi.org/https://doi.org/10.1002/adfm.202003451.

[7] R.W. Style, R. Tutika, J.Y. Kim, M.D. Bartlett, Solid–Liquid Composites for Soft Multifunctional Materials, Adv Funct Mater. 31 (2021) 2005804. https://doi.org/10.1002/adfm.202005804.

[8] N. Kazem, T. Hellebrekers, C. Majidi, Soft Multifunctional Composites and Emulsions with Liquid Metals, Advanced Materials. 29 (2017) 1605985. https://doi.org/10.1002/adma.201605985.

[9] M.H. Malakooti, M.R. Bockstaller, K. Matyjaszewski, C. Majidi, Liquid metal nanocomposites, Nanoscale Adv. 2 (2020) 2668–2677. https://doi.org/10.1039/D0NA00148A.

[10] M. Carey, M.W. Barsoum, MXene polymer nanocomposites: a review, Mater Today Adv. 9 (2021) 100120. https://doi.org/10.1016/J.MTADV.2020.100120.

[11] K. Gong, K. Zhou, X. Qian, C. Shi, B. Yu, MXene as emerging nanofillers for high-performance polymer composites: A review, Compos B Eng. 217 (2021) 108867. https://doi.org/10.1016/J.COMPOSITESB.2021.108867.

[12] R. Tutika, A.B.M.T. Haque, M.D. Bartlett, Self-healing liquid metal composite for reconfigurable and recyclable soft electronics, Commun Mater. 2 (2021) 64. https://doi.org/10.1038/s43246-021-00169-4.

[13] Y. Ohm, C. Pan, M.J. Ford, X. Huang, J. Liao, C. Majidi, An electrically conductive silver–polyacrylamide–alginate hydrogel composite for soft electronics, Nat Electron. 4 (2021) 185–192. https://doi.org/10.1038/s41928-021-00545-5.

[14] J.-E. Park, H.S. Kang, J. Baek, T.H. Park, S. Oh, H. Lee, M. Koo, C. Park, Rewritable, Printable Conducting Liquid Metal Hydrogel, ACS Nano. 13 (2019) 9122–9130. https://doi.org/10.1021/acsnano.9b03405.

[15] Z. Wang, Y. Liu, D. Zhang, K. Zhang, C. Gao, Y. Wu, Tough, stretchable and self-healing C-MXenes/PDMS conductive composites as sensitive strain sensors, Compos Sci Technol. 216 (2021) 109042. https://doi.org/10.1016/J.COMPSCITECH.2021.109042.

[16] B. Qi Yu Chan, Z. Wei Kenny Low, S. Jun Wen Heng, S. Yin Chan, C. Owh, X. Jun Loh, Recent Advances in Shape Memory Soft Materials for Biomedical Applications, ACS Applied Materials & Interfaces. 8 (2016) 10070–10087. https://doi.org/10.1021/acsami.6b01295.

[17] Q. Meng, J. Hu, A review of shape memory polymer composites and blends, Compos Part A Appl Sci Manuf. 40 (2009) 1661–1672. https://doi.org/10.1016/J.COMPOSITESA.2009.08.011.

[18] T.A. Kent, M.J. Ford, E.J. Markvicka, C. Majidi, Soft actuators using liquid crystal elastomers with encapsulated liquid metal joule heaters, Multifunctional Materials. (2020). https://doi.org/10.1088/2399-7532/ab835c.

[19] Y. Wang, J. Liu, S. Yang, Multi-functional liquid crystal elastomer composites, Appl Phys Rev. 9 (2022) 011301. https://doi.org/10.1063/5.0075471.

[20] J. Zhang, Y. Guo, W. Hu, R.H. Soon, Z.S. Davidson, M. Sitti, Liquid Crystal Elastomer-Based Magnetic Composite Films for Reconfigurable Shape-Morphing Soft Miniature Machines, Advanced Materials. 33 (2021) 2006191. https://doi.org/10.1002/adma.202006191.

[21] S. V. Ahir, Y.Y. Huang, E.M. Terentjev, Polymers with aligned carbon nanotubes: Active composite materials, Polymer (Guildf). 49 (2008) 3841–3854. https://doi.org/10.1016/J.POLYMER.2008.05.005.

[22] M.P. Wolf, G.B. Salieb-Beugelaar, P. Hunziker, PDMS with designer functionalities—Properties, modifications strategies, and applications, Prog Polym Sci. 83 (2018) 97–134. https://doi.org/10.1016/J.PROGPOLYMSCI.2018.06.001.

[23] S. Wan, J. Peng, L. Jiang, Q. Cheng, Bioinspired Graphene-Based Nanocomposites and Their Application in Flexible Energy Devices, Advanced Materials. 28 (2016) 7862–7898. https://doi.org/10.1002/adma.201601934.

[24] W. Yang, J.-J. Liu, L.-L. Wang, W. Wang, A.C.Y. Yuen, S. Peng, B. Yu, H.-D. Lu, G.H. Yeoh, C.-H. Wang, Multifunctional MXene/natural rubber composite films with exceptional flexibility and durability, Compos B Eng. 188 (2020) 107875. https://doi.org/10.1016/j.compositesb.2020.107875.

[25] Z. Han, A. Fina, Thermal conductivity of carbon nanotubes and their polymer nanocomposites: A review, Prog Polym Sci. 36 (2011) 914–944. https://doi.org/10.1016/J.PROGPOLYMSCI.2010.11.004.

[26] L. Bokobza, C. Belin, Effect of strain on the properties of a styrene–butadiene rubber filled with multiwall carbon nanotubes, J Appl Polym Sci. 105 (2007) 2054–2061. https://doi.org/10.1002/app.26153.

[27] L. Cai, L. Song, P. Luan, Q. Zhang, N. Zhang, Q. Gao, D. Zhao, X. Zhang, M. Tu, F. Yang, W. Zhou, Q. Fan, J. Luo, W. Zhou, P.M. Ajayan, S. Xie, Super-stretchable, Transparent Carbon Nanotube-Based Capacitive Strain Sensors for Human Motion Detection, Sci Rep. 3 (2013) 3048. https://doi.org/10.1038/srep03048.

[28] R.C. Chiechi, E.A. Weiss, M.D. Dickey, G.M. Whitesides, Eutectic gallium-indium (EGaIn): A moldable liquid metal for electrical characterization of self-assembled monolayers, Angewandte Chemie - International Edition. (2008). https://doi.org/10.1002/anie.200703642.

[29] B. Kim, J. Jang, I. You, J. Park, S.B. Shin, G. Jeon, J.K. Kim, U. Jeong, Interfacing liquid metals with stretchable metal conductors, ACS Appl Mater Interfaces. (2015). https://doi.org/10.1021/am508899z.

[30] A. Miner, U. Ghoshal, Cooling of high-power-density microdevices using liquid metal coolants, Appl Phys Lett. (2004). https://doi.org/10.1063/1.1772862.

[31] X.-D. Zhang, X.-H. Yang, Y.-X. Zhou, W. Rao, J.-Y. Gao, Y.-J. Ding, Q.-Q. Shu, J. Liu, Experimental investigation of galinstan based minichannel cooling for high heat flux and large heat power thermal management, Energy Convers Manag. 185 (2019) 248–258. https://doi.org/10.1016/j.enconman.2019.02.010.

[32] J.-H. Kim, S. Kim, J.-H. So, K. Kim, H.-J. Koo, Cytotoxicity of Gallium–Indium Liquid Metal in an Aqueous Environment, ACS Appl Mater Interfaces. 10 (2018) 17448–17454. https://doi.org/10.1021/acsami.8b02320.

[33] Y. Plevachuk, V. Sklyarchuk, S. Eckert, G. Gerbeth, R. Novakovic, Thermophysical properties of the liquid Ga-In-Sn eutectic alloy, J Chem Eng Data. (2014). https://doi.org/10.1021/je400882q.

[34] D. Zrnic, D.S. Swatik, On the resistivity and surface tension of the eutectic alloy of gallium and indium, Journal of the Less Common Metals. 18 (1969) 67–68. https://doi.org/10.1016/0022-5088(69)90121-0.

[35] S. Chen, H.Z. Wang, R.Q. Zhao, W. Rao, J. Liu, Liquid Metal Composites, Matter. 2 (2020) 1446–1480. https://doi.org/10.1016/j.matt.2020.03.016.

[36] K. Kalantar-Zadeh, J. Tang, T. Daeneke, A.P. O'Mullane, L.A. Stewart, J. Liu, C. Majidi, R.S. Ruoff, P.S. Weiss, M.D. Dickey, Emergence of Liquid Metals in Nanotechnology, ACS Nano. 13 (2019) 7388–7395. https://doi.org/10.1021/acsnano.9b04843.

[37] Z.J. Farrell, C. Tabor, Control of Gallium Oxide Growth on Liquid Metal Eutectic Gallium/Indium Nanoparticles via Thiolation, Langmuir. 34 (2018) 234–240. https://doi.org/10.1021/acs.langmuir.7b03384.

[38] T. Daeneke, K. Khoshmanesh, N. Mahmood, I.A. De Castro, D. Esrafilzadeh, S.J. Barrow, M.D. Dickey, K. Kalantar-Zadeh, Liquid metals: Fundamentals and applications in chemistry, Chem Soc Rev. (2018). https://doi.org/10.1039/c7cs00043j.

[39] Y. Yang, S. Sun, S.-Y. Tang, W. Li, S. Zhang, Viscoelastic Properties of Gallium-indium Alloy, Applied Rheology. 28 (2018) 201842903. https://doi.org/https://doi.org/10.3933/applrheol-28-42903.

[40] M.R. Khan, C.B. Eaker, E.F. Bowden, M.D. Dickey, Giant and switchable surface activity of liquid metal via surface oxidation, Proceedings of the National Academy of Sciences. 111 (2014) 14047–14051. https://doi.org/10.1073/pnas.1412227111.

[41] C. Ladd, J.H. So, J. Muth, M.D. Dickey, 3D printing of free standing liquid metal microstructures, Advanced Materials. (2013). https://doi.org/10.1002/adma.201301400.

[42] F.C. Simeone, H.J. Yoon, M.M. Thuo, J.R. Barber, B. Smith, G.M. Whitesides, Defining the Value of Injection Current and Effective Electrical Contact Area for EGaIn-Based Molecular Tunneling Junctions, J Am Chem Soc. 135 (2013) 18131–18144. https://doi.org/10.1021/ja408652h.

[43] J. Chen, T.J. Giroux, Y. Nguyen, A.A. Kadoma, B.S. Chang, B. VanVeller, M.M. Thuo, Understanding interface (odd–even) effects in charge tunneling using a polished EGaIn electrode, Phys. Chem. Chem. Phys. 20 (2018) 4864–4878. https://doi.org/10.1039/C7CP07531F.

[44] S. Park, S. Kang, H.J. Yoon, Power Factor of One Molecule Thick Films and Length Dependence, ACS Cent Sci. 5 (2019) 1975–1982. https://doi.org/10.1021/acscentsci.9b01042.

[45] S. Park, H.J. Yoon, New Approach for Large-Area Thermoelectric Junctions with a Liquid Eutectic Gallium–Indium Electrode, Nano Lett. 18 (2018) 7715–7718. https://doi.org/10.1021/acs.nanolett.8b03404.

[46] S. Park, J. Jang, H.J. Yoon, Validating the Mott Formula with Self-Assembled Monolayer (SAM)-Based Large-Area Junctions: Effect of Length, Backbone, Spacer, Substituent, and Electrode on the Thermopower of SAMs, The Journal of Physical Chemistry C. 125 (2021) 20035–20047. https://doi.org/10.1021/acs.jpcc.1c05623.

[47] R. Rao, K.G. Eyink, B. Maruyama, Single-walled carbon nanotube growth from liquid gallium and indium, Carbon N Y. 48 (2010) 3971–3973. https://doi.org/10.1016/j.carbon.2010.06.065.

[48] M. Mousavi, M.B. Ghasemian, J. Han, Y. Wang, R. Abbasi, J. Yang, J. Tang, S.A. Idrus-Saidi, X. Guan, M.J. Christoe, S. Merhebi, C. Zhang, J. Tang, R. Jalili, T. Daeneke, T. Wu, K. Kalantar-Zadeh, M. Mayyas, Bismuth telluride topological insulator synthesized using liquid metal alloys: Test of NO2 selective sensing, Appl Mater Today. 22 (2021) 100954. https://doi.org/10.1016/j.apmt.2021.100954.

[49] H. Khan, N. Mahmood, A. Zavabeti, A. Elbourne, Md.A. Rahman, B.Y. Zhang, V. Krishnamurthi, P. Atkin, M.B. Ghasemian, J. Yang, G. Zheng, A.R. Ravindran, S. Walia, L. Wang, S.P. Russo, T. Daeneke, Y. Li, K. Kalantar-Zadeh, Liquid metal-based synthesis of high performance monolayer SnS piezoelectric nanogenerators, Nat Commun. 11 (2020) 3449. https://doi.org/10.1038/s41467-020-17296-0.

[50] D.P. Parekh, C. Ladd, L. Panich, K. Moussa, M.D. Dickey, 3D printing of liquid metals as fugitive inks for fabrication of 3D microfluidic channels, Lab Chip. (2016). https://doi.org/10.1039/c6lc00198j.

[51] J.N. Hohman, M. Kim, G.A. Wadsworth, H.R. Bednar, J. Jiang, M.A. LeThai, P.S. Weiss, Directing Substrate Morphology via Self-Assembly: Ligand-Mediated Scission of Gallium–Indium Microspheres to the Nanoscale, Nano Lett. 11 (2011) 5104–5110. https://doi.org/10.1021/nl202728j.

[52] Y. Lin, Y. Liu, J. Genzer, M.D. Dickey, Shape-transformable liquid metal nanoparticles in aqueous solution, Chem. Sci. 8 (2017) 3832–3837. https://doi.org/10.1039/C7SC00057J.

[53] Y. Liu, W. Zhang, H. Wang, Synthesis and Application of Core-Shell Liquid Metal Particles: A Perspective of Surface Engineering, Mater. Horiz. (2020). https://doi.org/10.1039/D0MH01117G.

[54] W. Zhang, J.Z. Ou, S.-Y. Tang, V. Sivan, D.D. Yao, K. Latham, K. Khoshmanesh, A. Mitchell, A.P. O'Mullane, K. Kalantar-zadeh, Liquid Metal/Metal Oxide Frameworks, Adv Funct Mater. 24 (2014) 3799–3807. https://doi.org/10.1002/adfm.201304064.

[55] L. Ren, J. Zhuang, G. Casillas, H. Feng, Y. Liu, X. Xu, Y. Liu, J. Chen, Y. Du, L. Jiang, S.X. Dou, Nanodroplets for Stretchable Superconducting Circuits, Adv Funct Mater. 26 (2016) 8111–8118. https://doi.org/10.1002/adfm.201603427.

[56] M.H. Malakooti, N. Kazem, J. Yan, C. Pan, E.J. Markvicka, K. Matyjaszewski, C. Majidi, Liquid Metal Supercooling for Low-Temperature Thermoelectric Wearables, Adv Funct Mater. 29 (2019) 1906098. https://doi.org/10.1002/adfm.201906098.

[57] A. Yamaguchi, Y. Mashima, T. Iyoda, Reversible Size Control of Liquid-Metal Nanoparticles under Ultrasonication, Angewandte Chemie International Edition. 54 (2015) 12809–12813. https://doi.org/10.1002/anie.201506469.

[58] Y. Lin, J. Genzer, W. Li, R. Qiao, M.D. Dickey, S.-Y. Tang, Sonication-enabled rapid production of stable liquid metal nanoparticles grafted with poly(1-octadecene-alt-maleic anhydride) in aqueous solutions, Nanoscale. 10 (2018) 19871–19878. https://doi.org/10.1039/C8NR05600E.

[59] A. Fassler, C. Majidi, Liquid-Phase Metal Inclusions for a Conductive Polymer Composite, Advanced Materials. 27 (2015) 1928–1932. https://doi.org/10.1002/adma.201405256.

[60] M.D. Bartlett, A. Fassler, N. Kazem, E.J. Markvicka, P. Mandal, C. Majidi, Stretchable, High- k Dielectric Elastomers through Liquid-Metal Inclusions, Advanced Materials. 28 (2016) 3726–3731. https://doi.org/10.1002/adma.201506243.

[61] E.J. Markvicka, M.D. Bartlett, X. Huang, C. Majidi, An autonomously electrically self-healing liquid metal-elastomer composite for robust soft-matter robotics and electronics, Nat Mater. (2018). https://doi.org/10.1038/s41563-018-0084-7.

[62] I.D. Tevis, L.B. Newcomb, M. Thuo, Synthesis of Liquid Core–Shell Particles and Solid Patchy Multicomponent Particles by Shearing Liquids Into Complex Particles (SLICE), Langmuir. 30 (2014) 14308–14313. https://doi.org/10.1021/la5035118.

[63] S. Çınar, I.D. Tevis, J. Chen, M. Thuo, Mechanical Fracturing of Core-Shell Undercooled Metal Particles for Heat-Free Soldering, Sci Rep. 6 (2016) 21864. https://doi.org/10.1038/srep21864.

[64] R. Tutika, S. Kmiec, A.B.M.T. Haque, S.W. Martin, M.D. Bartlett, Liquid Metal–Elastomer Soft Composites with Independently Controllable and Highly Tunable Droplet Size and Volume Loading, ACS Appl Mater Interfaces. 11 (2019) 17873–17883. https://doi.org/10.1021/acsami.9b04569.

[65] C. Pan, E.J. Markvicka, M.H. Malakooti, J. Yan, L. Hu, K. Matyjaszewski, C. Majidi, A Liquid-Metal–Elastomer Nanocomposite for Stretchable Dielectric Materials, Advanced Materials. 31 (2019) 1900663. https://doi.org/10.1002/adma.201900663.

[66] J.J. Chang, A. Martin, C. Du, A.M. Pauls, M. Thuo, Heat-Free Biomimetic Metal Molding on Soft Substrates, Angewandte Chemie International Edition. 59 (2020) 16346–16351. https://doi.org/https://doi.org/10.1002/anie.202008621.

[67] A. Martin, B.S. Chang, Z. Martin, D. Paramanik, C. Frankiewicz, S. Kundu, I.D. Tevis, M. Thuo, Heat-Free Fabrication of Metallic Interconnects for Flexible/Wearable Devices, Adv Funct Mater. 29 (2019) 1903687. https://doi.org/https://doi.org/10.1002/adfm.201903687.

[68] J. Yan, X. Zhang, Y. Liu, Y. Ye, J. Yu, Q. Chen, J. Wang, Y. Zhang, Q. Hu, Y. Kang, M. Yang, Z. Gu, Shape-controlled synthesis of liquid metal nanodroplets for photothermal therapy, Nano Res. 12 (2019) 1313–1320. https://doi.org/10.1007/s12274-018-2262-y.

[69] S.A. Chechetka, Y. Yu, X. Zhen, M. Pramanik, K. Pu, E. Miyako, Light-driven liquid metal nanotransformers for biomedical theranostics, Nat Commun. 8 (2017) 15432. https://doi.org/10.1038/ncomms15432.

[70] Y. Lu, Y. Lin, Z. Chen, Q. Hu, Y. Liu, S. Yu, W. Gao, M.D. Dickey, Z. Gu, Enhanced Endosomal Escape by Light-Fueled Liquid-Metal Transformer, Nano Lett. 17 (2017) 2138–2145. https://doi.org/10.1021/acs.nanolett.6b04346.

[71] L. Castilla-Amorós, D. Stoian, J.R. Pankhurst, S.B. Varandili, R. Buonsanti, Exploring the chemical reactivity of gallium liquid metal nanoparticles in galvanic replacement, J Am Chem Soc. (2020). https://doi.org/10.1021/jacs.0c09458.

[72] P. Fan, Z. Sun, Y. Wang, H. Chang, P. Zhang, S. Yao, C. Lu, W. Rao, J. Liu, Nano liquid metal for the preparation of a thermally conductive and electrically insulating material with high stability, RSC Adv. (2018). https://doi.org/10.1039/c8ra00262b.

[73] J. Mingear, Z. Farrell, D. Hartl, C. Tabor, Gallium–indium nanoparticles as phase change material additives for tunable thermal fluids, Nanoscale. 13 (2021) 730–738. https://doi.org/10.1039/D0NR06526A.

[74] M.J. Ford, M. Palaniswamy, C.P. Ambulo, T.H. Ware, C. Majidi, Size of liquid metal particles influences actuation properties of a liquid crystal elastomer composite, Soft Matter. 16 (2020) 5878–5885. https://doi.org/10.1039/D0SM00278J.

[75] N. Kazem, M.D. Bartlett, C. Majidi, Extreme Toughening of Soft Materials with Liquid Metal, Advanced Materials. 30 (2018) 1706594. https://doi.org/10.1002/adma.201706594.

[76] H. Wang, Y. Yao, Z. He, W. Rao, L. Hu, S. Chen, J. Lin, J. Gao, P. Zhang, X. Sun, X. Wang, Y. Cui, Q. Wang, S. Dong, G. Chen, J. Liu, A Highly Stretchable Liquid Metal Polymer as Reversible Transitional Insulator and Conductor, Advanced Materials. (2019). https://doi.org/10.1002/adma.201901337.

[77] M.J. Ford, D.K. Patel, C. Pan, S. Bergbreiter, C. Majidi, Controlled Assembly of Liquid Metal Inclusions as a General Approach for Multifunctional Composites, Advanced Materials. 32 (2020) 2002929. https://doi.org/10.1002/adma.202002929.

[78] N.J. Morris, Z.J. Farrell, C.E. Tabor, Chemically modifying the mechanical properties of core–shell liquid metal nanoparticles, Nanoscale. 11 (2019) 17308–17318. https://doi.org/10.1039/C9NR06369B.

[79] J.W. Boley, E.L. White, R.K. Kramer, Mechanically Sintered Gallium-Indium Nanoparticles, Advanced Materials. 27 (2015) 2355–2360. https://doi.org/10.1002/adma.201404790.

[80] B. Abismaïl, J.P. Canselier, A.M. Wilhelm, H. Delmas, C. Gourdon, Emulsification by ultrasound: drop size distribution and stability, Ultrason Sonochem. 6 (1999) 75–83. https://doi.org/10.1016/S1350-4177(98)00027-3.

[81] H. Lu, S.-Y. Tang, Z. Dong, D. Liu, Y. Zhang, C. Zhang, G. Yun, Q. Zhao, K. Kalantar-Zadeh, R. Qiao, W. Li, Dynamic Temperature Control System for the Optimized Production of Liquid Metal Nanoparticles, ACS Appl Nano Mater. 3 (2020) 6905–6914. https://doi.org/10.1021/acsanm.0c01257.

[82] J. He, F. Shi, J. Wu, J. Ye, Shape Transformation Mechanism of Gallium–Indium Alloyed Liquid Metal Nanoparticles, Adv Mater Interfaces. 8 (2021) 2001874. https://doi.org/10.1002/admi.202001874.

[83] Y. Lin, C. Cooper, M. Wang, J.J. Adams, J. Genzer, M.D. Dickey, Handwritten, Soft Circuit Boards and Antennas Using Liquid Metal Nanoparticles, Small. 11 (2015) 6397–6403. https://doi.org/10.1002/smll.201502692.

[84] M. Zadan, M.H. Malakooti, C. Majidi, Soft and Stretchable Thermoelectric Generators Enabled by Liquid Metal Elastomer Composites, ACS Appl Mater Interfaces. 12 (2020) 17921–17928. https://doi.org/10.1021/acsami.9b19837.

[85] M. Zadan, C. Chiew, C. Majidi, M.H. Malakooti, Liquid metal architectures for soft and wearable energy harvesting devices, Multifunctional Materials. 4 (2021) 012001. https://doi.org/10.1088/2399-7532/abd4f0.

[86] H. Bark, M.W.M. Tan, G. Thangavel, P.S. Lee, Deformable High Loading Liquid Metal Nanoparticles Composites for Thermal Energy Management, Adv Energy Mater. 11 (2021) 2101387. https://doi.org/10.1002/aenm.202101387.

[87] M. Naguib, V.N. Mochalin, M.W. Barsoum, Y. Gogotsi, 25th Anniversary Article: MXenes: A New Family of Two-Dimensional Materials, Advanced Materials. 26 (2014) 992–1005. https://doi.org/10.1002/adma.201304138.

[88] C. Ma, M.-G. Ma, C. Si, X.-X. Ji, P. Wan, Flexible MXene-Based Composites for Wearable Devices, Adv Funct Mater. 31 (2021) 2009524. https://doi.org/10.1002/adfm.202009524.

[89] Y. Wang, Y. Yue, F. Cheng, Y. Cheng, B. Ge, N. Liu, Y. Gao, Ti3C2Tx MXene-Based Flexible Piezoresistive Physical Sensors, ACS Nano. 16 (2022) 1734–1758. https://doi.org/10.1021/acsnano.1c09925.

[90] K. Nasrin, V. Sudharshan, K. Subramani, M. Sathish, Insights into 2D/2D MXene Heterostructures for Improved Synergy in Structure toward Next-Generation Supercapacitors: A Review, Adv Funct Mater. 32 (2022) 2110267. https://doi.org/10.1002/adfm.202110267.

[91] S. Faisal, A. Mohamed, H.C. B., A. Babak, M.H. Soon, K.C. Min, G. Yury, Electromagnetic interference shielding with 2D transition metal carbides (MXenes), Science (1979). 353 (2016) 1137–1140. https://doi.org/10.1126/science.aag2421.

[92] C. (John) Zhang, B. Anasori, A. Seral-Ascaso, S.-H. Park, N. McEvoy, A. Shmeliov, G.S. Duesberg, J.N. Coleman, Y. Gogotsi, V. Nicolosi, Transparent, Flexible, and Conductive 2D Titanium Carbide (MXene) Films with High Volumetric Capacitance, Advanced Materials. 29 (2017) 1702678. https://doi.org/10.1002/adma.201702678.

[93] T.S. Mathis, K. Maleski, A. Goad, A. Sarycheva, M. Anayee, A.C. Foucher, K. Hantanasirisakul, C.E. Shuck, E.A. Stach, Y. Gogotsi, Modified MAX Phase Synthesis for Environmentally Stable and Highly Conductive Ti 3 C 2 MXene, ACS Nano. 15 (2021) 6420–6429. https://doi.org/10.1021/acsnano.0c08357.

[94] R. Liu, W. Li, High-Thermal-Stability and High-Thermal-Conductivity Ti 3 C 2 T x MXene/Poly(vinyl alcohol) (PVA) Composites, ACS Omega. 3 (2018) 2609–2617. https://doi.org/10.1021/acsomega.7b02001.

[95] C.E. Shuck, A. Sarycheva, M. Anayee, A. Levitt, Y. Zhu, S. Uzun, V. Balitskiy, V. Zahorodna, O. Gogotsi, Y. Gogotsi, Scalable Synthesis of Ti3C2Tx MXene, Adv Eng Mater. 22 (2020) 1901241. https://doi.org/10.1002/adem.201901241.

[96] X. Zhao, A. Vashisth, J.W. Blivin, Z. Tan, D.E. Holta, V. Kotasthane, S.A. Shah, T. Habib, S. Liu, J.L. Lutkenhaus, M. Radovic, M.J. Green, pH, Nanosheet Concentration, and Antioxidant Affect the Oxidation of Ti3C2Tx and Ti2CTx MXene Dispersions, Adv Mater Interfaces. 7 (2020) 2000845. https://doi.org/10.1002/admi.202000845.

[97] C. John Zhang, S. Pinilla, N. McEvoy, C. P. Cullen, B. Anasori, E. Long, S.-H. Park, A. Seral-Ascaso, A. Shmeliov, D. Krishnan, C. Morant, X. Liu, G. S. Duesberg, Y. Gogotsi, V. Nicolosi, Oxidation Stability of Colloidal Two-Dimensional Titanium Carbides (MXenes), Chemistry of Materials. 29 (2017) 4848–4856. https://doi.org/10.1021/acs.chemmater.7b00745.

[98] X. Zhao, A. Vashisth, E. Prehn, W. Sun, S.A. Shah, T. Habib, Y. Chen, Z. Tan, J.L. Lutkenhaus, M. Radovic, M.J. Green, Antioxidants Unlock Shelf-Stable Ti3C2Tx (MXene) Nanosheet Dispersions, Matter. 1 (2019) 513–526. https://doi.org/10.1016/J.MATT.2019.05.020.

[99] J. Zhang, N. Kong, D. Hegh, K. Aldren S. Usman, G. Guan, S. Qin, I. Jurewicz, W. Yang, J. M. Razal, Freezing Titanium Carbide Aqueous Dispersions for Ultra-long-term Storage, ACS Applied Materials & Interfaces. 12 (2020) 34032–34040. https://doi.org/10.1021/acsami.0c06728.

[100] M. Alhabeb, K. Maleski, B. Anasori, P. Lelyukh, L. Clark, S. Sin, Y. Gogotsi, Guidelines for Synthesis and Processing of Two-Dimensional Titanium Carbide (Ti3C2Tx MXene), Chemistry of Materials. 29 (2017) 7633–7644. https://doi.org/10.1021/acs.chemmater.7b02847.

[101] M. Naguib, M. Kurtoglu, V. Presser, J. Lu, J. Niu, M. Heon, L. Hultman, Y. Gogotsi, M.W. Barsoum, Two-dimensional nanocrystals produced by exfoliation of Ti 3AlC 2, Advanced Materials. (2011). https://doi.org/10.1002/adma.201102306.

[102] S. Mazhar, A.A. Qarni, Y. Ul Haq, Z. Ul Haq, I. Murtaza, Promising PVC/MXene based flexible thin film nanocomposites with excellent dielectric, thermal and mechanical properties, Ceram Int. 46 (2020) 12593–12605. https://doi.org/10.1016/J.CERAMINT.2020.02.023.

[103] L. Wang, L. Chen, P. Song, C. Liang, Y. Lu, H. Qiu, Y. Zhang, J. Kong, J. Gu, Fabrication on the annealed Ti3C2Tx MXene/Epoxy nanocomposites for electromagnetic interference shielding application, Compos B Eng. 171 (2019) 111–118. https://doi.org/10.1016/J.COMPOSITESB.2019.04.050.

[104] Y. Sliozberg, J. Andzelm, C.B. Hatter, B. Anasori, Y. Gogotsi, A. Hall, Interface binding and mechanical properties of MXene-epoxy nanocomposites, Compos Sci Technol. 192 (2020) 108124. https://doi.org/10.1016/J.COMPSCITECH.2020.108124.

[105] J. Meng, J. Luo, H. Wang, Y. Quan, J. Li, X. Sun, Silver-decorated MXene nanosheets as a radical initiator for polymerization and multifunctional hydrogels, Chemical Communications. (2022). https://doi.org/10.1039/D2CC00504B.

[106] X. Wu, H. Liao, D. Ma, M. Chao, Y. Wang, X. Jia, P. Wan, L. Zhang, A wearable, self-adhesive, long-lastingly moist and healable epidermal sensor assembled from conductive MXene nanocomposites, J Mater Chem C Mater. 8 (2020) 1788–1795. https://doi.org/10.1039/C9TC05575D.

[107] M. Qin, W. Yuan, X. Zhang, Y. Cheng, M. Xu, Y. Wei, W. Chen, D. Huang, Preparation of PAA/PAM/MXene/TA hydrogel with antioxidant, healable ability as strain sensor, Colloids Surf B Biointerfaces. 214 (2022) 112482. https://doi.org/10.1016/J.COLSURFB.2022.112482.

[108] H. Yuk, T. Zhang, G.A. Parada, X. Liu, X. Zhao, Skin-inspired hydrogel–elastomer hybrids with robust interfaces and functional microstructures, Nat Commun. 7 (2016) 12028. https://doi.org/10.1038/ncomms12028.

[109] Z. Li, Z. Liu, T.Y. Ng, P. Sharma, The effect of water content on the elastic modulus and fracture energy of hydrogel, Extreme Mech Lett. 35 (2020) 100617. https://doi.org/10.1016/J.EML.2019.100617.

[110] X. Zhao, Y. Xia, X. Zhang, X. Lin, L. Wang, Design of mechanically strong and tough alginate hydrogels based on a soft-brittle transition, Int J Biol Macromol. 139 (2019) 850–857. https://doi.org/10.1016/J.IJBIOMAC.2019.08.057.

[111] M. Aakyiir, J.A. Oh, S. Araby, Q. Zheng, M. Naeem, J. Ma, P. Adu, L. Zhang, Y.W. Mai, Combining hydrophilic MXene nanosheets and hydrophobic carbon nanotubes for mechanically resilient and electrically conductive elastomer nanocomposites, Compos Sci Technol. 214 (2021) 108997. https://doi.org/10.1016/J.COMPSCITECH.2021.108997.

[112] S. Ma, S. Zhu, M. Liu, B. Zhong, Y. Chen, Y. Luo, F. Liu, Z. Jia, D. Jia, A high-performance, thermal and electrical conductive elastomer composite based on Ti3C2 MXene, Compos Part A Appl Sci Manuf. 145 (2021) 106292. https://doi.org/10.1016/j.compositesa.2021.106292.

[113] D. Wang, Y. Lin, D. Hu, P. Jiang, X. Huang, Multifunctional 3D-MXene/PDMS nanocomposites for electrical, thermal and triboelectric applications, Compos Part A Appl Sci Manuf. 130 (2020) 105754. https://doi.org/10.1016/j.compositesa.2019.105754.

[114] Y. Zeng, C. Xiong, W. Li, S. Rao, G. Du, Z. Fan, N. Chen, Significantly improved dielectric and mechanical performance of Ti3C2Tx MXene/silicone rubber nanocomposites, J Alloys Compd. 905 (2022) 164172. https://doi.org/10.1016/j.jallcom.2022.164172.

[115] D. Hu, X. Huang, S. Li, P. Jiang, Flexible and durable cellulose/MXene nanocomposite paper for efficient electromagnetic interference shielding, Compos Sci Technol. 188 (2020) 107995. https://doi.org/10.1016/J.COMPSCITECH.2020.107995.

[116] D. Jiang, J. Zhang, S. Qin, Z. Wang, K. Aldren S. Usman, D. Hegh, J. Liu, W. Lei, J. M. Razal, Superelastic Ti3C2Tx MXene-Based Hybrid Aerogels for Compression-Resilient Devices, ACS Nano. 15 (2021) 5000–5010. https://doi.org/10.1021/acsnano.0c09959.

[117] K. Rajavel, S. Luo, Y. Wan, X. Yu, Y. Hu, P. Zhu, R. Sun, C. Wong, 2D Ti3C2Tx MXene/polyvinylidene fluoride (PVDF) nanocomposites for attenuation of electromagnetic radiation with excellent heat dissipation, Compos Part A Appl Sci Manuf. 129 (2020) 105693. https://doi.org/10.1016/j.compositesa.2019.105693.

[118] X. Wu, B. Han, H. Bin Zhang, X. Xie, T. Tu, Y. Zhang, Y. Dai, R. Yang, Z.Z. Yu, Compressible, durable and conductive polydimethylsiloxane-coated MXene foams for high-performance electromagnetic interference shielding, Chemical Engineering Journal. 381 (2020) 122622. https://doi.org/10.1016/J.CEJ.2019.122622.

[119] P. Yi, H. Zou, Y. Yu, X. Li, Z. Li, G. Deng, C. Chen, M. Fang, J. He, X. Sun, X. Liu, J. Shui, R. Yu, MXene-Reinforced Liquid Metal/Polymer Fibers via Interface Engineering for Wearable Multifunctional Textiles, ACS Nano. 16 (2022) 14490–14502. https://doi.org/10.1021/acsnano.2c04863.

[120] C. Jiang, X. Li, Y. Yao, L. Lan, Y. Shao, F. Zhao, Y. Ying, J. Ping, A multifunctional and highly flexible triboelectric nanogenerator based on MXene-enabled porous film integrated with laser-induced graphene electrode, Nano Energy. 66 (2019) 104121. https://doi.org/10.1016/j.nanoen.2019.104121.

[121] M. Salauddin, S.M.S. Rana, Md. Sharifuzzaman, M.T. Rahman, C. Park, H. Cho, P. Maharjan, T. Bhatta, J.Y. Park, A Novel MXene/Ecoflex Nanocomposite-Coated Fabric as a Highly Negative and Stable Friction Layer for High-Output Triboelectric Nanogenerators, Adv Energy Mater. 11 (2021) 2002832. https://doi.org/10.1002/aenm.202002832.

[122] Y.W. Cai, X.N. Zhang, G.G. Wang, G.Z. Li, D.Q. Zhao, N. Sun, F. Li, H.Y. Zhang, J.C. Han, Y. Yang, A flexible ultra-sensitive triboelectric tactile sensor of wrinkled PDMS/MXene composite films for E-skin, Nano Energy. 81 (2021) 105663. https://doi.org/10.1016/J.NANOEN.2020.105663.

[123] K. Hyuck Lee, Y.-Z. Zhang, Q. Jiang, H. Kim, A. A. Alkenawi, H. N. Alshareef, Ultrasound-Driven Two-Dimensional Ti3C2Tx MXene Hydrogel Generator, ACS Nano. 14 (2020) 3199–3207. https://doi.org/10.1021/acsnano.9b08462.

[124] M. Ghebremedhin, S. Seiffert, T.A. Vilgis, Physics of agarose fluid gels: Rheological properties and microstructure, Curr Res Food Sci. 4 (2021) 436–448. https://doi.org/10.1016/J.CRFS.2021.06.003.

[125] V. Normand, D.L. Lootens, E. Amici, K.P. Plucknett, P. Aymard, New insight into agarose gel mechanical properties, Biomacromolecules. (2000). https://doi.org/10.1021/bm005583j.

[126] R. Pomfret, G. Miranpuri, K. Sillay, The substitute brain and the potential of the gel model, Ann Neurosci. (2013). https://doi.org/10.5214/ans.0972.7531.200309.

[127] P.S. De Freitas, D. Wirz, M. Stolz, B. Göpfert, N.F. Friederich, A.U. Daniels, Pulsatile dynamic stiffness of cartilage-like materials and use of agarose gels to validate mechanical methods and models, J Biomed Mater Res B Appl Biomater. (2006). https://doi.org/10.1002/jbm.b.30494.

[128] F.A. Urrea, F. Casanova, G.A. Orozco, J.J. García, Evaluation of the friction coefficient, the radial stress, and the damage work during needle insertions into agarose gels, J Mech Behav Biomed Mater. (2016). https://doi.org/10.1016/j.jmbbm.2015.11.024.

[129] G. Cheng, J. Tse, R.K. Jain, L.L. Munn, Micro-environmental mechanical stress controls tumor spheroid size and morphology by suppressing proliferation and inducing apoptosis in cancer cells, PLoS One. (2009). https://doi.org/10.1371/journal.pone.0004632.

[130] J. Chen, J. Irianto, S. Inamdar, P. Pravincumar, D.A. Lee, D.L. Bader, M.M. Knight, Cell mechanics, structure, and function are regulated by the stiffness of the three-dimensional microenvironment, Biophys J. (2012). https://doi.org/10.1016/j.bpj.2012.07.054.

[131] S. Takao, M. Taya, C. Chiew, Mechanical stress-induced cell death in breast cancer cells, Biol Open. 8 (2019). https://doi.org/10.1242/bio.043133.

[132] J.M. Tse, G. Cheng, J.A. Tyrrell, S.A. Wilcox-Adelman, Y. Boucher, R.K. Jain, L.L. Munn, Mechanical compression drives cancer cells toward invasive phenotype, Proc Natl Acad Sci U S A. (2012). https://doi.org/10.1073/pnas.1118910109.

[133] E.N. Horst, C.M. Novak, K. Burkhard, C.S. Snyder, R. Verma, D.E. Crochran, I.A. Geza, W. Fermanich, P. Mehta, D.C. Schlautman, L.A. Tran, M.E. Brezenger, G. Mehta, Injectable three-dimensional tumor microenvironments to study mechanobiology in ovarian cancer, Acta Biomater. 146 (2022) 222–234. https://doi.org/10.1016/J.ACTBIO.2022.04.039.

[134] P.K. Chaudhuri, B. Chuan Low, C. Teck Lim, Mechanobiology of Tumor Growth, Chem Rev. 118 (2018) 6499–6515. https://doi.org/10.1021/acs.chemrev.8b00042.

[135] T. Mura, Theory of Inclusions and Inhomogeneities, Micromechanics of Defects in Solids. (1987). https://doi.org/10.1007/978-94-009-3489-4.

[136] M. Hori, S. Nemat-Nasser, Double-inclusion model and overall moduli of multi-phase composites, Mechanics of Materials. (1993). https://doi.org/10.1016/0167-6636(93)90066-Z.

[137] Y. Benveniste, A new approach to the application of Mori-Tanaka's theory in composite materials, Mechanics of Materials. (1987). https://doi.org/10.1016/0167-6636(87)90005-6.

[138] C. Friebel, I. Doghri, V. Legat, General mean-field homogenization schemes for viscoelastic composites containing multiple phases of coated inclusions, Int J Solids Struct. 43 (2006) 2513–2541. https://doi.org/10.1016/j.ijsolstr.2005.06.035.

[139] B. Raju, S.R. Hiremath, D. Roy Mahapatra, A review of micromechanics based models for effective elastic properties of reinforced polymer matrix composites, Compos Struct. (2018). https://doi.org/10.1016/j.compstruct.2018.07.125.

[140] B. Mortazavi, M. Baniassadi, J. Bardon, S. Ahzi, Modeling of two-phase random composite materials by finite element, Mori–Tanaka and strong contrast methods, Compos B Eng. 45 (2013) 1117–1125. https://doi.org/10.1016/j.compositesb.2012.05.015.

[141] B. Mortazavi, J. Bardon, S. Ahzi, Interphase effect on the elastic and thermal conductivity response of polymer nanocomposite materials: 3D finite element study, Comput Mater Sci. 69 (2013) 100–106. https://doi.org/10.1016/j.commatsci.2012.11.035.

[142] F. Nosouhi Dehnavi, M. Safdari, K. Abrinia, A. Sheidaei, M. Baniassadi, Numerical study of the conductive liquid metal elastomeric composites, Mater Today Commun. (2020). https://doi.org/10.1016/j.mtcomm.2019.100878.

[143] A. Thoopul Anantharanga, M.S. Hashemi, A. Sheidaei, Linking properties to microstructure in liquid metal embedded elastomers via machine learning, Comput Mater Sci. 218 (2023) 111983. https://doi.org/10.1016/J.COMMATSCI.2022.111983.

[144] K. Zhou, H.J. Hoh, X. Wang, L.M. Keer, J.H.L. Pang, B. Song, Q.J. Wang, A review of recent works on inclusions, Mechanics of Materials. 60 (2013) 144–158. https://doi.org/10.1016/J.MECHMAT.2013.01.005.

[145] J.D. Eshelby, R.E. Peierls, The elastic field outside an ellipsoidal inclusion, Proc R Soc Lond A Math Phys Sci. 252 (1997) 561–569. https://doi.org/10.1098/rspa.1959.0173.

[146] M.H. Malakooti, H.A. Sodano, Multi-Inclusion modeling of multiphase piezoelectric composites, Compos B Eng. (2013). https://doi.org/10.1016/j.compositesb.2012.10.034.

[147] R.W. Style, R. Boltyanskiy, B. Allen, K.E. Jensen, H.P. Foote, J.S. Wettlaufer, E.R. Dufresne, Stiffening solids with liquid inclusions, Nat Phys. 11 (2015) 82–87. https://doi.org/10.1038/nphys3181.

[148] X. Zhang, P. Li, D. Lyu, X. Jin, P.K. Liaw, L.M. Keer, The interactions between multiple arbitrarily orientated inhomogeneities with thermo-porous eigenstrains and its applications in geothermal resources, Comput Geosci. 145 (2020) 104623. https://doi.org/10.1016/j.cageo.2020.104623.

[149] J.F. Barthélémy, A. Giraud, F. Lavergne, J. Sanahuja, The Eshelby inclusion problem in ageing linear viscoelasticity, Int J Solids Struct. (2016). https://doi.org/10.1016/j.ijsolstr.2016.06.035.

[150] J. Shaw, Viscoelastic Eshelby Analysis of the Cell-in-Gell System, Biophys J. (2018). https://doi.org/10.1016/j.bpj.2017.11.3354.

[151] M.A. Kazemi-Lari, J.A. Shaw, A.S. Wineman, R. Shimkunas, Z. Jian, B. Hegyi, L. Izu, Y. Chen-Izu, A viscoelastic Eshelby inclusion model and analysis of the Cell-in-Gel system, Int J Eng Sci. 165 (2021) 103489. https://doi.org/10.1016/J.IJENGSCI.2021.103489.

[152] M. Taya, Electronic Composites, Cambridge University Press, 2005. https://doi.org/10.1017/CBO9780511550508.

[153] H. Hatta, M. Taya, Effective thermal conductivity of a misoriented short fiber composite, J Appl Phys. 58 (1985) 2478–2486. https://doi.org/10.1063/1.335924.

[154] T. Mori, K. Tanaka, Average stress in matrix and average elastic energy of materials with misfitting inclusions, Acta Metallurgica. (1973). https://doi.org/10.1016/0001-6160(73)90064-3.

[155] M.D. Dickey, Stretchable and Soft Electronics using Liquid Metals, Advanced Materials. (2017). https://doi.org/10.1002/adma.201606425.

[156] L. Zhu, B. Wang, S. Handschuh-Wang, X. Zhou, S. Handschuh-Wang, X. Zhou, Liquid Metal–Based Soft Microfluidics, Wiley-VCH Verlag, 2020. https://doi.org/10.1002/smll.201903841.

[157] D. Zrnic, D.S.-J. of the less common metals, undefined 1969, On the resistivity and surface tension of the eutectic alloy of gallium and indium, Elsevier. (n.d.).

[158] Y.L. Park, B.R. Chen, R.J. Wood, Design and fabrication of soft artificial skin using embedded microchannels and liquid conductors, IEEE Sens J. 12 (2012) 2711–2718. https://doi.org/10.1109/JSEN.2012.2200790.

[159] Y. Gao, H. Ota, E.W. Schaler, K. Chen, A. Zhao, W. Gao, H.M. Fahad, Y. Leng, A. Zheng, F. Xiong, C. Zhang, L.C. Tai, P. Zhao, R.S. Fearing, A. Javey, Wearable Microfluidic Diaphragm Pressure Sensor for Health and Tactile Touch Monitoring, Advanced Materials. (2017). https://doi.org/10.1002/adma.201701985.

[160] M.D. Bartlett, N. Kazem, M.J. Powell-Palm, X. Huang, W. Sun, J.A. Malen, C. Majidi, High thermal conductivity in soft elastomers with elongated liquid metal inclusions, Proceedings of the National Academy of Sciences. 114 (2017) 2143–2148. https://doi.org/10.1073/pnas.1616377114.

[161] S.H. Jeong, S. Chen, J. Huo, E.K. Gamstedt, J. Liu, S.-L. Zhang, Z.-B. Zhang, K. Hjort, Z. Wu, Mechanically Stretchable and Electrically Insulating Thermal Elastomer Composite by Liquid Alloy Droplet Embedment, Sci Rep. 5 (2016) 18257. https://doi.org/10.1038/srep18257.

[162] J. Zhang, M. Liu, G. Pearce, Y. Yu, Z. Sha, Y. Zhou, A.C.Y. Yuen, C. Tao, C. Boyer, F. Huang, M. Islam, C.H. Wang, Strain stiffening and positive piezoconductive effect of liquid metal/elastomer soft composites, Compos Sci Technol. 201 (2021) 108497. https://doi.org/10.1016/j.compscitech.2020.108497.

[163] C. Pan, E.J. Markvicka, M.H. Malakooti, J. Yan, L. Hu, K. Matyjaszewski, C. Majidi, A Liquid-Metal–Elastomer Nanocomposite for Stretchable Dielectric Materials, Advanced Materials. 31 (2019) 1900663. https://doi.org/10.1002/adma.201900663.

[164] Y. Xin, H. Peng, J. Xu, J. Zhang, Ultrauniform Embedded Liquid Metal in Sulfur Polymers for Recyclable, Conductive, and Self-Healable Materials, Adv Funct Mater. 29 (2019) 1808989. https://doi.org/10.1002/adfm.201808989.

[165] M. Zadan, C. Chiew, C. Majidi, M.H. Malakooti, Liquid Metal Architectures for Soft and Wearable Energy Harvesting Devices, Multifunctional Materials. (2020).

[166] P. Fan, Z. Sun, Y. Wang, H. Chang, P. Zhang, S. Yao, C. Lu, W. Rao, J. Liu, Nano liquid metal for the preparation of a thermally conductive and electrically insulating material with high stability, RSC Adv. (2018). https://doi.org/10.1039/c8ra00262b.

[167] J. Yan, M.H. Malakooti, Z. Lu, Z. Wang, N. Kazem, C. Pan, M.R. Bockstaller, C. Majidi, K. Matyjaszewski, Solution processable liquid metal nanodroplets by surface-initiated atom transfer radical polymerization, Nat Nanotechnol. 14 (2019) 684–690. https://doi.org/10.1038/s41565-019-0454-6.

[168] M.H. Malakooti, N. Kazem, J. Yan, C. Pan, E.J. Markvicka, K. Matyjaszewski, C. Majidi, Liquid Metal Supercooling for Low-Temperature Thermoelectric Wearables, Adv Funct Mater. 29 (2019) 1906098. https://doi.org/10.1002/adfm.201906098.

[169] M.D. Dickey, Emerging applications of liquid metals featuring surface oxides, ACS Appl Mater Interfaces. (2014). https://doi.org/10.1021/am5043017.

[170] M. Regan, H. Tostmann, P. Pershan, O. Magnussen, E. DiMasi, B. Ocko, X-ray study of the oxidation of liquid-gallium surfaces, Phys Rev B Condens Matter Mater Phys. (1997). https://doi.org/10.1103/PhysRevB.55.10786.

[171] T.R. Lear, S.H. Hyun, J.W. Boley, E.L. White, D.H. Thompson, R.K. Kramer, Liquid metal particle popping: Macroscale to nanoscale, Extreme Mech Lett. (2017). https://doi.org/10.1016/j.eml.2017.02.009.

[172] R.W. Style, J.S. Wettlaufer, E.R. Dufresne, Surface tension and the mechanics of liquid inclusions in compliant solids, Soft Matter. (2015). https://doi.org/10.1039/c4sm02413c.

[173] N. Cohen, K. Bhattacharya, A numerical study of the electromechanical response of liquid metal embedded elastomers, Int J Non Linear Mech. (2019). https://doi.org/10.1016/j.ijnonlinmec.2018.10.011.

[174] N. Zolfaghari, P. Khandagale, M.J. Ford, K. Dayal, C. Majidi, Network topologies dictate electromechanical coupling in liquid metal–elastomer composites, Soft Matter. (2020). https://doi.org/10.1039/d0sm01094d.

[175] P. Lu, Y.W. Leong, P.K. Pallathadka, C.B. He, Effective moduli of nanoparticle reinforced composites considering interphase effect by extended double-inclusion model - Theory and explicit expressions, Int J Eng Sci. (2013). https://doi.org/10.1016/j.ijengsci.2013.08.003.

[176] J.D. Eshelby, The determination of the elastic field of an ellipsoidal inclusion, and related problems, in: Proc R Soc Lond A Math Phys Sci, 2007. https://doi.org/10.1098/rspa.1957.0133.

[177] K. Baek, H. Shin, T. Yoo, M. Cho, Two-step multiscale homogenization for mechanical behaviour of polymeric nanocomposites with nanoparticulate agglomerations, Compos Sci Technol. (2019). https://doi.org/10.1016/j.compscitech.2019.05.006.

[178] J. Jung, S.H. Jeong, K. Hjort, S. Ryu, Investigation of thermal conductivity for liquid metal composites using the micromechanics-based mean-field homogenization theory, Soft Matter. 16 (2020) 5840–5847. https://doi.org/10.1039/D0SM00279H.

[179] M. Passlack, N.E.J. Hunt, E.F. Schubert, G.J. Zydzik, M. Hong, J.P. Mannaerts, R.L. Opila, R.J. Fischer, Dielectric properties of electron-beam deposited Ga2O 3 films, Appl Phys Lett. (1994). https://doi.org/10.1063/1.111452.

[180] Z. Guo, A. Verma, X. Wu, F. Sun, A. Hickman, T. Masui, A. Kuramata, M. Higashiwaki, D. Jena, T. Luo, Anisotropic thermal conductivity in single crystal β-gallium oxide, Appl Phys Lett. (2015). https://doi.org/10.1063/1.4916078.

[181] Y. Han, L.-E. Simonsen, M.H. Malakooti, Printing Liquid Metal Elastomer Composites for High-Performance Stretchable Thermoelectric Generators, Adv Energy Mater. 12 (2022) 2201413. https://doi.org/10.1002/aenm.202201413.

[182] Y. Xin, S. Zhang, Y. Lou, J. Xu, J. Zhang, Determinative Energy Dissipation in Liquid Metal Polymer Composites for Advanced Electronic Applications, Adv Mater Technol. 5 (2020) 2000018. https://doi.org/10.1002/admt.202000018.

[183] L. Tang, S. Cheng, L. Zhang, H. Mi, L. Mou, S. Yang, Z. Huang, X. Shi, X. Jiang, Printable Metal-Polymer Conductors for Highly Stretchable Bio-Devices, IScience. 4 (2018) 302–311. https://doi.org/10.1016/J.ISCI.2018.05.013.

[184] T. V Neumann, E.G. Facchine, B. Leonardo, S. Khan, M.D. Dickey, Direct write printing of a self-encapsulating liquid metal–silicone composite, Soft Matter. 16 (2020) 6608–6618. https://doi.org/10.1039/D0SM00803F.

[185] Y. Liu, X. Ji, J. Liang, Rupture stress of liquid metal nanoparticles and their applications in stretchable conductors and dielectrics, Npj Flexible Electronics. 5 (2021) 11. https://doi.org/10.1038/s41528-021-00108-w.

[186] R. Tutika, S.H. Zhou, R.E. Napolitano, M.D. Bartlett, Mechanical and Functional Tradeoffs in Multiphase Liquid Metal, Solid Particle Soft Composites, Adv Funct Mater. 28 (2018) 1804336. https://doi.org/10.1002/adfm.201804336.

[187] S. Zhu, J.H. So, R. Mays, S. Desai, W.R. Barnes, B. Pourdeyhimi, M.D. Dickey, Ultrastretchable fibers with metallic conductivity using a liquid metal alloy core, Adv Funct Mater. (2013). https://doi.org/10.1002/adfm.201202405.

[188] L. Zhu, Y. Chen, W. Shang, S. Handschuh-Wang, X. Zhou, T. Gan, Q. Wu, Y. Liu, X. Zhou, Anisotropic liquid metal–elastomer composites, J Mater Chem C Mater. 7 (2019) 10166–10172. https://doi.org/10.1039/C9TC03222C.

[189] P. Won, C.S. Valentine, M. Zadan, C. Pan, M. Vinciguerra, D.K. Patel, S.H. Ko, L.M. Walker, C. Majidi, 3D Printing of Liquid Metal Embedded Elastomers for Soft Thermal and Electrical Materials, ACS Appl Mater Interfaces. 14 (2022) 55028–55038. https://doi.org/10.1021/acsami.2c14815.

[190] P.S. Owuor, S. Hiremath, A.C. Chipara, R. Vajtai, J. Lou, D.R. Mahapatra, C.S. Tiwary, P.M. Ajayan, Nature Inspired Strategy to Enhance Mechanical Properties via Liquid Reinforcement, Adv Mater Interfaces. 4 (2017) 1700240. https://doi.org/10.1002/admi.201700240.

[191] Y. Mikata, M. Taya, Stress Field in and Around a Coated Short Fiber in an Infinite Matrix Subjected to Uniaxial and Biaxial Loadings, J Appl Mech. 52 (1985) 19–24. https://doi.org/10.1115/1.3168996.

[192] M.A. Sadowsky, E. Sternberg, Stress Concentration Around a Triaxial Ellipsoidal Cavity, J Appl Mech. 16 (2021) 149–157. https://doi.org/10.1115/1.4009928.

[193] H.M. Shodja, A.S. Sarvestani, Elastic Fields in Double Inhomogeneity by the Equivalent Inclusion Method, J Appl Mech. 68 (2000) 3–10. https://doi.org/10.1115/1.1346680.

[194] X. Jin, D. Lyu, X. Zhang, Q. Zhou, Q. Wang, L.M. Keer, Explicit Analytical Solutions for a Complete Set of the Eshelby Tensors of an Ellipsoidal Inclusion, J Appl Mech. 83 (2016). https://doi.org/10.1115/1.4034705.

[195] I.D. Johnston, D.K. McCluskey, C.K.L. Tan, M.C. Tracey, Mechanical characterization of bulk Sylgard 184 for microfluidics and microengineering, Journal of Micromechanics and Microengineering. (2014). https://doi.org/10.1088/0960-1317/24/3/035017.

[196] Z.A. Moschovidis, T. Mura, Two-Ellipsoidal Inhomogeneities by the Equivalent Inclusion Method, J Appl Mech. 42 (1975) 847–852. https://doi.org/10.1115/1.3423718.

[197] Y. Gogotsi, B. Anasori, The Rise of MXenes, ACS Nano. 13 (2019) 8491–8494. https://doi.org/10.1021/acsnano.9b06394.

[198] A. VahidMohammadi, J. Rosen, Y. Gogotsi, The world of two-dimensional carbides and nitrides (MXenes), Science (1979). 372 (2021) eabf1581. https://doi.org/10.1126/science.abf1581.

[199] H. Liu, R. Fu, X. Su, B. Wu, H. Wang, Y. Xu, X. Liu, Electrical insulating MXene/PDMS/BN composite with enhanced thermal conductivity for electromagnetic shielding application, Composites Communications. 23 (2021) 100593. https://doi.org/10.1016/J.COCO.2020.100593.

[200] Q. Guo, X. Zhang, F. Zhao, Q. Song, G. Su, Y. Tan, Q. Tao, T. Zhou, Y. Yu, Z. Zhou, C. Lu, Protein-Inspired Self-Healable Ti3C2 MXenes/Rubber-Based Supramolecular Elastomer for Intelligent Sensing, ACS Nano. 14 (2020) 2788–2797. https://doi.org/10.1021/acsnano.9b09802.

[201] K. Zhang, J. Sun, J. Song, C. Gao, Z. Wang, C. Song, Y. Wu, Y. Liu, Self-Healing Ti3C2 MXene/PDMS Supramolecular Elastomers Based on Small Biomolecules Modification for Wearable Sensors, ACS Applied Materials & Interfaces. 12 (2020) 45306–45314. https://doi.org/10.1021/acsami.0c13653.

[202] M. Yang, Y. Yuan, Y. Li, X. Sun, S. Wang, L. Liang, Y. Ning, J. Li, W. Yin, Y. Li, Anisotropic Electromagnetic Absorption of Aligned Ti3C2Tx MXene/Gelatin Nanocomposite Aerogels, ACS Applied Materials & Interfaces. 12 (2020) 33128–33138. https://doi.org/10.1021/acsami.0c09726.

[203] M. Li, J. Lu, K. Luo, Y. Li, K. Chang, K. Chen, J. Zhou, J. Rosen, L. Hultman, P. Eklund, P. O. Å. Persson, S. Du, Z. Chai, Z. Huang, Q. Huang, Element Replacement Approach by Reaction with Lewis Acidic Molten Salts to Synthesize Nanolaminated MAX Phases and MXenes, J Am Chem Soc. 141 (2019) 4730–4737. https://doi.org/10.1021/jacs.9b00574.

[204] S. Tu, Q. Jiang, X. Zhang, H.N. Alshareef, Large Dielectric Constant Enhancement in MXene Percolative Polymer Composites, ACS Nano. 12 (2018) 3369–3377. https://doi.org/10.1021/acsnano.7b08895.

[205] W. Ma, K. Yang, H. Wang, H. Li, Poly(vinylidene fluoride- co -hexafluoropropylene)-MXene Nanosheet Composites for Microcapacitors, ACS Appl Nano Mater. 3 (2020) 7992–8003. https://doi.org/10.1021/acsanm.0c01459.

[206] M. Aakyiir, H. Yu, S. Araby, W. Ruoyu, A. Michelmore, Q. Meng, D. Losic, N.R. Choudhury, J. Ma, Electrically and thermally conductive elastomer by using MXene nanosheets with interface modification, Chemical Engineering Journal. 397 (2020) 125439. https://doi.org/10.1016/j.cej.2020.125439.

[207] L. Wei, J.-W. Wang, X.-H. Gao, H.-Q. Wang, X.-Z. Wang, H. Ren, Enhanced Dielectric Properties of a Poly(dimethyl siloxane) Bimodal Network Percolative Composite with MXene, ACS Appl Mater Interfaces. 12 (2020) 16805–16814. https://doi.org/10.1021/acsami.0c01409.

[208] G. Monastyreckis, L. Mishnaevsky, C.B. Hatter, A. Aniskevich, Y. Gogotsi, D. Zeleniakiene, Micromechanical modeling of MXene-polymer composites, Carbon N Y. 162 (2020) 402–409. https://doi.org/10.1016/J.CARBON.2020.02.070.

[209] S. Kilikevičius, S. Kvietkaitė, K. Žukienė, M. Omastová, A. Aniskevich, D. Zeleniakienė, Numerical investigation of the mechanical properties of a novel hybrid polymer composite

reinforced with graphene and MXene nanosheets, Comput Mater Sci. 174 (2020) 109497. https://doi.org/10.1016/J.COMMATSCI.2019.109497.

[210] S. Kilikevičius, S. Kvietkaitė, L. Mishnaevsky, M. Omastová, A. Aniskevich, D. Zeleniakienė, Novel Hybrid Polymer Composites with Graphene and MXene Nano-Reinforcements: Computational Analysis, Polymers . 13 (2021). https://doi.org/10.3390/polym13071013.

[211] S. Tarasovs, A. Aniskevich, Influence of the formation of clusters on the effective elastic properties of platelet reinforced polymers, Mechanics of Materials. 167 (2022) 104247. https://doi.org/10.1016/j.mechmat.2022.104247.

[212] E. Ghossein, M. Lévesque, A comprehensive validation of analytical homogenization models: The case of ellipsoidal particles reinforced composites, Mechanics of Materials. 75 (2014) 135–150. https://doi.org/10.1016/J.MECHMAT.2014.03.014.

[213] G. Lielens, P. Pirotte, A. Couniot, F. Dupret, R. Keunings, Prediction of thermo-mechanical properties for compression moulded composites, Compos Part A Appl Sci Manuf. (1998). https://doi.org/10.1016/S1359-835X(97)00039-0.

[214] R. Hashemi, G.J. Weng, A theoretical treatment of graphene nanocomposites with percolation threshold, tunneling-assisted conductivity and microcapacitor effect in AC and DC electrical settings, Carbon N Y. 96 (2016) 474–490. https://doi.org/10.1016/J.CARBON.2015.09.103.

[215] X. Xia, Z. Zhong, G.J. Weng, Maxwell–Wagner–Sillars mechanism in the frequency dependence of electrical conductivity and dielectric permittivity of graphene-polymer nanocomposites, Mechanics of Materials. 109 (2017) 42–50. https://doi.org/10.1016/J.MECHMAT.2017.03.014.

[216] Y. Su, J.J. Li, G.J. Weng, Theory of thermal conductivity of graphene-polymer nanocomposites with interfacial Kapitza resistance and graphene-graphene contact resistance, Carbon N Y. 137 (2018) 222–233. https://doi.org/10.1016/J.CARBON.2018.05.033.

[217] I. Doghri, A. Ouaar, Homogenization of two-phase elasto-plastic composite materials and structures study of tangent operators, cyclic plasticity and numerical algorithms, Int J Solids Struct. (2003). https://doi.org/10.1016/S0020-7683(03)00013-1.

[218] P. Franciosi, Mean and axial green and Eshelby tensors for an inclusion with finite cylindrical 3D shape, Mech Res Commun. 59 (2014) 26–36. https://doi.org/10.1016/J.MECHRESCOM.2014.04.006.

[219] P. Franciosi, S. Barboura, Y. Charles, Analytical mean Green operators/Eshelby tensors for patterns of coaxial finite long or flat cylinders in isotropic matrices, Int J Solids Struct. 66 (2015) 1–19. https://doi.org/10.1016/J.IJSOLSTR.2015.03.027.

[220] G.M. Odegard, T.S. Gates, K.E. Wise, C. Park, E.J. Siochi, Constitutive modeling of nanotube–reinforced polymer composites, Compos Sci Technol. 63 (2003) 1671–1687. https://doi.org/10.1016/S0266-3538(03)00063-0.

[221] Y. Wang, J.W. Shan, G.J. Weng, Percolation threshold and electrical conductivity of graphene-based nanocomposites with filler agglomeration and interfacial tunneling, J. Appl. Phys. 118 (2015) 65101. https://doi.org/10.1063/1.4928293.

[222] Y. Sheng, C. Li, J. Wang, X. Xia, G.J. Weng, Y. Su, Multiscale modeling of thermal conductivity of hierarchical CNT-polymer nanocomposite system with progressive agglomeration, Carbon N Y. 201 (2023) 785–795. https://doi.org/10.1016/j.carbon.2022.09.057.

[223] K. Hbaieb, Q.X. Wang, Y.H.J. Chia, B. Cotterell, Modelling stiffness of polymer/clay nanocomposites, Polymer (Guildf). 48 (2007) 901–909. https://doi.org/10.1016/J.POLYMER.2006.11.062.

[224] I.M. Gitman, H. Askes, L.J. Sluys, Representative volume: Existence and size determination, Eng Fract Mech. 74 (2007) 2518–2534. https://doi.org/10.1016/J.ENGFRACMECH.2006.12.021.

[225] J. Come, Y. Xie, M. Naguib, S. Jesse, S. V Kalinin, Y. Gogotsi, P.R.C. Kent, N. Balke, Nanoscale Elastic Changes in 2D Ti3C2Tx (MXene) Pseudocapacitive Electrodes, Adv Energy Mater. 6 (2016) 1502290. https://doi.org/10.1002/aenm.201502290.

[226] F. Schneider, T. Fellner, J. Wilde, U. Wallrabe, Mechanical properties of silicones for {MEMS}, Journal of Micromechanics and Microengineering. 18 (2008) 65008. https://doi.org/10.1088/0960-1317/18/6/065008.

[227] C. Ji, Y. Wang, Z. Ye, L. Tan, D. Mao, W. Zhao, X. Zeng, C. Yan, R. Sun, D. Joon Kang, J. Xu, C.-P. Wong, Ice-Templated MXene/Ag–Epoxy Nanocomposites as High-Performance Thermal Management Materials, ACS Applied Materials & Interfaces. 12 (2020) 24298–24307. https://doi.org/10.1021/acsami.9b22744.

[228] C.-W. Nan, Y. Shen, J. Ma, Physical Properties of Composites Near Percolation, Annu Rev Mater Res. 40 (2010) 131–151. https://doi.org/10.1146/annurev-matsci-070909-104529.

[229] S. Tu, Q. Jiang, J. Zhang, X. He, M.N. Hedhili, X. Zhang, H.N. Alshareef, Enhancement of Dielectric Permittivity of Ti 3 C 2 T x MXene/Polymer Composites by Controlling Flake Size and Surface Termination, ACS Appl Mater Interfaces. 11 (2019) 27358–27362. https://doi.org/10.1021/acsami.9b09137.

[230] M.J. Ford, C.P. Ambulo, T.A. Kent, E.J. Markvicka, C. Pan, J. Malen, T.H. Ware, C. Majidi, A multifunctional shape-morphing elastomer with liquid metal inclusions, Proc Natl Acad Sci U S A. (2019). https://doi.org/10.1073/pnas.1911021116.

[231] D.H. Kim, E.A. Rozhkova, I. V. Ulasov, S.D. Bader, T. Rajh, M.S. Lesniak, V. Novosad, Biofunctionalized magnetic-vortex microdiscs for targeted cancer-cell destruction, Nat Mater. (2010). https://doi.org/10.1038/nmat2591.

[232] S. Leulmi, X. Chauchet, M. Morcrette, G. Ortiz, H. Joisten, P. Sabon, T. Livache, Y. Hou, M. Carrière, S. Lequien, B. Dieny, Triggering the apoptosis of targeted human renal cancer cells by the vibration of anisotropic magnetic particles attached to the cell membrane, Nanoscale. (2015). https://doi.org/10.1039/c5nr03518j.

[233] D.W. Wong, W.L. Gan, Y.K. Teo, W.S. Lew, Interplay of cell death signaling pathways mediated by alternating magnetic field gradient, Cell Death Discov. (2018). https://doi.org/10.1038/s41420-018-0052-7.

[234] E. Zhang, M.F. Kircher, M. Koch, L. Eliasson, S.N. Goldberg, E. Renström, Dynamic magnetic fields remote-control apoptosis via nanoparticle rotation, ACS Nano. (2014). https://doi.org/10.1021/nn406302j.

[235] L. Cacopardo, G. Mattei, A. Ahluwalia, A new load-controlled testing method for viscoelastic characterisation through stress-rate measurements, Materialia (Oxf). 9 (2020) 100552. https://doi.org/10.1016/J.MTLA.2019.100552.

[236] M. Kazemi-Lari, J. Shaw, A. Wineman, R. Shimkunas, L. Izu, Y. Chen-Izu, Viscoelastic eshelby analysis of cardiomyocyte contraction in the cell-in-gel system, in: ASME 2018 Conference on Smart Materials, Adaptive Structures and Intelligent Systems, SMASIS 2018, 2018. https://doi.org/10.1115/SMASIS2018-8244.

[237] M. Baghban, A. Mojra, Early relaxation time assessment for characterization of breast tissue and diagnosis of breast tumors, J Mech Behav Biomed Mater. (2018). https://doi.org/10.1016/j.jmbbm.2018.07.037.

[238] B. Carmichael, H. Babahosseini, S.N. Mahmoodi, M. Agah, The fractional viscoelastic response of human breast tissue cells, Phys Biol. (2015). https://doi.org/10.1088/1478-3975/12/4/046001.

[239] Y.M. Efremov, W.H. Wang, S.D. Hardy, R.L. Geahlen, A. Raman, Measuring nanoscale viscoelastic parameters of cells directly from AFM force-displacement curves, Sci Rep. (2017). https://doi.org/10.1038/s41598-017-01784-3.

[240] M. Taya, K. Kadooka, Review on viscoelastic behavior of dielectric polymers and their actuators, in: 2018. https://doi.org/10.1117/12.2295116.

[241] Y. Nematbakhsh, K.T. Pang, C.T. Lim, Correlating the viscoelasticity of breast cancer cells with their malignancy, Converg Sci Phys Oncol. (2017). https://doi.org/10.1088/2057-1739/aa7ffb.

[242] J. Hu, Y. Zhou, J.D. Obayemi, J. Du, W.O. Soboyejo, An investigation of the viscoelastic properties and the actin cytoskeletal structure of triple negative breast cancer cells, J Mech Behav Biomed Mater. (2018). https://doi.org/10.1016/j.jmbbm.2018.05.038.

[243] F. Lavergne, K. Sab, J. Sanahuja, M. Bornert, C. Toulemonde, Homogenization schemes for aging linear viscoelastic matrix-inclusion composite materials with elongated inclusions, Int J Solids Struct. (2016). https://doi.org/10.1016/j.ijsolstr.2015.10.014.

[244] C. Henderson, E.N.D.C. Andrade, The application of Boltzmann's superposition theory to materials exhibiting reversible β flow, Proc R Soc Lond A Math Phys Sci. 206 (1951) 72–86. https://doi.org/10.1098/rspa.1951.0057.

[245] G. Subhash, Q. Liu, D.F. Moore, P.G. Ifju, M.A. Haile, Concentration Dependence of Tensile Behavior in Agarose Gel Using Digital Image Correlation, Exp Mech. (2011). https://doi.org/10.1007/s11340-010-9354-2.

[246] M.W. Hyer, A.M. Waas, 1.12 Micromechanics of Linear Elastic Continuous Fiber Composites, in: Comprehensive Composite Materials II, 2018. https://doi.org/10.1016/b978-0-12-803581-8.09880-5.

[247] Q. Liu, G. Subhash, D.F. Moore, Loading velocity dependent permeability in agarose gel under compression, J Mech Behav Biomed Mater. (2011). https://doi.org/10.1016/j.jmbbm.2011.02.009.

[248] T. Liu, P. Sen, C.J. Kim, Characterization of nontoxic liquid-metal alloy galinstan for applications in microdevices, Journal of Microelectromechanical Systems. (2012). https://doi.org/10.1109/JMEMS.2011.2174421.

[249] P.R. Dvornic, Thermal Properties of Polysiloxanes, in: Silicon-Containing Polymers, 2000. https://doi.org/10.1007/978-94-011-3939-7_7.

[250] F. Mancarella, R.W. Style, J.S. Wettlaufer, Surface tension and the Mori-Tanaka theory of non-dilute soft composite solids, Proceedings of the Royal Society A: Mathematical, Physical and Engineering Sciences. (2016). https://doi.org/10.1098/rspa.2015.0853.

[251] C. Pan, E.J. Markvicka, M.H. Malakooti, J. Yan, L. Hu, K. Matyjaszewski, C. Majidi, A Liquid-Metal–Elastomer Nanocomposite for Stretchable Dielectric Materials, Advanced Materials. 31 (2019) 1900663. https://doi.org/10.1002/adma.201900663.

[252] J.W. Ju, L.Z. Sun, A Novel Formulation for the Exterior-Point Eshelby's Tensor of an Ellipsoidal Inclusion, J Appl Mech. 66 (1999) 570–574. https://doi.org/10.1115/1.2791090.

[253] S.W. Park, R.A. Schapery, Methods of interconversion between linear viscoelastic material functions. Part I - A numerical method based on Prony series, Int J Solids Struct. (1999). https://doi.org/10.1016/S0020-7683(98)00055-9.